University of Glasgow

A Series Of Experimental Investigations Into Different Manifestations Of The Vortex Ring State.

David Jonathan Pickles

Submitted in fulfilment of the requirements for the
Degree of Doctor of Philosophy

Aerospace Sciences Research Division
School of Engineering
College of Science and Engineering
University of Glasgow

October 2020

Dedicated to the memories of my 'Grandfather' Dr. Alan Gibson Heaton. BSc, PhD. (1925-2017).

" We have come a long way from balancing helium balloons using bits of cardboard in the living room."

ABSTRACT

The fluid dynamics of a helicopter rotor present many challenging phenomena. The flow is dominated by a system of intertwined helical vortices that trail from the rotor blades, which persist and remain in the vicinity of the rotor for many rotor revolutions. Of interest here is the vortex ring state (VRS), which is typically associated with the descent of a rotor into its own wake. In the vortex ring state the trailed vortex system collapses from its usual helical structure to form a toroidal vortex ring of the same scale as the rotor diameter. The vortex ring is highly unsteady, and sheds off and reforms, leading to large unpredictable thrust fluctuations. It is currenty believed that the mutual-inductance instability of helical vortices is responsible for the breakdown of the rotor wake into the toroidal form associated with the vortex ring state. Subsequently, computational investigations have revolved around modelling the trailed vortex system for extended periods of time. Experimental investigations have also typically been configured to generate a trailed vortex wake.

The aim of this work is to explore the role blade tip vortices have on the breakdown of the helical rotor wake into the unsteady toroidal form associated with the vortex ring state. In order to achieve this, a series of experimental investigations into the structure of the flow field produced by a shrouded rotor, a unshrouded rotor, a ventilated open core annular jet and a rotor with a large root cut out were performed. Each of these experimental configurations produced mean velocity profiles that were notionally similar. With a ring of high velocity flow surrounding a low velocity core. However, the structure of the wake produced by each configuration differed considerably. Unlike the wake produced by an unshrouded rotor, the wake produced by the shrouded rotor and the ventilated open core annular jet did not contain a helical vortex system. Despite this, in axial descent, each of the experimental configurations investigated entered states analogous to the vortex ring state of an isolated rotor. The results presented in this thesis show that the mechanism by which the wake produced by the shrouded rotor and the ventilated open core annular jet broke down into the toroidal form associated with the VRS of an unshrouded rotor were similar. Indicating that the breakdown of the rotor wake, into the toroidal form of the VRS is a result of the interaction between an axially induced flow, which consists of a low velocity core surrounded by a ring of higher velocity air, and a uniform counterflow.

CONTENTS

LIST OF FIGURES

LIST OF TABLES

PREFACE

This thesis presents work carried out by the author in the Aerospace Sciences Research Division at the University of Glasgow during the period from October 2016 to October 2020, supervised by Dr Richard Green and Dr Angela Busse. The work was funded by the EPSRC. Acknowledgement is given to the National Wind Tunnel Facility, EPSRC Grant Number EP/L024888/1, for the provision of experimental equipment.

ACKNOWLEDGEMENTS

Firstly, I would like to express my deepest gratitude to my advisor Dr. Richard Green, for his continuous support of my PhD. research. His guidance and knowledge has been invaluable in helping me bring this dissertation to fruition. I would also like to express my gratitude to Dr. Angela Busse for the insightful discussions we had.

Furthermore, i would like to extend my thanks to Angel Zarev for the countless hours we spent working at the wind tunnels; Sarah Fitzpatrick for her unwavering support; Dr Daniele Zagaglia for his valuable advice; Dr. Saun Skinner, Michael Waznawrenka, Ross Higgins and Blaga Nenkova for our discussions and your encouragement; Andrew McIntyre, Eleanor Holden, Johnny Young and Hannah Young for checking in on me when I was having a hard time. Thanks should also go to Dr Ana Costa for her support and patience over the last ten months. The process would have been much harder without you.

Finally, a special thank you to my family: especially my parents, my sister and my grandma for supporting me through this thesis and my life in general. Thank you for always being there to support me, for listening to my incessant ramblings on wind tunnel testing and for proof reading every last word I wrote.

AUTHOR'S DECLARATION

"I declare that, except where explicit reference is made to the contribution of others, that this dissertation is the result of my own work and has not been submitted for any other degree at the University of Glasgow or any other institution."

Printed Name: David Jonathan Pickles

Signature: _____

Date: 02.10.2020

NOMENCLATURE & ABBREVIATIONS

UNITS

All units of measurement throughout this thesis conform to the *Système Internationale*, with deviations from this rule noted where appropriate.

NOTATION

This section describes the general form of notation for properties such as scalars, vectors and matrices and their derivatives.

SCALARS, VECTORS AND MATRICES

A	Rotor Disk Area πR^2, (m^2)
A_e	Shroud Diffuser Exit Area πR_s^2, (m^2)
A_o	Jet Outlet Area $\pi(D_o^2 - D_i^2)/4$, (m^2)
B	Counter Flow Diameter, (m)
B_o	Buoyancy Flux
c	Chord, (m)
D	Rotor Diameter, (m)
D	Nozzle Outlet Diameter, (m)
D_i	Annular Slot Inner Diameter, (m)
D_j	Round Jet Diameter, (m)

D_o	Annular Slot Outer Diameter, (m)
$[F]$	Notional Flow Field
i	PIV Image Pair
L_d	Shroud Diffuser Length, (m)
$[U]$	Velocity Matrix, (ms^{-1})
U_{ex}	Jet Slot Exit Velocity, (ms^{-1})
U_i	Notional Induced Velocity, (ms^{-1})
U_{i_R}	Induced Velocity Ratio Of The Unshrouded Rotor, (ms^{-1})
U_j	Round Jet Velocity, (ms^{-1})
U_o	Descent Velocity/ Counter Flow Velocity, (ms^{-1})
u	Axial Velocity Component, (ms^{-1})
k	Number Of Histogram Bins
M	Magnification Factor , $(pixel/mm)$
m	POD mode
N_b	Number Of Rotor Blades
n	Rotor Speed, (Hz)
Q_o	Flow Rate, $(m^3 s^{-1})$
R	Rotor Radius, (m)
R_c	Root cut out, (m)
R_e	Reynolds $\frac{\rho V_{Tip} c}{v}$
R_s	Diffuser Exit Radius, (m)
r_{lip}	Shroud Inlet Lip Radius, (m)
S_k	Skewness
T	Thrust, (N)
t	Time, (s)
t	Thickness, (m)

V_{Tip}	Rotor Tip Speed ΩR, (ms^{-1})
V_{mag}	Velocity Magnitude, (ms^{-1})
v	Radial/ Tangential Velocity Component, (ms^{-1})
v	Dynamic Viscosity, $(kgm^{-1}s^{-1})$
x, y, z	Cartesian Coordinate System
x_p	Penetration Length, (m)
α	Velocity ratio U_o/U_i
α_{TPP}	Rotor tip-path-plane angle of attack, (Positive tilted forward) $(^o)$
β	Blade Pitch, $(^o)$
β	Non-Dimensional Time Parameter $t\|U_o\|/D$
γ	Descent Angle, $(^o)$
δ_{tip}	Blade Tip Clearance, (m)
ϵ_u	Error, (ms^{-1})
θ_d	Shroud Included Angle, $(^o)$
Ω	Rotor rotational speed $2\pi n$, $(rads^{-1})$
ρ	Density, (kgm^{-3})
Σ	Singular Values
σ_d	Shroud Diffuser Expansion Ratio A_e/A
Φ	Left Singular Vectors
Ψ	Right Singular Vectors (POD Mode Reconstruction Coefficient)

ABBREVIATIONS

CFD	Computational Fluid Dynamics
FAA	Federal Aviation Administration
LDA	Laser Doppler Anemometry
NTSB	National Transportation Safety Board
OCAJ	Open Core Annular Jet
PIV	Particle Image Velocimetry
POD	Proper Orthogonal Decomposition
RMS	Root Mean Square
SPIV	Stereoscopic Particle Image Velocimetry
UAV	Unmanned Aerial Vehicles
VRS	Vortex Ring State
VTM	Vorticity Transport Model

CHAPTER 1

INTRODUCTION

The fluid dynamics of a helicopter rotor present many challenging flow phenomena, one of which is known as the vortex ring state (VRS). The wake from a rotor is typically dominated by a system of intertwined helical vortices that trail from the rotor blades as shown in figure 1.1a and 1.1b. These blade tip vortices remain in the vicinity of the rotor for a long period of time causing significant interactional, vibrational and aeroelastic effects. When operating against a counter flow the trailed vortex system can collapse forming a highly unsteady vortex ring of a similar scale to that of the rotors diameter, otherwise known as the vortex ring state, as shown in figure 1.1c and 1.1d. The build-up and subsequent shedding of the vortex ring occurs over a number of rotor revolutions. Shedding of the vortex ring from the rotor leads to the large unpredictable thrust oscillations characteristic of rotors operating in the VRS. The mutual inductance instability of helical vortex filaments is currently believed to be responsible for the breakdown of the rotor wake into the toroidal form associated with the VRS. Bhagwat and Leishman. (2000), Leishman et al. (2004) and Ananthan and Leishman (2006) showed numerically that the mutual-inductance instability is responsible for the bundling of vortex filaments into rings which move towards the rotor as it approaches the VRS. Despite our knowledge of this mechanism, low-order momentum theory based models, such as those developed by Gessow (1948), Newman et al. (2003) and Johnson (2005) continue to be used to define the boundary of the VRS and rotor performance characteristics of helicopters and tiltrotors operating in descent despite not incorporating blade tip vortices in their analysis. Therefore, the role of the blade tip vortices on the formation of the VRS will be explored experimentally in this thesis.

1.1 LITERATURE REVIEW

The VRS is a fluid dynamic phenomenon often associated with rotorcraft, multi rotor unmanned aerial vehicles (Marino et al., 2015) and wind turbines (Leble and Barakos

Rotor Type	Operational Condition
Helicopter Main Rotor	Under certain axial descent conditions (Leishman, 2006). Low descent and low forward velocity. Power recovery manoeuvre after a engine power off (Ferrell and Shapley, 1968). During an up draft. Quick stop/pull up manoeuvres (Ananthan and Leishman, 2006). Accelerations (Ananthan and Leishman, 2006). Pull Ups (Ahlin and Brown, 2005).
Helicopter Tail Rotor	In sidewards flight (Durand (1978), Faulkner and Buchner (1980), Glauert (1926)). When hovering in a crosswind (Taamallah, 2010). Whilst rotating on the spot during hover.
Multi-rotor UAV's	In axial descent.
Floating Wind Turbines	Pitching oscillations (Leble and Barakos, 2016). Floating offshore wind turbines during surge (Kyle et al., 2020).
Tiltrotor	Under certain axial descent conditions (Abrego et al., 2002). Low descent and low forward velocity (Washizu et al., 1966b).

TABLE 1.1: Table summarising the operational conditions that lead a variety of rotors to enter the VRS.

(2016), Kyle et al. (2020)). For rotorcraft, on which this research will focus, entry into the VRS leads to large unpredictable thrust oscillations, an increase in the average rotor power required, and the loss of control efficiency, which can, in some conditions, lead to the loss of the aircraft (Reeder and Gustafson (1949),Brotherhood (1949)). The U.S. NTSB, U.S. Navy and Army and the U.K. Air Accidents Investigation Branch identified that the VRS was responsible for the loss of thirty two helicopters between 1982 and 1997 (Hoydonck et al., 2009), and was also a contributing factor to the loss of the U.S. Marines V22 Osprey in April 2000 (Dailey et al., 2001). This accident acted as a catalyst to re-energise research into the VRS, as a lot of the design traits of the V22, such as the incorporation of highly twisted and highly loaded blades, can also be found in modern helicopters. These modern design traits have developed to allow rotor craft to meet an ever-expanding list of operational requirements. Despite this resurgence, helicopters continue to encounter the VRS as demonstrated by the loss of the EuroCopter AS 332 L2 Super Puma in August 2013 (SKYbrary). A summary of the operating conditions that have been associated with the VRS are presented in table 1.1.

Despite the dangers associated with operating in the VRS, a small number of experiments have been performed on full scale helicopters in order to characterise their response to the VRS. (See table 1.2). Reeder and Gustafson (1949) showed that the helicopter experienced violent thrust, yaw and roll fluctuations which resulted in a loss

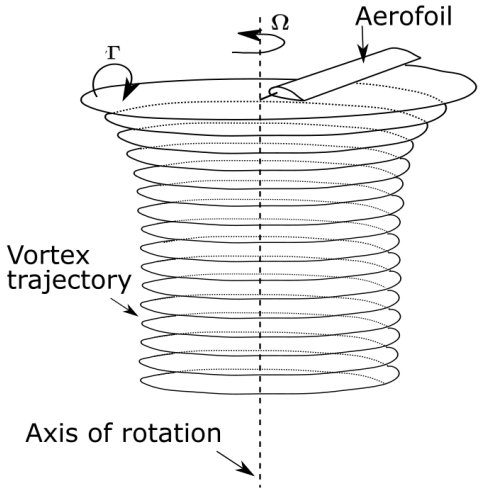

(A) Schematic diagram of a helical vortex wake produced by a rotor.

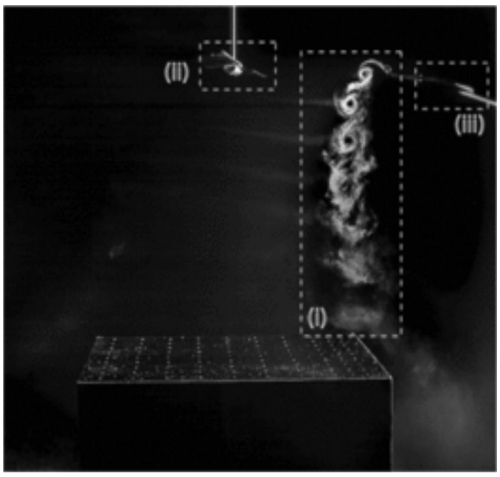

(B) Smoke Flow Visualisation of a rotor operating above an obstacle taken from Pickles et al. (2018).

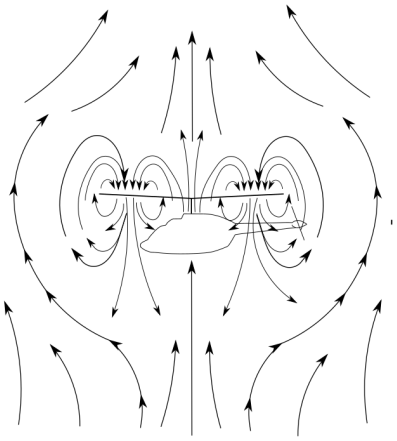

(C) Schematic of the VRS redrawn from FAA (2019).

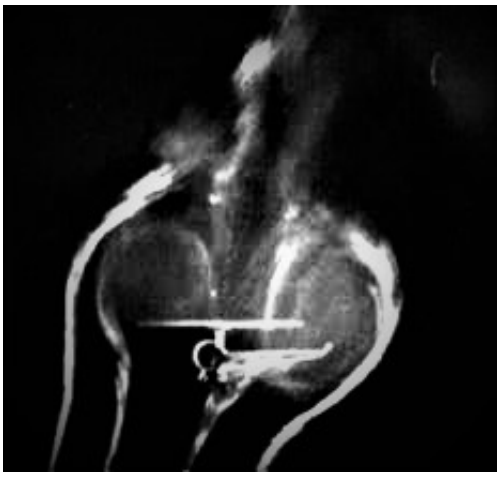

(D) Smoke Flow Visualisation of a helicopter in the VRS taken from the work of Drees and Hendal (1951a).

FIGURE 1.1: Standard Rotor wake depiction

of control efficiency, a nose-down pitching moment, and a significant loss of altitude before the pilot could regain control. Motion picture studies of the tufted blades of this rotor indicated that these effects were not a result of the aerodynamic stall, however, pronounced and highly irregular blade bending was observed. Investigations by Brotherhood (1949) and Stewart (1951) found that the response of individual helicopters to the VRS varied, from mild wallowing in some, to a complete loss of control in others. Stewart (1951) attributed these effects to the turbulent nature of the flow field, and its interaction with the fuselage of the helicopters. Drees and Hendal (1950) later identified, using smoke flow visualisation, that the nose-down pitching moment was a result of the tail boom operating in an up flow which results from the formation of the vortex ring, as shown in figure 1.1d.

Escape from the VRS can be achieved by increasing the pitch of the helicopter

blades, a sustained demand for forward motion (Reeder and Gustafson, 1949), or by entering the windmill brake state. Both of these techniques require the rotor to escape the vortex and enter 'clean' air, after which control can be reacquired. Increasing blade pitch will tend to allow the rotor to climb free of the VRS, however, if insufficient power is available, this can aggravate the VRS. The Vuichard recovery technique (FAA, 2019) eliminates the descent rate characteristic of entry into the VRS. Upon entry into the VRS, the pilot should increase collective to the maximum available power, and simultaneously apply pedal controls to maintain heading and a bank of between $(15 - 20^o)$ to get a lateral movement until the rotor escapes the upwind part of the vortex. For helicopters with counter-clockwise rotating main rotor systems, escape should be to the right hand side of the aircraft (Helicopters with clockwise rotating main rotors should escape to the left hand side of the aircraft). This technique reduces the average height loss, as a result of entering the VRS from approximately $120m$ to between $(6$ and $15)m$, dependent on the duration of the recovery manoeuvre (FAA, 2019). Tandem rotor helicopters like Boeing's H-47 Chinook should manoeuvre laterally so that both rotors recover and enter clean air at the same time (FAA, 2019). The VRS manifests itself as a 'roll off' in tiltrotors where one rotor enters the VRS. Pilots of these vehicles are taught to escape the VRS by a lateral cyclic input or by applying a forward nacelle tilt (Johnson, 2005). It should be noted that the complexity of the VRS means that flight tests are of limited use to deepen our understanding of the underlying flow mechanisms responsible for the onset of the VRS. Therefore, several researchers have performed investigations into the VRS under controlled laboratory conditions.

1.1.1 MEAN FORCE AND ROTOR PERFORMANCE PARAMETERS OF THE VRS.

Since its initial identification by Bothezat (1919), there have been a number of experimental and numerical investigations into this complex flow phenomenon which occurs when a rotor descends into its own wake. Initial investigations performed by Lock et al. (1925), Glauert (1926), Castle and Gray (1951) ,Taghizad et al. (2002), and Gessow (1948), attempted to calculate steady, mean, rotor performance parameters such as: rotor inflow, induced velocity, thrust and power, by applying constants to helicopter actuator disk theory.

Actuator disk theory is a low order model that applies the conservation of momentum to a stream tube that passes through the rotor disk (Leishman (2006), Newman (1994) and Spalart (2003)). The flow through the rotor is assumed to be one-dimensional, quasi-steady, incompressible and inviscid. The rotor itself is represented as a discontinuity over which a pressure jump occurs. This produces a stream tube that contains no discrete vortex filaments, and does not incorporate any of the complex flow features associated with rotor wakes. Actuator disk theory is only valid in flight conditions where a well defined stream tube exists, therefore it is typically defined as invalid within the VRS (i.e when the ratio of descent velocity U_o to hover induced

Investigation	Helicopter
Reeder and Gustafson (1949)	Sikorsky R4
Brotherhood (1949)	Sikorsky R4
Stewart (1951)	Sikorsky R-4B, R-6, S-51
	Bell 47, Bristol 171
Gustafson and Gessow (1945), Gustafson (1945)	YR-4B
Gessow (1948)	YR-4B
Yeates (1958)	Unspecified tandem helicopter
Scheiman (1964)	H-34
Padfield (1996)	Wessex 2
Taghizad et al. (2002)	SA 365N Dauphin 6075

TABLE 1.2: Table documenting the full scale experimental investigations into the VRS, and and the helicopters used.

velocity U_i is between $-2 < \alpha = (U_o/U_i) < 0$. At higher descent rates the wake re-establishes itself into a structured stream tube. Therefore, momentum theory is valid in the windmill brake state, hover and during axial climb. It was noted by Washizu et al. (1966a) that momentum theory predictions for the induced velocity of a rotor in inclined descent followed the same trends as their experiments, however momentum theory under-predicted the inclined rotors induced velocity (U_i), as shown in figure 1.2 In figure 1.2 the averaged induced velocity of the rotor, at rotor disk angles of attack (α_{TPP}) of $20, 50$ and 70^o are compared with the theoretical values calculated from momentum theory assuming that the velocity components of the rotor which are normal and parallel to the rotor disk plane are $-u_o \sin(\alpha_{TPP})$ and $u_o \cos(\alpha_{TPP})$ respectively.

The scatter of data observable in figure 1.3 and figure 1.2, is believed to be a result of the large fluctuations in thrust and the increase in the average torque associated with operating in the VRS. These thrust fluctuations reportedly reach a maximum of between 45% and 80% of the mean at a axial descent velocity of $\alpha \approx 1.2$. (Yaggy and Mort, 1962). Fluctuations of this magnitude cause significant blade flapping and a loss of rotor control. One set of experimental results presented in figure 1.4 shows that the magnitude of these thrust fluctuations was dependent on the rotor disk loading (T/A). Rotors with higher disk loading experienced lower magnitude thrust fluctuations over a smaller range of decent velocities. Similar experiments performed by Washizu et al. (1966a) found that disk loading had no effect. The unsteadiness arises from the gradual build up of vorticity around the rotor, which then sheds generally aperiodically into the free stream. Savas et al. (2009) showed experimentally that the build up of vorticity occurs over a number of rotor revolutions. Primary frequency data, produced by analysing the thrust fluctuations for several experimental investigations, presented in table 1.3 does not show any clear data trends.

It is generally accepted, thanks to the numerical simulations of Azuma and Obata

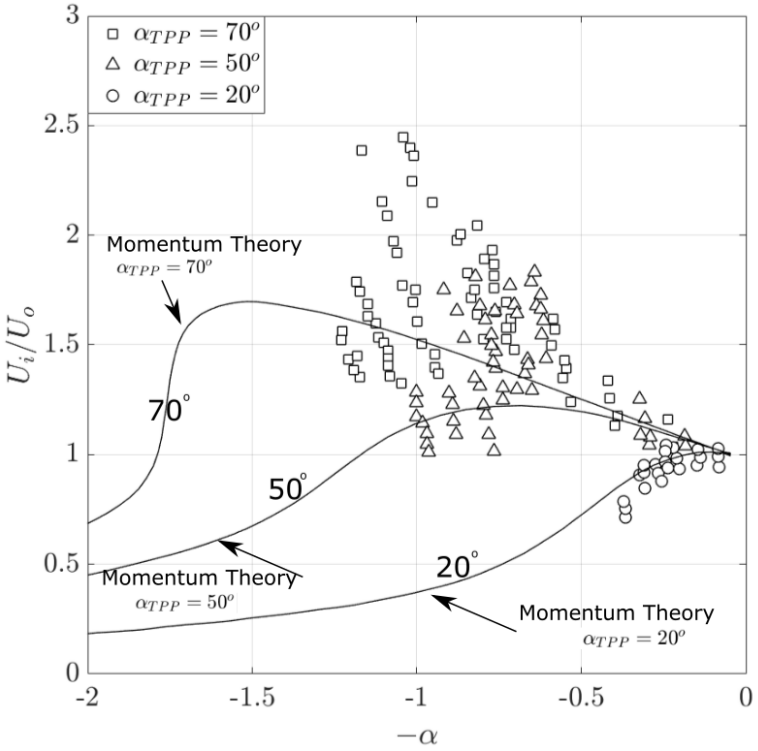

FIGURE 1.2: Thrust fluctuations plotted as a percentage of the mean thrust produced by a rotor operating in axial descent, including the VRS, as the rotor tip-path-plane angle of attack varied. The data which was originally presented by Yaggy and Mort (1962) and Washizu et al. (1966a).

(1968), that the mean thrust loss associated with the VRS is a result of a reduction in loading on the outboard section of the rotor blades This occurs because the re-circulation around the rotor tip leads to an increase in the local inflow, effectively reducing the lifting capability of these sections of the blades (Azuma and Obata, 1968). The build up of vorticity near to the rotor results in the loss of thrust, if the pitch of the rotor is held constant (Yaggy and Mort (1962), Azuma and Obata (1968)), or an increase in the power required by the rotor if the thrust produced by the rotor is maintained constant. (Castle and Gray, 1951).

Several attempts have been made to characterise the effect rotor geometry has on the behaviour of the VRS, however it is not possible to find agreement between individual investigations, as the rotors investigated differ considerably. Disk loading and blade twist were investigated experimentally by Castle and Gray (1951), Yaggy and Mort (1962), Washizu et al. (1966a), Azuma and Obata (1968), Gao (1999) and Newman et al. (2004). In these experiments the thrust and torque produced by a variety of different rotors was measured as the descent velocity of the rotors was varied. However, no clear conclusions can be drawn. Trends resulting from blade twist were observed in some of these experiments. However other experimental investigations, such as those performed by Azuma and Obata (1968), indicate that there is no clear pattern of behaviour for blade twist or blade loading. The operation

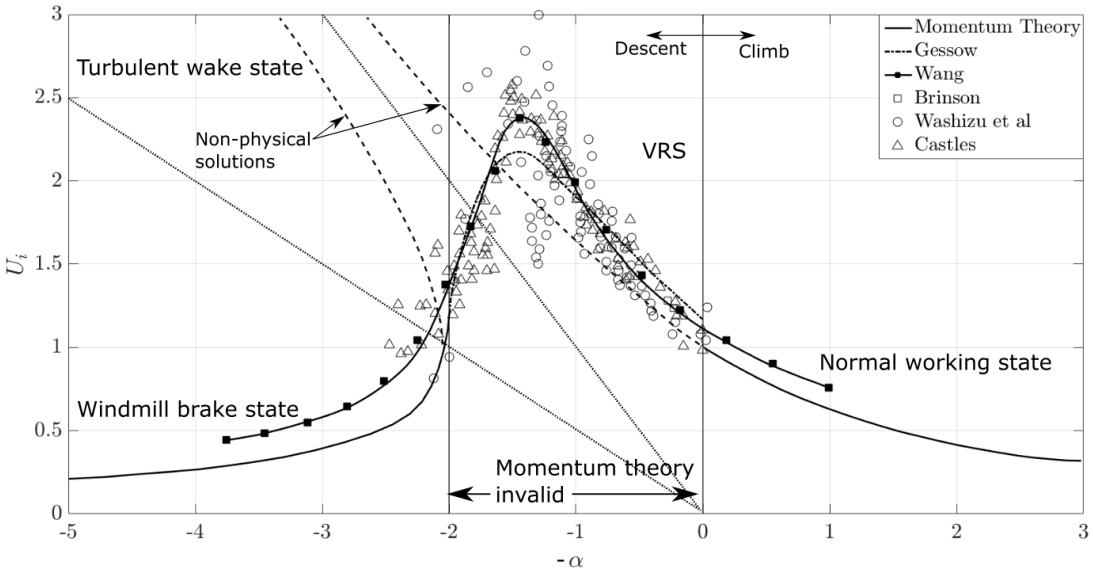

FIGURE 1.3: Mean induced velocity (U_i) produced by a rotor operating in axial flight. The momentum theory based predictions of Gessow (1948) and Wang (1990) are compared against several experimental investigations (Washizu et al. (1966a), Castles (1958) and Brinson (1998)).

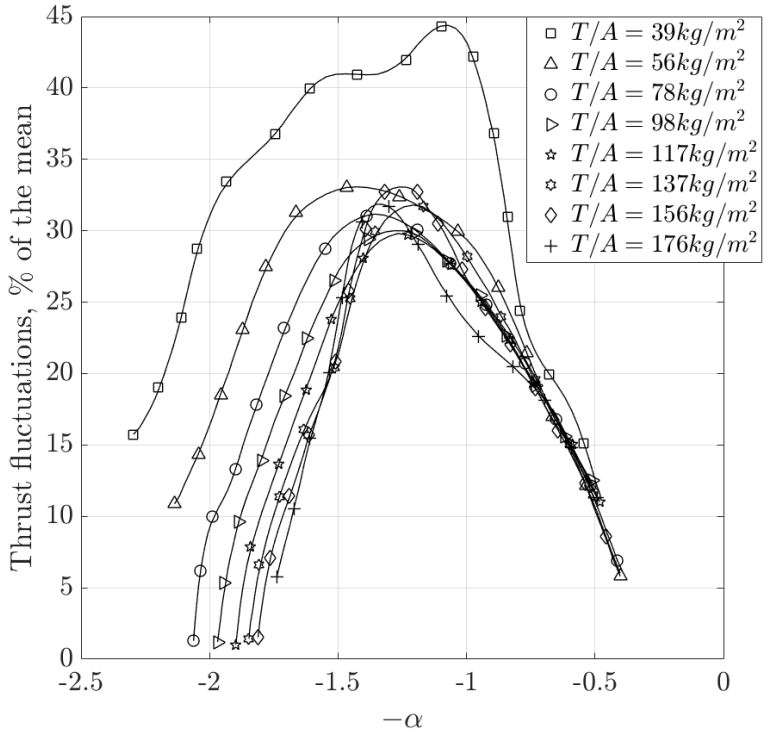

FIGURE 1.4: Measured rotor thrust fluctuations in axially descending flight through the VRS for different rotor disk loadings. Data replotted from Yaggy and Mort (1962).

Investigation	$\omega R/U_i$	Operational Condition
Yaggy and Mort (1962)	$3-5$	all
Yeates (1958)	$1.4-2$	axial $\alpha = 0.4$
	$0.95-1.1$	axial $\alpha = 1.1$
Washizu et al. (1966a)	$0.7-1.4, 0.14-0.3$	axial
Xin and Gao (1994)	$1.3, 2.5, 0.8$	axial $\alpha = 0.75$
Brinson (1998)	0.6	axial
Betzina (2001)	0.2	axial $\alpha = 0.7$
Savas et al. (2009)	0.06	axial $\alpha = 0.79, 0.82$

TABLE 1.3: Measured frequencies of the Vortex Ring State

of the rotor can also differ between individual investigations. Castle and Gray (1951) varied the pitch of their rotor to ensure that rotor thrust was held constant for each descent velocity investigated. Later investigations by Yaggy and Mort (1962) and Washizu et al. (1966a) ensured that the rotor pitch angle was held constant, resulting in an increase in rotor thrust with descent rate. The numerical simulations of Brown et al. (2002) and Ahlin and Brown (2005) suggest that unidentified blade stall may have modified the rotor performance of experimental investigations where pitch was kept constant or where disc loading was high. However no experimental data exists to support these assumptions.

1.1.2 FLUID DYNAMICS OF THE VRS.

Research into the VRS has mainly focused on the accurate estimation of steady mean rotor performance parameters, whilst the dynamics of the flow field have only recently started to be qualitatively investigated. The smoke flow visualisations, performed by Drees and Hendal (1950) and Drees and Hendal (1951a), which have been referenced in nearly every investigation into the VRS since, showed the general features of the flow field (figure 1.1d). Hot wire anemometry and smoke flow visualisation was also used by Brinson (1998) and Drees and Hendal (1951b) to identify a conical region of reverse flow which can penetrate up through the centre of the rotor.

Quantitative PIV measurements of the flow field produced by a model rotor operating in axial descent were performed by Green et al. (2005). At low descent velocities, the mean flow field resembled that of a rotor operating in hover. Increasing the descent velocity revealed the formation of a saddle point, and the conical region of reverse flow, located directly underneath the rotational axis, which approached the rotor disk as the descent velocity was increased. The wake from the rotor breaks down into a ring of vorticity characteristic of the VRS, an example of which is shown in figure 1.5b. Proper Orthogonal Decomposition (POD) indicated that the flow field intermittently switched between the two flow topologies shown in figure 1.5. The geometry of the flow field can differ considerably from the mean flow field, and at a fixed descent velocity the distance of the saddle point from the rotor varied as a

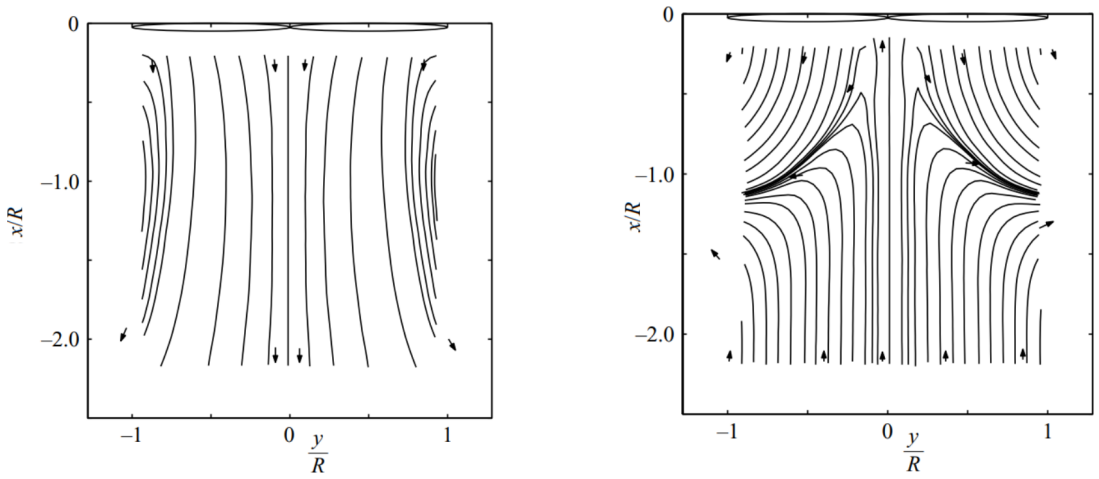

(A) Hover (B) VRS

FIGURE 1.5: Images of the characteristic flow topologies associated with a rotor operating in hover (figure 1.5a), and within the VRS (figure 1.5b). Images taken from Green et al. (2005).

result of the flow fields unsteadiness. The frequency with which of the flow entering the VRS topology occurred, increased as the descent rate increased, until the flow remains locked within the toroidal form. The unsteadiness of the flow field and, therefore, the behaviour of the rotor, results from the generally aperiodic and spatially non-uniform way that vorticity builds up around the rotor, before being shed into the free stream. In some flight conditions, Stack et al. (2005) and Savas et al. (2009) showed experimentally that the periodic detachment of the vortex ring, from the rotor disk plane caused periodic oscillations of the rotors thrust to occur. Large area PIV experiments were also performed by Newman et al. (2001). These investigations, whilst providing some insight into the structure of the flow field, did not outline the underlying fluid dynamic processes that govern the behaviour of the rotor wake. This is in contrast to the synchronised thrust and flow visualisations of Stack et al. (2005), which identified leapfrogging of the blade tip vortices as the mechanism responsible for the formation of the vortex ring. Leapfrogging is typically associated with the interaction of two or more axially aligned vortex loops, as shown in figure 1.6, for which induced velocity causes them to contract and expand, thereby altering their individual descent velocities. Linear stability analysis of helical vortex filaments revealed the existence of small geometric perturbations to the helix, that manifest themselves with wavelengths equal to a few core diameters, or over several helix diameters. The theoretical analysis of helical vortex filaments performed by Gupta and Loewy (1974) and Widnall (1972) identified a third instability, 'mutual-inductance', as the interaction between immediately adjacent turns of the helix.

Free-wake simulations of a helicopter rotor in axial descent performed by Bhagwat and Leishman. (2000), Leishman et al. (2004), and Ananthan and Leishman (2006) associated this mutual-inductance instability, sometimes known as the 'vortex pairing' mode, with the bundling of vortex filaments into rings, which move towards the rotor

as it approached the VRS. Ahlin (2007) showed that, within the linear range and for finite amplitude disturbances, the mutual induction mode results in the entanglement of individual turns of the helix. A cross section through the entangled helix shown in figure 1.7b resembles the leapfrogging of vortex filaments identified by Stack et al. (2005). These investigations showed that the wake of a rotor is inherently unstable, even when operating in hover. The growth rate of disturbances to the helical structures are related to the relative spacing between adjacent vortex filaments (Widnall (1972), Bhagwat and Leishman. (2000)). In hover, the growth of these disturbances leads to the breakdown of the helix away from the rotor. In descending flight, this breakdown occurs in the vicinity of the rotor leading to the development of the vortex ring (Newman et al. (2003), Ahlin and Brown (2007), Brown et al. (2004)). These results must be viewed with some caution, because the complexity of the flow field means that a linear stability analysis cannot completely describe the highly non-linear process that causes the helical vortex system to break down into the toroidal form of the VRS.

High resolution computational fluid dynamic simulations (CFD) of a rotor entering the VRS from the windmill brake state and from hover, using the Vorticity Transport Model (VTM) developed by Brown (2000), were performed by Ahlin and Brown (2009). When the rotor transitioned into the VRS from the windmill brake state, the blade tip vortices reorientated themselves to form a hairpin structure which was then ejected into the free stream, as shown in figure 1.8. The ejection of the hairpin vortex disrupted the formation of the normal helical vortex structure for several rotor revolutions. Hairpin vortices were not observed in the rotor wake when it transitioned from hover into the VRS, indicating that the underlying mechanism may differ depending on the way the rotor enters the VRS. These simulations also showed that the up flow through the rotors root section, identified by Brinson (1998) and Green et al. (2005) was dependent on the 'mutual-inductance' of the root-vortex system. When entering the VRS from hover, Ahlin and Brown (2009) concluded that the collapse of the blade tip vortex system was driven by a reduction of the rotors downwash resulting from the collapse of the root vortex system. This is particularly important as the root vortex system is typically omitted from other numerical simulations of the VRS, such as the work of Bhagwat and Leishman. (2000).

Studies using the vorticity transport model suggest that the two flow topologies identified by Green et al. (2005) are, in fact, different manifestations of the same flow topology. Perry et al. (2007) concluded that the topology of the velocity field of a rotor operating in hover and within the VRS, were all toroidal in nature, with a saddle point located underneath the rotor. This can be observed in the mean velocity fields of a rotor operating in axial descent, as shown in figure 1.9. The relatively small size of experimental fields of view examples was theorised to be the reason this was not observed before, an example of which is shown in figure 1.9a. The linear decaying vortex tube method, which was initially developed by Wang (1990), and later extended by Perry et al. (2007) predicts mean rotor inflow, to a reasonable level of accuracy.

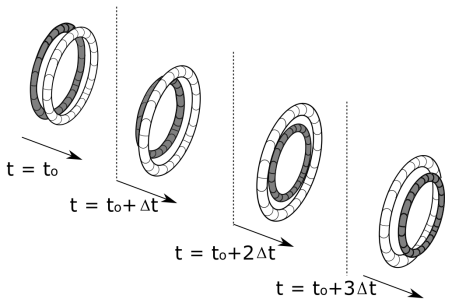

(A) 3D Schematic redrawn from Ahlin and Brown (2009)

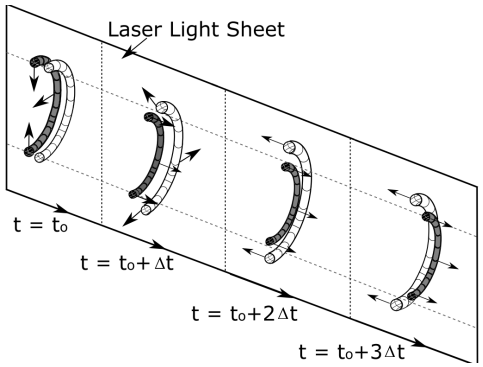

(B) Cross Sectional view

FIGURE 1.6: Schematic diagrams depicting the classical leapfrogging of vortex rings identified by Stack et al. (2005), in three dimensions (figure 1.6a) and the cross section that would be observed if this process was investigated using a thin laser light sheet, aligned through the centre of the vortex ring. (figure 1.6b).

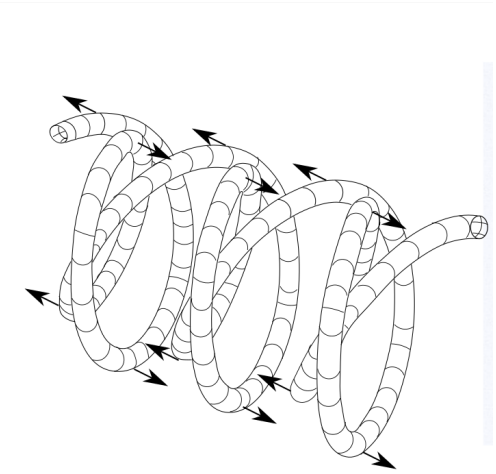

(A) 3D Schematic redrawn from Ahlin and Brown (2009)

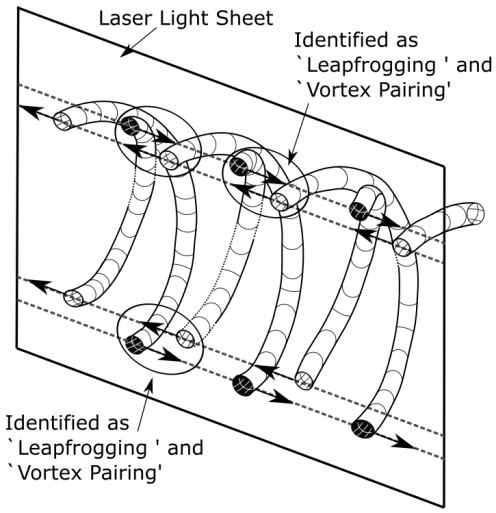

(B) Cross section through the entangled Vortex.

FIGURE 1.7: Schematic diagrams depicting the mutual inductance instability of a helical vortex identified by Widnall (1972), in three dimensions (figure 1.7a), and the cross section that would be observed if this process was investigated using a thin laser light sheet, aligned through the centre of the vortex ring. (figure 1.7b).

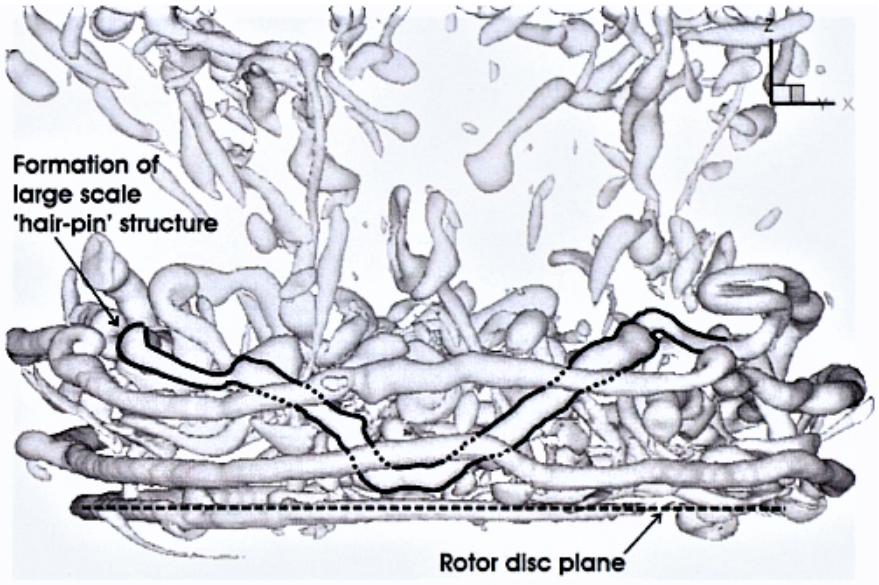

FIGURE 1.8: Numerical simulation of a rotor entering the VRS from the windmill brake state performed by Ahlin (2007) showing the formation of a 'hair-pin' vortex from the 'mutual-inductance' instability of a helical vortex. Figure adapted from Ahlin (2007).

An alternative study by Brand et al. (2011), using a ring emitter model, suggested that the use of steady speed wind tunnel tests, which make up a large proportion of the research into the VRS, did not appropriately simulate the unsteady effects of the VRS. They argue that the rotors thrust and descent velocity must be coupled in order to accurately simulate this flow phenomenon. The vortex rings transition from below to above the rotor, and its subsequent shedding, is responsible for the sudden loss of altitude characteristic of entry into the VRS. In free flight, this only happens once, whilst steady speed wind tunnel tests force this mechanism to continuously repeat itself. Contrary to the research described earlier, Brand et al. (2011) postulated that disorganization of the vortex filaments is not a characterising feature that enables the VRS to occur. There is little direct experimental support for these numerical simulations investigating how the VRS develops.

1.1.3 MODELING THE ONSET OF THE VRS.

Numerous attempts at developing models to accurately predict the onset of the VRS have been made, as this would aid in the design of flight safety systems. The first onset model, derived by Wolkovitch (1972) combined momentum theory and actuator disk theory in order to predict the critical speeds and descent angles at which unsteady flow occurs. The model assumed that the VRS occurred when the rotors descent speed approached that of the induced convection speed of the blade tip vortices in hover.

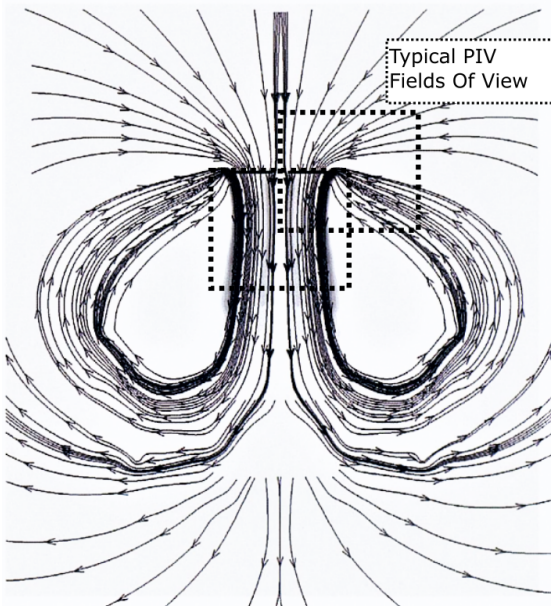

(A) $\alpha = 0.0$

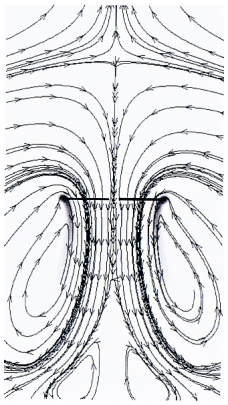

(B) Perturbed hover

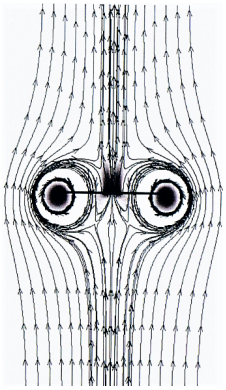

(C) $\alpha = 0.38$

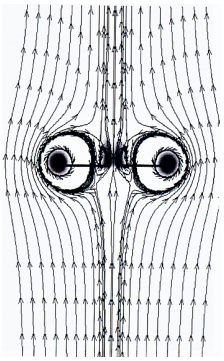

(D) $\alpha = 0.5$

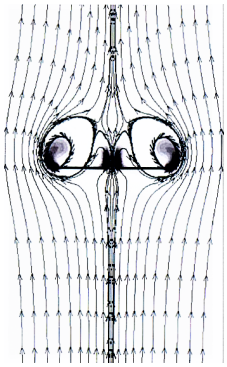

(E) $\alpha = 0.75$

FIGURE 1.9: Mean flow field analysis of the flow field produced by a rotor operating in axial descent over a range of descent velocities from $\alpha = 0.0$ to 0.75. These images were produced by Perry et al. (2007) using a VTM. Note the formation of a toroidal flow field around the rotor at all descent velocities.

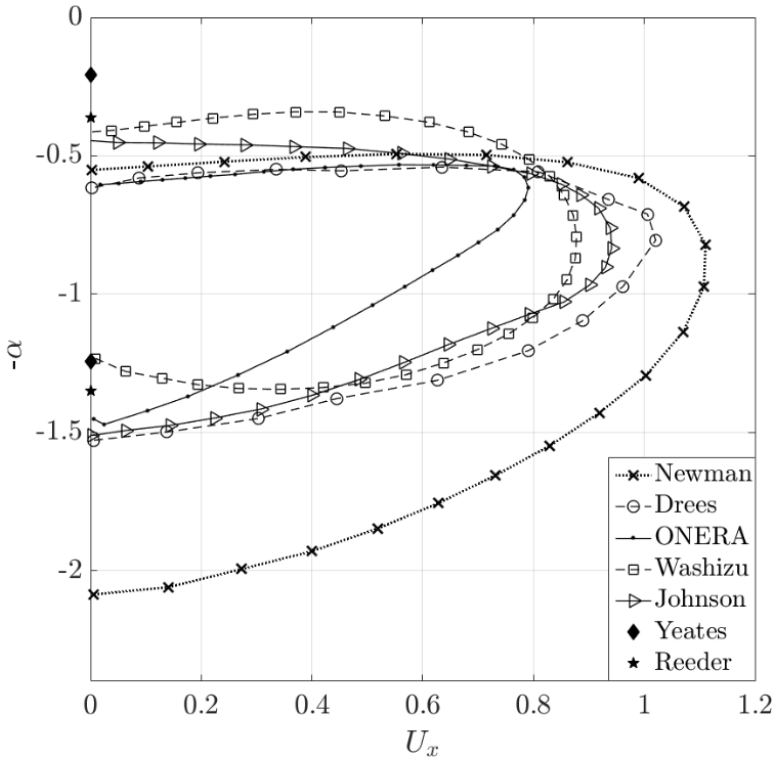

FIGURE 1.10: VRS boundaries defined by Yeates (1958), Drees and Hendal (1951a), Johnson (2005), Newman et al. (2003), Washizu et al. (1966a) and Reeder and Gustafson (1949) are compared. Data replotted from Johnson (2005).

This model was extended by Peters and Chen (1982) to include the dynamic inflow model which has been used to determine the response of hingeless rotors to unsteady inflows Peters (1974) and the flap-lag stability of helicopters in powered flight and autorotation Wei (1978). In the model the normalised induced flow and the velocity of the free stream flow were used to determine the boundary of the VRS. Instabilities in the dynamic inflow perturbations were also used to defined the boundary of the windmill brake state i.e. when the rotor exited the VRS. Available experimental data suggests that the onset of the VRS occurs at a descent speed that is significantly lower than the convection speed of the tip-vortices. An alternative model more commonly used in the literature was derived by Newman et al. (2003). This model is based on the notion that disturbances in the wake convect up to the rotor plane once a critical velocity is reached. The critical velocity was calculated from the experimental data produced by Drees and Hendal (1950) using momentum theory considerations. The unstable nature of the wake, resulting from the separation of the vortex filaments from the rotor blades when operating in forward flight, is also incorporated. When a low threshold of thrust fluctuations is used as a measure of VRS onset, this model agrees with existing experimental data for moderately twisted rotors, (Brown et al., 2002) and was used by Brand et al. (2004) and Kisor et al. (2004) when they investigated the behaviour of the V22 Osprey in descent. Unfortunately, the model becomes less accurate for highly twisted rotor blades. Later, Johnson (2005) developed a parametric extension to helicopter momentum theory that allowed the mean inflow of a rotor to

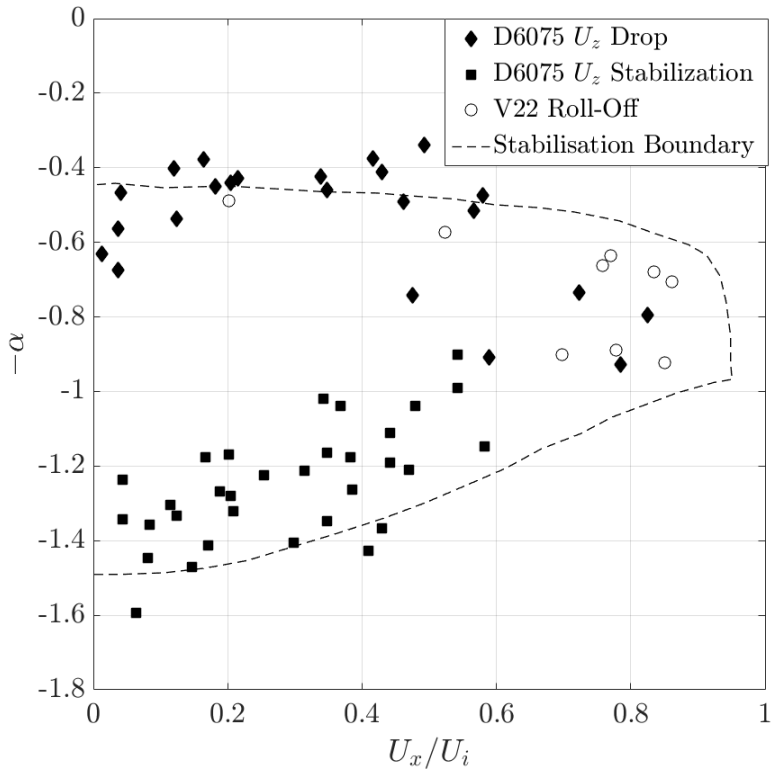

FIGURE 1.11: Helicopter and tiltrotor VRS encounters plotted against the stability boundary derived by Johnson (2005). Figure replotted from Johnson (2005). Experimental data originally sourced from Kisor et al. (2004) and Taghizad et al. (2002).

be calculated. This model allowed for the real time simulation of both helicopters and tilt rotors in the vortex ring state, despite the different manifestations of the VRS. The boundary of the VRS for a selection of these models is presented in figure 1.10. These models all depict approximately the same region of the flight envelope. However the variations observed could potentially lead to a helicopter encountering the VRS unexpectedly. It is for this reason that pilots are taught that the VRS boundary is highly dependent on the type of rotorcraft they are flying (Reimer, 2007). An additional aspect that may influence the development of the VRS is the interaction between the rotor wake and the helicopter fuselage (Brown et al. (2004) and Felker and McKillip (1994)). There is no evidence at the moment to suggest that the velocity at which the rotor enters the VRS changes in the presence of a fuselage, however it seems logical that it would do.

1.1.4 OTHER ROTOR CONFIGURATIONS.

The VRS manifests itself in both tandem helicopters and tiltrotors. For tandem rotors the VRS manifests itself as large irregular thrust fluctuations and vibrations which result in the helicopter becoming difficult to control and experiencing a steady increase in its rate of descent (Yeates, 1958). For tiltrotors the VRS manifests itself as 'roll-off'

because of the differences in the aerodynamic response of the two rotors. Washizu et al. (1966b), Betzina (2001) and Abrego et al. (2002) studied counter-rotating, side by side rotors in the VRS, thereby simulating the flow field produced by a tiltrotor. These investigations showed that the characteristic reduction in thrust and the large unpredictable thrust fluctuations experienced by single rotors operating in the VRS were also present for tiltrotors. Washizu et al. (1966b) and colleagues reported that the VRS operational envelope was larger than that of an isolated rotor. A study by Abrego et al. (2002) concluded that the image plane used by Betzina (2001) did not replicate the interference effects between the two rotors, however it did show that the presence of a second rotor altered the response of the rotors helical vortices. The relative spacing between adjacent vortex filaments increased the growth rate of disturbances to the vortex system, therefore the presence of a second rotor would make both of the rotors helical vortices more susceptible to breaking down into a torus (Bhagwat and Leishman., 2000). However when the parametric extension of momentum theory, derived by Johnson (2005) and the experimental data of Taghizad et al. (2002) and Kisor et al. (2004) are compared, as shown in figure 1.11 the VRS boundary of helicopters and tiltrotors are notionally similar indicating that the presence of the second rotor may not be as significant as previously thought. Kisor et al. (2004) reported that the V22's response to the VRS was delayed in terms of descent speed if it accelerated through the theoretical VRS boundary. This phenomena was also noted by investigations performed by Newman et al. (2003), Ananthan and Leishman (2006) and Ahlin and Brown (2005). Differences in how individual researchers define the boundary of the VRS, may explain some of the differences in the VRS boundary, as shown in figure 1.10.

1.1.5 ASSESSMENT OF THE EXISTING LITERATURE.

Despite its age and the numerous investigations into the phenomenon, a complete understanding of the VRS remains elusive, as shown by the frequency with which accidents involving the VRS still occur. An analysis of the existing literature shows that the influence of blade twist, solidity and disk loading on the aerodynamics of the VRS has yet to be determined. In fact, quite often there are opposing views in the effect of these rotor parameters. In general there are too many unaccounted variables related to the geometry of the rotors, and the test conditions used in the investigations described earlier, for a rigorous comparison between individual investigations to be made. Other factors that may influence the results of experimental investigations of the VRS are blade stall and the interaction of the rotor wake with the wind tunnel walls. If stall did occur, then both the thrust and the fluctuations of the thrust reported would have been modified, which could explain some of the variation of the existing literature, however no experimental data exists to support this hypothesis. The effect of rotor geometry on the aerodynamics of the VRS was not investigated in this thesis, instead this thesis focused on the fluid dynamics of the VRS.

Entry into the VRS results in a reduction in the mean thrust of the rotor and large, mostly aperiodic thrust fluctuations. Thrust fluctuations can last for a large number of rotor revolutions and spectral analysis has revealed no clear trends in the frequency of these fluctuations. For helicopter main rotors these symptoms can manifest themselves as the loss of control efficiency and the loss of altitude. However, the VRS can also affect tiltrotors, multi-rotor UAVs and wind turbines.

The sketches in figure 1.12 represents the time-averaged flow fields, previously shown in figure 1.5. A description of the phenomenon also requires an analysis of the instantaneous flow field, because the flow can differ considerably from the mean flow field. Depending on the velocity ratio ($\alpha = U_o/U_i$), two typical flow patterns are observed. At low velocity ratios, the flow field penetrates into the counterflow and can be divided into two main regions: near and far fields. In the near field the behaviour is similar to that of a hovering rotor. In the far field, as the velocity decays, the rotor wake interacts with the counterflow forming a saddle point on the geometric centre line of the rotor. At a descent velocity, approximately equal to the hover induced velocity of the rotor, the flow forms a axisymmetric vortex ring in the vicinity of the rotor, which can shed aperiodically into the free stream. This is coupled with the formation of a conical region of reversed flow which can penetrate through the rotor hub. The region of the rotor which experiences this reversed flow increases until the rotor enters the windmill brake state. At some α values the flow field intermittently switches between a flow field notionally similar to that of a hovering rotor and the toroidal form shown in figure 1.12a and figure 1.12c. The frequency with which the flow exists in the toroidal form increases as the descent rate of the rotor increases until the flow remains locked within the toroidal state.

The mechanism with which the trailed vortex system collapses into the toroidal form associated with the VRS is based on the linear stability analysis of helical vortex filaments performed by Gupta and Loewy (1974) and Widnall (1972) along with the free wake simulations of helicopter rotors operating in axial descent performed by Bhagwat and Leishman. (2000), Leishman et al. (2004) and Ananthan and Leishman (2006). These investigations showed that the wake from a hovering rotor is inherently unstable. The small geometric perturbations to the helix, with wavelengths equal to a few core diameters or over several helix diameters identified by Gupta and Loewy (1974) and the mutual-inductance instability of helical vortices identified by Widnall (1972) lead to the breakdown of the helical structure. Typically this occurs some distance away from the rotor, however in descending flight this occurs in the vicinity of the rotor Newman et al. (2003), as shown in figure 1.13a. Free-wake simulations performed by Bhagwat and Leishman. (2000), Leishman et al. (2004) and Ananthan and Leishman (2006) identified the mutual-inductance instability as the mechanism responsible for the bundling of vortex filaments into rings, which move towards the rotor as it approaches the VRS. Planar smoke flow visualisation of a rotor performed by Stack et al. (2005) identified leapfrogging of vortex filaments as the mechanism responsible for the bundling of the vortex filaments. However it was shown numerically by Ahlin and Brown (2007), Ahlin (2007) and Brown et al. (2004) that the mutual inductance instability can result in the entanglement of helical vortices which, upon closer inspection would appear like the vortex pairing of vortices, identified by Stack et al. (2005) on a two dimensional plane. Outboard of the rotor this leads to the build up of vorticity around the rotor blade tips (Savas et al., 2009), as shown in figure 1.13b. The build up and subsequent shedding of the recirculation is responsible for the large thrust fluctuations associated with rotor operating in the VRS, as shown in figure 1.13c. Ahlin and Brown (2007) indicated that the breakdown of the blade root system is responsible for the formation of the saddle point and the conical region of reverse flow which penetrates towards the rotor disk plane identified by Green et al. (2005) however there is no experimental data that supports this conclusion. Despite our knowledge of this mechanism the development of the VRS continues to lead to the loss of rotorcraft and therefore greater understanding of this mechanism is required in order to prevent these accidents from occurring. It is interesting that low order momentum theory models, such as those developed by Gessow (1948), Wang (1990), Newman et al. (2003) and Johnson (2005) have continued to be useful tools used by researchers to predict the boundary of the VRS and rotor performance characteristics of helicopters and tiltrotors operating in descent despite not considering blade tip vortices in their analysis. Which according to the mechanism described above are primarily responsible for the breakdown of the helical vortex system and the roll up of the rotor wake into the highly unsteady toroidal form associated with the VRS. Therefore, the role of the blade tip vortices on the formation of the VRS will be investigated experimentally in this thesis.

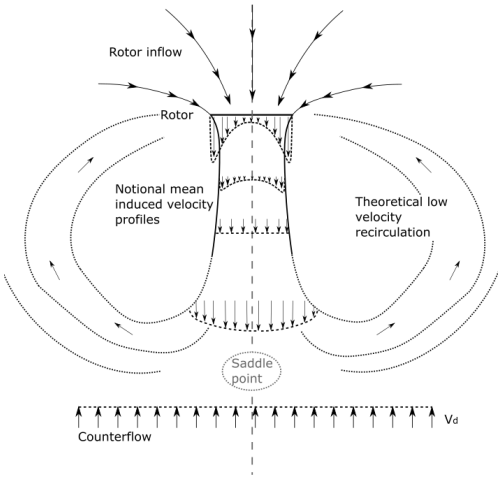

(A) Hover $\alpha \approx 0$

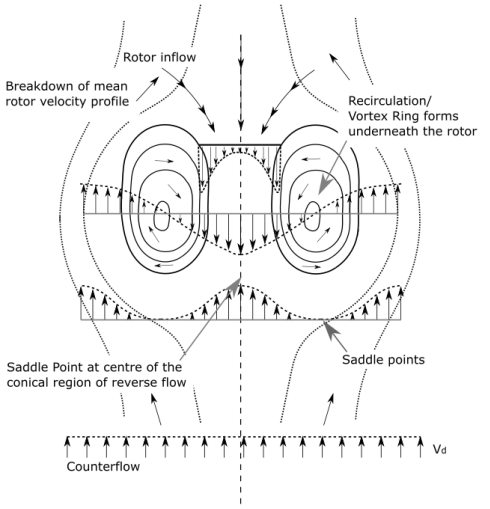

(B) $\alpha \approx 0.6$

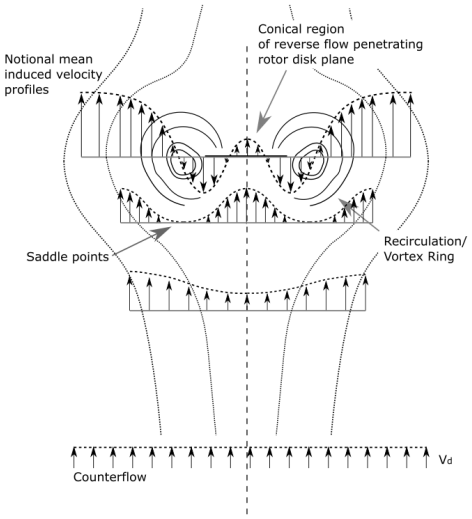

(C) $\alpha \approx 1.0$

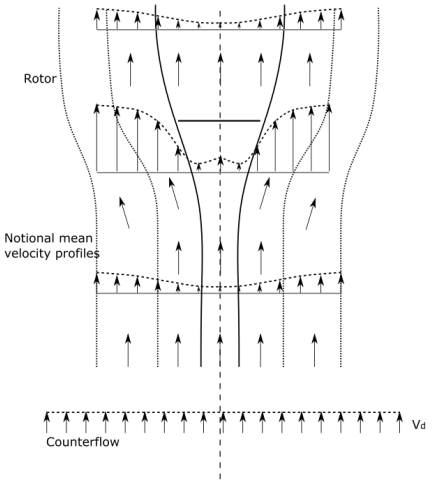

(D) Windmill brake state $\alpha \approx > 2.0$

FIGURE 1.12: Schematic diagrams of the general mean flow topologies associated with the VRS. At low descent velocities a large recirculation forms underneath the rotor and a mean flow stagnation point forms, as shown in this figure.

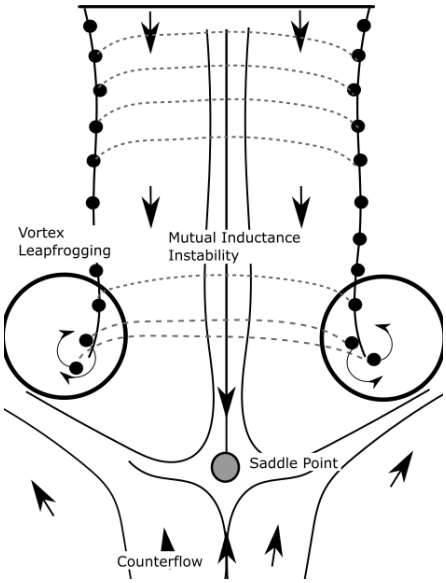

(A) Stage:1-2

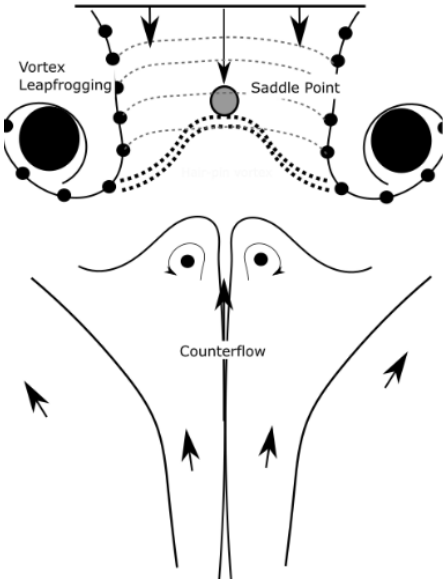

(B) Stage:2-3

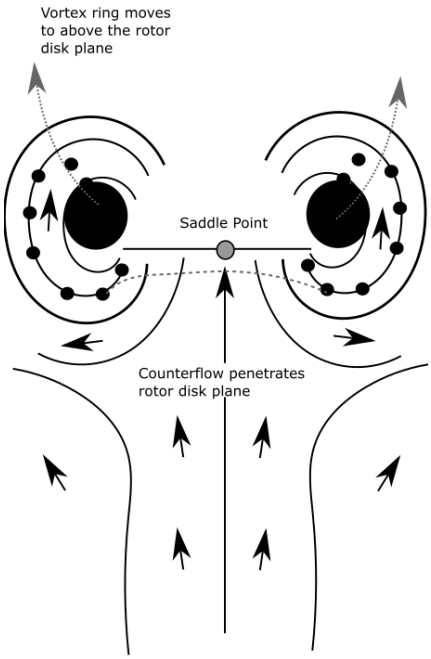

(C) Stage:3-4

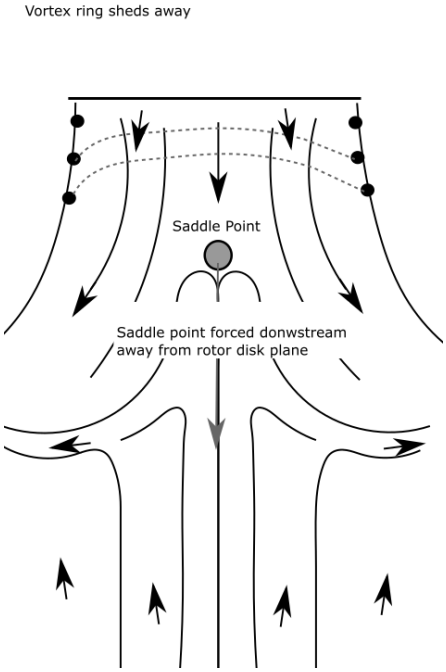

(D) Stage:4-1

FIGURE 1.13: Schematic diagram depicting the mechanism responsible for the development of the VRS for an isolated rotor according to the mutual inductance instability theory of helical vortex filaments developed by Leishman et al. (2004)

.

1.2 AIMS AND OBJECTIVES OF RESEARCH.

A series of experimental test campaigns were carried out in the University of Glasgow De-Havilland wind tunnel to evaluate the role of the trailing vortices in the VRS mechanism, principally by generating flow fields that do not contain a helical vortex wake but collapse into a vortex ring like state. The first consisted of an experiment designed to investigate the flow field produced by a shrouded rotor operating in axial descent. LDA and PIV were used to identify if a shrouded rotor can enter the VRS, and if the shroud has any effect on the characteristic topological features associated with the development of the VRS, described earlier and shown in figure 1.12.

The second test campaign consisted of an investigation into the flow field produced by a custom ventilated open core annular jet issuing into a uniform counterflow. LDA, PIV and smoke flow visualisation were used to investigate the structure of the flow field produced by the ventilated open core annular jet. The jet was designed to produce a mean flow field which is notionally similar to that of a hovering rotor. When introduced to a counterflow the flow field shares many of the significant topological features associated with the VRS, however it does not contain any blade tip vortices.

The third test campaign consisted of an investigation into the flow field produced by a rigid, unarticulated rotor with a large root cut out, operating in axial descent. This rotor was designed to produce a mean flow field similar to that of the ventilated open core annular jet. When introduced to a counter flow however the flow field collapsed into the VRS, however it did not enter the incipient flow regime. The main objectives and scope of these experimental test campaigns are summarised below:

- Identify if a shrouded rotor can enter the VRS.
- Quantify the influence of a shroud on the flow field produced by a rotor operating in axial descent.
- Identify the topological features produced by a shrouded rotor operated in axial descent.
- Investigate the structure of the flow field produced by a ventilated open core annular jet when issuing into quiescent surroundings and when issuing into a uniform counterflow.
- Quantify the effect mean velocity profile has on the development of the VRS.
- Quantify the contribution the blade tip vortices have on the formation of the VRS.

1.3 STRUCTURE OF THESIS

Following on from the introduction in chapter 1, this thesis is divided into the following sections:

Chapter 2 describes an experimental investigation into the flow field of a shrouded rotor in axial descent. Results from a shrouded rotor and a unshrouded rotor are compared and the effect of the shroud on the fluid dynamics of the flow field is investigated.

Chapter 3 presents a detailed account of an experimental investigation into the flow field produced by a ventilated Open Core Annular Jet in a uniform counterflow. Initially the flow field produced by the custom ventilated open core annular jet is characterised, after which the effects of a counter flow on the flow field are then presented.

Chapter 4 presents an experimental investigation into the flow field produced by a rotor with a large root cut out designed to recreate the mean flow field produced by the ventilated open core annular jet.

Chapter 5 explores the relationship between the four experiments performed. The finding of each experiment are compared and critically discussed. The contribution of the blade tip vortices to the development of the VRS is also explored.

Chapter 6 presents the main conclusions of this study along with recommendations for future work to be conducted.

Appendix *A* includes details of the test facility including the wind tunnel test section size,and a very brief summary of the theory behind particle image velocimetry and laser doppler anemometry.

Appendix *B* includes supplementary experimental data relating to the flow field produced by a shrouded rotor and a isolated rotor operating in axial descent.

Appendix *C* includes supplementary experimental data relating to the flow field produced by a ventilated open core annular jet operating in a uniform counterflow.

Appendix *D* includes supplementary experimental data relating to the flow field produced by a rotor with a large root cut out operating in axial descent.

Appendix *E* includes a brief description of momentum theory and the assumptions applied when it is used to estimate the thrust produced by a rotor when it is operating in axial flight.

1.4 CONFERENCE PRESENTATIONS

- D.Pickles, R.B.Green and A. Busse (2019). Experimental Simulation Of The Vortex Ring State. In: 32^{nd} Scottish Fluid Mechanics Meeting, University of Dundee, UK.

- D.Pickles, R.B.Green and A. Busse (2019). Experimental Simulation OF The Vortex Ring State. In UK Fluids Conference, Churchill College, Cambridge, UK.

1.5 JOURNAL PUBLICATIONS

- D.Pickles, R.B.Green and A. Busse. Flow development of a ventilated open core annular jet in uniform counterflow. (Under preparation for submission). Journal Of Fluid Mechanics.

- D.Pickles, R.B.Green, D. Zagaglia and A. Busse. Experimental investigation into the flow field of a shrouded rotor in axial descent. (Under preparation for submission). Physics of Fluids.

- D.Pickles, R.B.Green and A. Busse. The nature of the vortex ring state. (Under preparation for submission). Experiments In Fluids.

CHAPTER 2

THE VORTEX RING STATE OF A SHROUDED ROTOR

An experimental investigation into the flow field produced by a shrouded rotor, operating in axial descent is presented. Laser Doppler Anemometry was used to determine the induced velocity of the rotors, whilst particle image velocimetry was used to investigate the dynamics of the unsteady flow field produced.

At low descent velocities, the mean flow field resembled that produced by a shrouded rotor operating in hover. At slightly higher descent velocity ratios, the wake from the shrouded rotor broke down, leading to the formation of a large region of recirculation outboard of the shroud which aperiodically sheds into the free stream. The diameter of the recirculation is approximately equal to the diameter of the rotor. Further increases in descent velocity lead the centre of recirculation to form around the external surface of the shroud. The wake from the shrouded rotor is re-ingested by the shroud. The formation of the recirculation is coupled with the formation of a saddle point located on the geometric centre line of the shroud. As with the isolated rotor, the mean location of the saddle point approached the shroud outlet plane as the descent velocity increased. The flow field produced is highly unsteady and is a different manifestation of the classical formation of the vortex ring state, commonly associated with rotors operating in descent. This investigation showed that shrouded rotors entered the VRS at a lower descent velocity ratio than an isolated rotor. The shrouded rotor entered the VRS when the descent velocity ratio was approximately equal to to the mean induced velocity of the shrouded rotor at the shroud outlet plane.

The wake produced by the shrouded rotor contained no clear helical vortex system, however the results presented in this chapter indicate that the mechanism responsible for the formation of the VRS of a shrouded rotor and an unshrouded rotor are similar. Indicating that the mutual-inductance instability of helical vortices may not be responsible for the formation of the VRS as previously thought. The results presented in this chapter indicate that VRS may be a manifestation of an axially induced flow interacting with a uniform counterflow.

2.1 INTRODUCTION

Shrouded rotors have been extensively used in the rotorcraft industry owing to the inherent safety (Young et al., 2002) and potential static performance improvements of the design when compared to an isolated rotor Hubbard (1950). It is for these reasons that shrouded rotors have been applied to compound helicopters for axillary propulsion (Piasecki, 1966), hovercraft, helicopter tail rotor fenestrons for counteracting the torque of the main rotor ('fan in fin') (Mouille (1970), Vuillet and Morelli (1986) and Abrego et al. (2002)), tilt ducted fan aircraft (Newson, 1963), flying platforms, fan in wing aircraft (Hamel, 1923), marine propellers (Schultz and Vistai, 1984), wind turbines (Bontempo and Manna, 2016), and vertical take off and landing (VTOL) unmanned aerial vehicles (UAVs) (Colin et al., 2016). The performance improvements occur as a result of the diffusion of the propeller jet stream into a non-contracting wake, the formation of a region of suction on the shrouds inlet, and the formation of a region of large static pressure at the outlet of the shroud. A simplified schematic diagram of a shrouded rotor is presented in figure 2.1 and a summary of the aircraft which have incorporated shrouded rotors in their design are presented in table 2.1. It should be noted that most of the aircraft, apart from the helicopters listed in table 2.1, were prototypes or research aircraft which did not enter service.

2.1.1 MEAN FORCE AND SHROUDED ROTOR PERFORMANCE PARAMETERS.

Since the initial patent application by Hamel (1923), which describes a fixed wing aircraft with propellers embedded inside the wings perpendicular to the wing chord, there have been a number of experimental and numerical investigations into the performance of shrouded rotors. A shrouded rotor, sometimes referred to in the literature as a 'ducted fan', is defined as a propeller which is mounted inside a circular duct or an annular wing (Fletcher, 1957). The term 'fenestron' has been used to describe a specific installation where a ducted fan is used to replace the unshrouded tail rotor of a conventional helicopter. Initial investigations performed by Stipa (1932), Krüger (1949), Platt (1948) and Gunwald and Goodson (1962) and others, attempted to characterise the performance of a variety of shroud designs operating in hover, forward flight, and in edge wise flight. The performance of the shroud is highly dependent on the blade tip clearance (δ_{tip}), the inlet lip radius (r_{lip}), the diffuser included angle (θ_d), the diffuser length (L_d), and the diffusers expansion ratio $\sigma_d = A_e/A$ which is defined as the ratio between the diffuser exit area (A_e) and the rotor disk area (A). These parameters are illustrated in the cross section through a shrouded rotor presented in figure 2.1.

It is generally accepted, as a result of the experimental investigations of Hubbard (1950), Taylor (1958), Black et al. (1968), Martin and Tung (2004) and Oweis et al. (2006b), that blade tip clearance significantly affects the performance of shrouded

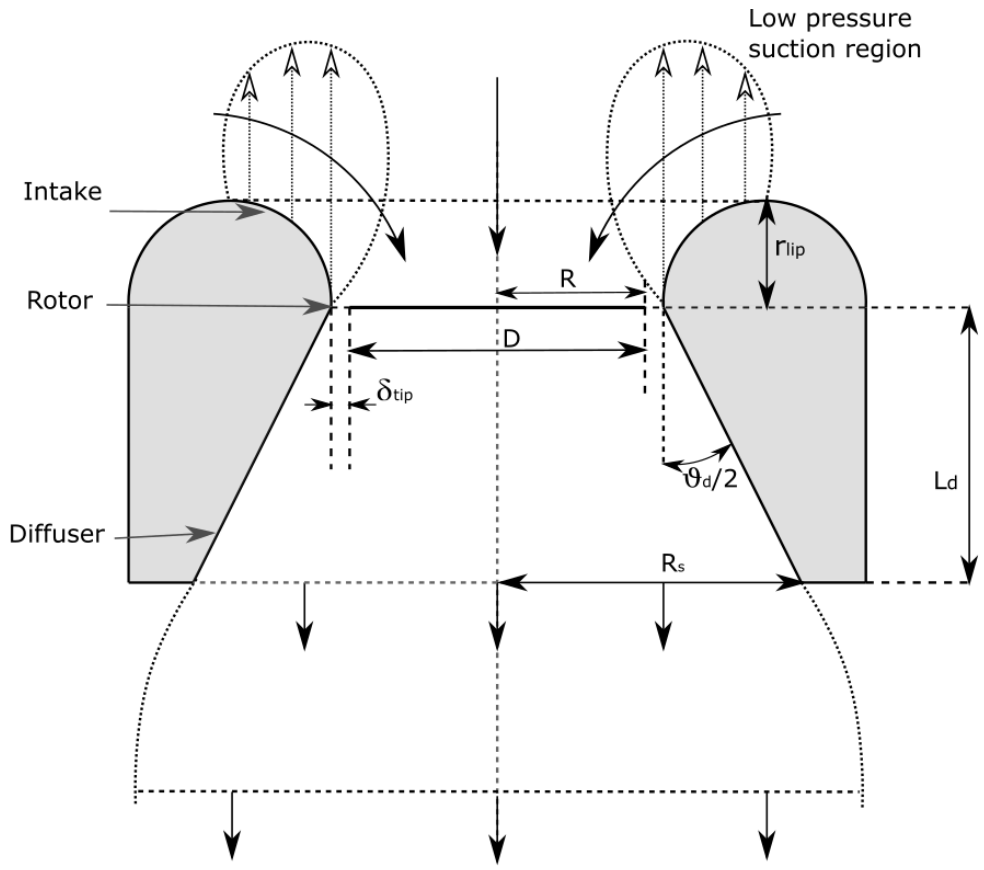

(A) Schematic diagram of a shrouded rotor

Figure 2.1: Schematic diagrams of the general parameters found to affect the performance of a shrouded rotor. Figure adapted from Pereira (2008).

Aircraft Name	Aircraft Type	Entered Service
Hiller VZ-1 Pawnee (Parlett, 1955)	Flying platform	No
Piasecki VZ-8 AirGeep (Parlett, 1955)	Flying platform	No
GE/Ryan XV-5 (Moser (1959))	Fan in wing aircraft	No
Vanguard Omniplane (Ham and Moser (1958))	Fan in wing aircraft	No
Doak VZ-4 (Nelson, 1959)	Tilt-duct aircraft	No
Bell Aerospace: X-22A (Newson (1963), Rhodes (1970), Maki and Giulianetti (1966))	Tilt duct aircraft	No
XAZ-1/ MA18-B Marvelette (Thompson and Roberts, 1966)	Fixed wing aircraft	No
Piasecki: 16H-1 Pathfinder (Corporation., 1962)	Compound helicopter	Yes
Piasecki: 16H-1A Pathfinder II (Corporation., 1965)	Compound helicopter	Yes
Nord: 500 Cadet (Lazareff, 1968)	Research aircraft	No
Bell Helicopters - Model 222 (Fairchild et al., 1973)	Helicopter tail rotor	Yes
Model 206- JetRanger (Lemont (1982), Harr et al. (1985))	Helicopter tail rotor	Yes
Sikorsky S-67 Blackhawk (Clark, 1975)	Helicopter tail rotor	No
BoeingâĂŞSikorsky: RAH-Comanche (Clemmons, 1992)	Helicopter tail rotor	Yes
Kawasaki: XOH-1 (Basset and Brocard, 2004)	Helicopter tail rotor	Yes
Eurocopter: SA/AS365 (Mouille and d'Ambra (1986))	Helicopter tail rotor	Yes
Eurocopter: Dauphin 2 (Vuillet and Morelli (1986))	Helicopter tail rotor	Yes
Eurocopter: AS565 Panther (Mouille and d'Ambra (1986),Vuillet (1989))	Helicopter tail rotor	Yes
Eurocopter: Dauphin 2 (Mouille and d'Ambra (1986), Basset and Brocard (2004))	Helicopter tail rotor	Yes
Eurocopter: EC120/ EC130/ EC135/635 (Mouille and d'Ambra (1986))	Helicopter tail rotor	Yes
US Marine Corps: AROD (Weir (1988), Murphy and Bott (1995))	UAV	Yes
Sikorsky: Cypher/ Cypher II Murphy and Bott (1995)	UAV	No
Honeywell: RQ-16A T-Hawk (Wilson and Schnepf (2002), Lipera et al. (2001))	UAV	Yes
Perching (Gupta and Plump (2001))	UAV	No

TABLE 2.1: Table containing a summary of the different aircraft which have incorporated a shrouded rotor in their design.

rotors. The proximity of the shroud to the blade tip impedes the formation of the blade tip vortices, which reduces the thrust produced by an isolated rotor (Leishman, 2006). Larger blade tip clearances allow stronger blade tip vortices to form, reducing the thrust produced by both the rotor and the shroud (Ahn, 2005). It was noted by Oweis et al. (2006b) that the radius of the core of the vortices produced by their shrouded rotor was not significantly different to that of blade tip vortices produced by unshrouded rotors. Stronger blade tip vortices reduce the thrust due to suction produced on the shroud's inlet, by reducing the inflow velocity at the wall of the shroud (Ahn, 2005). Safety considerations designed to prevent the rotor blades from striking the shroud wall limit the minimum size of the blade tip clearance (Fleming et al., 2003). However this blade tip clearance can be approximated to zero by lining the shroud wall with a brush or an expandable material that allows the passage of the rotor blades (Clemmons, 1992). The primary blade tip vortices were found by Oweis et al. (2006a) and Oweis et al. (2006b) to be of a similar scale to that of the blade tip clearance. The strength and core size of the blade tip vortices was weakly dependent on Reynolds number (Oweis et al., 2006a). When a shrouded rotor is operating in forward axial flight (or climb), the detrimental effects of large blade tip clearances become smaller as the advance ratio increases (Mort, 1965). The drag (D) experienced by a shrouded rotor was shown by Black et al. (1968) to increase as the advance ratio increased, thereby reducing the performance benefits associated with shrouded rotors.

The effect of varying the shroud inlet lip radius and the shape of the shroud inlet was investigated experimentally by Krüger (1949), Taylor (1958), Parlett (1955), Yaggy and Mort (1961), Weir (1988) and Graf et al. (2008). These investigations showed that the shape of the shroud inlet significantly affected the performance of the shrouded rotors. Shrouded rotors with larger lip radii (r_{lip}) typically produced an increase in the rotor's figure of merit. The smaller the lip radius the greater the likelihood that

flow separates from the inlet surface (Taylor, 1958).

Black and Rohrbach (1968) and Black et al. (1968) found that one of the main parameters that affected the performance of a shrouded rotor was the design of the diffuser. Experimental investigations performed by Hubbard (1950), Fairchild et al. (1973), Taylor (1958) and Cycon et al. (1992) identified diffuser length as an important design parameter. Increasing the diffuser length postponed aerodynamic stalling of the rotor to higher blade collective angles, thereby increasing the linearity of the thrust collective curves and increasing the total thrust produced by the shrouded rotor (Sheng et al., 2015). More recent CFD simulations of shrouded rotors performed by Sheng et al. (2015) support this conclusion. The contribution of thrust produced by the shroud increased as the shroud length was increased (Fairchild et al., 1973). Aerodynamic stall of shrouded rotors starts at the tip of the rotor blades and works radially inwards as the rotors rotational speed increases (Wright et al., 1991).

Due to the rapid uptake of vertical lift drone technology by the general public, recent experimental studies have focused on small scale shrouded rotors designed to be used on UAV/MAV (Abrego et al. (2002), Akturk et al. (2009) and Rhee et al. (2013)). These UAVs are often required to operate in highly cluttered urban environments in close proximity to humans. In these operational conditions, the shroud acts as a safety feature, preventing the rotor blades from impacting with anything (Mouille (1970), Basset and Brocard (2004)). If the effects of flow separation at the duct lip are avoided, these small scale investigations can be used to approximate the performance of larger scaled shrouded rotors (Goodson and Grunwald, 1962). Reynolds number effects make the flow more likely to separate in these small scale investigations, which utilize small rotors operating at very high rotational speeds.

2.1.2 Fluid dynamics of a shrouded rotor

Research involving shrouded rotors has mainly focused on their performance when operating in hover, axial (forward/climbing flight), and edgewise flight. The wake from a shrouded rotor with a centre body blockage can be characterised as a region of low velocity air which is surrounded by a ring of higher velocity air associated with the passage of the rotor blades. The low velocity core forms as a result of the blockage and viscous losses of the rotor centre body. The rotor centre body typically houses the motor and the control systems of a shrouded rotor. A shrouded rotor produces a more uniform velocity wake compared to that of an isolated rotor. The uniformity of the wake was found by Pereira (2008) to depend on the rotors blade tip clearance. Shrouded rotors with larger blade tip clearances produce wakes which closely resemble that of wakes produced by isolated rotors. Smoke flow visualisations, performed by Krüger (1949), showed that the diameter of the wake produced by a

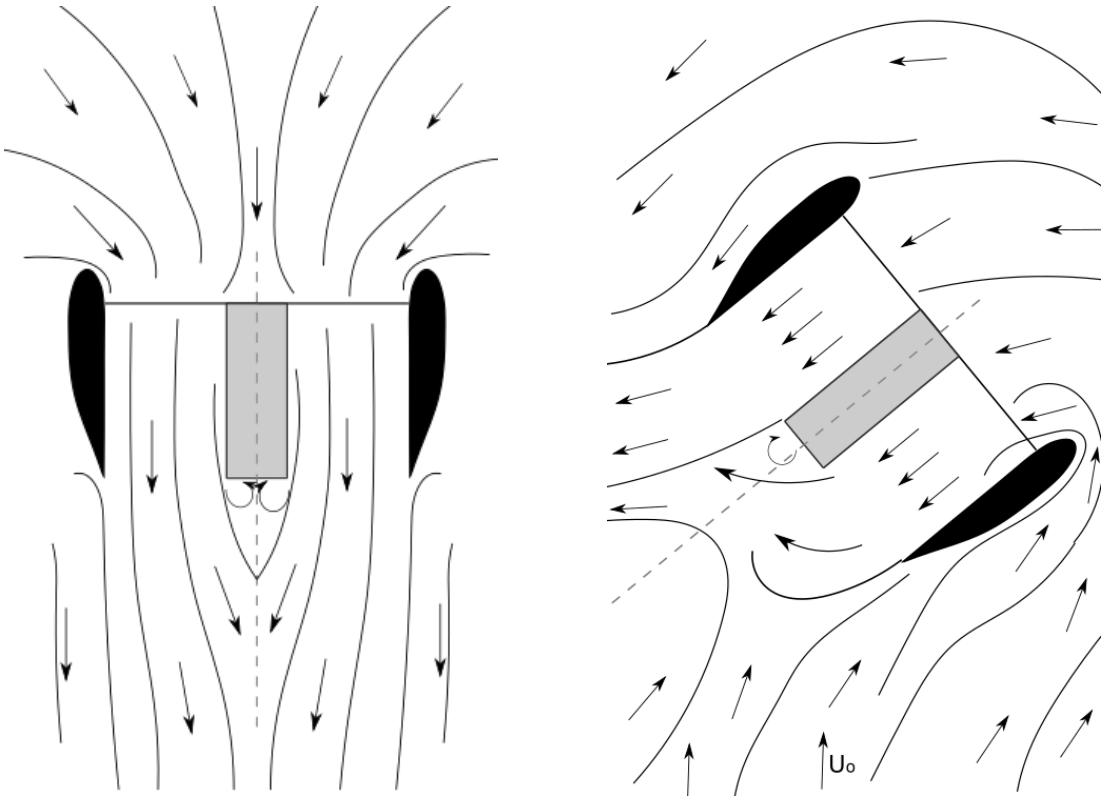

(A) Hover - $\gamma = 0^o$ (B) Edge Wise Flight $\gamma = 120^o$

FIGURE 2.2: Schematic diagrams of the general flow topologies associated with shrouded rotors operating in axial flight: figure 2.2a and edgewise flight at an angle of $(\gamma = 120^o)$ 2.2b.

shrouded rotor was dependent on the shape of the shroud. Hot wire anemometry surveys, performed by Martin and Tung (2004), showed that the diameter of the wake remains constant after it exits from the diffuser if the flow has become fully expanded at the diffuser exit plane.

Quantitative PIV measurements and computational simulations of the flow field produced by a shrouded rotor UAV operating in edgewise flight were performed by Akturk et al. (2009), Akturk and Camci (2010) and Ryu et al. (2017). In edgewise flight $(\gamma = 90^o)$ the effective breathing area of the rotor reduced as a result of flow separating from the leading edge of the shrouds inlet. The wake of the shrouded rotor impinged upon the rotor centre body. Pressure measurements showed that a large increase in suction pressure is produced on the windward side of the shroud, and a large suction force is produced on the leeward side of the shroud (Pereira, 2008). Both of these factors contribute to the large pitching moment, characteristic of shrouded rotors operating in edgewise flight. The magnitude of the nose-up pitching moment increased as the crosswind velocity increased. At a large cross wind angle of $\gamma = 120^o$, the rotor wake was deflected by the crosswind and a saddle point formed underneath the rotor on the windward side of the shroud (Ryu et al., 2016). A schematic diagram of the mean flow field produced by a shrouded rotor operating at a large cross wind

angle $\gamma = 120^o$ is shown in figure 2.2b.

2.1.3 Assessment of the existing literature.

Whilst a large amount of data exists regarding the effect shroud design parameters such as blade tip clearance, inlet lip radius, diffuser length, diffuser angle and diffuser expansion ratio have on the performance and the structure of the flow field produced by shrouded rotors operating in hover, forward flight and edge wise flight, there is a lack of detailed experimental or numerical data related to shrouded rotors operating in axial descent. This is particularly interesting given the recent surge in the number of military and civilian unmanned aerial vehicles which incorporate shrouded rotors. These UAVs try to take advantage of the increased thrust and safety benefits shrouded rotors offer when compared to unshrouded rotors. UAVs are often required to operate in urban environments where there ability to take off, hover, and descend axially can be exploited. In axial descent, unshrouded rotors can experience a flow phenomenon known as the VRS. In the VRS, the trailed vortex system from the rotor collapses, forming a highly unsteady vortex-ring located around the rotor disk plane. Entry into the VRS leads to large unpredictable thrust oscillations, the loss of control efficiency and, in some cases, the loss of the rotorcraft. The present study aims to identify if a shrouded rotor operating in axial descent will enter the VRS whilst providing insight into the flight envelope of UAVs. This investigation also provides insight into the role blade tip vortices play in the development of the VRS, because the strength of the blade tip vortices, produced by a shrouded rotor is typically less than that of an isolated rotor, as a result of the shroud.

2.1.4 AIMS AND OBJECTIVES OF THIS INVESTIGATION.

The objectives and scope of this investigation are summarised below:

- Characterise the flow field produced by a shrouded rotor operating in hover;
- Characterise the flow field produced by a shrouded rotor operating in axial descent;
- Identify if a shrouded rotor can enter the VRS;
- Quantify the influence of a shroud on the flow field produced by a rotor operating in axial descent;
- Develop the flight envelope of a shrouded rotor.

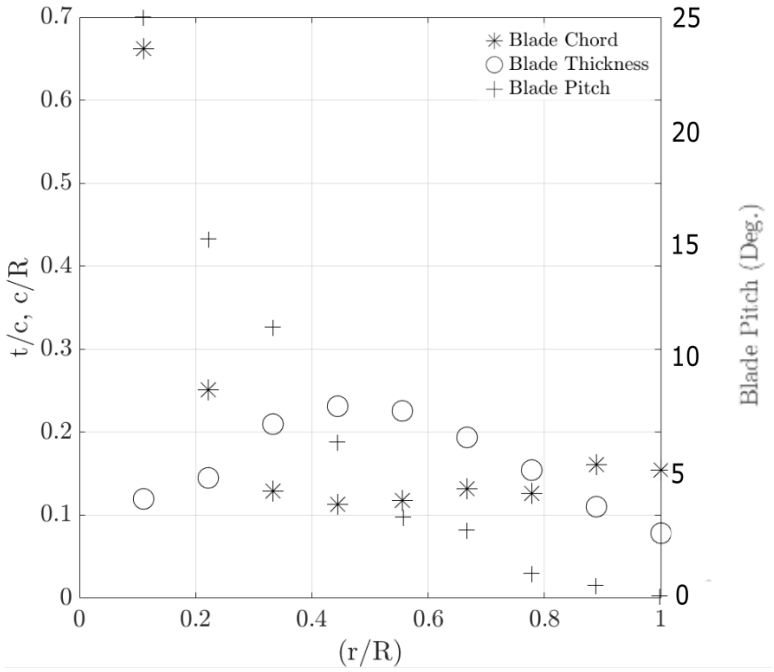

FIGURE 2.3: Chord, thickness, and pitch profiles of the rotor blade used in this investigation.

2.2 EXPERIMENTAL METHOD.

2.2.1 DESCRIPTION OF APPARATUS.

An experimental investigation into the flow field produced by a $0.1778m$ diameter, two bladed, twisted, tapered, fixed pitch rotor mounted inside a shroud, operating in axial descent, was performed. In order to allow the influence of the shroud on the flow field to be characterised, the flow field produced by the unshrouded rotor was also investigated. Figure 2.3 shows the chord (c), thickness (t) and blade pitch distribution of the blade. The rotor had no cyclic input and there was no lead-lag or flap degrees of freedom. The fibreglass rotor was lightly loaded and therefore was assumed to be rigid. The rotor was powered by an AXI-2820/12-V2 brushless motor which was mounted on a stand located inside the wind tunnel. The shroud was connected to the motor using three support struts located on the inlet side of the rotor, as shown in Figure 2.4. The rotor was operated at a constant rotational frequency of $66.3 \pm 1Hz$, producing a rotor tip speed of $V_{tip} = 37m/s^{-1}$ and a blade tip Reynolds number of $15,000$. The rotor was connected to the motor using a commercially available reverse threaded taper lock propeller adaptor. The motors and propellers chosen were all commercial components readily available from most UAV drone retailers.

The shroud, shown in figure 2.4, was 3D printed out of Prototyping PLA (FDM), and was designed based on the investigation performed by Pereira (2008) to optimise the hovering performance of a shrouded rotor. The shroud had an inlet lip radius of

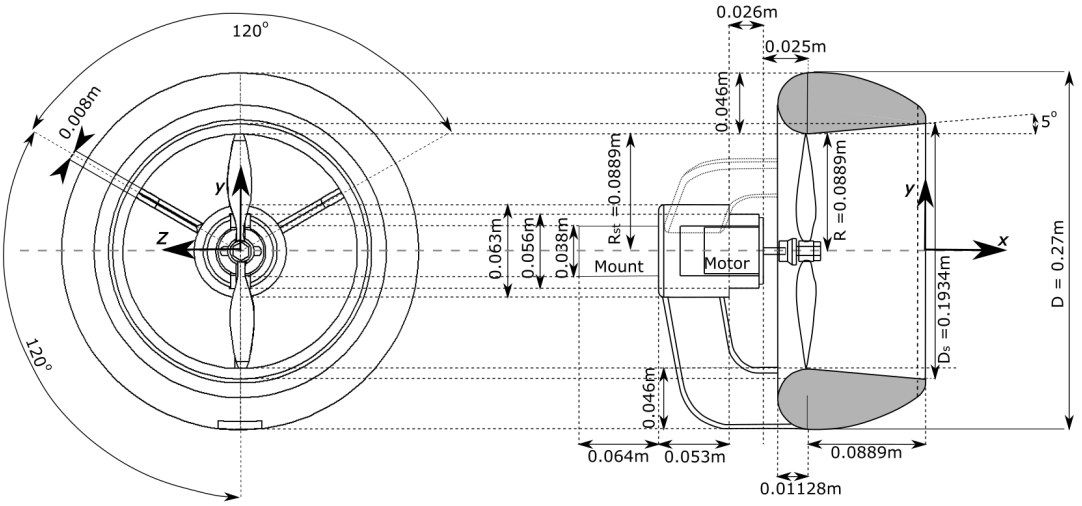

FIGURE 2.4: Schematic diagram of the shroud used for this investigation.

$r_{lip} = 0.13D_t = 0.02m$, a blade tip clearance ($\delta_{tip} \approx 0.001m$), a diffuser angle $\theta_d = 10^o$, and a diffuser length of $L_d = 0.5D_t = 0.089m$. The rotor disk plane was located at the throat of the shroud. Rather than a single surface, inner wall-only shroud, which is characteristic of shrouds used in earlier investigations to characterise the performance of hovering shrouded rotors, a smooth curve was used to describe the external profile of the shroud. A schematic diagram of the shrouded rotor installed in the wind tunnel is shown in figure 2.5. The shrouded rotor was orientated to induce velocity (U_i) against the wind tunnel, so that the wind tunnel speed (U_o) represented the descent velocity of the shrouded or unshrouded rotor.

The small blade tip clearance ensured that the strength of the blade tip vortices contained within in the wake of the shrouded rotor was significantly less than those produced by the isolated rotor Oweis et al. (2006b) thereby allowing the role of the blade tip vortices on the development of the VRS to be investigated.

A Cartesian (x,y,z)-coordinate system, with its origin at the geometric centre of the shroud outlet plane, is defined so that the y-axis is vertically upwards and the x-axis is orientated against the direction of the wind tunnel free stream. The counter-flow was produced using University of Glasgow's, DeHavilland wind tunnel. This atmospheric closed return, low speed wind tunnel is capable of achieving speeds of up to $|U_o| = 50m/s$ in the $2.65m$ wide by $2.04m$ high octagonal test section with a turbulence intensity below 0.4%. The shrouded and unshrouded rotors were both exposed to a range of descent velocities ranging from $\alpha = (|U_o|/U_i) = 0$ to $\alpha = 2.5$. The test rig shown in figure 2.5, had a negligible wind tunnel blockage of 2%. Previous experiments performed by Ganzer and Rae (1960) and Lehman and Besold (1971) showed that the wake from a rotor, operating in forward flight, did not interact with the wind tunnel walls so long as the diameter of the wind tunnel is at least twice the diameter of the rotor and the advance ratio is greater than 0.1 (Leishman, 2006). Rae and Shindo (1969) showed that at advance ratios less than 0.1 a stagnation point forms

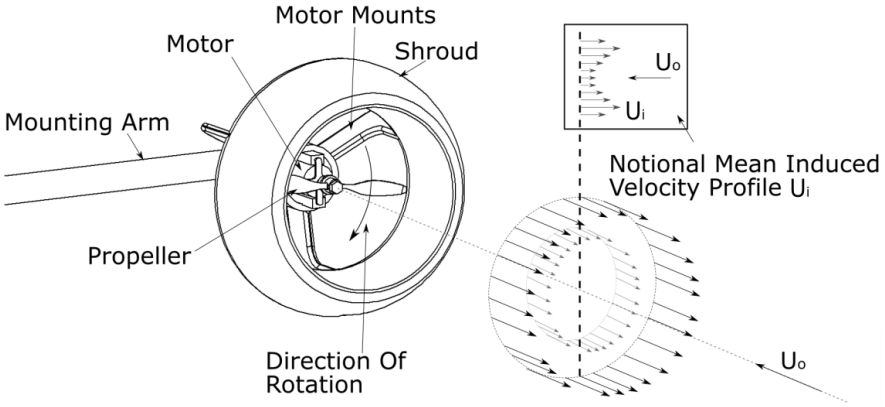

Figure 2.5: Schematic diagram of the shrouded rotor installed in the DeHavilland wind tunnel.

at the interaction between the rotor wake and the wind tunnel boundary layer. Once this occurs the structure of the flow field produced no longer represents that of an unrestricted rotor. Therefore the advance ratio at which this occurs is typically used to define the minimum advance ratio experiments on a rotor, operating in forward flight, can be performed inside a specific wind tunnel (Barlow et al., 1999). To the authors knowledge the effect wind tunnel dimensions have on the structure of the flow field produced by a rotor inducing flow against the wind tunnel flow has not been investigated therefore smoke flow visualisation was used to ensure that the rotor wake did not interact with the wind tunnel walls. Homogeneous seeding of the wind tunnel for both PIV and LDA was achieved using a Pivtec-GmbH seeder, incorporating 160 Laskin nozzles with a mean olive oil particle substrate diameter of $0.9\mu m$, as stated by the manufacturer (PIVTechGmbH., 2019).

A commercially available Dantec Dynamics two-component Laser Doppler Anemometry (LDA) system was used to investigate the velocity profile produced by both the shrouded and unshrouded rotors $1.48R$ upstream of the rotor disk plane $(x/R = 0.48)$. Throughout this thesis upstream and downstream are used to describe locations in the flow field with respect to the direction of the wind tunnels flow. Optical axis prevented measurements of the velocity profile inside the shroud, however additional measurements were taken $0.48R$ upstream of the rotor disk plane $(x/R = -0.52)$. The system consists of two diode pumped solid state $1W$ lasers with wavelengths of $488nm$ and $514nm$ mounted on a Dantec $9041T3332$ $3D$ $(1m$ x $1m$ x $1m)$ traverse system, capable of scanning the measurement volume with a positional accuracy of $\pm 0.01mm$. The lasers were both orientated at an angle of 2.5^o coinciding to form a 2.62 x 0.12 x $0.12mm$ measurements volume.The system was operated in burst mode with transit (residence) time enabled to allow for the accurate calculation of the mean flow velocity, and prevent high velocity bias for high turbulent flows as defined by Zhang (2010), George (1988) and Albrecht et al. (2013). The measurement planes through out this thesis were defined on the basis of where important features of the manifestation

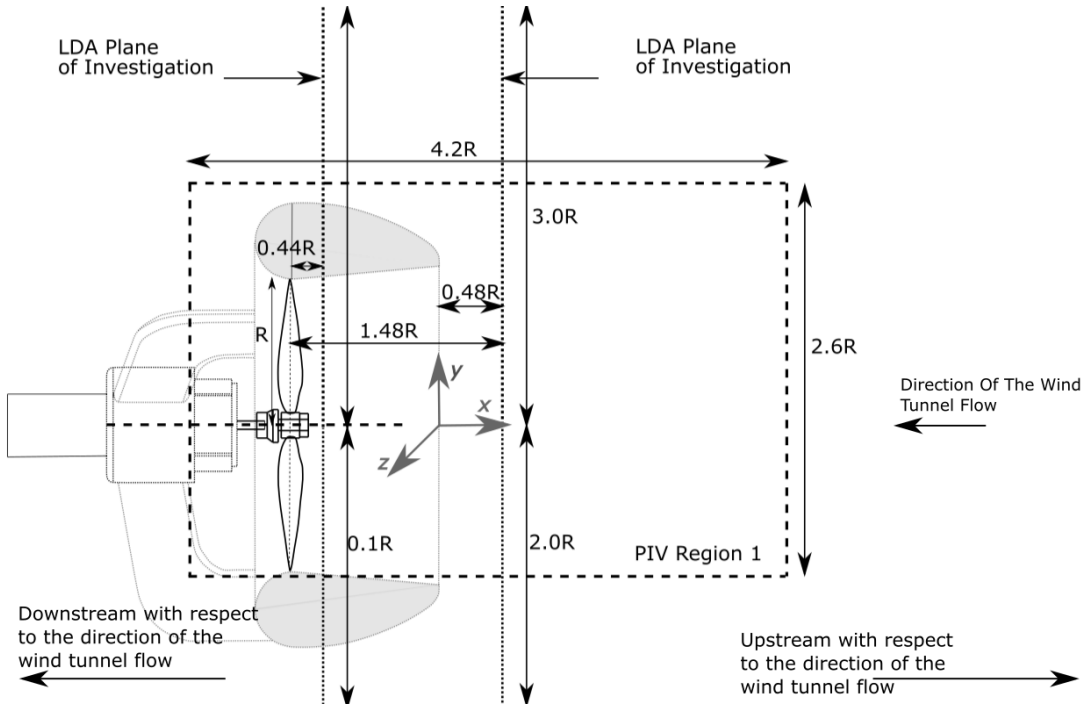

FIGURE 2.6: Schematic diagram of the PIV regions of interest and LDA planes investigated for the unshrouded rotor in axial descent. The outline of the shroud has been included to contextualise the investigation of the isolated rotor with the shrouds location.

of the VRS occurred.

Two component PIV in the symmetry plane along the longitudinal centre line of the rotor was performed in order to assess the structure of the flow field. A $532nm$ wavelength Litron double cavity oscillator amplified, Nd:YAG laser with an output energy of $100mJ$ per pulse was used to deliver the light sheet. A Phantom V341 digital high speed 4 Megapixel camera with a 2560 X 1600 pixel CMOS sensor fitted with a Samyang $135mm$ focal length set to $f\# = 2.0$ was used to acquire the raw images. The flow field produced by the shrouded rotor was split into two distinct regions: Region 1: Shroud Outlet; Region 2: Around the Shroud, as shown in figure 2.7. A single region of interest, presented in figure 2.6, was used to investigate the flow field produced by the unshrouded rotor. This was used because the flow field produced by an isolated rotor in axial descent has previously been investigated in detail (Green et al., 2005). Three sets of 600 image pairs were recorded at a frequency of $200Hz$ for a range of counterflow velocities for each of the regions of interest investigated. A time delay of $\Delta t = 200\mu s$ was used for all experimental configurations investigated. Optical access, smoke flow visualisation results, laser safety and camera resolution were responsible for the determination of the PIV regions of interest used in each of the experimental configurations investigated in this thesis.

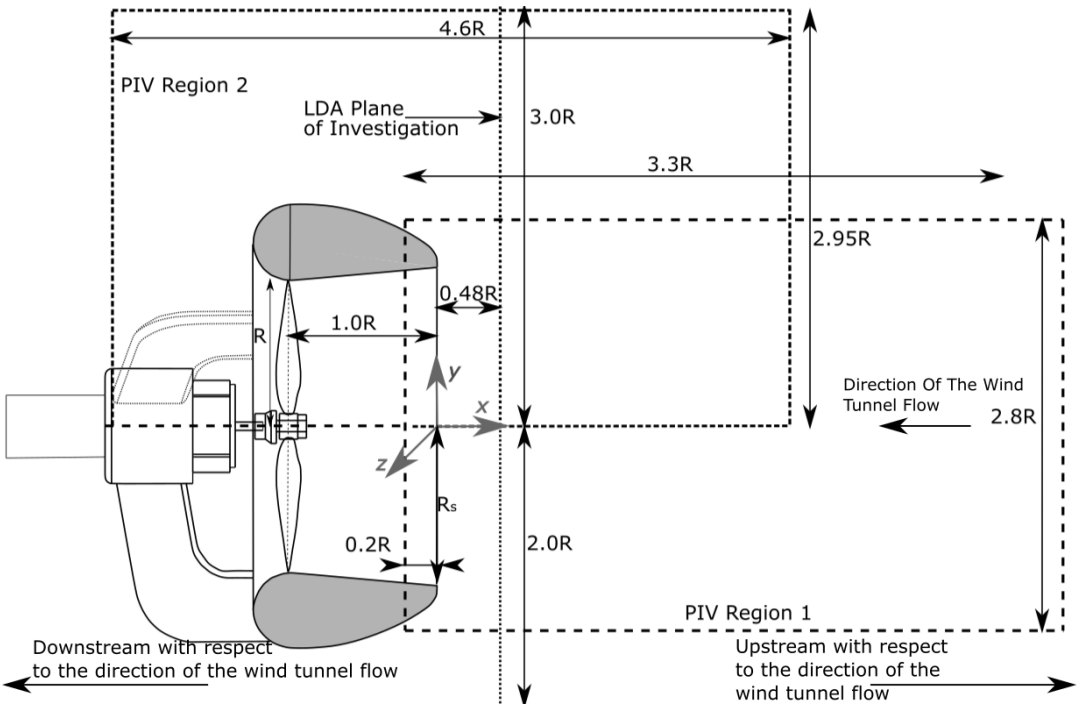

FIGURE 2.7: Schematic diagram of the PIV regions of interest and LDA planes investigated for the shrouded rotor in axial descent.

Rotor configuration	Plane of investigation (x/R)	Radial Resolution	Error ϵ_u
Isolated Rotor	-0.52	$0.08R$	0.2%
Isolated Rotor	0.48	$0.08R$	0.3%
Shrouded Rotor	0.48	$0.08R$	0.3%

TABLE 2.2: Table summarising the accuracy of the LDA.

2.2.2 LDA ANALYSIS METHODOLOGY AND ACCURACY.

Characterisation of the flow field produced by the isolated rotor operating in hover, was performed on a grid of sample points concentrically spaced around the centre of the rotor, with azimuthal and radial resolutions of 15^o and $0.08R$ respectively. Each of the 289 points were sampled over a period of $10s$. The measurements were taken on a plane $0.48R$ upstream of the rotor disk plane $(x/R = -0.52)$. The approximate accuracy of the mean flow field of the isolated rotor, was calculated as being $\pm 0.01 ms^{-1}$, which corresponds to 0.2% of the rotors peak induced velocity. A similar grid of sample points with a radial and azimuthal resolution of $0.08R$ and 15^o was used to characterise the flow field produced by the shrouded and unshrouded rotor, $1.48R$ from the rotor disk plane. This corresponds to a plane $0.48R$ from the shroud outlet plane.

In descent 218 data points along the horizontal and vertical axes of symmetry of the isolated rotor, on both planes of investigation, were sampled for a period of $10s$ with a spatial resolution of $0.08R$. Optical axes prevented measurements from being taken inside the shroud (i.e. $-1.3 < (x/R < 0)$) therefore measurements of the flow field produced by the shrouded rotor were only taken on a plane $1.48R$ from the rotor

PIV region of interest	Resolution	Magnification factor (M)	Error ϵ_u
Shrouded Rotor Region 1	$0.0013R$ x $0.0017R$	$6.4 pixel/mm$	$0.078 m/s$
Shrouded Rotor Region 2	$0.0018R$ x $0.0018R$	$6.1 pixel/mm$	$0.08 m/s$
Unshrouded Rotor Region 1	$0.0016R$ x $0.0016R$	$6.922 pixel/mm$	$0.072 m/s$

TABLE 2.3: Table summarising the accuracy of the PIV.

disk plane $(x/R = 0.48)$. The position of the LDA measurement planes are shown in figure 2.6 and 2.7. The accuracy of the LDA system is dependent on the orientation of the LDA probe head and the traverse with respect to the wind tunnel free stream. The probe was aligned perpendicular to the free stream flow with an accuracy of $\pm 0.5^o$. The alignment of the traverse to the wind tunnel wind tunnel free stream was measured to be less than 0.5^o by measuring the displacement of the laser focal point from the centre line of the wind tunnel over a $1m$ traverse. Table 2.2 contains a summary of the resolution and relative accuracy of the LDA planes of investigation.

2.2.3 PIV ANALYSIS METHODOLOGY AND ACCURACY.

Post processing of the raw PIV images was completed using the commercially available software *Davis* V8.2. PIV of image regions closer than $0.004m$ to the solid surface of the shroud were unreliable as a result of glare, therefore measurements were only made to within $0.005m$ of the shroud surface. The results presented in this chapter were produced using a multi-pass cross correlation algorithm with interrogation windows of 48 x 48 pixels with a 50% overlap, followed by an interrogation window of 24 x 24 pixels with a 50% overlap. The resolution of the PIV was approximately $0.002R$ x $0.002R/pixel$ for all regions of interest. The uncertainty of the velocity measurements was estimated to be approximately $\epsilon_u = 0.077 ms^{-1}$ for each of the interrogation regions (Raffel et al., 2007). A maximum displacement error of $0.1 pixels$ was assumed for each of these PIV regions. By assessing the distortion of a calibration plate located coincidently with the laser light sheet across the camera lens. The alignment of the camera to the laser light sheet was calculated, by the software to be less than 1^o for all experimental investigations investigated in this thesis. A summary of the precise values for each region of interest is presented in table 2.3. The unsteadiness of the flow field was assessed by calculating the root mean square (RMS) of the fluctuations of the measured axial velocity about the mean axial velocity.

2.2.4 PROPER ORTHOGONAL DECOMPOSITION (POD).

Proper Orthogonal Decomposition (POD) by single value decomposition of the flow field was performed to identify the dominant structures of the flow field (F) was developed in accordance with the method summarised by Taira et al. (2017). Each PIV snapshot, of a sequence of n snapshots consists of a uniform grid of discrete velocity

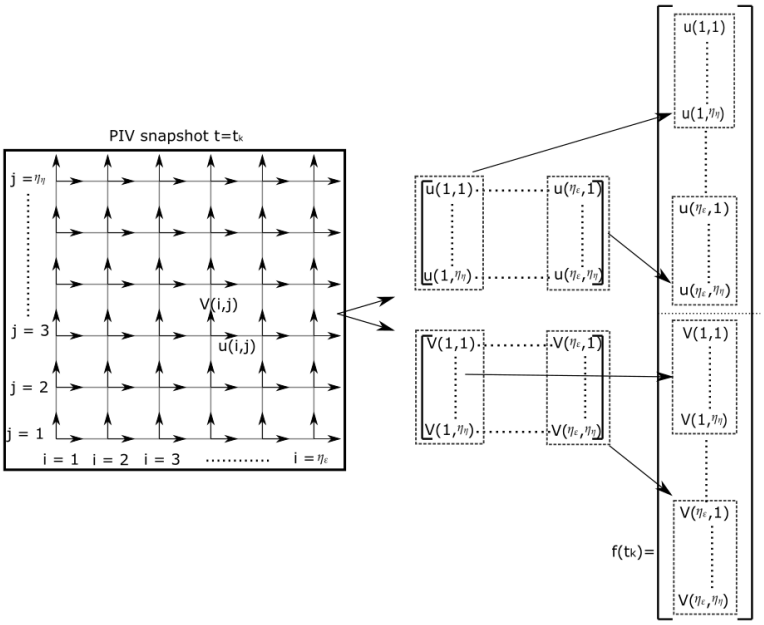

FIGURE 2.8: Example of the process used to decompose the discrete velocity data provided by PIV into the matrix (F) that Proper Orthogonal Decomposition was performed on.

components of size $\eta_\eta x \eta_\varepsilon$ as shown in figure 2.8. The two velocity components were separated into individual matrices of size $\eta_\eta x \eta_\varepsilon$ before being recombined to form a column vector $f(t_k)$ of size $2\eta_\eta\eta_\varepsilon$ as shown in figure 2.8. Matrix (F) is then produced by combining the column vectors $f(t)$ together $F = [f(t_1), f(t_2), f(t_3), ...f(t_n)]$. In POD, the martix (F), which contains the individual velocity components of each instantaneous PIV image pair, is decomposed into a set of orthonormal basis functions, using single value decomposition, that represent the flow field in the most 'optimal' way $(F = \Phi\Sigma\Psi)$. Matrices Φ and Ψ contain the left and right singular vectors of F, and matrix Σ contains the singular values along its leading diagonal. When referring to POD analysis, 'optimal' is used to describe the relative contribution of a given POD mode to the overall kinetic energy of the flow structures. That is, large energetic flow structures that systematically appear in the flow field are captured in the first few POD modes. Summation of the generated modes allow the mean flow field to be reconstructed from the POD modes as well as the reconstruction of individual velocity flow fields. Normalisation of the singular values with respect to the sum of all other singular values allowed the probability of occurrence of that mode in the fluctuating flow to be deduced. The non-zero values of F are the square roots of the non zero eigenvalues of FF^* and F^*F. In order to evaluate the importance of each POD mode on individual velocity fields, an analysis of the temporal coefficients, contained in matrix Ψ associated with each POD mode can be performed. Patter-Rouland et al. (2001) showed that the temporal coefficients of mode $\Psi(n)$ represent the influence mode 'm' has on the development of each instantaneous velocity field (f_n). An example of the variation of the reconstruction coefficients, and therefore the influence of the first three POD modes on 100 instantaneous velocity flow fields is shown in figure 2.9.

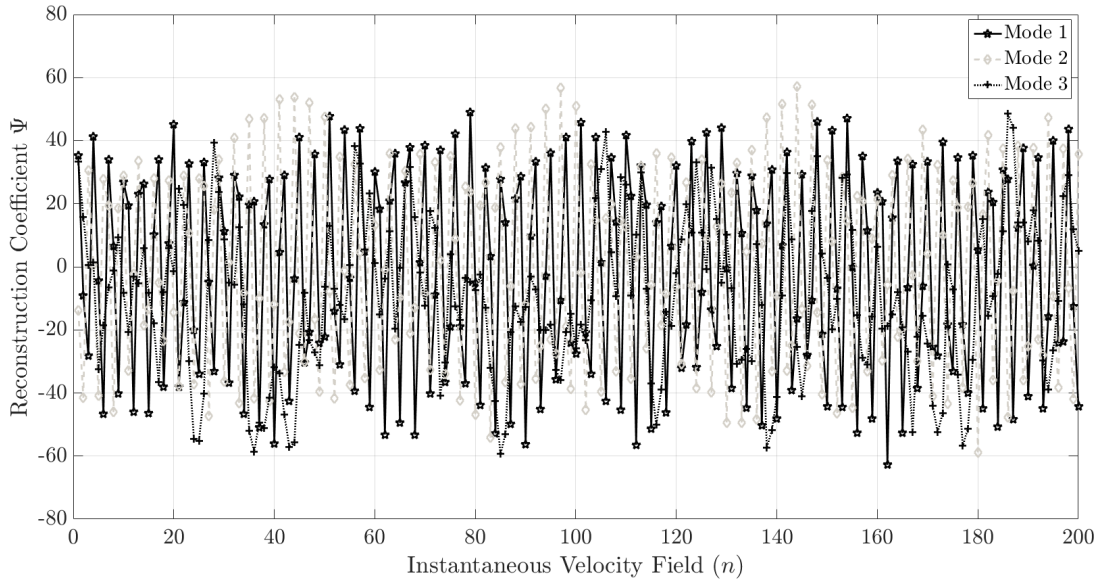

FIGURE 2.9: An example of the variation of the reconstruction coefficients of two POD modes in 300 instantaneous velocity fields.

Extracting the contribution of the 'mth' POD mode from the instantaneous velocity fields, which correspond to the maximum and minimum reconstruction coefficients forms of the flow field. Subtracting the reconstruction coefficient forms of the POD mode from the mean flow field allowed the influence of each POD mode on the structure of the flow field to be determined.

Flow fields with ordered unsteadiness (e.g. periodic vortex shedding) contain a large proportion of energy within their first few POD modes. Whilst highly disordered flow fields, which have a larger number of small scale flow structures have a larger number of low energy ratio POD modes. Therefore the energy distribution of the POD modes can be used to compare the unsteadiness and the disorder of the flow field.

To test the statistical convergence of the POD analysis, it was performed using 300 and 600 PIV image pairs. The results obtained from processing fewer vector maps were qualitatively similar to those obtained using 600 for the first few POD modes. However, for increased POD mode numbers $(m > 6)$, significant differences were observed, but the low modal energies contained within these modes meant that the effect of these modes to the structure of the flow field was negligible. For all experimental configurations investigated in this thesis, the first two POD modes were further assessed by varying the number of vector maps from 200 to 600 in each mode for assessment of convergence. For all low velocity cases the structure of the POD mode converged within 400 vector maps. At higher velocity ratios, the POD convergence occurred at around 500 vector maps (see Appendix B, C and D).

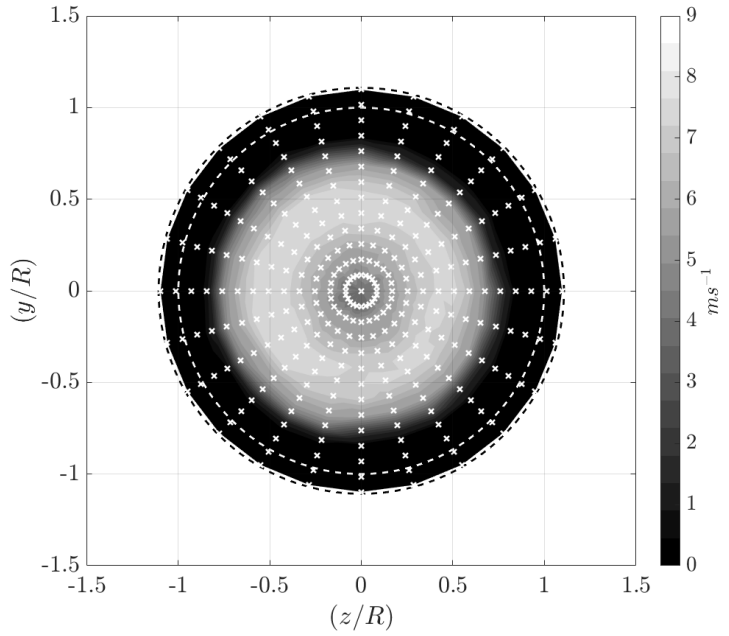

FIGURE 2.10: Averaged axial velocity component (u) produced by the unshrouded rotor operating in hover $0.48R$ from the rotor disk plane $(x/R = -0.52)$. This figure was produced using LDA, and each sample point location is displayed by a white cross. The rotor blade tip path $--$ $(white)$ and the shroud outlet lip $--$ $(black)$ have been projected onto the plane of investigation.

2.3 RESULTS

2.3.1 CHARACTERISATION OF THE FLOW FIELD PRODUCED BY A SHROUDED ROTOR OPERATING IN HOVER.

The flow field produced by the isolated and shrouded rotors operating in hover was characterised using LDA and PIV. This was deemed necessary in order to allow estimates of the averaged induced velocity across the rotor disk and the shroud outlet plane to be calculated. This was used to scale the descent velocity of the rotor. Previous investigations have used shrouds with a centre body located in the core of the shroud.

MEAN FLOW ANALYSIS.

LDA RESULTS.

The mean axial velocity component (u) in a cross-stream plane $0.48R$ upstream (with respect to the wind tunnel flow direction) of the rotor disk plane is presented in figure 2.10 $(x/R = -0.52)$. Based on the axial velocity profile generated by the rotor, the induced velocity $U_{i_R} = 3.8$ of the unshrouded rotor was calculated using equation 2.1, where u is the time averaged induced velocity of the rotor and (A_i) is the area of the region investigated using LDA. For unshrouded rotors operating in axial descent this

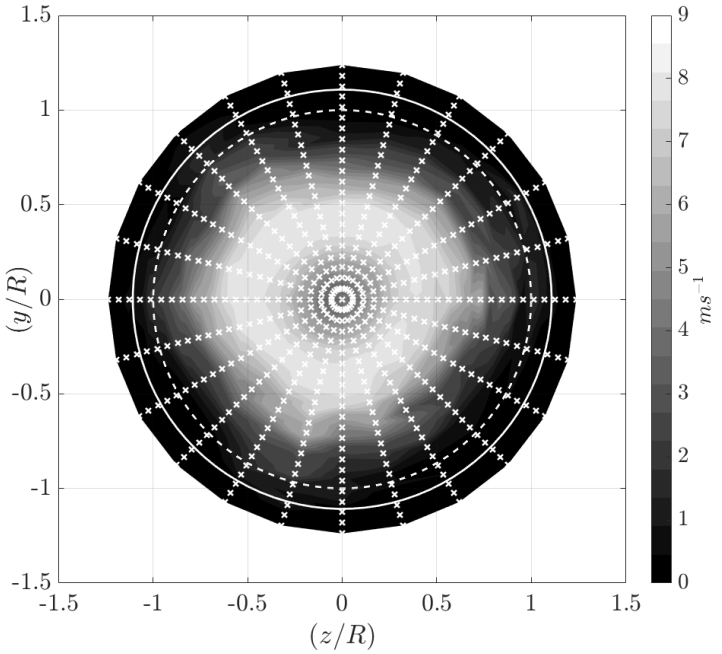

FIGURE 2.11: Averaged axial velocity component (u) produced by the shrouded rotor operating in hover $0.48R$ from the shroud outlet plane $(x/R = 0.48)$. This figure was produced using LDA and each sample point location is displayed by a white cross. The rotor blade tip path $--(white)$ and the shroud outlet lip $-(white)$ have been projected onto the plane of investigation.

is typically used to scale the descent velocity of the rotor. When the ratio of descent velocity $(|U_o|)$ to hover induced velocity U_{i_R} is approximately one $(|U_o|/U_{i_R} \approx 1)$ the rotor is operating in the VRS (Bothezat, 1919). It was not possible to characterise the induced velocity of the rotor inside the shroud, therefore measurements of the wake were taken on a plane $0.48R$ from the shroud outlet plane ($1.48R$ from the rotor disk plane). Figure 2.11 shows the mean axial velocity profile at the outlet of the shroud. A notional induced velocity $(U_i = 3.3ms^{-1})$ of the shrouded rotor was also calculated using equation 2.1. The notional induced velocity of the shrouded rotor was used to scale the descent velocity of both the isolated and the shrouded rotor $(\alpha = |U_o|/U_i)$. LDA velocity profiles along the vertical (y) and horizontal (z) axes of symmetry of both the unshrouded and shrouded rotor outlet planes extracted from figures 2.10 and 2.11 are presented in figure 2.12a. Radial and tangential velocity distribution are presented in figures 2.12b and 2.12c respectively . The results show that the wake from a shrouded rotor is approximately radially symmetric, with a maximum variation of 3.9%. Blockage effects resulting from the shroud support struts on the inlet side of the rotor are believed to be responsible for the slight variation of axial velocity profiles. The extracted profiles presented in figure 2.12 indicate that the shroud does not significantly affect the mean axial velocity profile produced by the rotor. As expected, the axial velocity component is significantly larger than the radial or tangential velocity components of the rotor wake. The mean axial velocity profile is represented as a region of low velocity air underneath the rotor hub surrounded by a region of higher velocity air. Analysis of figure 2.12b shows that, at a distance of

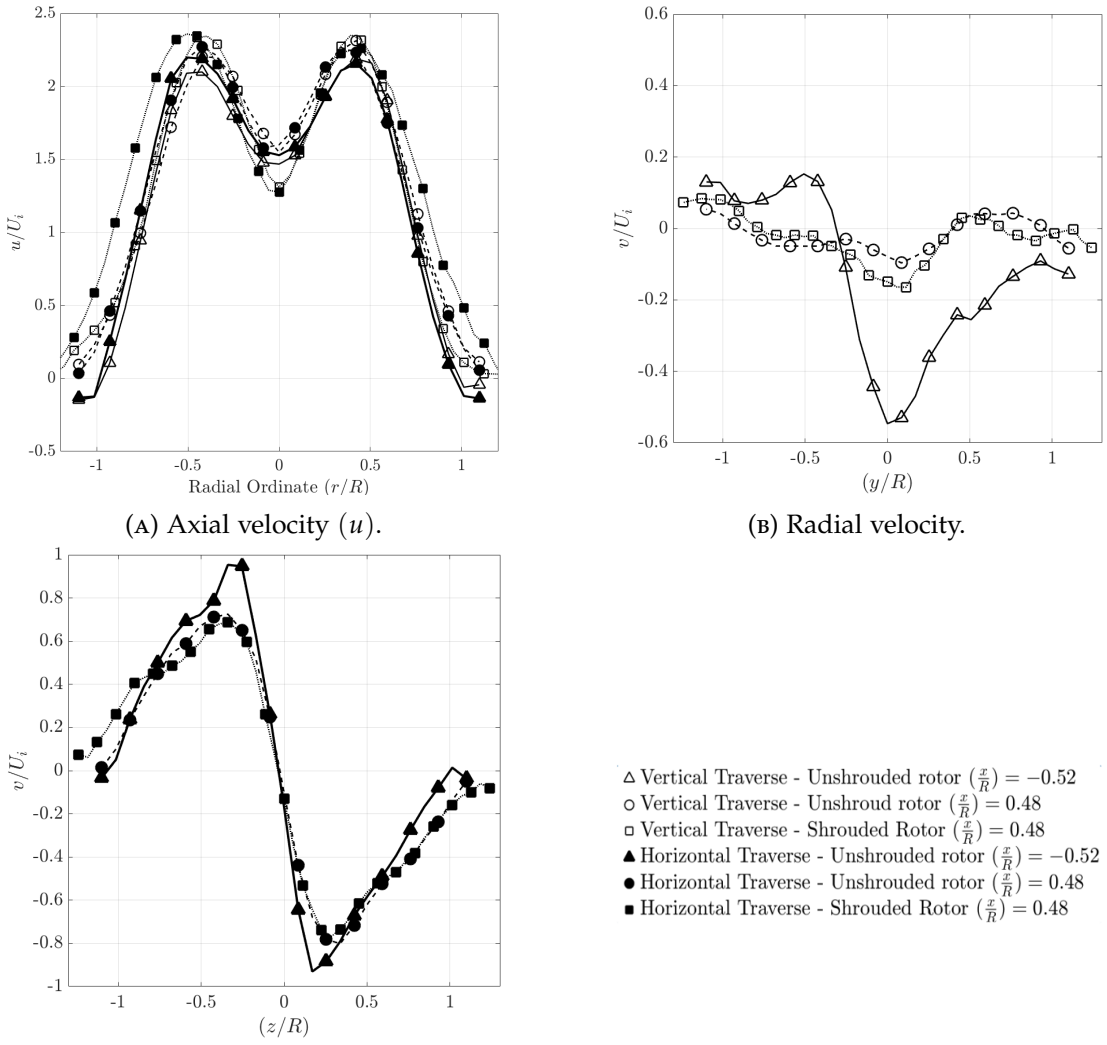

(A) Axial velocity (u).

(B) Radial velocity.

(C) Tangential velocity.

FIGURE 2.12: LDA velocity profiles along the horizontal and vertical axes of symmetry of the shrouded and unshrouded rotor are presented in this figure. Two planes of investigation are presented $0.48R$ from the rotor disk plane $(x/R = -0.52)$ and $1.48R$ from the rotor disk plane $(x/R = 0.48)$

$(x/R = 1.48)$ from the rotor disk plane, the mean axial and tangential velocity profiles are less sharp than those obtained on a plane $(x = 0.48R)$ from the rotor disk plane. Diffusion of the rotor wake is responsible for this variation of the rotor wake. By comparing the velocity profiles produced by the shrouded rotor and the unshrouded rotor on a plane $(x = 1.48R)$ from the rotor disk plane, it is clear that the effect of the shroud on the mean outflow is negligible. It is theorized that this is a consequence of this particular shroud design.

$$U_i = \frac{\int_0^{1.1R} 2\pi urdr}{A_i} \tag{2.1}$$

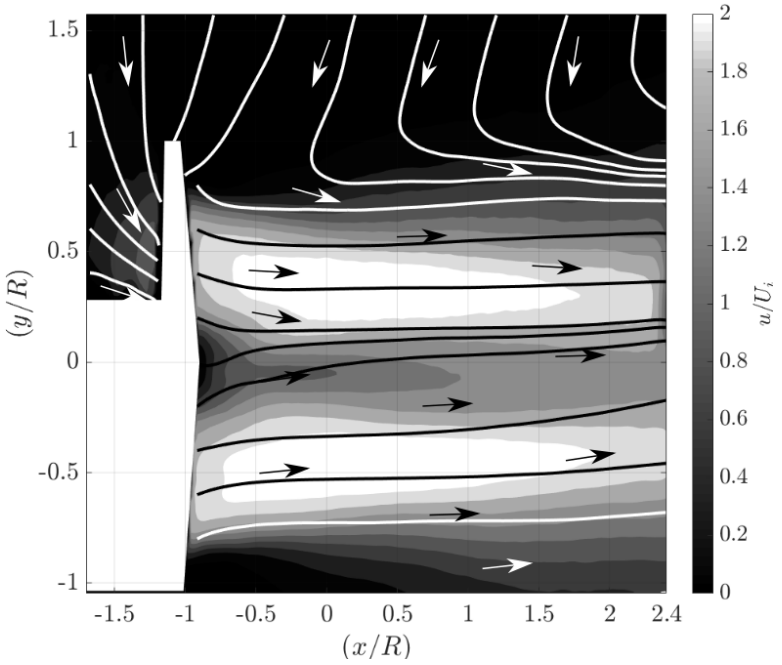

FIGURE 2.13: Mean axial velocity profile (u) produced by the isolated rotor operating in hover. The velocity has been scaled with respect to the notional induced velocity (U_i) at the shrouds outlet. Mean flow streamlines , calculated using a forward euler prediction algorithm implemented in the Matlab function *'streamline'* have been indicated to highlight specific features of the flow field.

PIV RESULTS.

The mean flow field produced by a hovering rotor is show in figure 2.13. As expected, the mean axial velocity profile of the rotors wake can be represented as a region of low velocity air surrounded by a ring of high velocity air. Mean flow streamlines, produced using a forward euler prediction algorithm implemented in the MATLAB Function '*streamline*', indicate that the rotor induces a downwash which extends more than $2.4R$ from the rotor disk plane. Analysis of figure 2.14 shows that the mean flow field produced by the shrouded rotor is topologically similar to that produced by the isolated rotor. The wake from the shrouded rotor propagates more than $4R$ from the shroud outlet plane. The average flow fields presented in figure 2.13 and figure 2.14 were both produced using the same rotor, operating under the same operational conditions, however one is shrouded and the other is unshrouded. The different thrust generation mechanisms were not considered important in this investigation as the focus was on the average induced velocity profiles of the two configurations. It should be noted that figure 2.14 was produced by stitching together the mean flow field results of two PIV regions of interest using linear interpolation. Earlier investigations into the flow field produced by a shrouded rotor, performed by Martin and Tung (2004), identified a region of reverse flow underneath the rotors centre body. This region of reverse flow is not observed in the mean flow field presented in figure 2.14 or the LDA velocity profiles presented in figure 2.12. The absence of a rotor centre body inside of the shroud is believed to be responsible for this variation of the mean

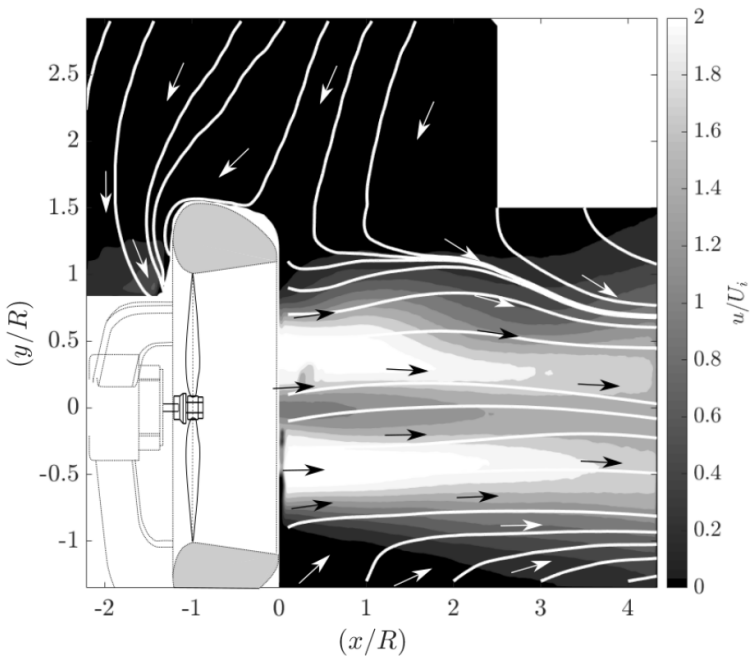

FIGURE 2.14: Mean axial velocity profile (u) produced by the shrouded rotor operating in hover. The velocity has been scaled with respect to the notional induced velocity (U_i) at the shrouds outlet. Mean flow streamlines , calculated using a forward euler prediction algorithm implemented in the Matlab function *'streamline'* have been indicated to highlight specific features of the flow field. Note this is a montage of the mean velocity profile of PIV region 1 and 2 stitched together using linear interpolation.

velocity profile.

The mean axial flow velocity profiles produced by the unshrouded and shrouded rotor on the rotor centreline, are presented in figure 2.15. The velocity profiles presented in figure 2.15 were extracted from figure 2.13 and figure 2.14. Figure 2.15 shows that the wake from the isolated rotor initially accelerated as the distance from the rotor disk plane increased. This occurs because of the conservation of momentum of the rotor wake and the influence of the blade tip vortices that are above and below the point of interest. The wake from the shrouded rotor also initially accelerated as the distance from the shroud outlet plane increased. However the rate of acceleration of the shrouded rotors wake was lower than that of the isolated rotor. Upon exiting the shroud the flow accelerates due to the conservation of momentum of the shrouded rotors wake. The wake from the unshrouded and the shrouded rotor reached a maximum mean axial velocity component of $u/U_i = 1.6$ at distances of $3R$ and $5.2R$ from the rotor disk plane. The velocity at the shroud outlet plane produced by the shrouded rotor is lower than the velocity produced by the unshrouded rotor at the same distance from the rotor disk plane $(x/R = 0)$.

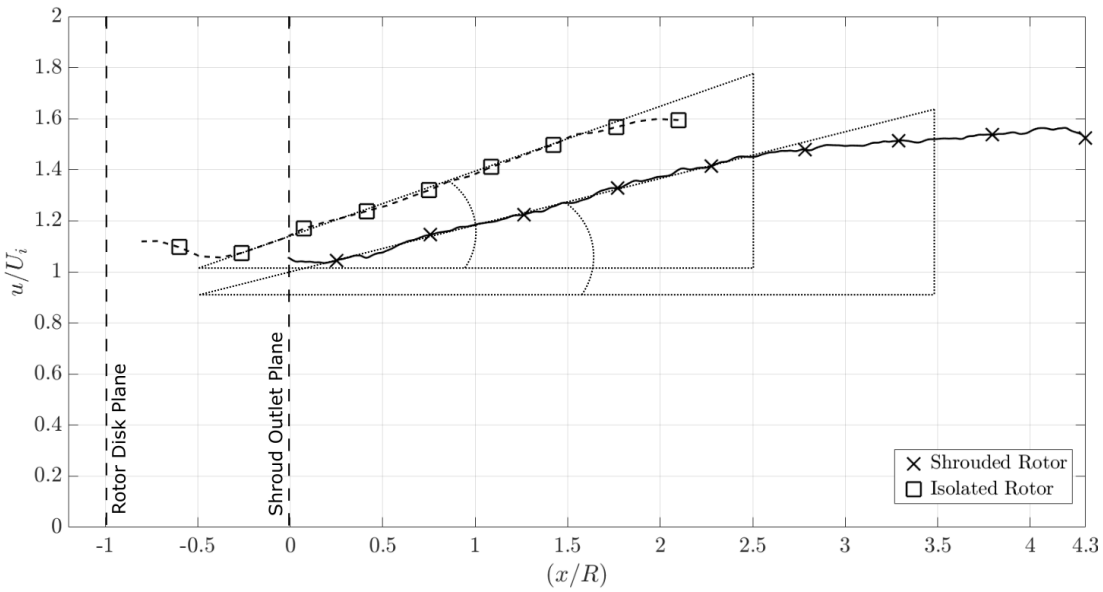

FIGURE 2.15: Mean axial velocity profile (u) along the longitudinal axis $u(x, 0, 0)$ scaled with respect to the notional induced velocity of the rotor. (U_i).

UNSTEADINESS OF THE FLOW FIELD PRODUCED BY A SHROUDED ROTOR OPERATING IN HOVER.

$$u_{rms} = \sqrt{\frac{1}{n}((u_1 - \bar{u})^2 + (u_2 - \bar{u})^2 + ... + (u_n - \bar{u})^2)} \tag{2.2}$$

The RMS of the axial velocity component (u_{rms}), produced by an unshrouded and a shrouded rotor, are presented in figure 2.16 and figure 2.17, respectively. The RMS of the fluctuations was calculated using equation 2.2 where n is the number of image pairs recorded, u_n is the instantaneous velocity component and $\bar{u}$ is the averaged velocity component. Analysis of figure 2.16 shows that four regions of unsteady flow extend downwards, away from the rotor disk plane. Analysis of individual PIV image pairs, such as the vorticity plots presented in figure 2.18, revealed that these regions are associated with the passage of the blade root and tip vortices. The vorticity plots presented throughout this thesis were calculated from the curl of the flow field $\vec{w} = \nabla \times f$ .The third component of the vorticity w_z of the flow can be expressed as a scalar value $[\frac{df_y}{dx} - \frac{df_x}{dy}]$ as shown in equation 2.3. The differentials of the flow field $\frac{df_y}{dx}$, $\frac{df_x}{dy}]$, were calculated using a least square method, which incorporated a weighted differential from four adjacent points in the x and the y direction, in accordance with the method described by Raffel et al. (2007).

$$\begin{bmatrix} \frac{d}{dx} \\ \frac{d}{dy} \\ \frac{d}{dz} \end{bmatrix} \times \begin{bmatrix} f_x \\ f_y \\ f_z \end{bmatrix} = \begin{bmatrix} \frac{df_z}{dy} - \frac{df_y}{dz} \\ \frac{df_x}{dz} - \frac{df_z}{dx} \\ \frac{df_y}{dx} - \frac{df_x}{dy} \end{bmatrix} = \begin{bmatrix} w_x \\ w_y \\ w_z \end{bmatrix} \tag{2.3}$$

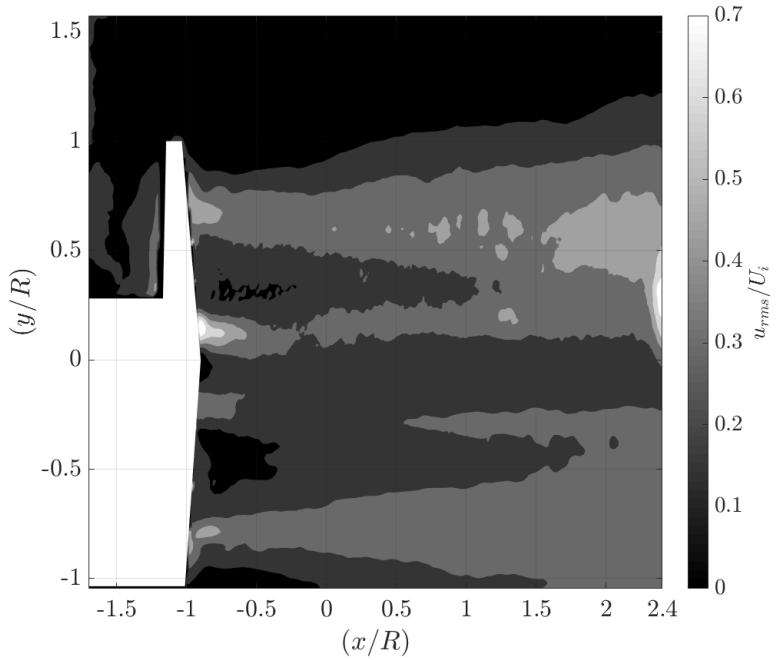

Figure 2.16: Contour plots of the RMS of the fluctuations about the mean axial velocity (u_{rms}) produced by the unshrouded rotor operating in hover. The RMS of the fluctuations is scaled with respect to the notional induced velocity of the shrouded rotor (U_i).

At a distance of $3R$ from the rotor disk plane $(x/R = 1.5)$ the structures of the rotor wake break down as a result of the three natural instability modes of helical vortices (Gupta and Plump, 2001). No clear structures could be observed in the wake at displacements greater than $(x/R > 1.5)$. The wake from a shrouded rotor also shows four distinct regions of unsteadiness, which broaden and merge together as the distance from the shroud outlet plane increased. However, no clear vortical structures could be observed in the wake from the shrouded rotor, as shown by the instantaneous vorticity plot presented in figure 2.18b. The unsteadiness is, therefore, associated with the shear layers produced by the shrouded rotors wake interacting with the quiescent surroundings. In general, the RMS of the fluctuations of the wake produced by the shrouded rotor was lower than those produced by the isolated rotor. This indicates that the flow field produced by the shrouded rotor is generally steadier than that of the isolated rotor.

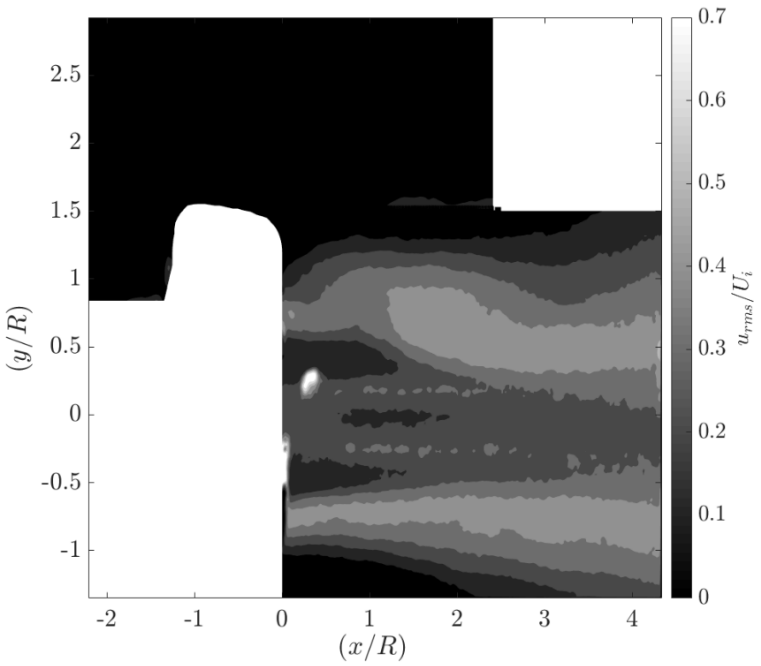

FIGURE 2.17: Contour plots of the RMS of the fluctuations about the mean axial velocity (u_{rms}) produced by the shrouded rotor operating in hover. The RMS of the fluctuations is scaled with respect to the notional induced velocity of the shrouded rotor (U_i). Note this is a montage of the RMS of the fluctuations about the mean axial velocity profiles of PIV regions 1 and 2 stitched together using linear interpolation.

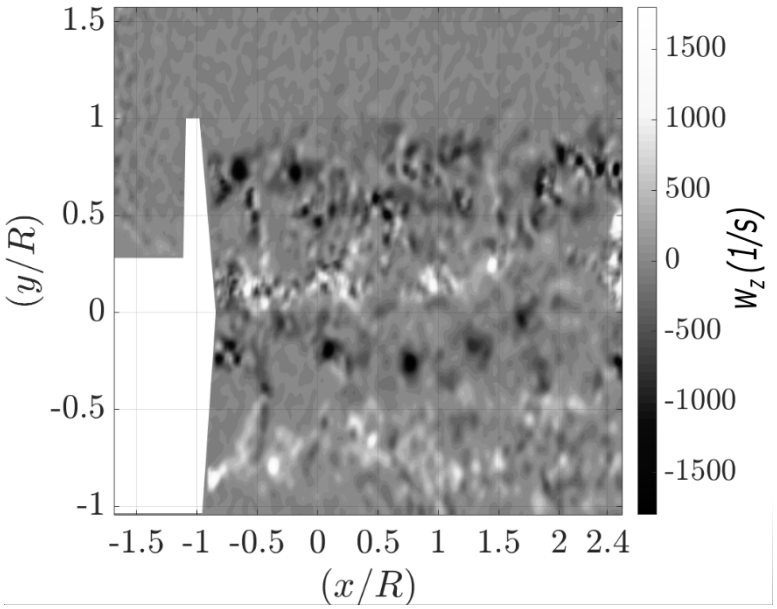

(A) Isolated Rotor

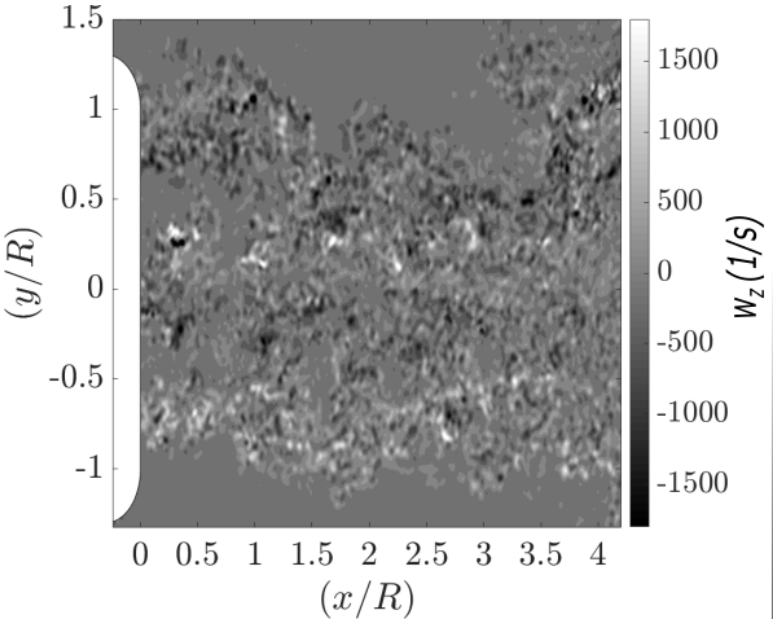

(B) Shrouded rotor

FIGURE 2.18: Instantaneous contour plots of the third component of vorticity $[\frac{df_y}{dx} - \frac{df_x}{dy}]$ contained within the flow field produced by the unshrouded (fig 2.18a), and the shrouded rotor (fig 2.18b), at a velocity ratio of $\alpha = 0.0$. Note the existence of a system of blade root and tip vortices in the unshrouded rotors wake.

2.3.2 EFFECT OF AXIAL DESCENT ON THE MEAN FLOW FIELD PRODUCED BY A SHROUDED ROTOR IN AXIAL DESCENT.

LDA RESULTS.

Figure 2.20 and figure 2.21 show the development of the mean velocity profiles produced by an isolated and a shrouded rotor on a plane $1.48R$ from the rotor disk plane $x/R = 0.48$, as the velocity ratio was increased from $\alpha = 0$ to $\alpha = 2.0$. At low velocity ratios ($\alpha < 1.2$), the mean axial velocity profile of the isolated rotor developed to resemble that of a round jet, with a single peak velocity located at the centre of the rotor ($y/R = 0$) (Bernero., 2000). The peak velocities associated with hovering rotors at a radial ordinate of $y/R = \pm 0.7$ could no longer be observed. This indicates that the helical structures associated with the passage of the blade tip vortices at this location have broken down as a result of the natural instabilities of helical vortices (Leishman et al., 2004). Coupled with the gradual formation of strong radial velocities, this indicates that the rotor wake is deflected radially outboard. Peak velocities occurred outboard of the rotor at radial ordinates of $y/R = \pm 1.4$. Analysis of figure 2.20c shows that the tangential velocity of the rotor wake, at a displacement of $1.48R$ from the rotor disk plane, gradually reduced from a maximum at $\alpha = 0.0$, to zero at a velocity ratio of $\alpha = 1.4$. Closer to the rotor disk plane, the tangential velocity of the rotor reduced to zero once the velocity ratio approached $\alpha = 2.0$. At descent velocities below $\alpha < 1.2$ the tangential velocity profile of the rotor appeared to be unaffected. At higher velocity ratios ($\alpha \geq 1.3$) the axial velocity profile becomes negative ($-u$) indicating that the interaction between the rotor wake and the wind tunnel free stream occurs downstream of the plane of investigation ($x/R < 0.0$). At $\alpha = 1.3$, a region of higher magnitude axial velocity flow forms in the centre of the rotor, surrounded by a region of lower velocity flow (figure 2.20a). This indicates that the wind tunnel free stream penetrates through the plane of investigation in line with the rotor hub ($y/R = 0.0$).

Analysis of the velocity profiles on a plane $0.48R$ from the rotor disk plane ($x/R = -0.52$), shown in figure 2.19, indicate that similar trends are observed in the velocity profiles on a plane closer to the rotor disk plane at different velocity ratios. Closer to the rotor, a region of lower velocity flow forms in the centre of the rotor. As the descent velocity increased this region develops into the conical region of reverse flow which was identified by Brinson (1998). The region of the rotor which experiences reversed flow increases until the entire plane of investigation experiences a negative axial velocity component ($-u$). At this point the rotor is operating in the windmill brake state. The location of the peak mean axial velocity component moves radially outboard from $y/R = \pm 0.43$ at $\alpha = 0.0$ to $y/R = \pm 0.78$ at $\alpha = 1.4$, as a result of the penetration of the wind tunnel free stream through the rotor disk plane. Close to the rotor, the radial velocity component of the rotor wake was not significantly affected until the rotor was operating at a decent velocity ratio of $\alpha \geq 1.3$. At velocity

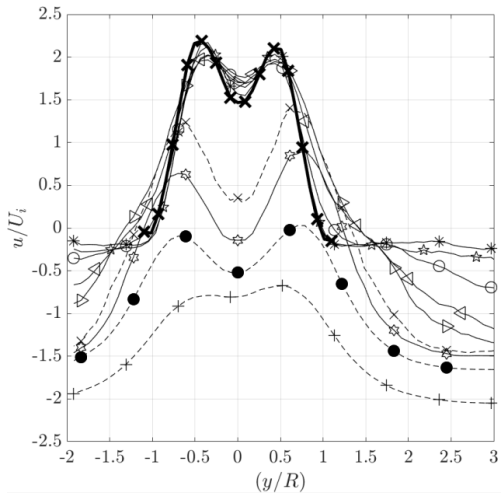

(A) Axial velocity (u).

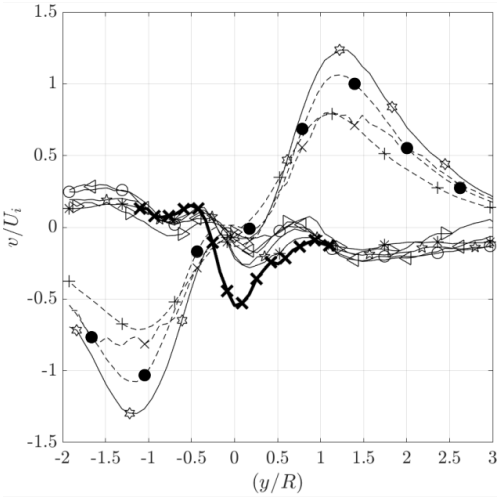

(B) Vertical velocity component (v).

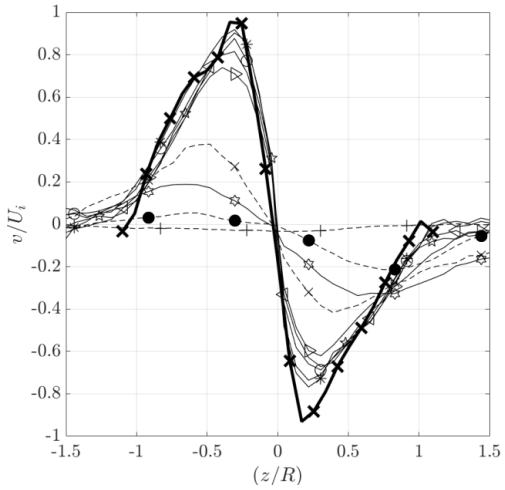

(C) Tangential velocity.

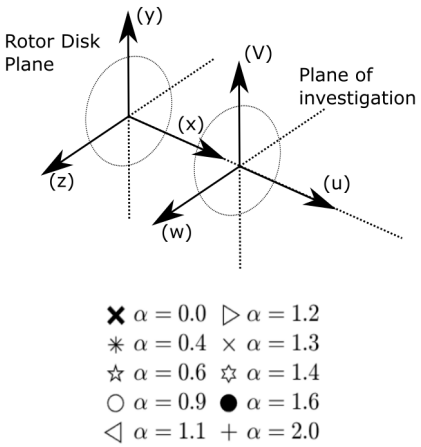

FIGURE 2.19: LDA mean velocity profiles along the axis of symmetry of the isolated rotor on a plane $0.48R$ from the rotor disk plane $(x/R = -0.52)$, as the descent velocity ratio was varied from $\alpha = 0$ to $\alpha = 2.0$.

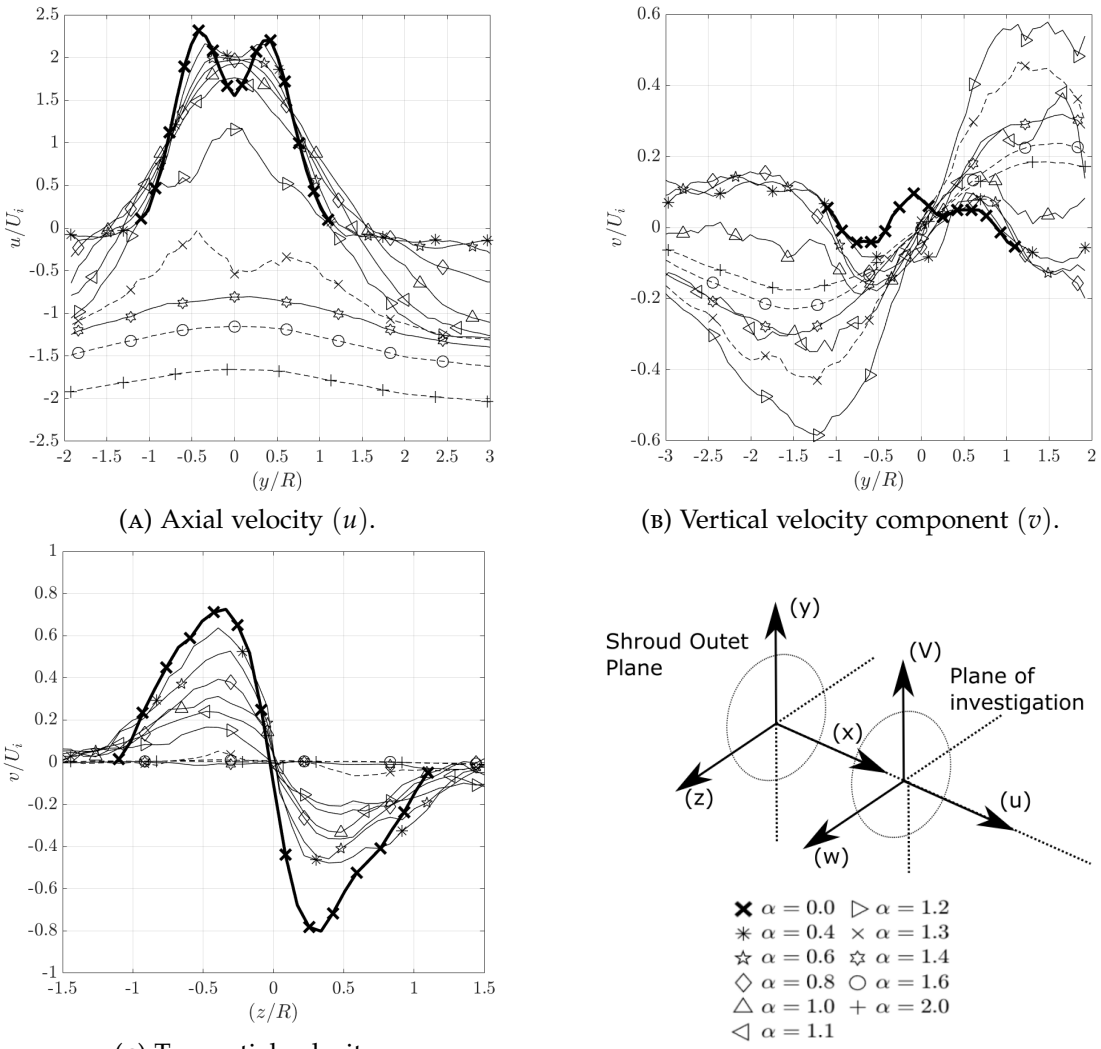

(A) Axial velocity (u).

(B) Vertical velocity component (v).

(C) Tangential velocity.

FIGURE 2.20: LDA mean velocity profiles along the axis of symmetry of the isolated rotor on a plane $1.48R$ from the rotor disk plane $(x/R = 0.48)$, as the descent velocity ratio was varied from $\alpha = 0$ to $\alpha = 2.0$.

ratios greater than $\alpha \geq 1.3$ the rotor wake and the wind tunnel free stream is deflected radially outboard. As expected, the magnitude of the velocity components are all higher close to the rotor disk plane, as shown in figure 2.19b. Similar trends can be observed in the radial velocity profiles produced by the shrouded rotor, presented in figure 2.21b. Once again, at low velocity ratios the radial velocity component of the shrouded rotor wake resembles that produced by the shrouded rotor when it is operating in hover. At higher velocity ratios $\alpha \geq 1.2$, strong radial velocity components were recorded, indicating that the shrouded rotor wake and the wind tunnel free stream are deflected around the shroud. Analysis of figure 2.21c shows that the tangential velocity profile of the shrouded rotor, operating in axial descent, is similar to that produced by the unshrouded rotor on the same plane of investigation. Both show the gradual reduction of the tangential velocity component to zero at $\alpha = 2.0$.

Figure 2.21a shows the mean axial velocity component of the shrouded rotor wake $1.48R$ from the rotor disk plane. As with the isolated rotor, as the velocity ratio was increased from $\alpha = 0.4$ to $\alpha = 0.9$, the mean axial velocity profile becomes uniform across a large portion of the shroud outlet plane $(y/R \leq |0.4|)$. No significant effect could be observed in the mean axial velocity profile across the shroud outlet plane $(y/R \leq |1.0|)$, when the descent velocity ratio was increased from $\alpha = 0.4$ to $\alpha = 1.2$. Increasing the descent velocity further, leads to a reduction in the mean axial velocity across the shroud outlet plane. At a velocity ratio of $\alpha = 1.4$, the mean flow across the shroud outlet plane is negative $(-u)$, indicating that the rotor wake does not extend through the plane of investigation. Instead, the wind tunnel free stream passes through the plane of investigation. Unfortunately, the velocity profile inside the shroud was beyond the scope of this investigation. A comparison of the mean velocity profiles produced by the shrouded and unshrouded rotor, on a plane $1.48R$ from the rotor disk plane $(x/R = 0.48)$, are presented in figure 2.22. From figure 2.22, it is clear that, at velocity ratios below $(\alpha = 1.2)$, the velocity profile produced by the shrouded rotor is similar to that produced by the unshrouded rotor at this plane of measurement. At low velocity ratios $\alpha \leq 1.2$ the velocity of the wake produced by the shrouded rotor was typically greater than that produced by the unshrouded rotor.

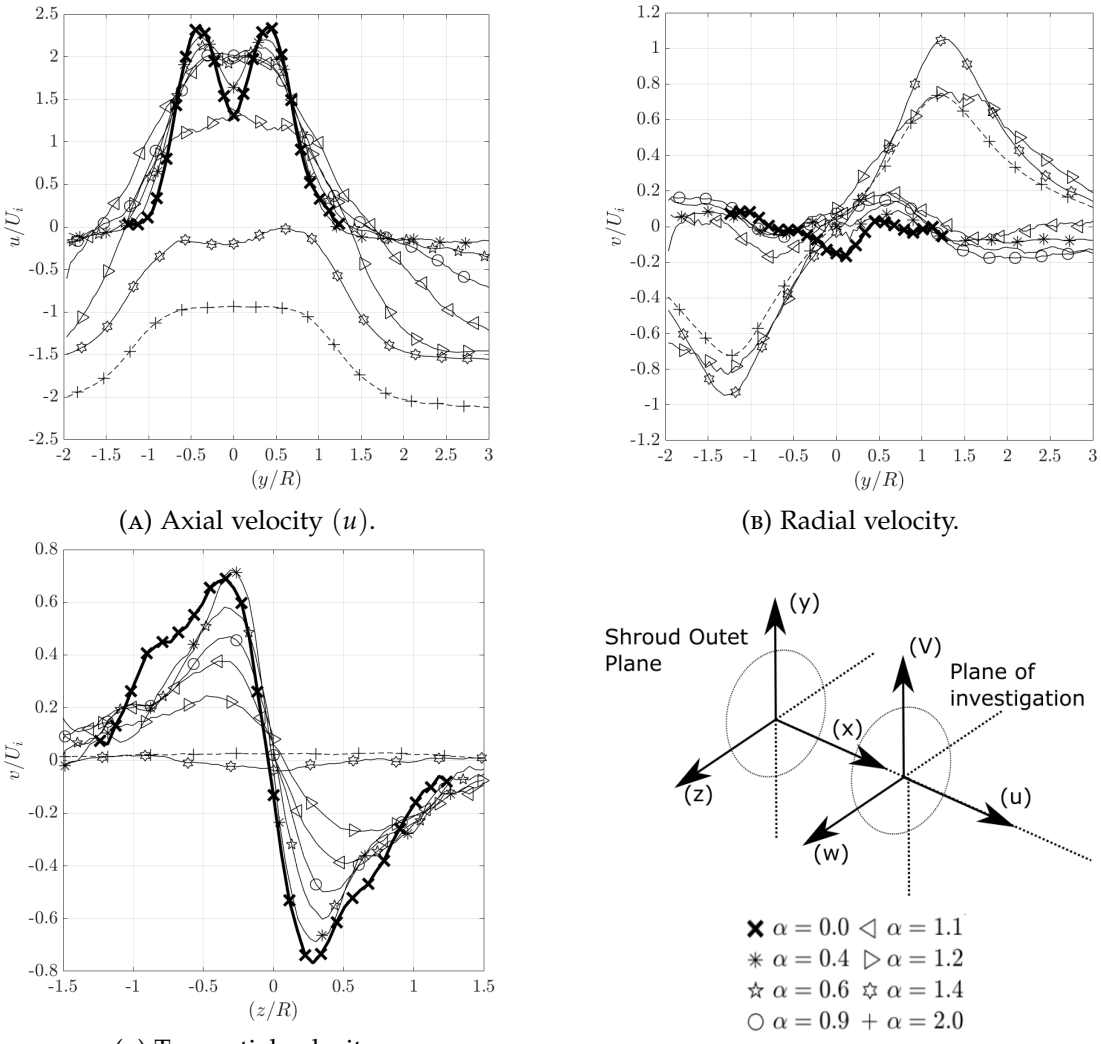

(A) Axial velocity (u).

(B) Radial velocity.

(C) Tangential velocity.

FIGURE 2.21: LDA mean velocity profiles along the axis of symmetry of the shrouded rotor on a plane $1.48R$ from the rotor disk plane $(x/R = 0.48)$, as the descent velocity ratio was varied from $\alpha = 0$ to $\alpha = 2.0$.

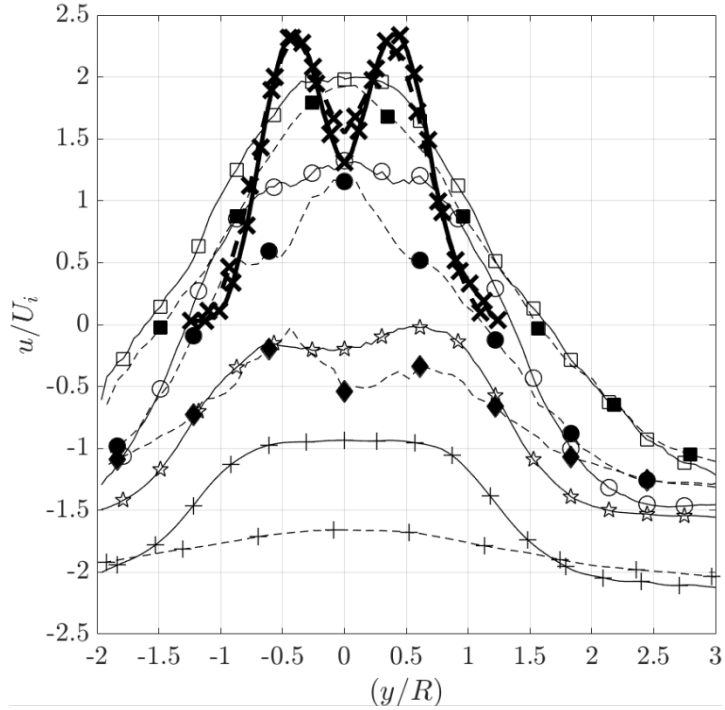

FIGURE 2.22: Selective comparison of the mean LDA velocity profiles along the vertical axis of symmetry of the shrouded and unshrouded rotor, on a plane $1.48R$ from the rotor disk plane $(x/R = 0.48)$, as the descent velocity was varied from $\alpha = 0$ to $\alpha = 2.0$.

PIV RESULTS.

Figure 2.23 and figure 2.24 show the development of the mean flow fields below the isolated and shrouded rotor, as the descent velocity was increased from hover $\alpha = 0$ to $\alpha = 1.4$. As expected, the results presented in figure 2.23 related to the mean flow field produced by an isolated rotor operating in axial descent were similar to those presented by Green et al. (2005). These results showed that, at low descent velocity, the near flow field is similar to that produced by a hovering rotor. As the descent velocity increased, the rotor wake was increasingly encroached upon by the wind tunnel free stream. At the interaction between the rotor wake and the wind tunnel free stream, a saddle point forms in line with the rotor hub. Analysis of figures 2.23d, 2.23e, 2.23f and 2.23g shows that the saddle point moves towards the rotor disk plane as the descent velocity increases, moving from $x/R \approx 1.8$ at $\alpha = 1.0$ to $x/R \approx -0.3$ at $\alpha = 1.3$. It is hypothesised that, at low descent velocities, the interaction between the rotor wake and the wind tunnel free stream will occur outside of the region of investigation $(x/R > 2.0)$. As in the research of Green et al. (2005), the fate of the saddle point upon reaching the rotor disk plane could not be determined. At higher descent velocity ratios a conical region of reverse flow penetrates up to the rotor disk plane. Outboard of the rotor a large region of recirculation forms. At a velocity ratio of $\alpha = 1.0$ the centre of the recirculation is located $1.2R$ from the rotor disk plane and $1.2R$ outboard of the rotor hub $(x/R = -0.3, y/R = 1.2)$. As the descent velocity was increased, the recirculation moves from below the rotor to above the rotor disk plane until the rotor enters the windmill brake state. The flow topology described above is characteristic of the flow field produced by a rotor operating in the VRS.

Figure 2.24 shows the development of the mean flow field produced by a shrouded rotor, as the descent velocity ratio was again increased from $\alpha = 0.0$ to $\alpha = 1.4$. When compared to the PIV measurements of an isolated rotor the same general topological features can be observed. At low descent velocities, the the flow field resembles that of a round jet, with a single centralised velocity peak located on the geometric centreline of the shroud. The ring of high velocity air surrounding a region of low velocity air can no longer be observed. Mean flow saddle points form at the interaction between the rotor wake and the wind tunnel free stream, on the geometric centreline of the shroud as a result of the radial deflection of the rotor wake. Analysis of figure 2.24 shows that the saddle point moves towards the shroud outlet plane as the descent velocity was increased, moving from $x/R \approx 3.5$ at $\alpha = 0.9$ to $x/R \approx 0.6$ at $\alpha = 1.3$.

The structure of the flow field inside the shroud was not investigated, therefore the fate of the saddle point, once it passes through the shroud outlet plane, could not be determined. Figure 2.26b shows the mean flow field produced by the shrouded rotor when it is operating at a descent velocity ratio of $\alpha = 2.0$. At this velocity ratio, no air exits the shroud through the shroud outlet plane. Instead, the wind tunnel free stream passes through and around the shroud. At this point, the shrouded rotor is

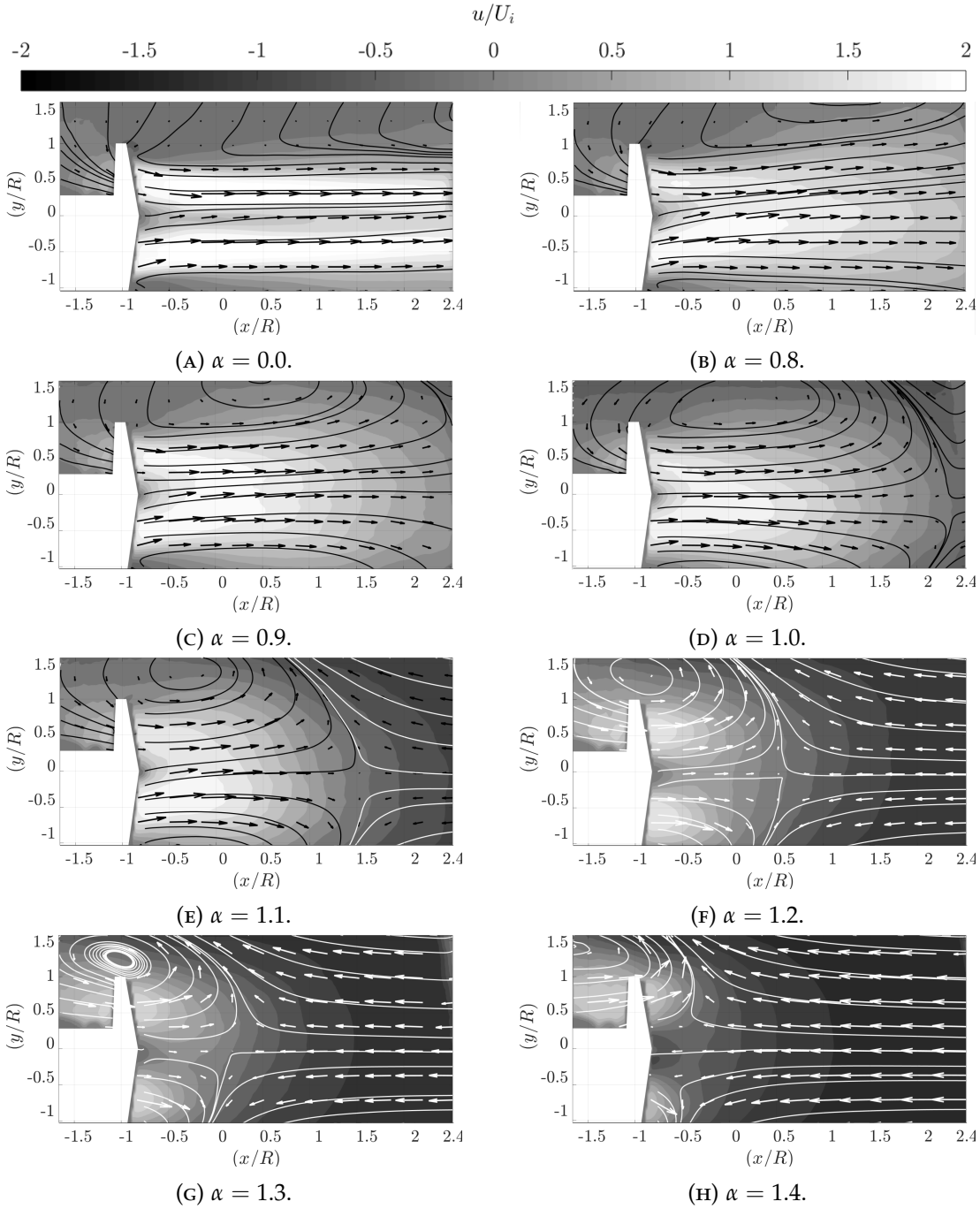

(A) $\alpha = 0.0$. (B) $\alpha = 0.8$.

(C) $\alpha = 0.9$. (D) $\alpha = 1.0$.

(E) $\alpha = 1.1$. (F) $\alpha = 1.2$.

(G) $\alpha = 1.3$. (H) $\alpha = 1.4$.

FIGURE 2.23: Averaged mean axial velocity contour plots of the unshrouded rotor (PIV: Region 1) as the descent velocity $|U_o|$ increases from $\alpha = 0.0$ to 1.4. Streamlines and a reduced number of velocity vectors are superimposed onto the contour plots. All of the velocity vectors are scaled with respect to the notional induced velocity, (U_i). Note: the formation of a saddle point in figure 2.23d, 2.23e, 2.23f and 2.23g.

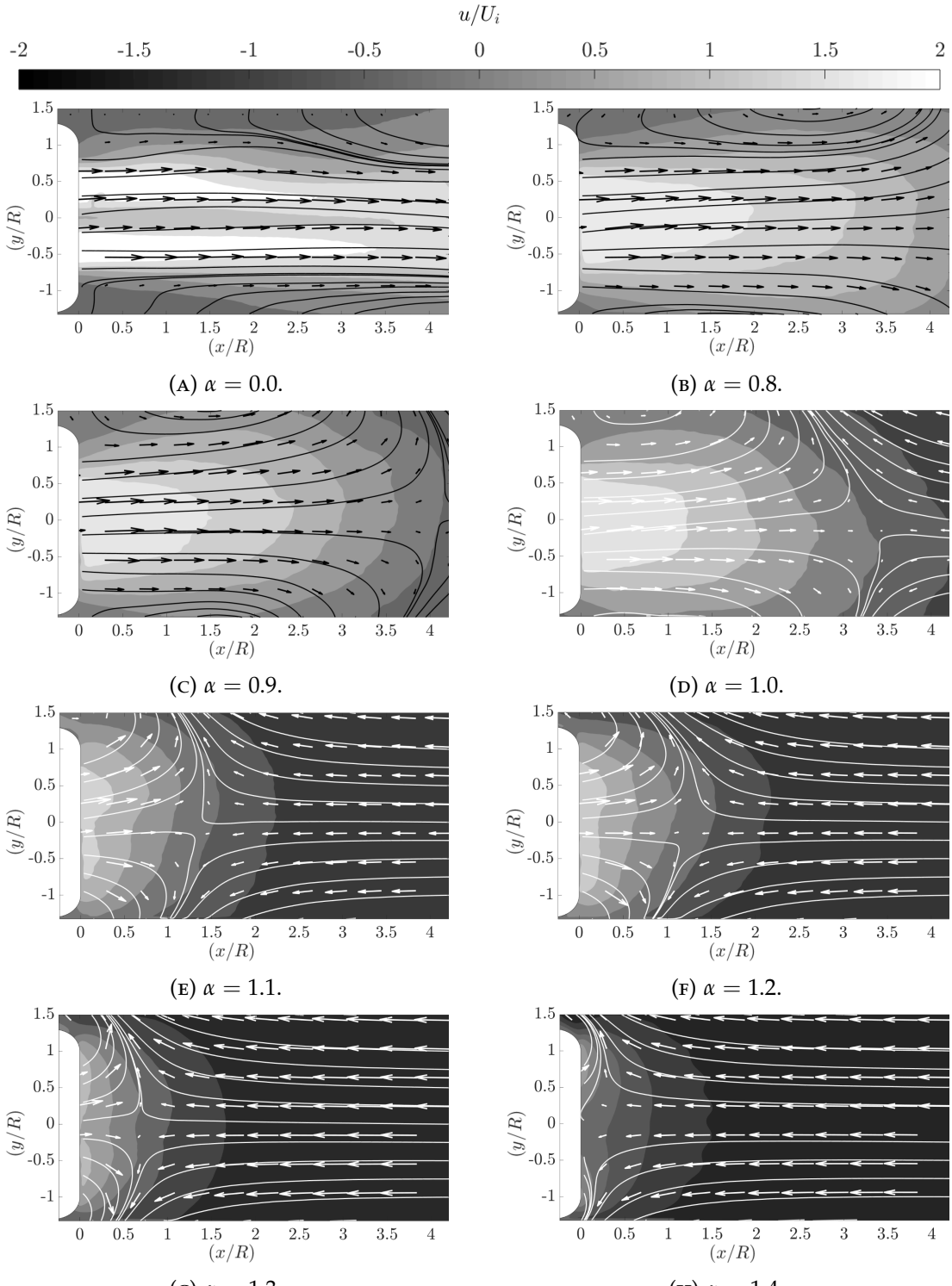

(A) $\alpha = 0.0$. (B) $\alpha = 0.8$.

(C) $\alpha = 0.9$. (D) $\alpha = 1.0$.

(E) $\alpha = 1.1$. (F) $\alpha = 1.2$.

(G) $\alpha = 1.3$. (H) $\alpha = 1.4$.

FIGURE 2.24: Averaged mean axial velocity plots of the shrouded rotor (PIV: Region 1) as the descent velocity $|U_o|$ increases from $\alpha = 0.0$ to 1.4. Streamlines and a reduced number of velocity vectors are superimposed onto the contour plots. All of the velocity vectors are scaled with respect to the notional induced velocity, (U_i). Note: the formation of a saddle point in figure 2.24c, 2.24d, 2.24e, 2.24f and 2.24g.

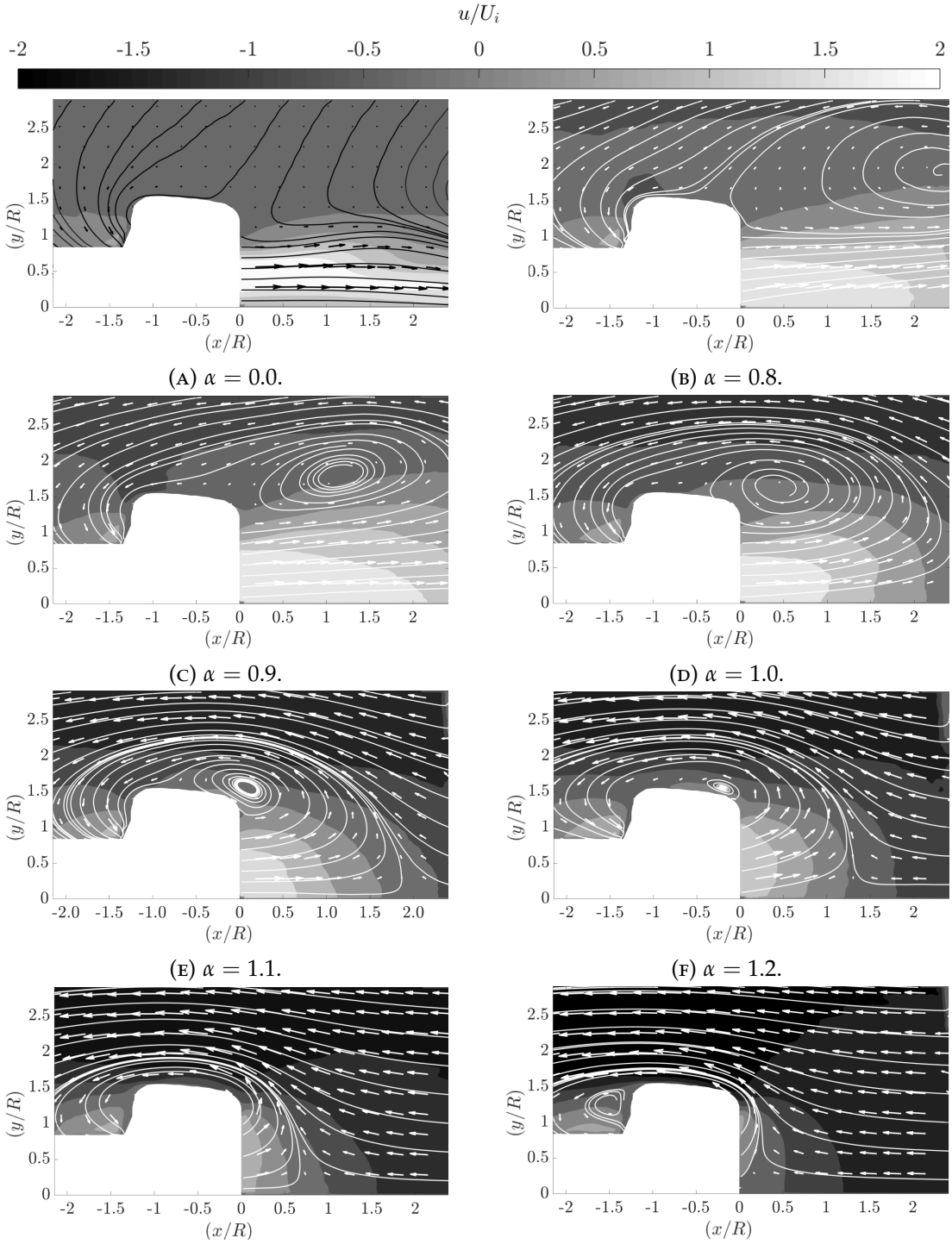

(A) $\alpha = 0.0$. (B) $\alpha = 0.8$.

(C) $\alpha = 0.9$. (D) $\alpha = 1.0$.

(E) $\alpha = 1.1$. (F) $\alpha = 1.2$.

(G) $\alpha = 1.3$. (H) $\alpha = 1.4$.

FIGURE 2.25: Averaged mean axial velocity plots of the shrouded rotor (PIV: Region 2) as the descent velocity $|U_o|$ increases from $\alpha = 0.0$ to 1.4. Streamlines and a reduced number of velocity vectors are superimposed onto the contour plots. All of the velocity vectors are scaled with respect to the notional induced velocity, (U_i). Note: Only half of the saddle point can be observed in figure 2.25e, 2.25f and 2.25g.

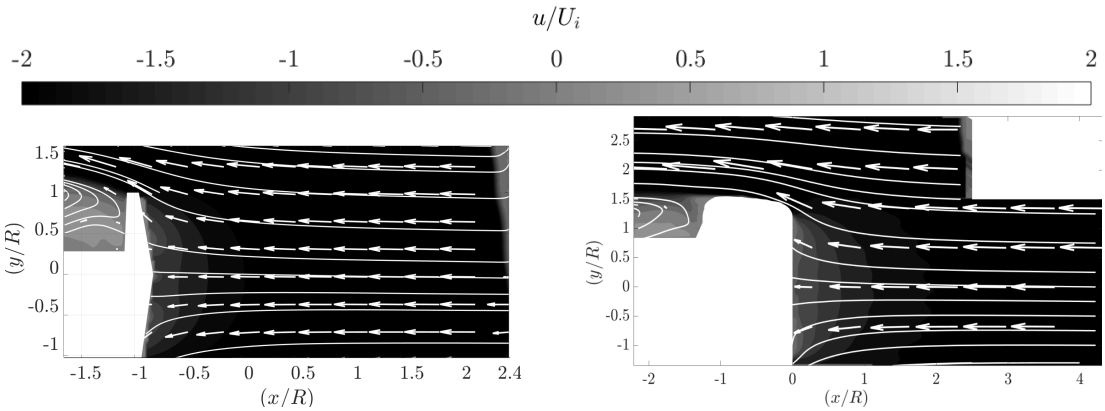

(A) Isolated rotor $\alpha = 2.0$ (B) Shrouded Rotor $\alpha = 2.0$

FIGURE 2.26: Mean axial velocity plots of flow field produced by a shrouded rotor operating at a descent velocity ratio of $\alpha = 2.0$. Streamlines and a reduced number of velocity vectors are superimposed onto the contour plots. All of the velocity vectors are scaled with respect to the notional induced velocity (U_i).

operating in a state analogous to the windmill brake state of an isolated rotor. Due to the penetration of the wind tunnel free stream through the shroud outlet plane, shown in figure 2.24h, and the rotor disk plane of the isolated rotor, shown in figure 2.23h, both show the formation of a conical region of reversed flow inline with the centre of the rotor. It is believed that the saddle point would continue to approach the rotor disk plane of the shrouded rotor. Once again the fate of the saddle point after it reached the rotor could not be determined.

The development of the mean flow field outboard of the shroud is shown in figure 2.25. This figure shows that, at low descent velocities, the mean flow field produced by a shrouded rotor is similar to that produced by the isolated rotor. Both configurations indicate the formation of a large region of recirculation outboard of the rotor or shroud. At $\alpha = 0.8$ the centre of the recirculation, shown in figure 2.25b, is located approximately $2.4R$ upstream of the shroud outlet plane and $2.0R$ from the core of the shroud. As the descent velocity increased the recirculation moved from upstream of the shroud to around the side of the shroud, as shown in figure 2.25e, where at $\alpha = 1.1$, the centre of the recirculation is located close to leading edge of the shroud outlet $(x/R \approx 0, y/R \approx 1.5)$. At velocity ratios greater than $\alpha \geq 1.4$ the recirculation is transported downstream, away from the shrouded rotor.

Analysis of figure 2.23f shows that the unshrouded rotor entered the VRS at a velocity ratio of $\alpha = 1.3$, (scaled with respect to the induced velocity of the isolated rotor this corresponds to a velocity ratio of 1), whilst figure 2.25d showed that the shrouded rotor entered the VRS at a velocity ratio of $\alpha = 1.0$. Therefore, it is hypothesised that the shrouded rotor enters the VRS at a slightly lower descent velocity ratio than the unshrouded rotor.

Mean centreline velocity profiles produced by the shrouded and unshrouded rotor,

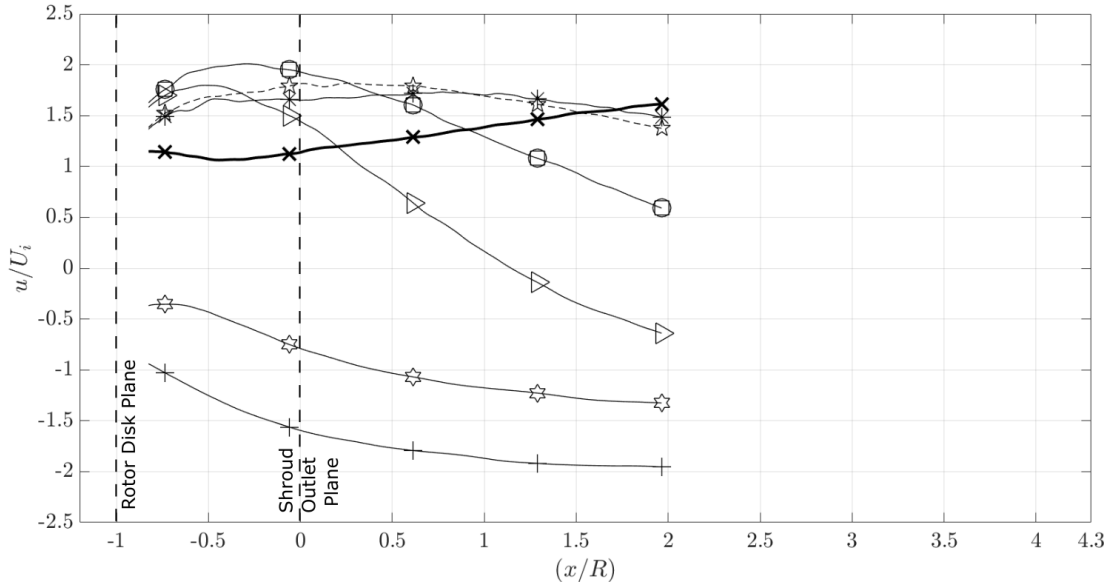

(A) Unshrouded Rotor

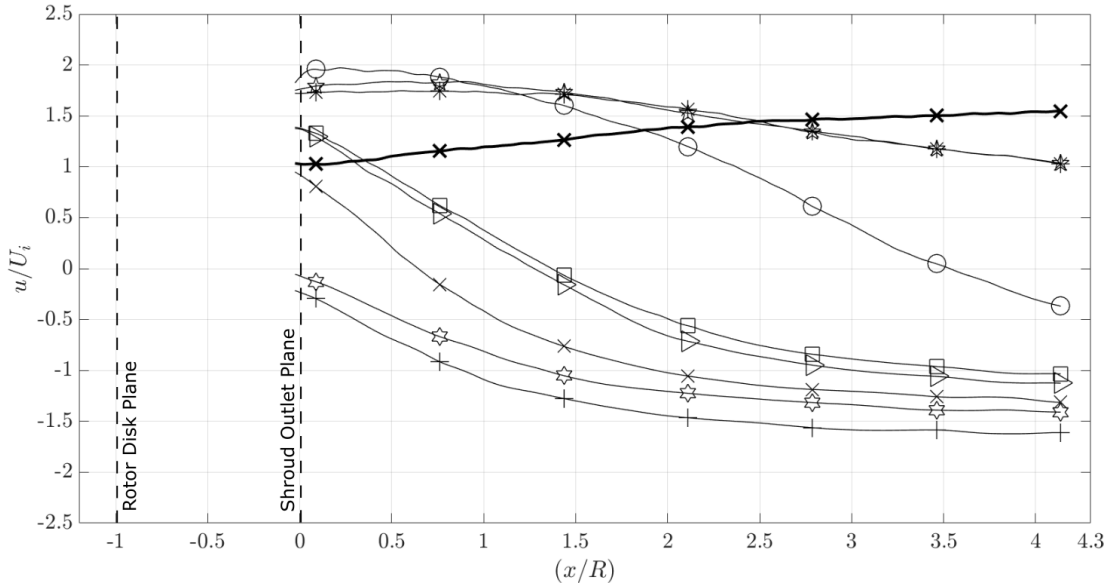

(B) Shrouded Rotor

$\alpha = 0.0$ $\alpha = 0.4$ $\alpha = 0.6$ $\alpha = 0.9$ $\alpha = 1.1$
$\alpha = 1.2$ $\alpha = 1.3$ $\alpha = 1.4$ $\alpha = 2.0$

FIGURE 2.27: Mean axial velocity profile (u) of the unshrouded rotor along the longitudinal axis $u(x, 0, 0)$ scaled with respect to the notional induced velocity of the rotor (U_i), for a range of descent velocity ratios.

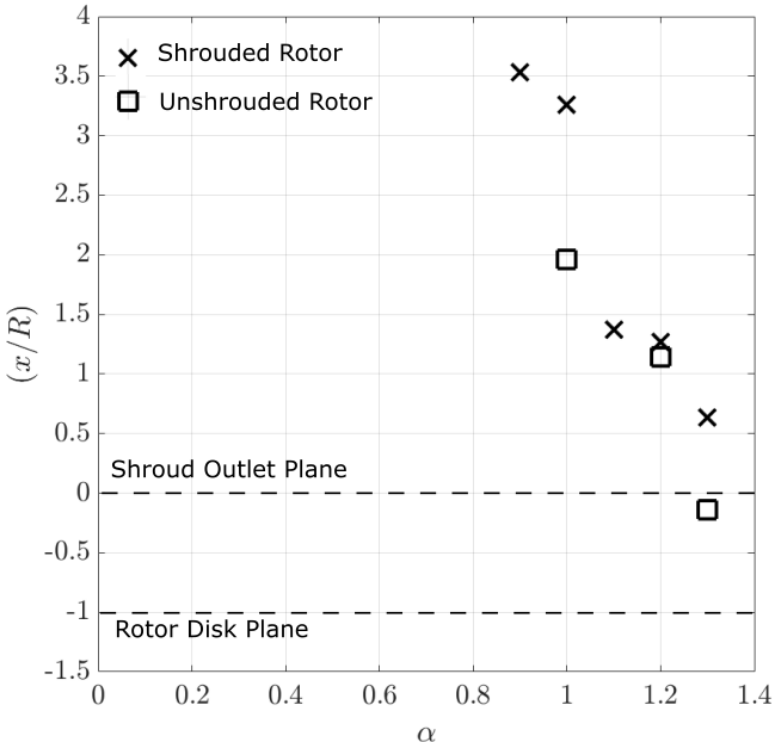

FIGURE 2.28: Mean location of the saddle point obtained from PIV measurements of the flow field produced by the unshrouded and the shrouded rotor in axial descent.

over a range of α values, are presented in figure 2.27. At low α values $(0.2 < \alpha < 1.1)$ the velocity profile of the isolated rotor presented in figure 2.27a shows an increase in the axial induced velocity at the rotor disk plane, when compared to that produced by the hovering rotor. The isolated rotor produces a flow field which accelerates until a maximum (approximately $0.75R$) from the rotor disk plane $(x/R = -0.8)$, after which the flow decelerates until it reaches zero at the saddle point. Beyond this point the mean axial velocity component will be negative $(-u)$ as a result of the wind tunnel flow. The rate of deceleration of the flow from the maximum increases as the descent velocity ratio increased from $\alpha = 0.4$ to $\alpha = 1.2$. Increasing α further moves the location of the stagnation point towards the rotor disk plane. At higher velocity ratios $1.4 < \alpha < 2.0$, the mean axial velocity profiles are dominated by the descent velocity. As expected the wind tunnel free stream decelerates as it approaches the rotor disk plane. The deceleration of the air, as it approaches the rotor disk plane, decreased as the velocity ratio increased. Similar trends can be observed in the velocity profiles of the shrouded rotor. At low velocity ratios $0 < \alpha < 0.4$, the velocity at the shroud outlet plane increased when compared to that produced by the hovering shrouded rotor. However, instead of initially increasing to a maximum the axial velocity produced by the shrouded rotor decelerated as the displacement from the shroud outlet plane increased. Once again, the flow produced by the shrouded rotor continued to decelerate until it became zero at the interaction between the wake and the counterflow. At a velocity ratio of $\alpha = 0.9$ the saddle point forms $3.5R$ from the shroud outlet plane. As with the isolated rotor, the rate of deceleration

increased as the descent velocity increased from $\alpha = 0.4$ to $\alpha = 1.3$. As described earlier, the saddle point approached the shroud outlet plane as the decent velocity increased. For velocity ratios above $\alpha > 1.4$, the mean centreline velocity profile is again dominated by the wind tunnel free stream, however, the velocity of air passing through the shroud outlet plane is lower than that passing through the rotor disk plane of the isolated rotor. Within the shroud $1.12 < x/R < 0$, the wake can not be radially deflected outboard, meaning that the shrouded rotor acts like a solid blockage.

The mean location of the saddle point was extracted from the centreline axial velocity profiles presented in figure 2.28. It was only possible to determine the location of the saddle point when it entered the interrogation area. Consequently, it was only possible to obtain a few data points for each test configuration. At velocity ratios less than 0.9 ($\alpha < 0.9$), the location of the saddle point could not be determined. As such, the relationship between the location of the saddle point and α could not be determined for the shrouded or the unshrouded rotor from this investigation.

UNSTEADINESS OF THE FLOW FIELD PRODUCED BY A SHROUDED ROTOR OPERATING IN AXIAL DESCENT.

PIV RESULTS.

Figures 2.29, 2.30 and 2.31 show contour plots of the RMS of the fluctuations of the local axial velocity about the local mean axial velocity for the isolated rotor and both regions of interest for the shrouded rotor (PIV Region 1 and 2), respectively. The RMS of the fluctuations is scaled with respect to the notional induced velocity of the shrouded rotor (U_i). At low descent velocity ratios α the flow shows higher levels of fluctuation, and the merged region of higher fluctuations occurs closer to the rotor than for hover.

Figure 2.29d shows that at a velocity ratio of $\alpha = 1.0$, a crescent shaped region of high RMS forms on the rotor centreline approximately $2.5R$ from the rotor disk plane. The location of this unsteadiness coincides with the location of the saddle point identified earlier in figure 2.23d. As the velocity ratio increases from $\alpha = 1.0$ to $\alpha = 1.2$, the location of unsteadiness moves with the saddle point. The disappearance of the saddle point from the field of view, means that the flow field returns to a form where the unsteadiness is dominated by the wake produced by the blade tip vortices, as they propagate around the rotor disk. The extent to which the unsteadiness propagates upstream, away from the rotor disk plane, decreases as α increases. Once the rotor enters the windmill brake state, the unsteadiness is confined to a thin region which extends downstream away from the rotor disk plane, as shown in figure 2.26a. This

region of unsteadiness is associated with the passage of the blade tip vortices of a rotor operating in the windmill brake state (Naumov et al., 2014).

It is believed that the region of unsteadiness observed in figure 2.29c is associated with the movement of a saddle point which forms outside of the field of view $(x/R > 2)$. Analysis of sequential PIV images confirmed that a saddle point appears in some of the images, however, in the majority of images the saddle point is not contained in the field of view. This explains why the saddle point cannot be observed in the mean flow field presented in figure 2.23c. The unsteadiness of the flow field produced by a shrouded rotor operating in axial descent is similar to that produced by the isolated rotor. At low velocity ratios $\alpha \leq 0.4$, the ring of high unsteadiness associated with the shear layer of the wake broadens, diffusing laterally as the wake propagates away from the shroud. At these low velocity ratios, the interaction between the rotor wake and the wind tunnel free stream upstream of the field of view leads to an increase in the RMS over the entire field of view (i.e. the wind tunnel free stream transports turbulent air back into the field of view). The re-ingestion of slightly more turbulent air by the rotor is believed to be responsible for the increase in core unsteadiness observed in figure 2.30b and figure 2.31b. As with the isolated rotor, at higher velocity ratios, a region of unsteadiness forms at the location of the saddle point. The magnitude of this unsteadiness is similar to that produced by the isolated rotor $(u_{rms} \approx 0.9U_i)$. Once again, the region of unsteadiness approached the shroud outlet plane as the descent velocity increased. The saddle points identified in figure 2.24 were always located inside the region of unsteadiness for $0.8 \leq \alpha \leq 1.3$. The formation of this region of unsteadiness is coupled with an increase in the unsteadiness of the flow field outboard of the shroud. It is clear from the analysis of figure 2.25 and figure 2.31 that the large recirculation which forms outboard of the rotor is responsible for the high RMS values observed in figure 2.31c. Once the saddle point can no longer be observed in the field of view the unsteadiness of the flow field, as with the isolated rotor, becomes dominated by the rotor wake as it propagates around the side of the shroud. At a velocity ratio of $\alpha > 1.1$, a region of unsteadiness forms at the lip of the shroud outlet. This unsteadiness coincides with the formation of the secondary vortex at the lip of the shroud. For $\alpha \geq 1.4$ the unsteadiness is limited to a thin layer near to the shrouds surface (figure 2.31h). At this velocity ratio, the unsteadiness occurs because of the deflection of the rotor wake around the shroud.

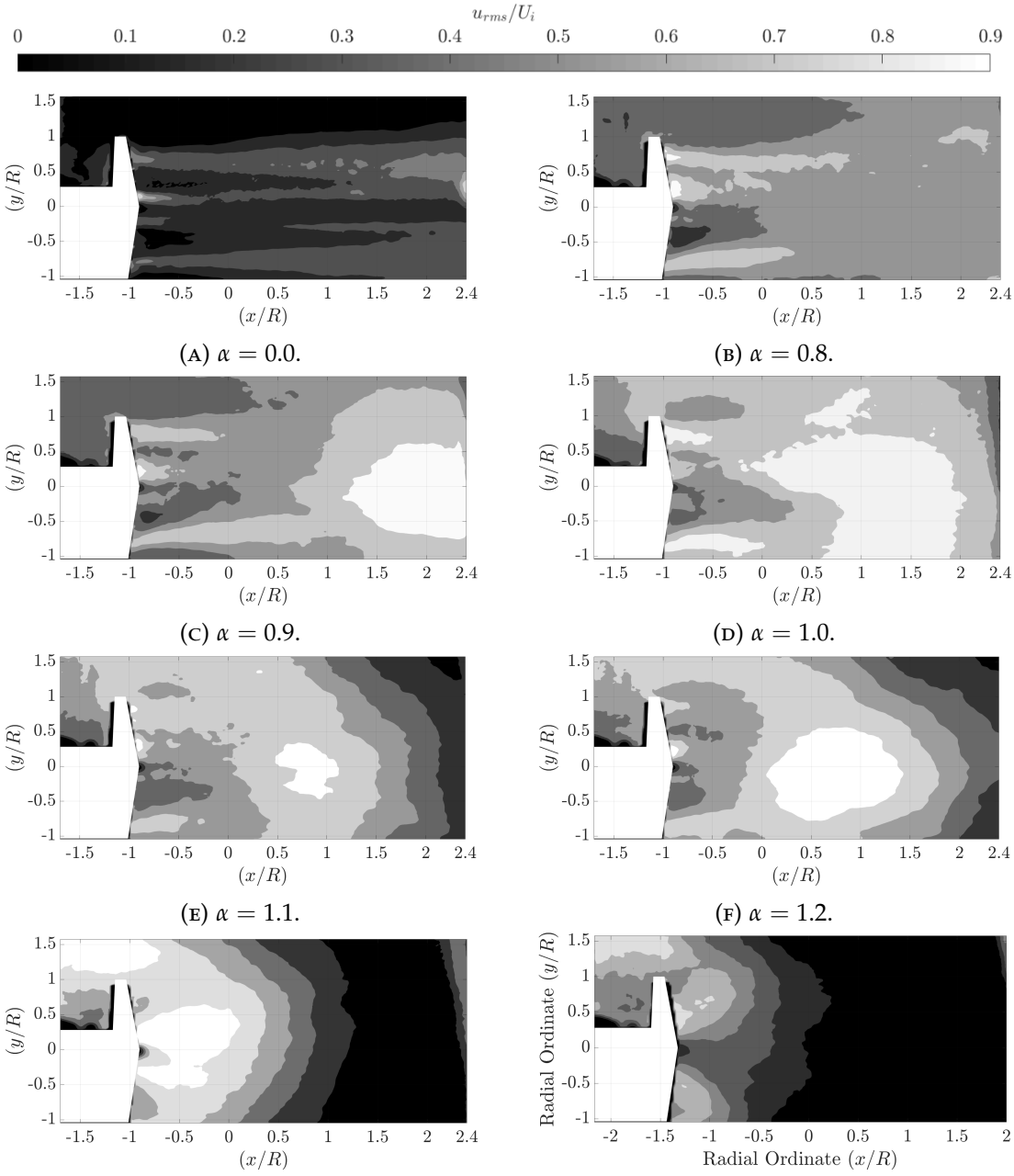

(A) $\alpha = 0.0$. (B) $\alpha = 0.8$.

(C) $\alpha = 0.9$. (D) $\alpha = 1.0$.

(E) $\alpha = 1.1$. (F) $\alpha = 1.2$.

(G) $\alpha = 1.3$. (H) $\alpha = 1.4$.

FIGURE 2.29: RMS of the axial velocity components of the flow field produced by the unshrouded rotor as the descent velocity ratio increases from $\alpha = 0.0$ to 1.4.

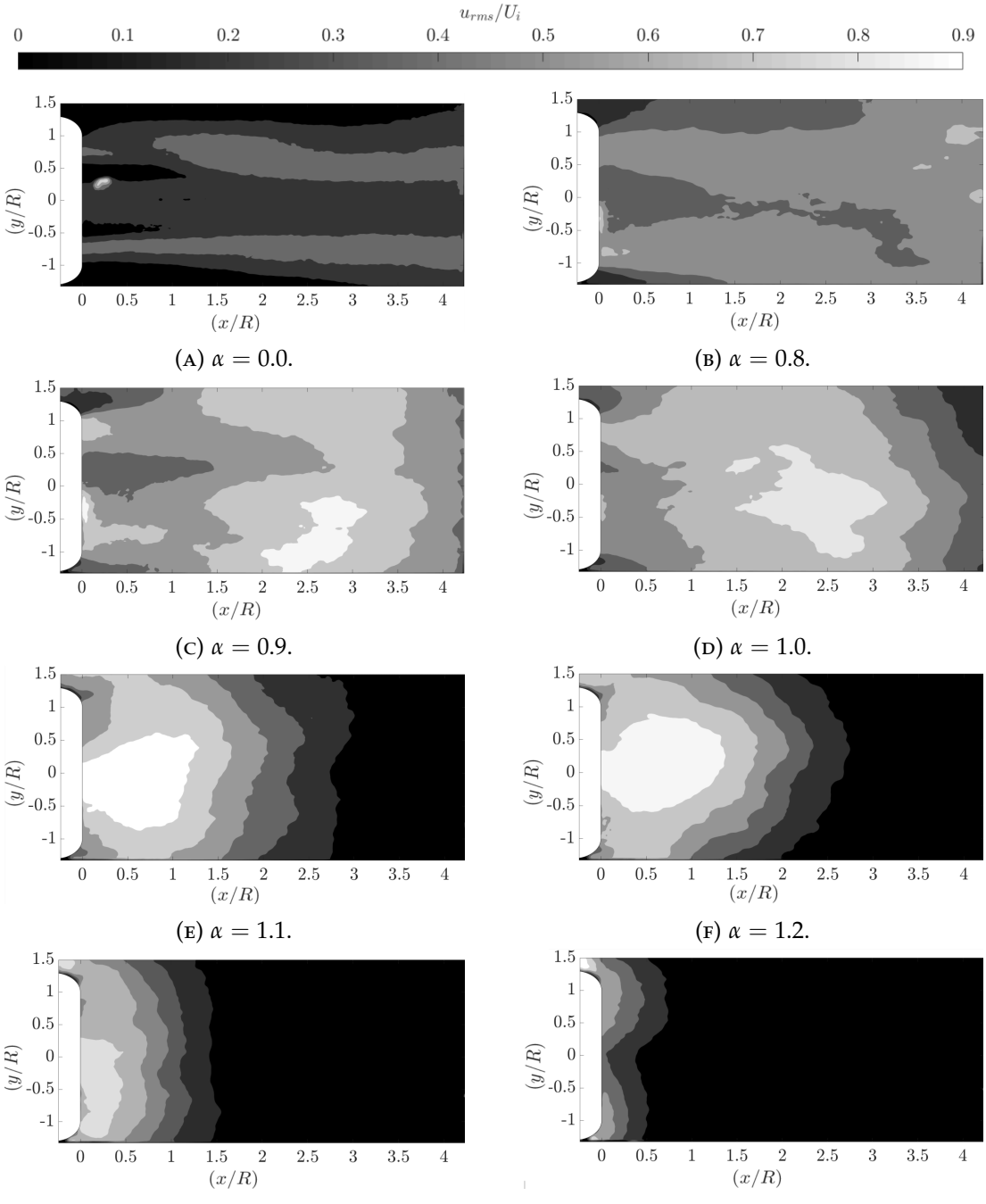

(A) $\alpha = 0.0$.

(B) $\alpha = 0.8$.

(C) $\alpha = 0.9$.

(D) $\alpha = 1.0$.

(E) $\alpha = 1.1$.

(F) $\alpha = 1.2$.

(G) $\alpha = 1.3$.

(H) $\alpha = 1.4$.

FIGURE 2.30: RMS of the axial velocity components of the flow field produced by the shrouded rotor (PIV:Region 1) as the descent velocity ratio increases from $\alpha = 0.0$ to 1.4.

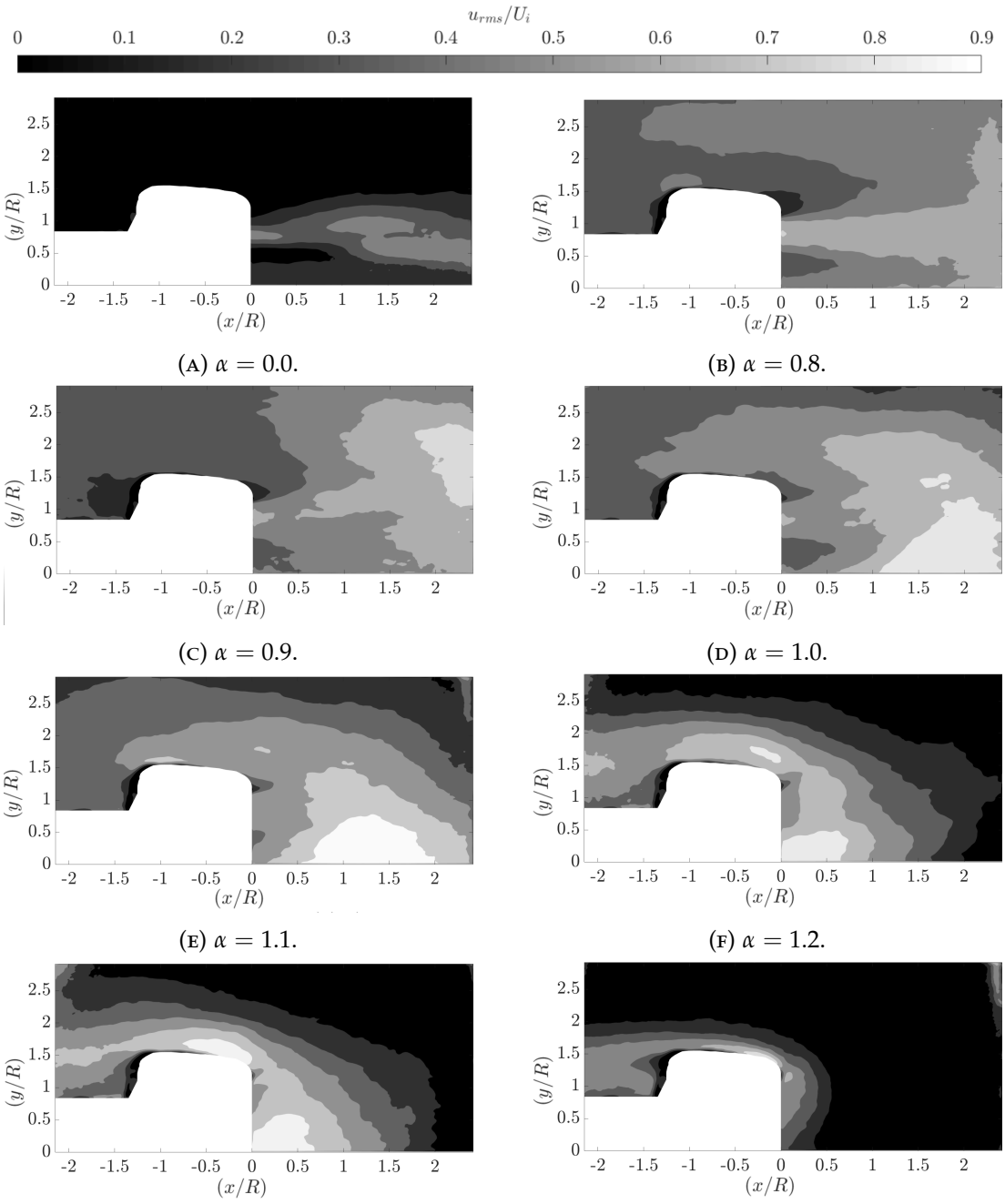

(A) $\alpha = 0.0$.

(B) $\alpha = 0.8$.

(C) $\alpha = 0.9$.

(D) $\alpha = 1.0$.

(E) $\alpha = 1.1$.

(F) $\alpha = 1.2$.

(G) $\alpha = 1.3$.

(H) $\alpha = 1.4$.

FIGURE 2.31: RMS of the axial velocity components contour plots of the shrouded rotor (PIV: Region 2) as the descent velocity (U_o) increases from $\alpha = 0.0$ to 1.4. The velocity is scaled with respect to the notional induced velocity, (U_i).

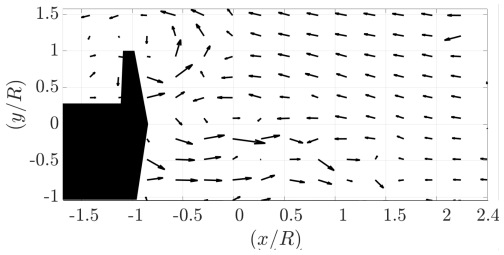

(A) Isolated rotor

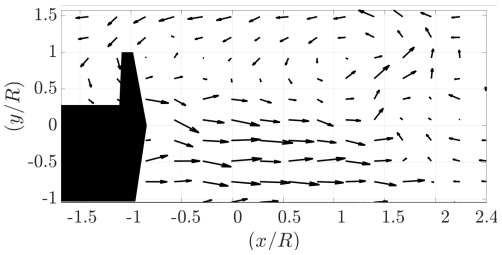

(B) Isolated rotor

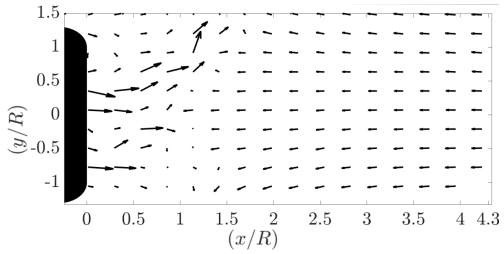

(C) Shrouded rotor (PIV:Region 1)

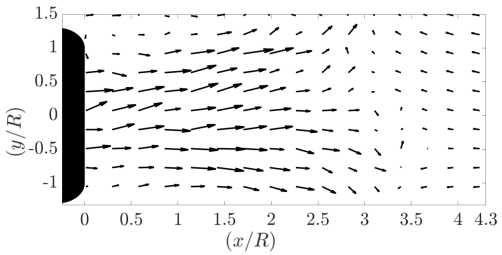

(D) Shrouded rotor (PIV:Region 1)

FIGURE 2.32: Instantaneous PIV image pairs of an isolated rotor and a shrouded rotor at a velocity ratio of $\alpha = 1.0$.

2.4 DISCUSSION.

Analysis of the PIV results revealed that, as with the results of Green et al. (2005), the flow field produced by both the shrouded rotor and the unshrouded rotor differed considerably from the mean flow fields presented earlier in figure 2.23, 2.24, 2.25 and 2.26. An example of this is shown in figure 2.32 where, at the same velocity ratio $\alpha = 1.0$, the flow produced by the shrouded rotor can extend up to $3R$ from the shroud outlet plane, as shown in figure 2.32c, or the wake can be deflected radially outboard, allowing the free stream flow to penetrate towards the shroud outlet plane, as shown in figure 2.32d. It should be noted that this tendency can also be observed in instantaneous PIV images of the flow field produced by an isolated rotor show in figure 2.32a and figure 2.32b.

POD ANALYSIS.

Visualisations of the first two eigenmodes produced by applying snapshot *energy* POD to the PIV results of the isolated rotor and the shrouded rotor (PIV: Region 1) in hover $(\alpha = 0)$ are presented in figure 2.33 and figure 2.34 respectively. The first two POD modes, of the isolated rotor used in this investigation, shown in figure 2.33a and figure 2.33b, indicate that the most probable and energetic representations of the flow field are dominated by the blade root vortices. The unsteadiness associated with the passage of the blade tip vortices and the passage of the vortex sheet trailed from behind the rotor blades was observed in higher POD modes. Figure 2.35 shows that the first 10 modes contain 9.0% of the kinetic energy of the fluctuations of the flow field whilst the following 20 modes only contain 9.8%. The influence of each

mode on the velocity field was evaluated by subtracting the reconstructed mode from the averaged flow field. The reconstructed modes were produced using both the maximum and minimum reconstruction coefficients of the *'m'th* mode $\Psi(m)$. Analysis of the reconstructed flow fields, shown in figure 2.33, shows that both modes are coupled and represent the same fluid dynamic mechanism. Spectral analysis of the reconstruction coefficients showed that both of these POD modes had a dominant frequency equal to the rotational frequency of the rotor $(66Hz)$.

The first two eigenmodes of the flow field produced by a hovering isolated rotor, shown in figure 2.33, differ considerably from those of the shrouded rotor shown in figure 2.34. The first two modes shown in figure 2.34a and 2.34b indicate that air moves radially across the diameter of the shroud outlet. The reconstructed flow fields, shown in figure 2.34, show that the first mode is primarily responsible for the radial flapping of the shrouded rotor wake, as shown by the radial deflection of the wake shown in figure 2.34c and 2.34e. The second mode also contributes to the radial flapping of the wake, however, the contribution is far lower than that of the first mode. Analysis of figure 2.35 shows that the first 10 modes contain 12.8% of the kinetic energy of the fluctuations of the flow field whilst the following 20 modes only contain 12%. Spectral analysis of the temporal coefficient of mode 1 $\Psi(1)$ indicated that the radial flapping of the shrouded rotor wake occurred at a frequency of $1.7Hz$.

The probability density function (PDF) of the reconstruction coefficients of the first POD mode $\Psi(1)$, for both the isolated and shrouded rotor, plotted against the respective values of $\Psi(1)$, are presented in figure 2.36. Due to the nature of snapshot POD, which forces unresolvable scales to be placed into other modes, the PDF exhibits sinusoidal behaviour. The underlying structure of the probability density functions presented in figure 2.36 were determined by generating histograms of the probability density function. The number of bins (k) used to capture the basic form of each distribution was calculated using Rices Rule $(k = 2\sqrt[3]{m} = 17)$. The PDF of the first POD mode of the shrouded and unshrouded rotor had skewness (s) values of $s = -0.07$ and $s = -0.1$, respectively. This indicates that both distributions are approximately *symmetric*, which implies that the radial flapping of the shrouded rotors wake is not significantly directionally biased. The radial flapping is associated with the shear layer of the wake opposed to the helical vortex trains.

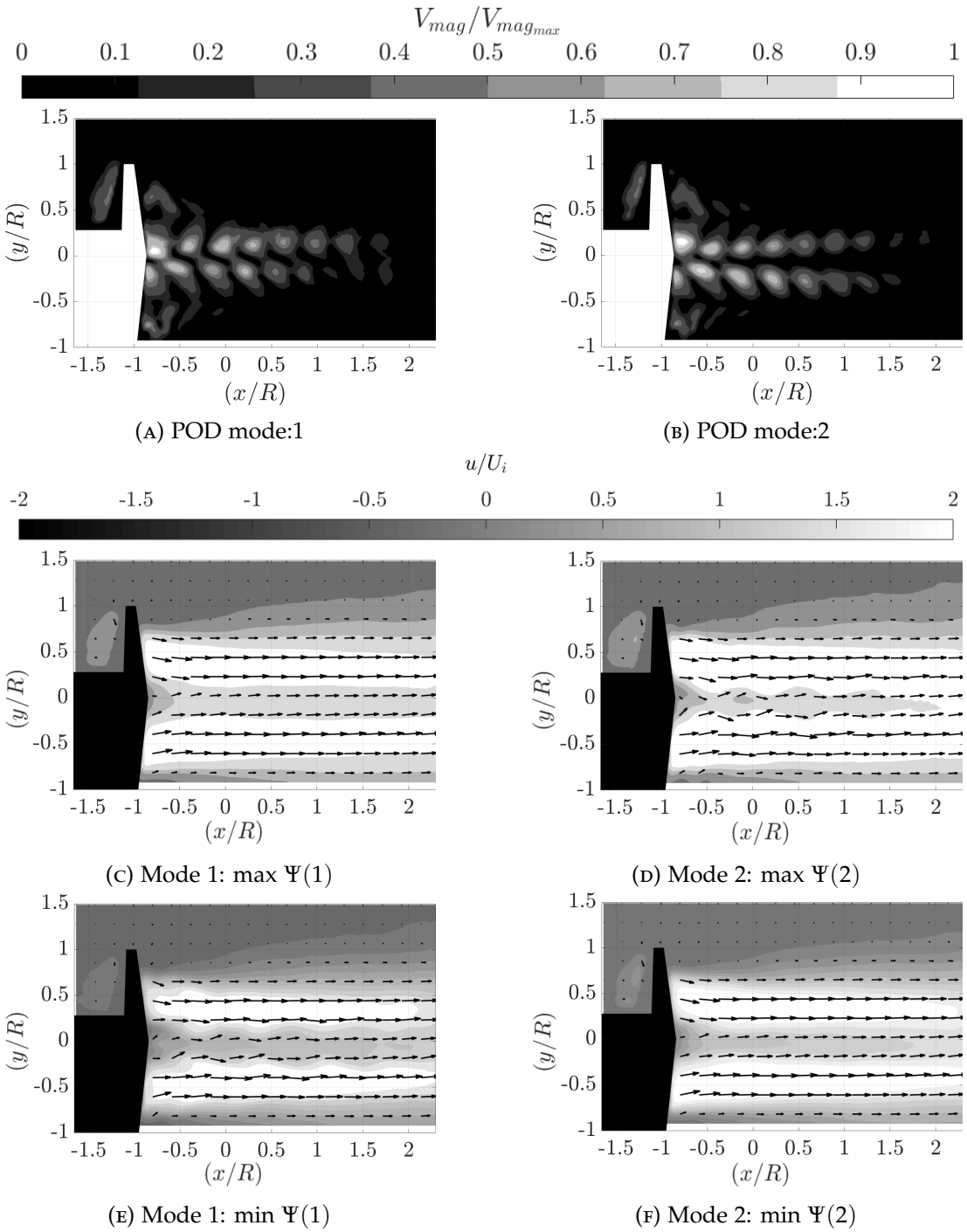

(A) POD mode:1

(B) POD mode:2

(C) Mode 1: max $\Psi(1)$

(D) Mode 2: max $\Psi(2)$

(E) Mode 1: min $\Psi(1)$

(F) Mode 2: min $\Psi(2)$

FIGURE 2.33: Visualisation of the first two POD eigenmodes of the velocity fluctuations produced by a hovering isolated rotor ($\alpha = 0.0$) are presented in figure 2.33a and figure 2.33b. The modes were calculated from a sequence of 600 instantaneous velocity fields. The vector lengths are scaled with respect to the maximum vector length of each individual mode. Reconstructed simulations of the velocity field produced by the subtraction of the maximum (c, e) and minimal (d, f) reconstruction coefficient representations of the first two modes from the mean field are presented in this figure.

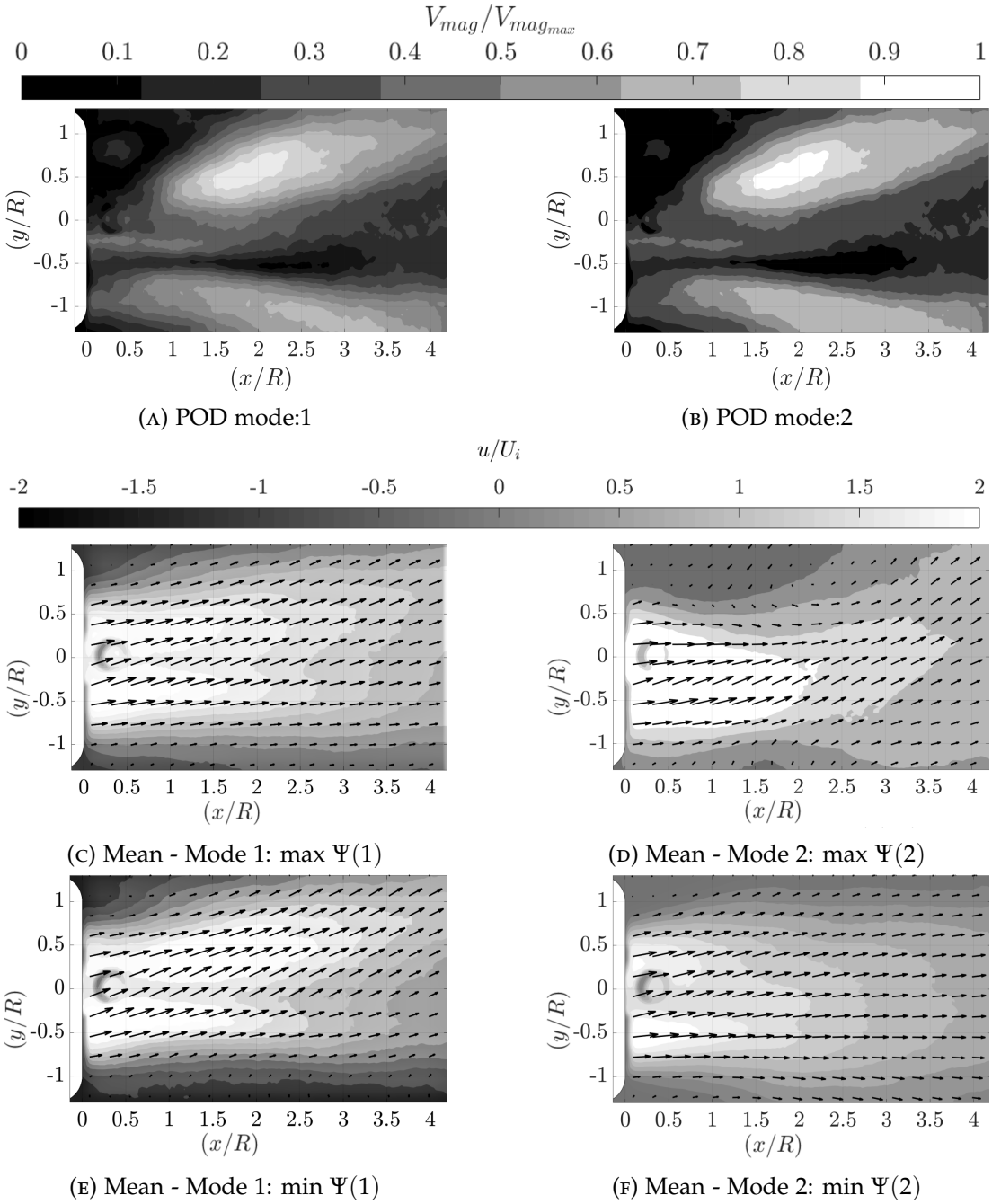

(A) POD mode:1

(B) POD mode:2

(C) Mean - Mode 1: max $\Psi(1)$

(D) Mean - Mode 2: max $\Psi(2)$

(E) Mean - Mode 1: min $\Psi(1)$

(F) Mean - Mode 2: min $\Psi(2)$

FIGURE 2.34: Visualisation of the first two POD eigenmodes of the velocity fluctuations produced by a hovering shrouded rotor ($\alpha = 0.0$) are presented in figure 2.34a and figure 2.34b. The modes were calculated from a sequence of 600 instantaneous velocity fields. The vector lengths are scaled with respect to the maximum vector length of each individual mode. Reconstructed velocity field produced by the subtraction of the maximum (c, e) and minimal (d, f) reconstruction coefficient representations of the first two modes from the mean field are presented in this figure.

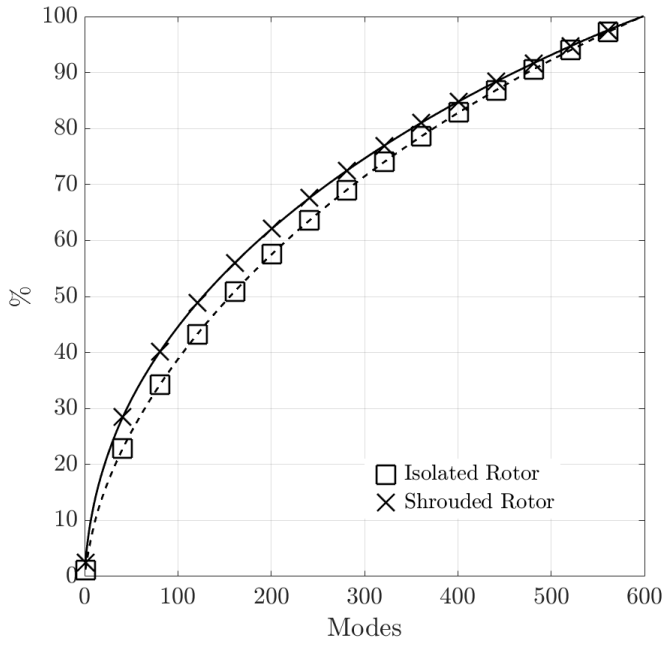

FIGURE 2.35: Progressive sum of singular values as a percentage of the total sum calculated from the POD of the flow field produced by the isolated rotor and the shrouded rotor when operating in hover ($\alpha = 0.0$).

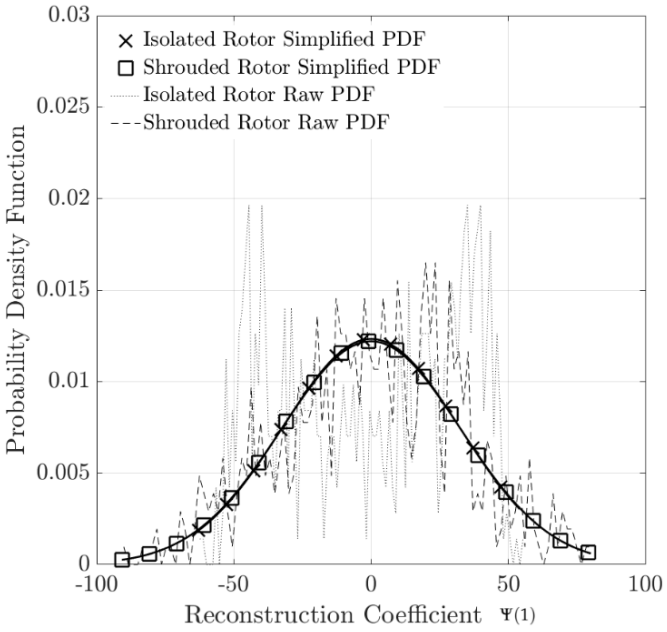

FIGURE 2.36: Probability density function of the first POD modes reconstruction coefficients $\Psi(1)$ plotted against the values of $\Psi(1)$ for the isolated rotor and shrouded rotors when operating in hover ($\alpha = 0.0$).

As expected, POD analysis of individual snapshots of the flow field produced by an isolated rotor, showed that at low descent velocity ratios the unsteadiness of the flow field is dominated by the blade tip and root vortices as they propagate away from the rotor disk plane (figure 2.33). However, as previously shown by Green et al. (2005), at higher velocity ratios the flow field enters an incipient flow regime, where the flow intermittently switches between the topology associated with a hovering rotor and the toroidal form associated with the VRS. The reconstructed flow fields formed as a result of the first POD mode of the isolated rotor operating at a velocity ratio of $\alpha = 1.0$, presented in figure 2.38c and figure 2.38d shows that the first POD mode is responsible for the variation of the penetration of the counterflow towards the rotor disk plane. Analysis of figure 2.38b shows that the unsteadiness associated with the passage of the blade tip vortices and the recirculation which forms around the side of the rotor blade tips are contained within higher POD modes.

POD analysis of individual snapshots of the flow field produced by a shrouded rotor operating in axial descent, shown in figure 2.39 provided insight into the underlying structure of the flow field. At low velocity ratios $(\alpha < 0.8)$ the first two POD eigenmodes are similar to those produced by a hovering shrouded rotor described earlier. At a velocity ratio of $\alpha = 0.9$, the first POD mode can still be characterised by the radial movement of air around across the shroud outlet plane (figure 2.39a). However, the second POD mode depicts the penetration of the wind tunnel free stream towards the shroud outlet plane (figure 2.39b). Reconstructed flow field, produced by subtracting the maximum and minimum reconstruction coefficient forms of the POD modes, are presented in figure 2.39. Figure 2.39c and 2.39e show that, at this velocity ratio, the unsteadiness of the flow field is still dominated by the radial flapping of the rotor wake. Spectral analysis of the reconstruction coefficient showed that this occurred at the same frequency as the wake produced by the shrouded rotor in hover $(1.7Hz)$. It should be noted that the magnitude of these radial fluctuations is small, as the flow is still dominated by the axially induced velocity produced by the rotor. At this velocity ratio, the second POD mode is associated with the variation of the wake penetration into the free stream flow. The location of these fluctuations coincides with the region of high RMS identified in figure 2.30c. The PDF of the reconstruction coefficient of the first POD mode, shown in figure 2.41, had a skewness value equal to $S_k = 0.0816$. This indicates that, at this velocity ratio, the flow field is marginally more likely to exist in the minimum form, as presented in figure 2.39f (i.e. the flow field is more likely to exist in the form where the shrouded rotor wake extends, in a stream tube, away from the shroud outlet plane).

When the descent velocity was greater than, or equal to the notional induced velocity of the rotor $(1.0 \leq \alpha \leq 1.3)$, POD analysis revealed that the unsteadiness of the flow field was dominated by the penetration of the descent velocity towards the shroud outlet plane. Reconstructions of the the flow field produced by a shrouded rotor operating at a descent velocity ratio of $\alpha = 1.1$, showed that the counterflow can penetrate up to the shroud outlet plane, as shown in figure 2.40. The location of the

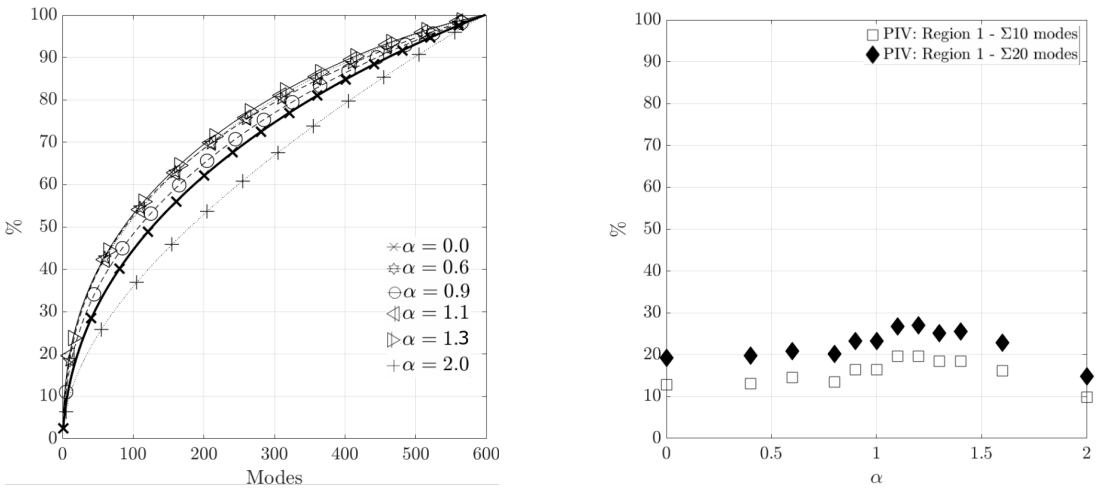

(A) Progressive sum of singular values. (B)

FIGURE 2.37: (a) Progressive sum of singular values as a percentage of the total sum calculated from the POD of the flow field produced by the shrouded rotor (PIV: Region 1; (b) The percentage sum of the first 10 and the first 20 modes over a range of α values from $(\alpha = 0.0)$ and $(\alpha = 2.0)$.

saddle point, identified in figure 2.24e, varied as a result of the flow fluctuations. The flow fields, produced as a result of the flows fluctuations resemble the two potential flow topologies, produced by a rotor operating in the VRS, as identified by Green et al. (2005). Radial flapping of the shrouded rotor wake can still be observed in higher POD modes as shown in figure 2.40d and 2.40f.

At $\alpha = 1.0$, the PDF of the first POD mode had a skewness value of $S_k = -0.1579$ indicating that the flow field had a greater tendency to exist in a form where the rotor wake is deflected radially outboard around the shroud. As the velocity ratio increased from $\alpha = 1.0$ to $\alpha = 1.2$, the skewness values of the probability density functions of the POD mode, which were responsible for the penetration of the wind tunnel free stream towards the shroud outlet plane, increased from $S_k = -0.1579$ to $S_k = -0.3062$. This indicates that the amount of time that the flow field spends in the toroidal like form increased as the descent velocity increased. At a velocity ratio of $\alpha = 1.4$ the flow field is permanently locked into the toroidal form. This intermittent nature of the flow field is characteristic of the flow field produced by an isolated rotor operating in the VRS (Green et al., 2005). At velocity ratios between $\alpha = 1.4$ and $\alpha = 1.6$, the penetration of the shroud outlet plane by the wind tunnel free stream results in the expulsion of the rotor wake from the shroud, at the lip of the shrouds outlet plane.

The cumulative sum of the singular values as a percentage sum of the the total sum of the kinetic energy associated with the fluctuations of the flow field, for a range of α values, is shown in figure 2.37b. At low velocity ratios $(\alpha \leq 0.8)$, the first ten POD modes contain approximately 12% of the total kinetic energy of the fluctuations of the flow field, whilst the first twenty modes contain approximately 20%. The percentage of the total kinetic energy contained within the first 10 and 20 POD modes increased

as the shrouded rotor entered the VRS, because the number of small scale structures observed within the flow field decreased.

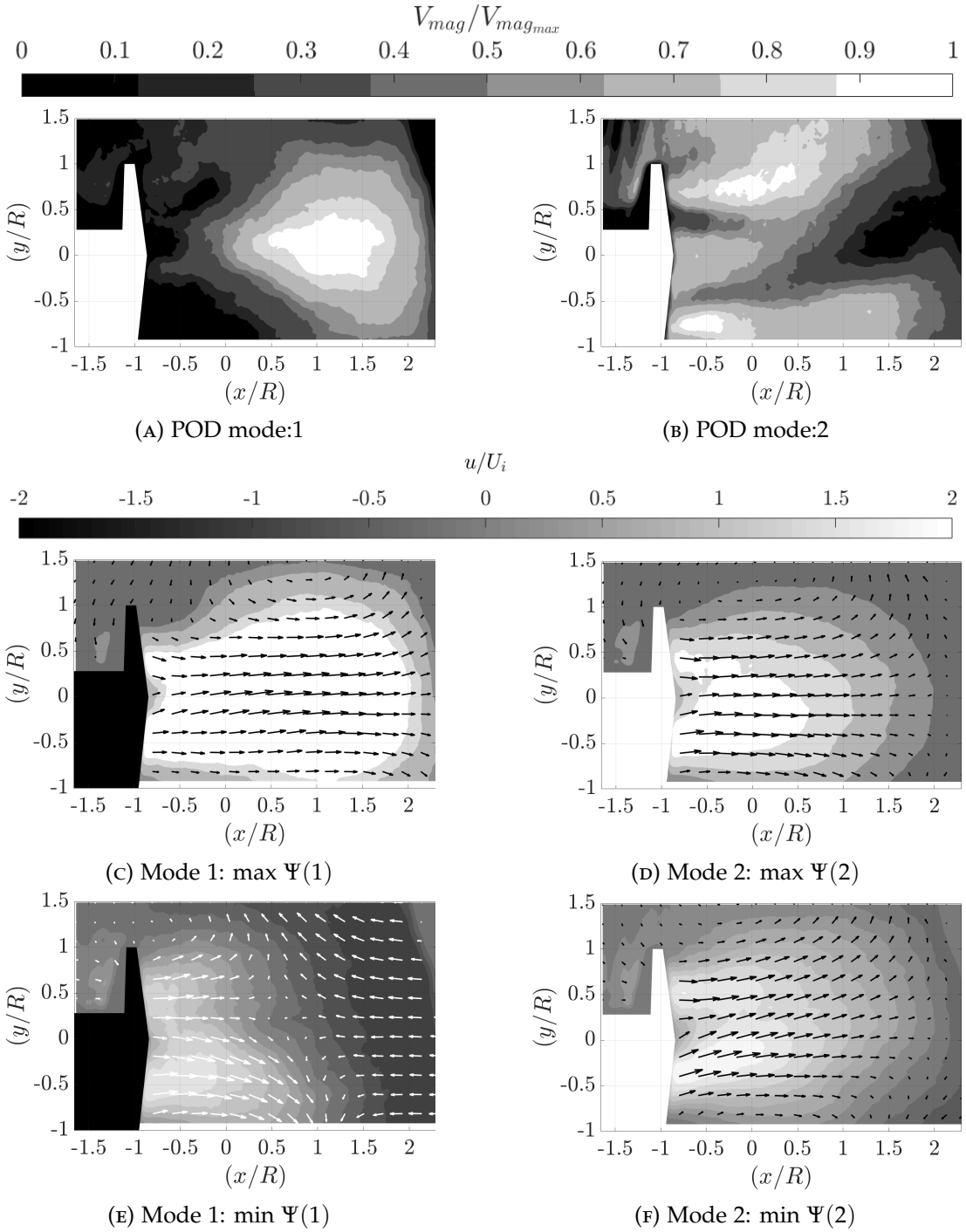

(A) POD mode:1

(B) POD mode:2

(C) Mode 1: max $\Psi(1)$

(D) Mode 2: max $\Psi(2)$

(E) Mode 1: min $\Psi(1)$

(F) Mode 2: min $\Psi(2)$

FIGURE 2.38: Visualisation of the first two POD eigenmodes of the velocity fluctuations produced by a isolated rotor $\alpha = 1.0$ calculated from 600 instantaneous velocity fields. (a) mode 1, (b) mode 2. The vector lengths are scaled with respect to the maximum vector length of each individual mode. Reconstructed simulations of the velocity field produced by the subtraction of the maximum (c, e) and minimal (d, f) reconstruction coefficient representations of the first two modes from the mean field are presented in this figure.

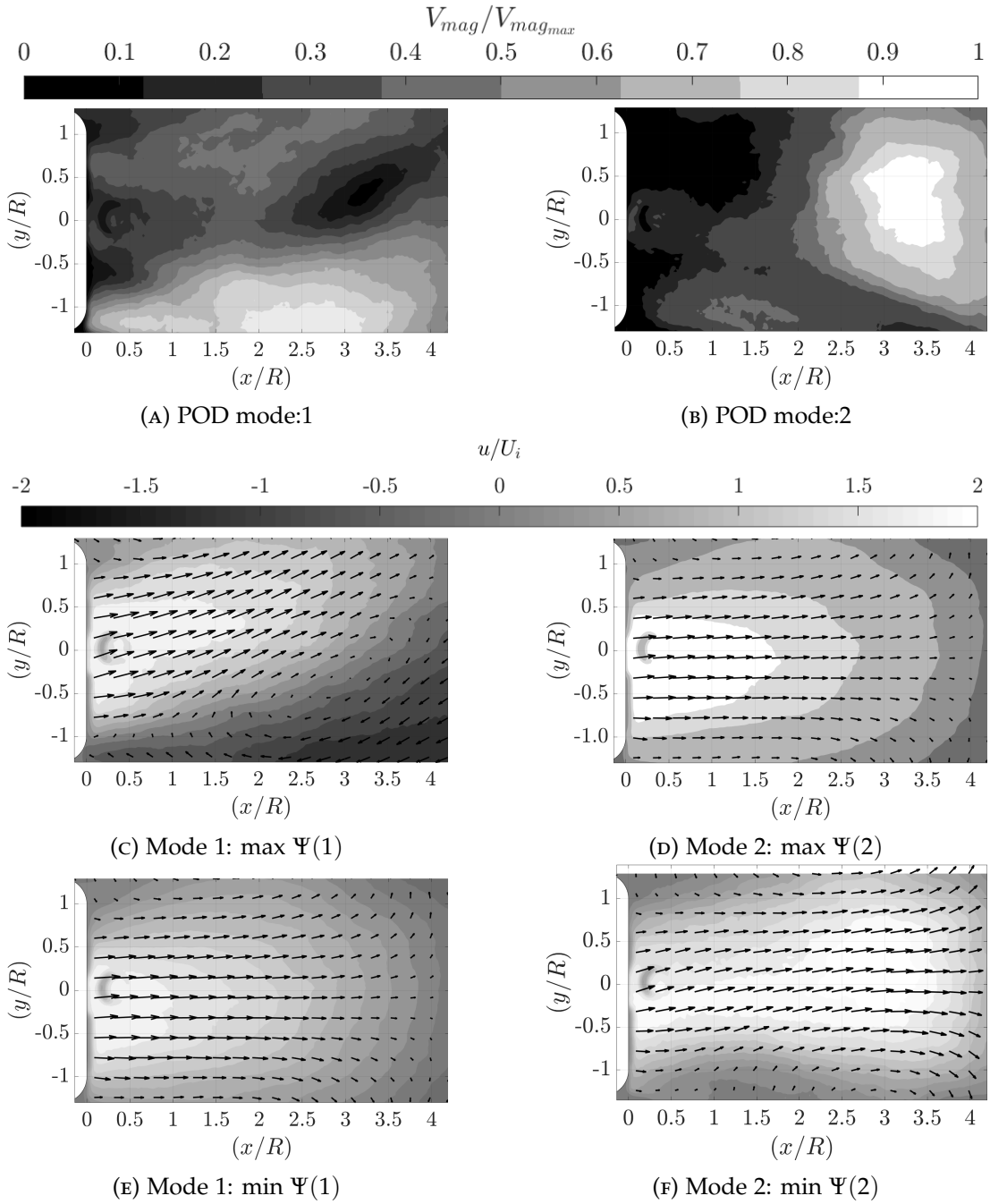

(A) POD mode:1

(B) POD mode:2

(C) Mode 1: max $\Psi(1)$

(D) Mode 2: max $\Psi(2)$

(E) Mode 1: min $\Psi(1)$

(F) Mode 2: min $\Psi(2)$

FIGURE 2.39: Visualisation of the first two POD eigenmodes of the velocity fluctuations produced by a shrouded rotor $\alpha = 0.9$ calculated from 600 instantaneous velocity fields. (a) mode 1, (b) mode 2. The vector lengths are scaled with respect to the maximum vector length of each individual mode. Reconstructed simulations of the velocity field produced by the subtraction of the maximum (c, e) and minimal (d, f) reconstruction coefficient representations of the first two modes from the mean field are presented in this figure.

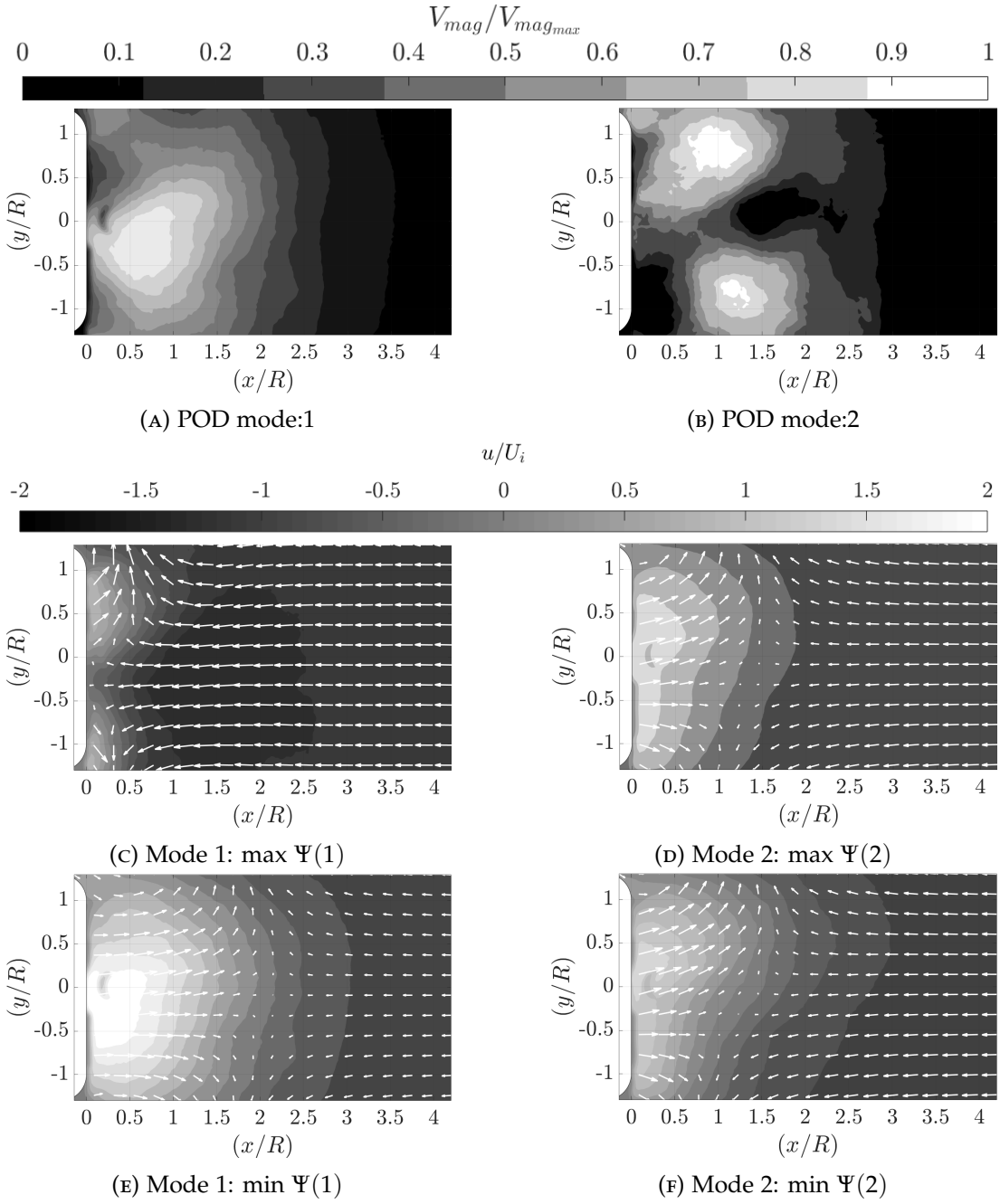

(A) POD mode:1

(B) POD mode:2

(C) Mode 1: max $\Psi(1)$

(D) Mode 2: max $\Psi(2)$

(E) Mode 1: min $\Psi(1)$

(F) Mode 2: min $\Psi(2)$

FIGURE 2.40: Visualisation of the first two POD eigenmodes of the velocity fluctuations produced by a shrouded rotor $\alpha = 1.1$ calculated from 600 instantaneous velocity fields. (a) mode 1, (b) mode 2. The vector lengths are scaled with respect to the maximum vector length of each individual mode. Reconstructed simulations of the velocity field produced by the subtraction of the maximum (c, e) and minimal (d, f) reconstruction coefficient representations of the first two modes from the mean field are presented in this figure.

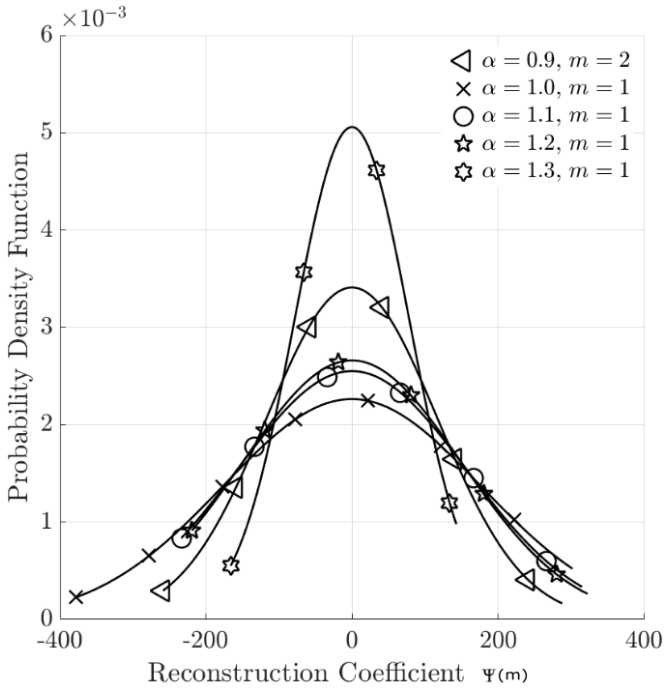

FIGURE 2.41: Probability density function of the reconstruction coefficients of the POD modes, which contribute to the variation of the shrouded rotors wakes' penetration into the wind tunnel free stream flow, plotted against the value of the reconstruction coefficients $\Psi(m)$.

2.5 CONCLUSION

An investigation into the structure of the flow field produced by a shrouded rotor operating in hover and axial descent has been performed using particle image velocimetry (PIV) and laser doppler anemometry (LDA). As with an isolated rotor operating in hover, the flow field produced by a shrouded rotor, without a shroud centre body, is characterised as a region of low velocity flow surrounded by a ring of high velocity flow. The shroud used in this investigation did not affect the velocity components of the wake. The notional induced velocity of the shrouded rotors wake, at the shroud outlet plane, was used to scale the decent velocity of both investigations performed. PIV revealed that the rate of acceleration of the wake produced by the shrouded rotor is significantly lower than that of the isolated rotor. In contrast to the isolated rotor, where the flow field is dominated by the blade root vortices, POD analysis showed that the most probable and energetic realisation of the fluctuations of the flow field produced by the shrouded rotor is dominated by the shear layers of the wake. This manifests itself as the radial flapping of the shrouded rotors wake.

At low descent velocity ratios, in the near flow field, the structure of the rotor wake is similar to that produced by a shrouded rotor operating in hover. In the far field, at the interaction between the shrouded rotor wake and the descent velocity a large region of recirculation forms upstream, outboard of the shroud. At higher velocity ratios the cylindrical wake of the shrouded rotor breaks down, forming a

large unsteady toroidal region of recirculation around the shroud. The formation of a large region of recirculation that forms around the side of the shroud, allows the rotors wake to be entrained back into the shroud through the shroud inlet plane. The diameter of the recirculation is approximately equal to the diameter of the rotor. The formation of the recirculation is coupled with the formation of a saddle point on the geometric centreline of the rotor. The saddle point approaches the shroud outlet plane as the descent velocity ratio increased. The fate of the saddle point, once it entered the shroud, was not investigated in this chapter.

The flow field produced by a shrouded rotor operating in axial descent is highly unsteady and the recirculation aperiodically sheds away from the shroud. Large regions of unsteadiness, with RMS values of a similar magnitude to the notional induced velocity of the shrouded rotor, occur at the location of the saddle point. Analysis of sequential PIV images showed that at these descent velocities the flow field can exist in one of two topological forms: a region of recirculating air outboard of the shroud, or that of a hovering shrouded rotor. In this incipient flow regime the saddle point can penetrate through the shroud outlet plane, where it can persist for a prolonged period of time before being expelled upstream away from the shroud outlet plane. Within the helicopter community, the flow topology and features described above, are characteristic of the flow field produced by an isolated rotor operating in the vortex ring state. Therefore, it is reasonable to conclude that the shrouded rotor used in this investigation, entered the VRS. This is significant because the VRS of shrouded rotors has not been reported before. The shrouded rotor entered the VRS at a lower descent velocity ratio than the isolated rotor. At higher velocity ratios, the shrouded rotor entered a state analogous to the windmill brake state of an isolated rotor. In the windmill brake state, the wind tunnel free stream penetrates through the shroud outlet plane and passes around the shroud.

When compared to the isolated rotor, the velocity profile of the wake produced by the shrouded rotor is notionally similar, with a ring of higher velocity air surrounding a low velocity core. The results presented in this chapter showed that, when introduced to a uniform counterflow the wake from the shrouded rotor developed into the unsteady toroidal form associated with the VRS. Unlike the isolated rotor the recirculation formed around the side of the shroud instead of around the tips of the rotor blades. The results presented in this chapter indicated that the mechanism by which the wake produced by the shrouded rotor broke down into the toroidal form associated with the VRS was similar to that produced by the unshrouded rotor. However, the wake from the shrouded rotor did not contain any clear helical vortex system. This is significant because the 'mutual-inductance' instability of helical vortex filaments (Leishman et al., 2004) and the leapfrogging of the blade tip vortices (Stack et al., 2005) was believed to be responsible for the development of the VRS. The results presented in this chapter suggest that the breakdown of the rotor wake into the toroidal form of the VRS is a result of the interaction between an axially induced flow, which consists of a low velocity core surrounded by a ring of higher velocity air,

and a uniform counterflow. In order to investigate if the mechanism with which the velocity profile was produced affects the breakdown of the flow field an investigation into the structure of the flow field produced by a ventilated open core annular jet was also performed. The ventilated OCAJ was designed to produce a jet with a mean velocity profile notionally similar to that produced by the shrouded rotor however it did not contain any flow structures characteristic of rotor wakes (i.e. blade tip vortices and trailed vortex sheets).

CHAPTER 3

THE VORTEX RING STATE OF A VENTILATED OPEN CORE ANNULAR JET

An experimental investigation into the interactions between the flow field produced by a ventilated Open Core Annular Jet, and a uniform counterflow performed in the University of Glasgow, De-Havilland wind tunnel is presented. Laser Doppler Anemometry (LDA) was used to determine the velocity profiles at both the inlet and outlet of the ventilated open core annular jet. The jet produced a mean velocity profile notionally similar to that produced by the rotor and the shrouded rotor investigated in chapter 2, with a ring of high velocity air surrounding a lower velocity core. Long-duration Particle Image Velocimetry (PIV) and Smoke Flow Visualisation were used to investigate the development of the flow field as the counter flow velocity increased. The formation of a large unsteady torus of recirculating air around the jet was observed when the counter flow approached that of a notional-induced velocity produced by the jet. Additionally, averaged velocity profiles of the flow field showed a stagnation point located on the geometric axis of the ventilated annular jet, which moved towards the jet outlet plane as the counter flow velocity was increased. Analysis of sequential Smoke Flow Visualisation images identified a periodic shedding frequency of this torus which, in turn, leads to the penetration of the counter flow through the jet's open core. The results presented in this chapter indicates that the structure and unsteadiness of the flow field produced by a jet issuing into a counterflow is similar to that produced by the shrouded rotor and an unshrouded rotor operating in axial descent discussed in chapter 2. POD analysis showed that the fluid structures responsible for the unsteadiness of the flow field produced by the shrouded rotor and the unshrouded rotor discussed in chapter 2 were also observed in the flow field produced by the jet.

3.1 INTRODUCTION

Despite the rapid uptake of ventilated open core annular jets (OCAJ) by the general public for personal cooling, as described by Li et al. (2016) and Mason et al. (2010), research into the structure of the flow field produced by these devices has been minimal. A ventilated open core annular jet consists of an annular jet located around an open core through which air can pass freely, as shown in figure 3.1. The jet is defined as ventilated when the annular jet induces flow through the open core, as defined by Padhani et al. (2018) whose experiments identified the structure and subsequent development of a ventilated open core annular jet issuing into quiescent surroundings. Stereoscopic Particle Image Velocimetry (SPIV) of the jet outlet showed that the flow field transitioned into that of a round jet downstream of the jet outlet. Laser Doppler Anemometry (LDA) performed by Warda et al. (1999) indicates that approximately $7.8D$ diameters (D) downstream of the jet orifice, the velocity profile tended towards that of a round jet for their particular jet profile. When compared to turbulent jets issuing from a circular source, the ventilated open core was found to increase dilution close to the jet outlet as a result of the induced air flow, (Jukes et al., 2015). Ventilated OCAJs experience lower rates of velocity decay as a result of the larger mass flow rates that can be achieved compared to that of closed core annular jets. The effect of varying the annular slot inner diameter (D_i) and the outer diameter (D_o), has been shown to have no effect on the jet structure for slender annuli $(D_i/D_o) \approx 1$ of closed core annular jets (Ko. (1980a) and Ko. (1980b)).
The aerodynamic performance of various geometric parameters (e.g. fan cross section height, slot thickness, hydraulic diameter, outlet angle and aspect ratio) of ventilated open core annular jets issuing into quiescent surroundings was investigated using Computational Fluid Dynamics (CFD) by Jafari et al. (2015) and Jafari et al. (2016b). Simulations showed that the jet outlet slot thickness was a significant parameter affecting the performance of the bladeless fan, whilst their performance decreased significantly for designs where the aspect ratio was greater than one. All of the designs simulated show that the velocity at the jet outlet was higher opposite the jet inlet pipe, thereby producing the non-symmetric velocity profile previously identified by Jafari et al. (2016a). Numerical aeroacoustic analysis of bladeless fans performed by Jafari et al. (2017) showed that the outlet slot thickness was a key factor affecting the amount of noise produced by a ventilated OCAJ once again issuing into quiescent surroundings. The interaction of both unventilated and ventilated OCAJs with any other flow field (e.g. counterflow or cross flow) remains uninvestigated. The present study aims to identify the flow characteristics associated with ventilated OCAJs operating in a uniform counterflow and, therefore, a brief summary of the literature relating to round jets issuing into counter flow is provided below in order to contextualise this investigation.

Round jets issuing into a uniform counter flow is a classical problem of fluid mechanics and has, therefore, received significant attention in the literature. At

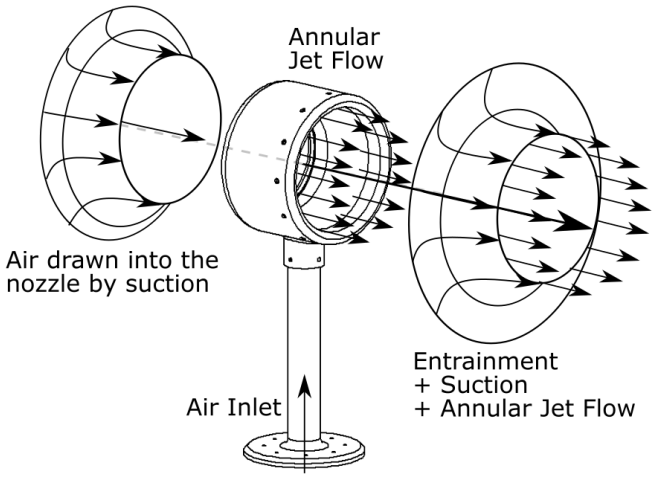

Figure 3.1: Schematic diagram of the airflow of a ventilated OCAJ issuing into quiescent surroundings.

low counter flow (U_o) to jet velocity (U_j) ratios $(\alpha = (|U_o|/U_j)$ the flow field is divided into two regions: the near field where the flow field is similar to that of a jet issuing into quiescent surroundings; and the far field where the jet interacts with the counterflow. The interaction of the jet with the counterflow is associated with the unstable movement of the jet tip, as described by König and Fiedler. (1991), Hopkins and Robertson. (1967), and Yoda and Fiedler (1996). This is referred to in the literature as the *unstable* flow condition. At higher counterflow to jet velocity ratios, a round jet forms an axisymmetric vortex ring around the nozzle exit which is periodically shed at between 3 to $5Hz$, otherwise referred to as the *stable* flow condition. The flow field was found to transition from an *unstable* to a *stable* flow condition at velocity ratios of $\alpha = 0.575$, 0.714 and between 0.714 and 0.769 by Hopkins and Robertson. (1967), König and Fiedler. (1991) and Yoda and Fiedler (1996) respectively. At velocity ratios below 0.714, Yoda and Fiedler (1996) identified that the *unstable* and *stable* flow phenomenon were observable at the same velocity ratios. At velocity ratios below 0.29 the stable flow phenomena was not observed however increasing the counter flow velocity from $\alpha = 0.29$ increased the probability that the flow field could be characterised as *stable*.

The average penetration length (x_p) of a round jet issuing into a uniform counterflow is used to determine the axial extent of the mixing region. The average penetration length was found to be linearly proportional to the velocity ratio of the jet to counterflow velocity for an unconfined jet(Arendt et al. (1956), Beltaos and Rajaratnam (1973), Yoda and Fiedler (1996), Lam. and Chan. (1997), Chan and Lam. (1998), Bernero. (2000)). Confinement of the counterflow by Sui and Ivanov. (1959), Sekundov. (1969), Morgan et al. (1976), and Sivapragasam et al. (2014) resulted in the reduction of the jet penetration length, which ceased to be linearly proportional to the jet to counterflow velocity ratio. In the investigations of Sui and Ivanov. (1959) and Sekundov. (1969) the jet was defined as confined when the counterflow diameter (B) to the penetration length x_p ratio $(\frac{B}{x_p})$ was ≤ 2.5 and 2.0, respectively. Morgan et al.

(1976) proposed an alternate relationship based on the jet to counterflow momentum flux ratio $Z = \left(\frac{U_j D_j}{|U_o|B}\right)^2 \leq 0.25$ where (D_j) is the diameter of the jet. This relationship was found to be independent of Reynolds number when the jet and counterflow Reynolds numbers were greater than $R_{e_j}\left(\frac{U_j D_j}{v}\right) > 3,000$ and $R_{e_o}\left(\frac{|U_o|B}{v}\right) > 100,000$, respectively. Experiments performed by Bernero. (2000) suggest a relaxation of these criteria to $Z \leq 0.06$ and $R_{e_j} > 2,000$. Proper Orthogonal Decomposition (POD) performed by Bernero and Fiedler (2000) identified that, at low $\alpha = 0.29$ ratios, the far field jet fluctuations were caused by a combination of the two dominant energy modes, radial jet flapping and the variation of the jet penetration. The transition between the *'unstable'* and *'stable'* flow conditions, occurred at $\alpha = 0.667$, and was caused by the switching of these dominant POD modes.

The geometry and flow topology produced by a round jet is significantly different to that of a ventilated OCAJ and this paper will illustrate the effect the introduction of a uniform counter flow velocity has on the structure of the near flow field.

3.2 EXPERIMENTAL METHOD.

3.2.1 DESCRIPTION OF APPARATUS.

To create an annular jet in counterflow, an annular nozzle was placed in a wind tunnel where the core-annular jet produced by the nozzle was exposed to a range of counterflow velocities ranging from $\alpha = 0$ to 1.8, where U_i is the induced velocity of the jet, and U_o is the free stream velocity in the wind tunnel, i.e. the counterflow velocity. The custom annular nozzle shown in figure 3.2, was designed using CFD, and was 3D printed out of Accura Xtreme White. The design of which was based heavily on that of commercially available air amplifiers (Gammack et al., 2009). The design consists of a plenum and a slot located around the internal curved surface of the nozzle. The nozzle had a slot outer diameter D_o and a slot inner diameter D_i of $D_o = 0.0684\ m$ and $D_i = 0.0667\ m$ respectively. When compared to the limiting slender case of $D_i/D_o = 1.0$ the nozzle had a ratio of $D_i/D_o = 0.98$. The slot nozzle width was found to vary by $\pm 0.5\%$ around the azimuth of the nozzle.

A HPC Kaeser SM 15 Aircentre compressor provided a continuous supply of air into the plenum at a rate of $Q_0 = 0.01 \pm 0.001\ m^3 s^{-1}$ with a back pressure of 7.7 *bar*. This flow rate was monitored using a Dwyer Instruments Visi-Float flow meter for the duration of each experiment. The air exited the plenum through the jet outlet, the axial slot located around the internal surface of the nozzle produced a jet outlet slot Reynolds number of $Re = \frac{U_i D}{v} = 5253$. The Coandă effect (Coandă, 1936) ensures that the jet remains attached to the internal surface of the nozzle. The nozzle had an expansion ratio between its inlet and outlet of 1 : 1.8, and uniformity of the jet velocity around the azimuth of the nozzle was achieved by varying the cross sectional area of the plenum around the nozzle azimuth, as shown in figure 3.2. Additional

nozzle parameters are presented in table 3.1. The temperature of the jet was equal to the ambient air flow meaning that the jet had a source buoyancy flux equal to zero $B_o = 0.0$.

For later reference, an (x,y,z)-coordinate system with its origin at the geometric centre of the nozzle outlet plane is defined such that the y-axis is vertically upwards and the x-axis is orientated against the direction of the counterflow. The counterflow was produced using the University of Glasgow DeHavilland wind tunnel. The test rig has a wind tunnel blockage of 2.9% and this investigation can defined as an investigation of a unconfined jet in counterflow. Homogeneous seeding of the wind tunnel for both PIV and LDA was once again achieved using a Pivtec-GmbH seeder, incorporating 160 Laskin nozzles, with a mean olive oil particle substrate diameter of 0.9 μm as stated by the manufacturer (PIVTechGmbH., 2019).

A commercially available Dantec Dynamics three-component Laser Doppler Anemometry (LDA) system was used to investigate the velocity profile $0.48R$ upstream of the nozzle outlet plane and $0.1R$ downstream of the nozzle inlet plane. Once again upstream and downstream are defined with respect to the direction of the wind tunnel flow. The system consists of three diode pumped solid state 1 W lasers at frequencies of 488 nm, 514 nm and 532 nm mounted on a Dantec 9041T3332 3D $(1m$ x $1m$ x $1m)$ traverse system capable of scanning the measurement volume with a positional accuracy of ± 0.01 mm. The lasers orientated at angles of 2.5^o,2.5^o and 28^o to the probe axes coincided to form a 2.62 x 0.12 x 0.12 mm elliptical measurement volume. In anticipation of elevated turbulence levels associated with jet counter flows and to avoid the velocity-bias effects, the system was operated in burst mode with transit(residence) time enabled for calculation of the mean flow velocity (Zhang, 2010), (George, 1988) and (Albrecht et al., 2013).

Two component PIV in the symmetry plane along the longitudinal centre line of the jet was performed in order to assess the structure of the flow field. A 532 nm wavelength Litron double cavity oscillator amplified, Nd:YAG laser with an output energy of 100 mJ per pulse was used to deliver the light sheet. A Phantom $v341$ digital high speed, 4 Megapixel camera with a 2560 x 1600 pixel CMOS sensors fitted with a 85 mm focal length set to f# = 1.8 was used to acquire the raw images. The flow field was split into three distinct regions: Region 1:Nozzle outlet; Region 2:Around the Nozzle; Region 3: Nozzle inlet, as shown in figure 3.3. 600 image pairs were recorded at $200Hz$ and $20Hz$ for a range of counterflow velocities, and a summary of the experiments conducted using PIV is shown in table 3.2. A time delay of $\Delta t = 100$ μs between each image pair was used for all experimental configurations investigated. Unless otherwise stated, all of the PIV images presented in this report were taken at $20Hz$ frequency over a 30 second time duration.

Smoke Flow Visualisation was used to investigate the structure of the flow field. A single oil based smoke filament, introduced using a Pea Soup - Wind Tunnel Air Flow Tracer Smoke Generator model: SGS-90 heated wand, was entrained into the large

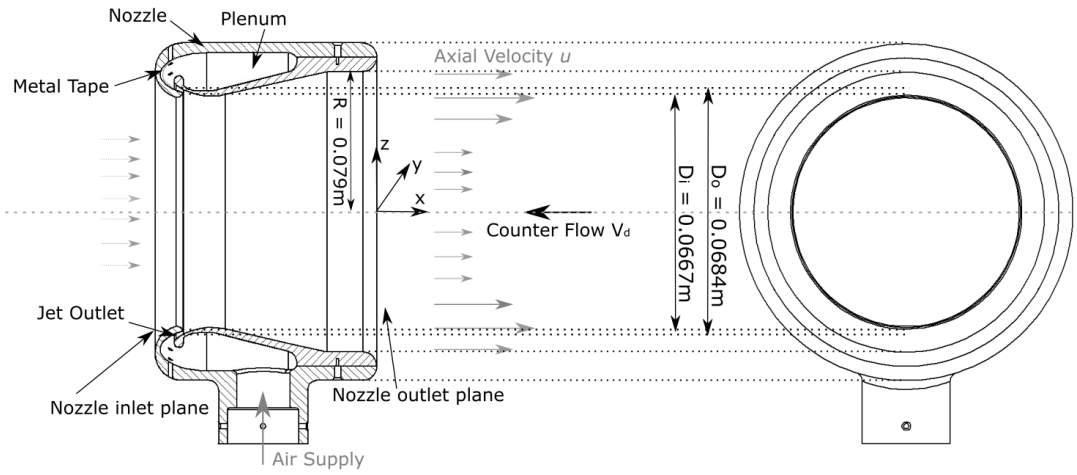

FIGURE 3.2: Design of the OCAJ

D_0	D_i	$\frac{D_i}{D_0}$	l	U_{ex}	A_0	R	R_{e_j}	v
(m)	(m)		(m)	ms^{-1}	m^2	(m)		m^2s^{-1}
0.0684	0.0667	0.98	0.0017	39.4	0.00118	0.079	5253	$1.5x10^{-5}$

TABLE 3.1: Table of OCAJ nozzle parameters: Jet outlet slot width l. Uniform exit velocity U_{ex} calculated using conservation of momentum theory as summarised by (Fox et al., 2008). Jet Outlet Reynolds number $R_e = \frac{U_{ex}l}{v}$. Jet outlet area $A_0 = \pi(D_0^2 - D_i^2)/4$. v is the kinematic viscosity of the source fluid.

recirculating vortices that formed as a result of the jet counter flow interaction. Images were recorded at 300 frames per second for up to 30 seconds using a Integrated Design Tools, Inc NX3-S4, 8MP high speed camera fitted with a $f = 135\ mm$ $F1.4$ Kowa lens.

3.2.2 LDA ANALYSIS METHODOLOGY AND ACCURACY.

Characterisation of the OCAJ nozzle inlet and outlet were performed on a grid of sample points concentrically spaced around the nozzle core with azimuthal and radial resolutions of 15^o and $0.05R$, respectively. Each of the 441 data points was sampled over a period of 10 seconds with data burst rates maintained above 300 counts per second. The approximate accuracy of the mean flow velocity was calculated as being $0.02ms^{-1}$, which corresponds to 0.22% of the peak nozzle outlet velocity. In counter-flow each of the 102 data points were sampled for $30s$ along the vertical and horizontal axes of symmetry of the nozzle, with a spatial resolution of $0.04R$, except for the cases where a counterflow velocity ratio was equal to $\alpha = 0.8$ & 0.9. For these test conditions each data point was sampled for a duration of $90s$ in order to obtain the time-averaged velocity with the same confidence. Only 2 component LDA (u,v) was achievable at the inlet of the OCAJ. Once again, the accuracy of the LDA system is dependent on the alignment of the laser system and the traverse with respect to the wind tunnel free stream. The mount onto which the probes were attached allowed the angle of

the probe to be measured with an accuracy of $\pm 0.5^o$. Once again, the alignment of the traverse to the wind tunnel wind tunnel free stream was measured to be less than 0.5^o by measuring the displacement of the laser focal point from the centre line of the wind tunnel over a $1m$ traverse.

3.2.3 PIV ANALYSIS, METHODOLOGY AND ACCURACY.

Post-processing of the raw PIV images was completed using a well established cross correlation-based procedure, implementing an image-based vector validation scheme (Green et al., 2000). A local vector map coherence method based on the work of Nogueira et al. (1997) was implemented to remove any false vectors. PIV of image regions closer than 3 mm to the solid surfaces were unreliable as a result of glare, therefore measurements were only made to within $3mm$ of the nozzle surface. The results presented in this report were all produced using a forward/reverse tile testing (FRTT) validation algorithm with an integration window size of 32 x 32 pixels with a 50% overlap. The resolution of the PIV was approximately $0.0016R$ x $0.0014R$ $/pixel$ for all regions of interest. To prevent peak-locking, a continuous window shift technique was incorporated into the correlation-based interrogation algorithm. This has been shown by Gui and Wereley (2002) to remove the effect that non-uniformly distributed bias errors have on the accuracy of the correlation-based tracking algorithm used to process PIV images. The uncertainty of the velocity measurements was estimated to be $\varepsilon_u = \frac{0.1}{M\Delta t} = \pm 0.05 ms^{-1}$ as defined by Prasad (2000). Assuming an optical magnification factor of $M = 7.45 pixel/mm$, and a maximum displacement error of $0.1 pixels$. Post-processing of the data produced the mean velocity profile of the flow field. The unsteadiness of the flow field was assessed by calculating the root-mean square (RMS) of the fluctuations of the measured axial velocity about the mean axial velocity.

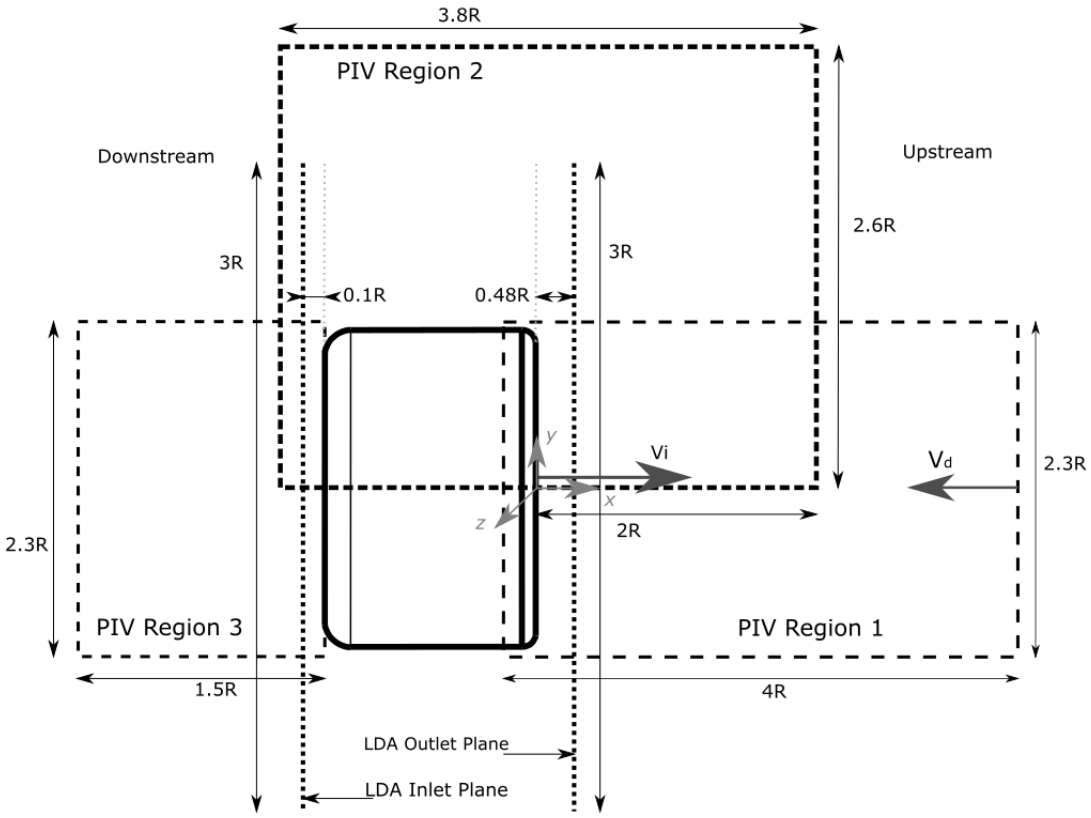

FIGURE 3.3: Schematic diagram of the PIV regions of interest and the LDA planes investigated.

	Region 1		Region 2		Region 3	
α	200Hz	20Hz	200Hz	20Hz	200Hz	20Hz
0.0	x	-	x	-	x	x
0.2	-	-	x	-	x	x
0.3	x	-	x	-	x	x
0.4	x	-	x	-	x	x
0.5	x	x	x	x	x	x
0.6	x	x	x	x	x	x
0.7	x	x	x	x	x	x
0.8	x	x	x	x	x	x
0.9	x	x	x	x	x	x
1.0	x	x	x	x	x	x
1.1	x	x	x	x	x	x
1.2	x	x	x	x	x	x
1.3	x	-	x	-	x	x
1.4	x	-	x	-	x	x
1.8	x	-	x	-	x	x

TABLE 3.2: Table of experimental configuration investigated using PIV.

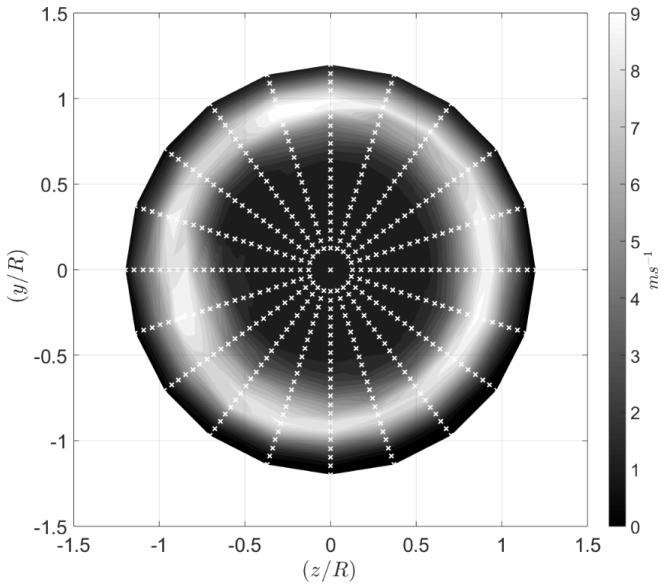

FIGURE 3.4: Averaged axial velocity component u, (ms^{-1}) of the OPAJ nozzle outlet, $0.48R$ upstream of the nozzle outlet plane with $U_o = 0.0\ m/s$. This figure was produced using LDA and each sample point location is displayed by the white crosses.

3.3 RESULTS.

3.3.1 CHARACTERISATION OF A VENTILATED OCAJ ISSUING INTO QUIESCENT CONDITIONS.

The ventilated OCAJ issuing into quiescent surroundings was characterised using LDA and PIV. This was deemed necessary as the nozzle used in this investigation is significantly different to that described in the limited literature relating to ventilated open core annular jets.

MEAN FLOW ANALYSIS.

LDA RESULTS.

The mean axial velocity component in a cross-stream plane $0.48R$ upstream (with respect to the wind tunnel flow direction) of the nozzle outlet plane is shown in figure 3.4. Based on the axial velocity, the induced velocity of the jet, U_i can be calculated using equation 3.1 where u is the time averaged axial velocity component and A_i is the area of the region investigated using LDA. This approach is commonly used in helicopter momentum theory to calculate the hover induced velocity of a rotor (Leishman, 2006). Previous investigations of jet flows in counterflows such as Morgan et al. (1976) have used momentum flux to scale the counterflow with respect to the jet flow. However this does not incorporate the influence of the ventilated core has on the velocity profile, therefore a notional induced velocity U_i was used instead. LDA velocity profiles along the vertical and horizontal axes of symmetry of both the

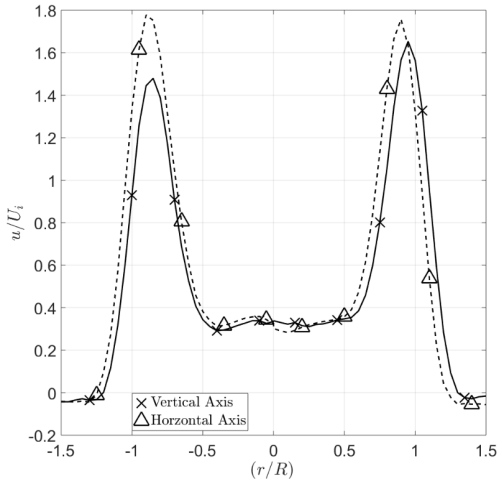

(A) Outlet axial velocity (u).

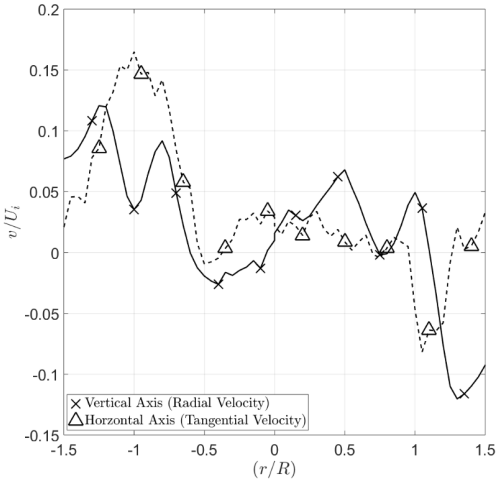

(B) Outlet vertical velocity component (v).

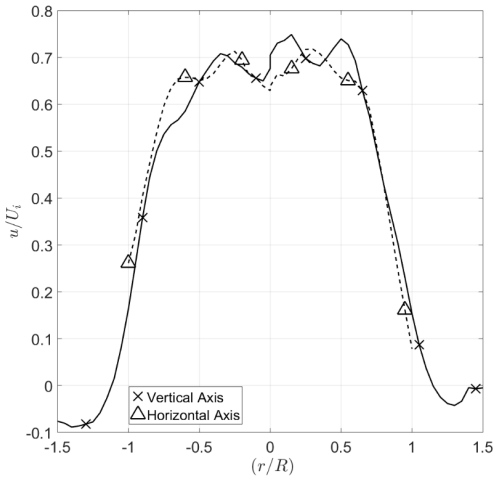

(C) Inlet axial velocity (u).

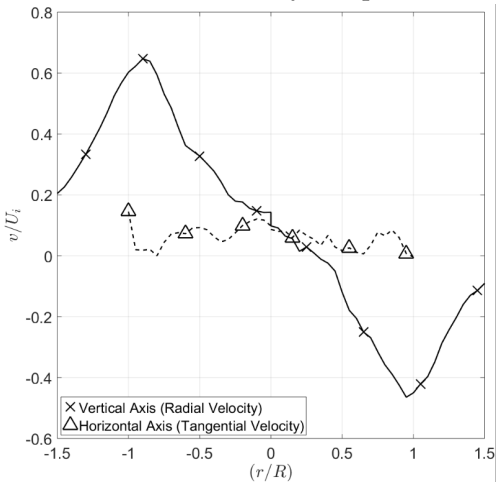

(D) Inlet vertical velocity component (v).

FIGURE 3.5: LDA Velocity Profiles along the vertical and horizontal axis of symmetry. Outlet plane ($\frac{x}{R} = 0.48$), figure(a) Outlet: axial velocity (u) and figure(b) Outlet: vertical velocity (v). Inlet plane ($\frac{x}{R} = -1.75$) figure(c) axial velocity and figure(d) vertical velocity. Data is scaled with respect to the notional induced velocity U_i.

nozzle inlet and outlet planes extracted from figure 3.4 are presented in figure 3.5a and figure 3.5b. The results show that the jet outlet mean axial velocity profile is not completely axisymmetric, however the maximum variation is 8%. The profiles presented in figure 3.5a and figure 3.5b indicate that, at the nozzle outlet, the flow is dominated by the axial velocity component which is significantly larger than that of the radial or tangential velocity components. The axial velocity profile is represented as a region of relatively uniform axial flow around the nozzle axis surrounded by a ring of high velocity air associated with the annular jet.

$$U_i = \frac{\int_0^{1.175R} 2\pi urdr}{A_i} \tag{3.1}$$

The mean axial velocity profile of air entrained into the nozzle inlet, figure 3.5c is approximately symmetric about the horizontal and vertical axes shows nearly uniform

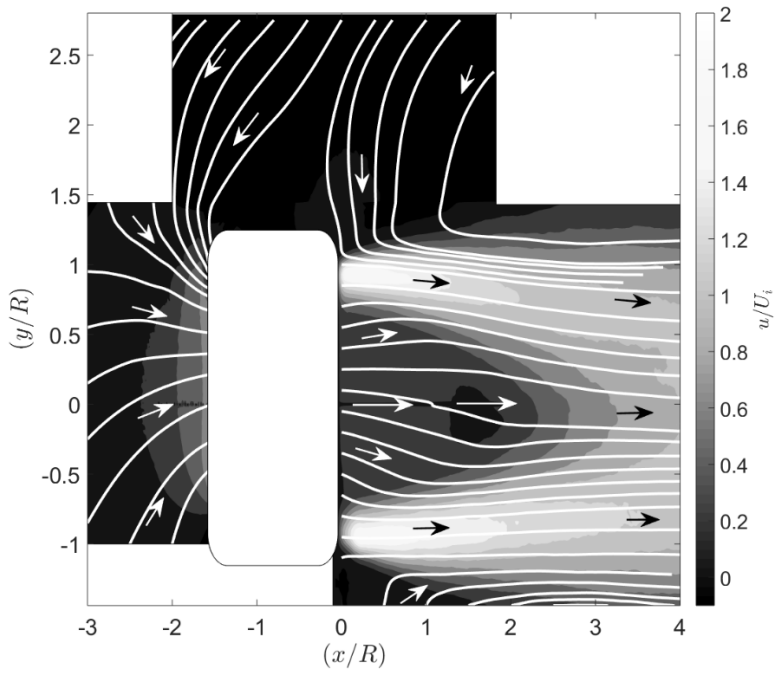

FIGURE 3.6: Mean axial velocity profile (u) produced by the OCAJ issuing into quiescent surroundings scaled with respect to the notional induced velocity U_i. Note this is a montage of the mean velocity profiles of PIV region 1, 2 and 3 stitched together using linear interpolation.

entrainment across approximately 70% of the nozzle inlet plane. Reversed flow is observed outboard of the nozzle $(|r/R| > 1.15)$ indicating that air is being drawn around the side of the nozzle into the inlet as a result of the jet. Figure 3.5d shows that on the horizontal axis of the nozzle inlet, there is very little tangential velocity, on the vertical axis, where air is entrained radially into the nozzle inlet there is high radial velocity which gradually decreases as it approaches the nozzles core. This radial velocity magnitude is not observed in the nozzle outlet velocity profile presented in figure 3.5b, however the jet has a slight velocity bias towards the lower velocity core of the nozzle. Through the nozzle the core velocity reduced from $u/U_i \approx 0.65$ to $u/U_i = 0.35$.

PIV RESULTS.

The mean axial velocity flow field around the ventilated open core annular jet issuing into quiescent surroundings is shown in figure 3.6. This figure was produced by stitching the result of all three PIV regions of interest together using linear interpolation. Mean flow streamlines indicate that, despite the different nozzle profiles the velocity profile produced by the ventilated OCAJ used in this investigation is similar to that of the profile presented by Padhani et al. (2018), with air being entrained into the shear layers of the jet. Streamline seed points were placed at various locations in the velocity field to highlight specific features of the flow field. Padhani et al.

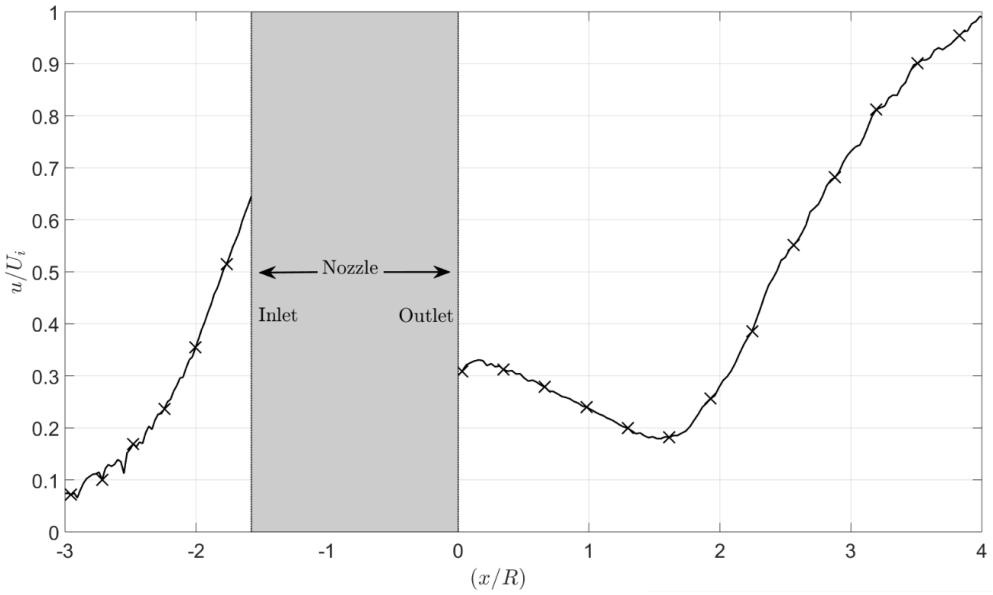

FIGURE 3.7: Mean axial velocity (u) along the nozzle longitudinal axis $u(x, 0, 0)$ scaled with respect to the notional induced velocity (U_i).

(2018) identified in their experiments, on a ventilated OCAJ issuing into quiescent surroundings a region of recirculation located on the axis of symmetry, $2.4R$ away from the nozzle. This region of recirculation was composed of a region of reverse flow bound on either side by a stagnation point. The induced flow initially increased from the nozzle outlet until $x/R = 0.1$, after which it decelerated to zero at the stagnation point closest to the nozzle outlet. In the current experiments, this feature cannot be observed in the mean axial flow velocity profile presented in figure 3.6 or the nozzle centreline mean axial velocity profiles presented in figure 3.7 which were extracted from figure 3.6. The flow does decelerate from the nozzle outlet but it does not approach a stagnation point. Instead it reaches a minimum $x/R = 1.6$ away from the nozzle outlet plane. The mean axial velocity increases for $x/R > 1.6$. Warda et al. (1999) associated this increase with the increasing coalescence of the jet. The reattachment point of the jet (when the jet shear layers have fully coalesced and the velocity reaches a maximum) was not in the region of interest of this investigation when the jet was issuing into quiescent surroundings. Further analysis of figure 3.7 shows that air is drawn into the nozzle outlet from distances greater than $1.5R$ downstream of the nozzle inlet plane. The air accelerates as it is drawn towards the nozzles inlet. Air is also drawn from around the side of the nozzle into the nozzle inlet.

A comparison between the mean axial flow velocity profiles produced by the ventilated OCAJ used in this investigation and the ventilated OCAJ investigated by Padhani et al. (2018) is shown in figure 3.8. From figure 3.8 it is clear that the velocity profiles produced by the two ventilated OCAJ differ considerably, however it is believed differences in nozzle profile such as the nozzle outlet angle, and the nozzle expansion ratio are responsible the variations observed.

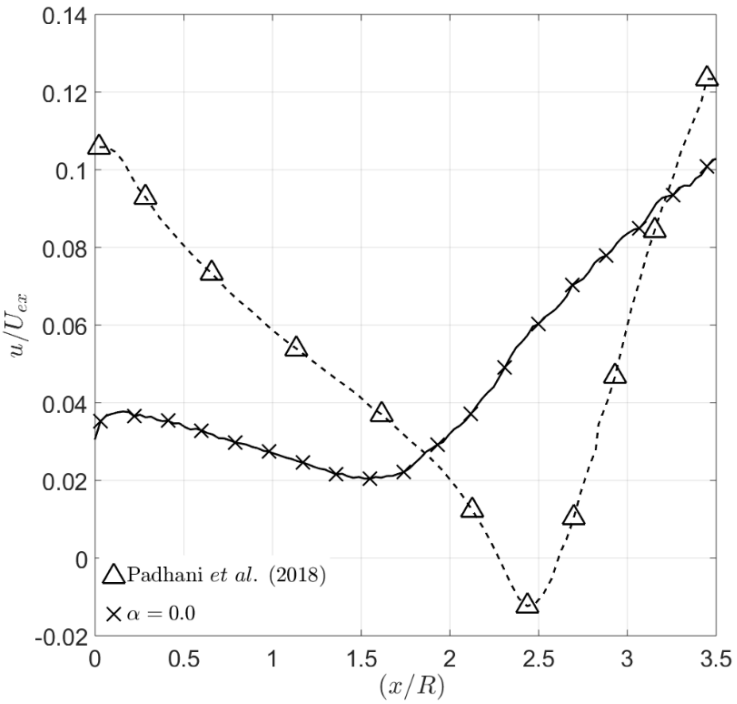

FIGURE 3.8: Mean axial velocity (u) along the nozzle longitudinal axis $u(x, 0, 0)$ scaled with respect to the jet nozzle exit velocity (U_{ex}).

UNSTEADINESS OF THE FLOW FIELD.

The unsteadiness of the velocity field is presented in figure 3.9 by means of the RMS of the fluctuations of the axial velocity u . The RMS of the fluctuations of the velocity field are predictably negligible outside of the jet flow. Whilst a ring of high-velocity fluctuations surrounding a relatively steady core extends away from the nozzle at a radial ordinate of $y/R = \pm 1.0$ with peak velocity-fluctuations of approximately $0.6U_i$ located closest to the nozzle outlet. The unsteadiness coincides with the shear layers of the jet whilst the jet coalescence leads to an increase in the velocity field fluctuations along the nozzle centreline. Figure 3.9 shows that the velocity fluctuations at the nozzle inlet are low, suggesting that the air entrained into the nozzle is relatively steady compared to the flow that leaves the nozzle. The same trends were observed when the unsteadiness of the LDA data signals were analysed, with both the horizontal and vertical axes of both the nozzle inlet and outlet profiles showing similar profiles, as shown in figure 3.10a and figure 3.10b, respectively. Further analysis of figure 3.10a highlights a region of relatively elevated unsteadiness in the centre of the nozzle outlet. Further analysis of figure 3.10 shows that the unsteadiness of the flow drawn into the nozzle is significantly lower than the unsteadiness of the jet flow the nozzle produced and is symmetric about the centre of the nozzle.

Visualisations of the first two eigenmodes, produced by applying snapshot *energy* POD to the PIV results (PIV:Region 1) obtained by the jet issuing into quiescent surroundings, are presented in figure 3.13. The first two modes shown in figure 3.13a and 3.13b indicate that the most probable and energetic realizations of the fluctuations

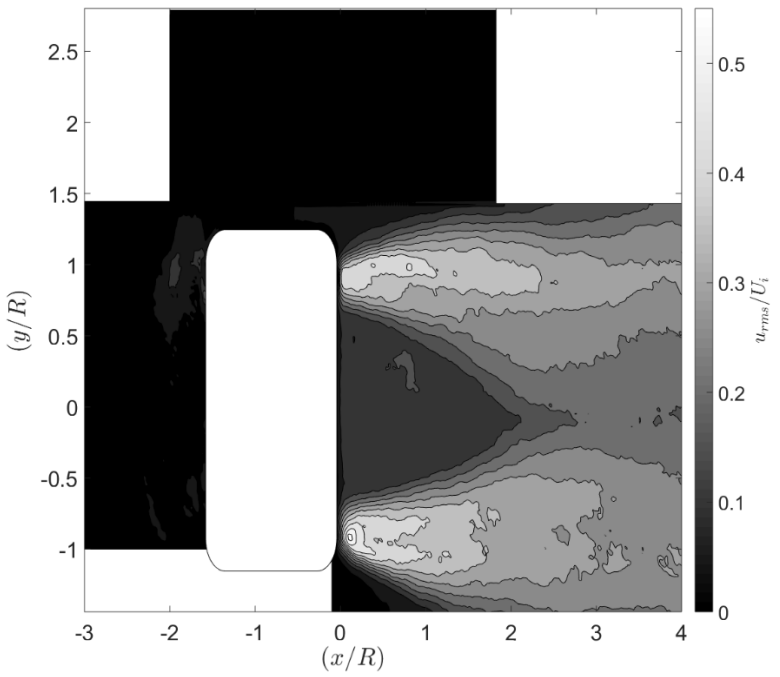

FIGURE 3.9: Contour plots of the RMS of the fluctuations about the mean axial velocity profile (u_{rms}) produced by the OCAJ issuing into quiescent surroundings scaled with respect to the notional induced velocity U_i. Note this is a montage of the RMS of the fluctuations about the mean axial velocity profiles of PIV region 1, 2 and 3 stitched together using linear interpolation.

of the flow field are dominated by the jet internal and external shear layers. Between the shear layers, there is radial movement of air across the diameter of the nozzle outlet. Figure 3.11 shows that the first 10 modes contain 9.00% of the kinetic energy of the fluctuations of the flow field whilst the following 20 modes only contain 9.76%. The influence of each mode on the velocity field was evaluated by subtracting the reconstructed mode from the averaged flow field. The reconstructed modes were produced using both the maximum and minimum reconstruction coefficient $\Psi(1)$. The reconstructed flow fields shown in figure 3.13 illustrate that mode 1 is primarily responsible for radial flapping of the jet, as shown by the radial deflection of the jet flow in figures 3.13c and 3.13e. Mode 2 also contributes to the radial flapping of the jet. However the contribution is far lower than that of mode 1.

The probability density function (PDF) of the reconstruction coefficients for the first POD modes $\Psi(m)$ plotted against their respective values $\Psi(m)$ are presented in figure 3.12. Due to the nature of snapshot PIV, which forces unresolvable scales to be placed into other modes, the PDF exhibits sinusoidal behaviour. The underlying structure of the probability density function presented in figure 3.12 was determined by generating a histogram of the probability density function. The number of bins (k) used to capture the basic form of the distribution was calculated using Rices Rule $(k = 2\sqrt[3]{m}) = 17$. The distribution has a skewness of -0.12 and a kurtosis value of 2.52 indicating that the distribution is approximately symmetric and platykurtic, i.e.

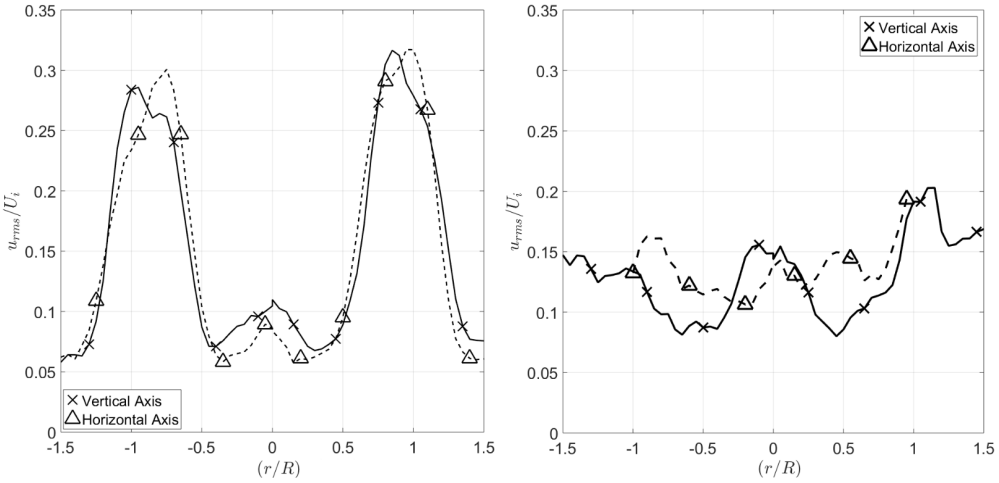

(A) Outlet (B) Inlet

FIGURE 3.10: Mean Axial Velocity Fluctuations u_{rms} for: (a) the nozzle outlet and (b) the nozzle inlet, scaled with respect to the notional induced velocity U_i.

the flow field displays no directional bias to the radial flapping of the jet.

Spectral analysis of the temporal coefficient of mode 1 $\Psi(1)$ indicates that the radial flapping occurs at a frequency of 20 Hz. Radial jet flapping is a POD mode also associated with both round jets (Bernero and Fiedler, 2000) and closed core annular jets issuing into quiescent surroundings (Patter-Rouland et al., 2001). At higher modes the effect of the reconstructed mode upon the mean flow became indistinguishable for this region of interest.

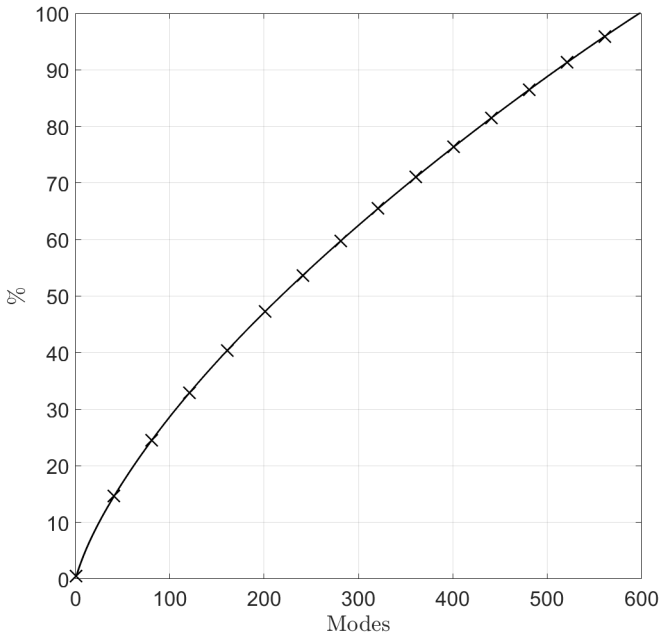

FIGURE 3.11: Progressive sum of eigenvalues as a percentage of the total sum calculated from the POD of the flow field produced for the ventilated OCAJ issuing into quiescent surroundings ($\alpha = 0.0$).

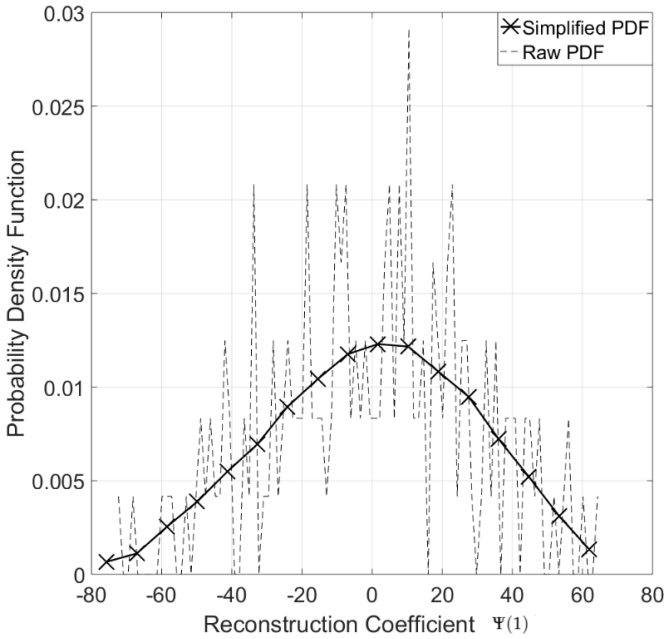

FIGURE 3.12: Probability Density Function of the first POD modes reconstruction coefficients $\Psi(1)$ plotted against the values of $\Psi(1)$ for $\alpha = 0.0$.

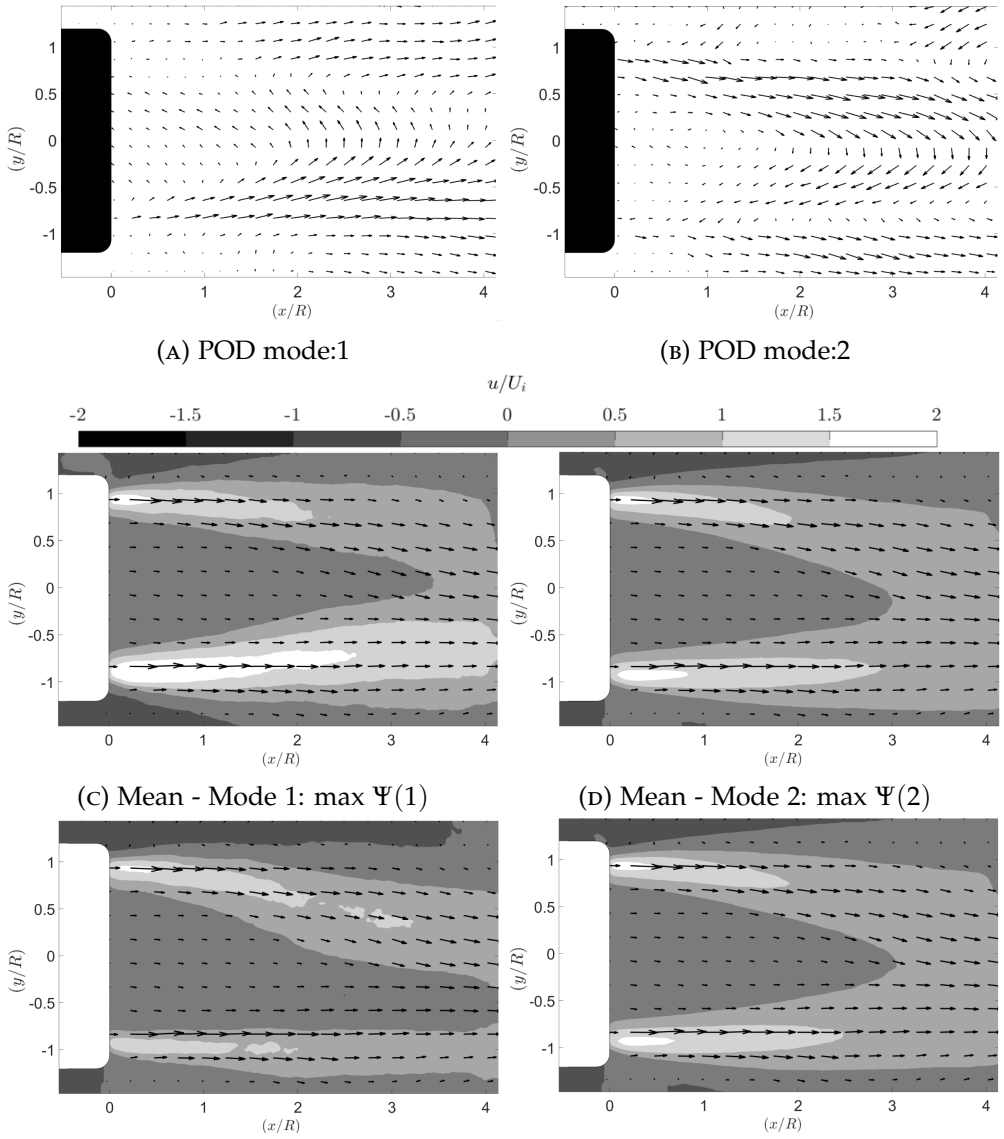

(A) POD mode:1

(B) POD mode:2

(C) Mean - Mode 1: max $\Psi(1)$

(D) Mean - Mode 2: max $\Psi(2)$

(E) Mean - Mode 1: min $\Psi(1)$

(F) Mean - Mode 2: min $\Psi(2)$

FIGURE 3.13: Visualisation of the first two POD eigenmodes of the velocity fluctuations at the nozzle outlet (PIV Region 1) calculated from 600 instantaneous velocity fields of the jet issuing into quiescent surroundings ($U_o = 0.0$), (a) mode 1, (b) mode 2. The vectors lengths are scaled with respect to the maximum vector length of each individual modes. Reconstructed simulations of the velocity fields produced by the subtraction of the maximum (c, e) and minimal (d, f) reconstruction coefficient representations of the first two modes from the mean flow field are presented in this figure. The axial velocity u is scaled with respect to the notional induced velocity U_i. Radial flapping of the jet can be observed in figure (c) and figure (e).

3.3.2 EFFECT OF COUNTERFLOW VELOCITY ON THE MEAN FLOW FIELD.

LDA RESULTS.

Figure 3.14 shows the development of the mean velocity profiles at the nozzle inlet and outlet planes as the velocity ratio was increased from $\alpha = 0.0$ to 2.0. At low velocity ratios $\alpha \leq 0.7$, the mean radial velocity profile at the nozzle outlet was not significantly affected by the introduction of a uniform counterflow. The mean axial velocity profiles at the nozzle outlet presented in figure 3.14a indicate that the peak velocities associated with the annular jet reduce slightly as the velocity ratios was varied from $\alpha = 0.0$ to $\alpha = 0.7$. The initial introduction of a counterflow slightly reduced the velocity in the low velocity core. The same trend was observed in the mean axial velocity profiles of the nozzle inlet presented in figure 3.14c. The initial introduction of a counterflow produced a small reduction in the inflow velocity, however further increases from $\alpha = 0.0$ to $\alpha = 0.7$ did not have any noticeable effect on the nozzle inlet's mean axial velocity profile. As with round jets issuing into a uniform counterflow, the jets interaction with the counterflow will occur in the far field with the near field resembling that of the jet issuing into quiescent surroundings.

Increasing the counter flow velocity to $\alpha = 0.8$ results in the formation of a region of reverse flow through the centre of the nozzle along with a large reduction in the peak velocities of the annular jet (figure 3.14a). This is coupled with the appearance of strong radial velocity at the nozzle outlet, implying that the jet flow is deflected radially outboard. The region of reverse flow does not extend through the nozzle inlet plane and the velocity of air entrained axially into the nozzle is reduced to approximately zero indicating that the ventilated open core annular jet is no longer acting as an efficient air multiplier. At higher velocity ratios $\alpha \geqslant 0.9$, the axial velocity at the nozzle inlet and outlet becomes negative $(-u)$ indicating that the counterflow penetrates both of these planes. All of the nozzle outlet experienced negative axial velocity for $\alpha \geq 1.0$ and the magnitude of u decreased despite the nozzles ventilated core. This is coupled with the increase in peak radial velocity at radial ordinates of $y/R \approx \pm 1.0$. Characterisation of the velocity profile inside the nozzle of the ventilated OCAJ was beyond the scope of this investigation.

Increasing the counterflow velocity from $\alpha = 0.8$ to $\alpha = 2.0$ leads to the formation and gradual increase in magnitude of a region of reverse flow through the centre of the nozzle inlet. i.e. the counterflow passes through the ventilated core of the nozzle. This is coupled with the appearance of strong radial velocity at the nozzle inlet, indicating that the counter flow passes through the nozzle and is radially diverted outward. The peak radial velocity component occurs inboard of the nozzle inlet at a radial ordinate of $y/R = \pm 0.5$. At $\alpha = 2.0$ the radial velocity is approximately linear and symmetric across the nozzle outlet plane.

In order to contextualise the velocity profiles presented in figure 3.14, sketches of the generalised flow field produced by the ventilated OCAJ at velocity ratios of $\alpha = 0.0$, of $\alpha \approx 0.7$ and $\alpha = 0.9$ are shown in figure 3.15. The sketches show the effect the sign of the velocity profile has on the structure of the flow field produced.

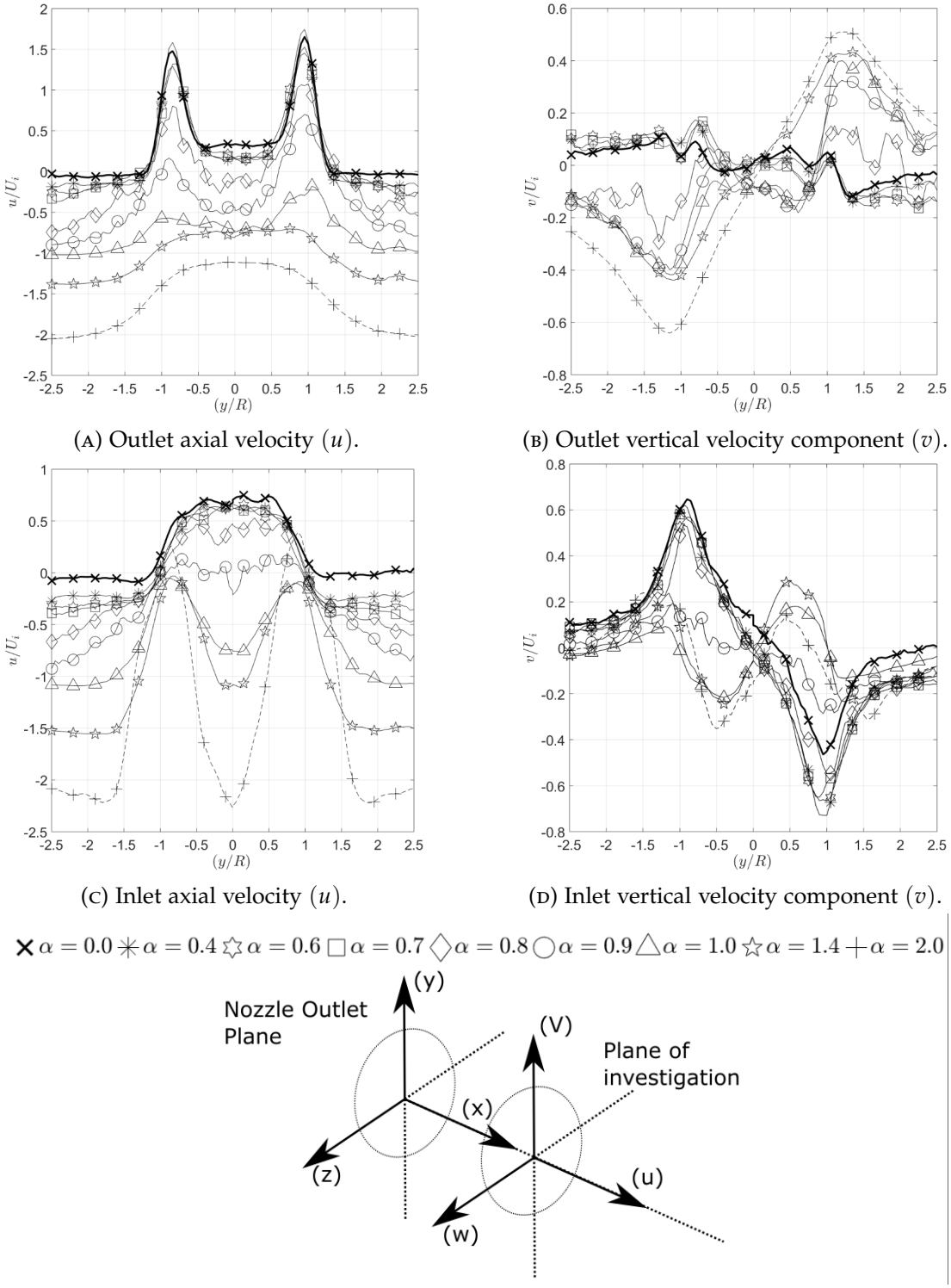

(A) Outlet axial velocity (u).

(B) Outlet vertical velocity component (v).

(C) Inlet axial velocity (u).

(D) Inlet vertical velocity component (v).

FIGURE 3.14: LDA mean axial velocity profiles along the vertical axis of symmetry. Outlet plane ($\frac{x}{R} = 0.48$), figure(a) Outlet: axial velocity (u) and figure(b) Outlet: vertical velocity (v). Inlet plane ($\frac{x}{R} = -1.75$) figure(c) axial velocity and figure(d) vertical velocity. Data is scaled with respect to the notional induced velocity U_i.

PIV Results.

Figure 3.15 shows the development of the mean flow field at the nozzle outlet as the counter flow velocity was increased from $\alpha = 0.0$ to $\alpha = 0.9$. At low counterflow velocity ratios ($\alpha < 0.6$), the near flow field is similar to that of the ventilated OCAJ issuing into quiescent surroundings. As the counter flow velocity was increased, the jet is increasingly encroached upon by the counterflow. At the interaction between the jet flow and the counterflow the magnitude of the radial velocity component increased as the flow turns outward away from the core of the nozzle. The axial velocity component decreases to approximately zero, leading to the formation of the saddle point on the geometric centreline of the nozzle. Analysis of figure 3.15c and figure 3.15d shows that the saddle point moves towards the nozzle as the counterflow velocity was increased, moving from $x/R = 4.0$ at $\alpha = 0.6$ to $x/R = 0.8$ to $\alpha = 0.7$. The saddle point on the nozzle centreline is not visible in the interrogation area at a velocity ratio of $\alpha = 0.8$, however a region of reverse flow penetrates through the nozzle outlet plane (fig3.15e). Despite the penetration of the counterflow through the core of the nozzle outlet, jet flow escapes the nozzle in an annulus around the core. The mean flow field indicates that very little air leaves the nozzle outlet when $\alpha \geq 0.9$.

The development of the mean flow outboard of the nozzle is shown in figure 3.16. This figure shows that the development of a large mean flow recirculation outboard of the nozzle is dependent on α. At a velocity ratio of $\alpha = 0.7$, the centre of the recirculation is located, in figure 3.16d, approximately $1.1R$ upstream of the nozzle and $1.8R$ outboard of the nozzle core. This recirculation is a result of the radial velocity component caused by the formation of the saddle point described earlier. As the velocity ratio increased the recirculation moved from downstream to around the side of the nozzle. This is coupled with the formation of a region of recirculation that forms around the side of the nozzle, allowing the jet flow to be entrained back into the nozzle inlet observable in figure 3.16e. A portion of the jet flow is deflected back into the nozzle outlet instead of being transported radially outboard around the side of the nozzle. The recirculation is transported away from the nozzle when $\alpha \geq 0.9$ and the free stream passes around and through the nozzle as shown in figure 3.16f.

The mean flow field at the nozzle inlet, as the counterflow velocity was varied from $\alpha = 0.0$ to $\alpha = 0.9$, is presented in figure 3.17. Increasing α leads to the formation of a persistent saddle point, shown in figure 3.17b, which forms approximately $1.4R$ downstream of the nozzle inlet for $\alpha = 0.5$. This saddle point can still be observed in the same location in figure 3.17e where $\alpha = 0.8$, and forms as a result of the interaction between air being drawn into the nozzle inlet and the counterflow which passes around the side of the nozzle. Increasing the counter flow velocity ratio further led to the reversal of the mean flow through the nozzle inlet, shown in figure 3.17f, indicating that the ventilated open core annular jet has ceased to entrain air through the nozzle.

Mean centreline velocity profiles for a range of α values are presented in figure 3.18. The centreline velocity decay profiles produced by the ventilated OCAJ are different to the hyperbolic relationships characteristic of round jets in counterflow derived by Beltaos and Rajaratnam (1973) and Yoda and Fiedler (1996). At low α values, the velocity profile along the nozzle centreline is notionally similar to that of the jet issuing into quiescent surroundings, driven by the entrained air and the coalescence of the jet shear layers. A velocity ratio of $\alpha = 0.6$ elicits a noticeable change in the development of the jet. Instead of decreasing, the velocity increases from the nozzle outlet to a maximum at $x/R = 1.7$ after which the velocity begins to decrease until it reaches zero at the mean penetration length $x_p = 4.0R$. Beyond this point u becomes negative as a result of the counterflow. A further increase in α moves the x_p towards the nozzle outlet, i.e. $x_p = 1.0R$ at $\alpha = 0.7$. For velocity ratios ranging from $0.8 \leq \alpha < 2.0$, the axial centreline velocity profile is dominated by the counterflow. The acceleration of the jet from the nozzle outlet is replaced by an acceleration of the counterflow as it passes through the nozzle outlet. The counterflow initially decelerates upstream of the nozzle before accelerating towards the outlet. The velocity of the flow entering the nozzle in this α range is approximately equal to the velocity of the counterflow as it enters the region of interest. The acceleration of the air, as it approaches the nozzle, reduces as α increases until, at $\alpha = 2.0$, the counterflow continuously decelerates as it approaches the nozzle.

The structure of the near field was the focus of this investigation and, as such, only two values for the mean penetration length of the jet into the counterflow could be obtained from the centreline axial velocity profiles presented in figure 3.18. Despite it is clear from figure 3.19 that the penetration length of a ventilated open core annular jet is different to that of a round jet, with a mean velocity equivalent to U_i issuing into counterflow. The exact nature of this relationship could not be determined from this investigation. With this focus, it was not possible to determine the growth rate of the jet.

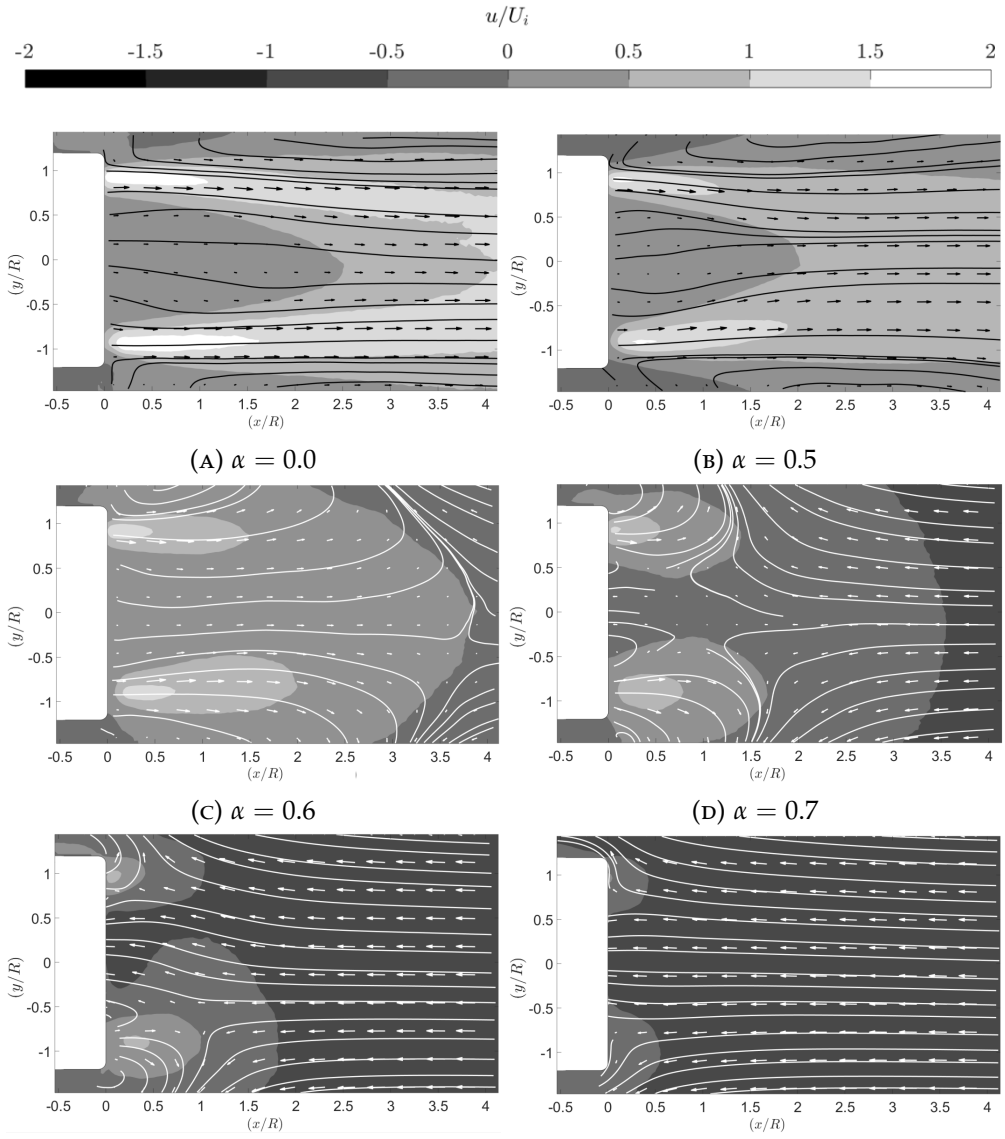

(A) $\alpha = 0.0$ (B) $\alpha = 0.5$

(C) $\alpha = 0.6$ (D) $\alpha = 0.7$

(E) $\alpha = 0.8$ (F) $\alpha = 0.9$

FIGURE 3.15: Averaged mean axial velocity contour plots of the ventilated OCAJ nozzle outlet (PIV: Region 1) as counter flow velocity $|U_o|$ increases. Streamlines and a reduced number of velocity vectors are superimposed onto the contour plots. All of the velocity vectors are scaled with respect to the notional induced velocity, U_i. Note: the formation of a saddle point in figure 3.15c and fig. 3.15d.

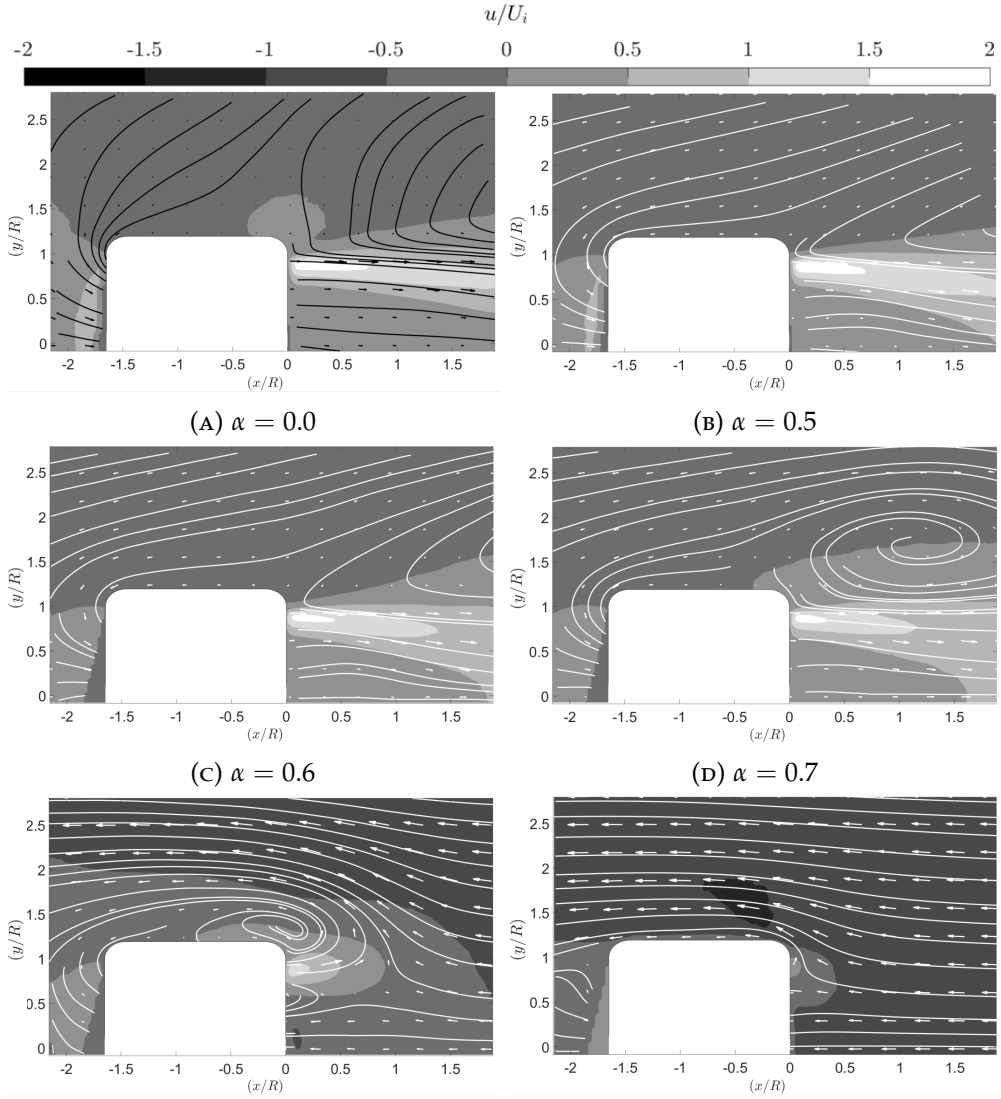

(A) $\alpha = 0.0$ (B) $\alpha = 0.5$

(C) $\alpha = 0.6$ (D) $\alpha = 0.7$

(E) $\alpha = 0.8$ (F) $\alpha = 0.9$

FIGURE 3.16: Averaged mean axial velocity contour plots around the ventilated OCAJ nozzle (PIV: Region 2) as the counter flow velocity $|U_o|$ increased. Streamlines and a reduced number of velocity vectors are superimposed onto the contour plot. All of the velocity vectors are scaled with respect to the notional induced velocity U_i. Note the formation of a large vortex which moves from below the nozzle to around the nozzle in fig. 3.16d and 3.16e.

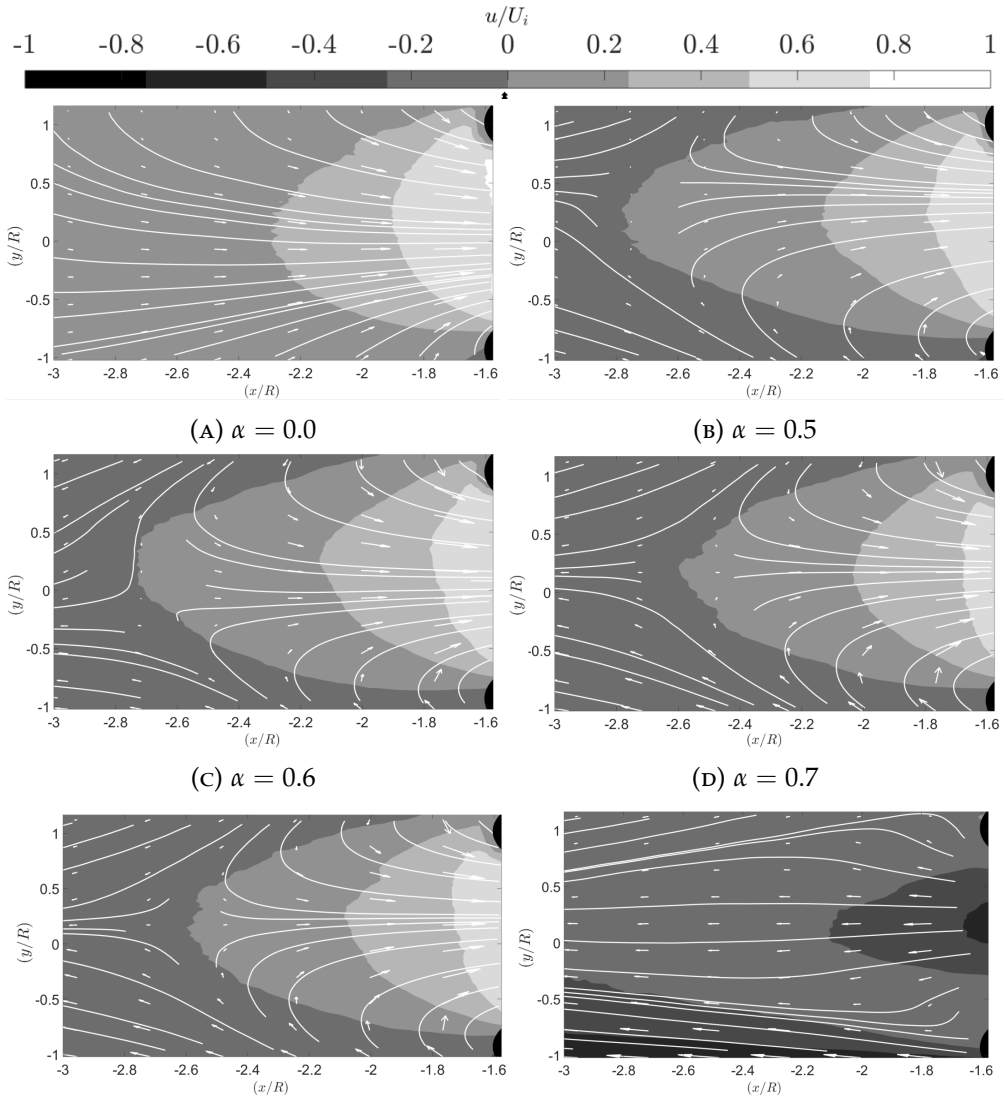

(A) $\alpha = 0.0$ (B) $\alpha = 0.5$

(C) $\alpha = 0.6$ (D) $\alpha = 0.7$

(E) $\alpha = 0.8$ (F) $\alpha = 0.9$

FIGURE 3.17: Averaged mean axial velocity contour plots around the ventilated OCAJ nozzle inlet (PIV: Region 3) as the counter flow velocity $|U_o|$ increased. Streamlines and a reduced number of velocity vectors are superimposed onto the contour plot. All of the velocity vectors are scaled with respect to the notional induced velocity U_i. Note the formation of a persistent saddle point in fig. 3.17b, fig. 3.17c, 3.17d and 3.17e.

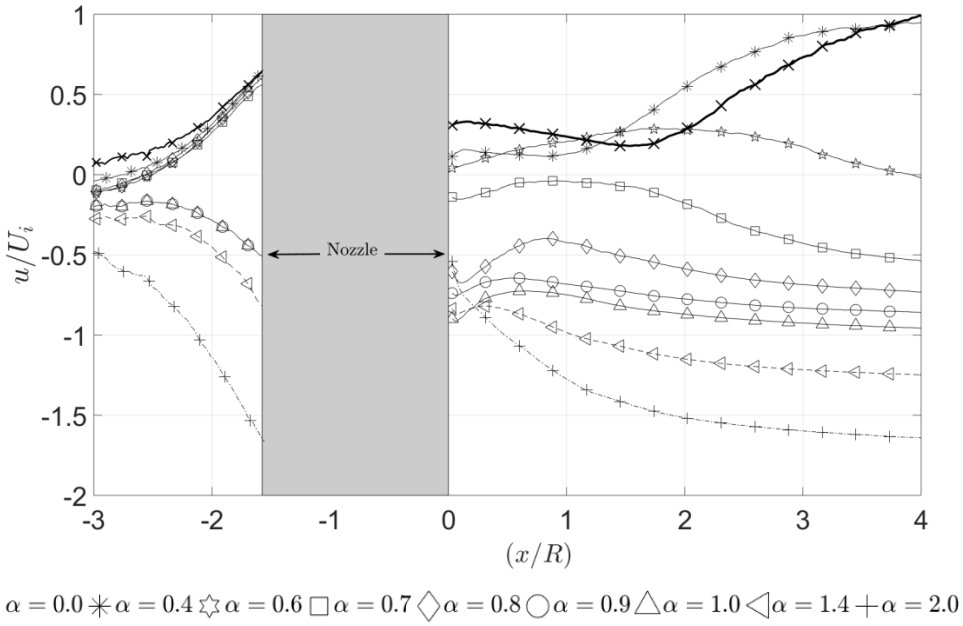

FIGURE 3.18: Mean axial velocity (u) profiles along the nozzle longitudinal axis $u(x, 0, 0)$ scaled with respect to the notional induced velocity (U_i).

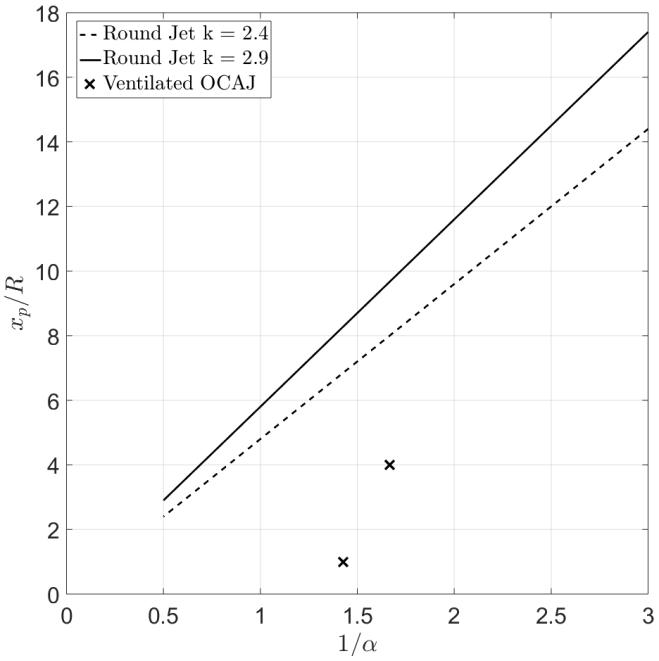

FIGURE 3.19: Mean penetration length x_p from PIV measurements for the ventilated OCAJ compared with the linear relationships defined by Morgan et al. (1976) characterising the penetration length of a round jet issuing into a uniform counterflow.

3.3.3 Effect of counterflow velocity on the unsteadiness of the flow field.

During the analysis of the PIV results, and the smoke flow visualisation, it became apparent that, as with a round jet issuing into counterflow, the flow produced by a ventilated OCAJ can differ considerably from the mean flow field presented earlier in figures 3.15, 3.16 and 3.17. An example of this is presented in figure 3.20 where, at the same $\alpha = 0.7$, the counterflow can penetrate the nozzle outlet, as shown in figure 3.20a, or the jet can propagate $2R$ upstream into the counterflow as shown in figure 3.20b. For this reason an analysis of the dynamics of this phenomena and an assessment of the unsteadiness of the jet's near flow field was performed.

PIV Results.

Figures 3.21 and 3.22 show contour plots of the RMS of the fluctuations of the local velocity around the local mean, scaled with respect to U_i. When initially introduced to a counterflow, the ring of high unsteadiness associated with the jet shear layer broadens, diffusing laterally as the jet propagates away from the nozzle. Figure 3.21b and 3.22b also show that the unsteadiness of the low velocity core increased. When $\alpha = 0.6$, the regions of high RMS merge to form a crescent of unsteadiness which covers most of figure 3.21c, containing the saddle point identified earlier in figure 3.15c. At this α value, a noticeable increase in the unsteadiness of the flow field outboard and upstream of the nozzle is observed. A region of near uniform unsteadiness equivalent to $(u_{rms} \approx 0.3U_i)$ extends more than $2.5R$ from the nozzle core. As the saddle point moves towards the nozzle outlet, the crescent of unsteadiness breaks down, leading to the formation of a ring of higher RMS $(u_{rms} \approx 0.7U_i)$ which extends away from the nozzle. The location of the saddle point identified in figure 3.15d is located in a region of unsteadiness located within the centre of this ring. The disappearance of the saddle point from the field of view means that the flow field returns to a form where the unsteadiness is solely dominated by the structures of the jet flow, as it is moves around the outside of the nozzle. The extent to which the regions associated with the jet extend upstream reduced as α increased until it was confined to a region close to the lip of the nozzle at $\alpha = 0.9$. The maximum unsteadiness $(u_{rms_{max}} \approx 0.8U_i)$ occurred at the lip of the nozzle outlet when $\alpha = 0.8$. Figure 3.22e shows that the flow around the side of the nozzle, at this α value, is relatively unsteady. For $\alpha = 0.9$ the unsteadiness is limited to a thin layer near to the nozzle surface.

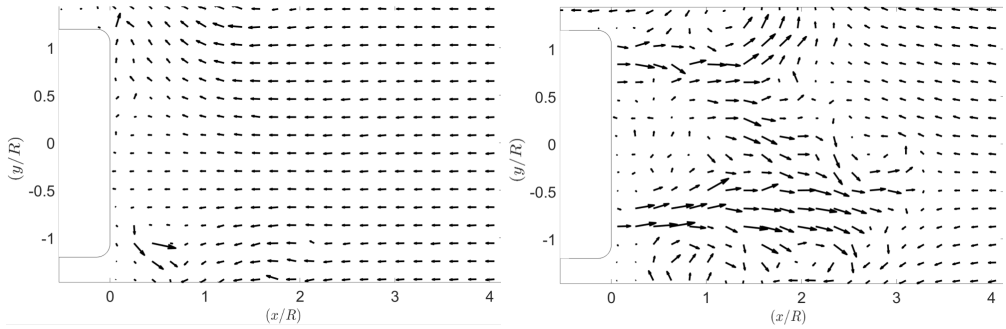

(A) (B)

FIGURE 3.20: Individual PIV snapshots of the nozzle outlet (PIV: Region 1) at $\alpha = 0.7$.

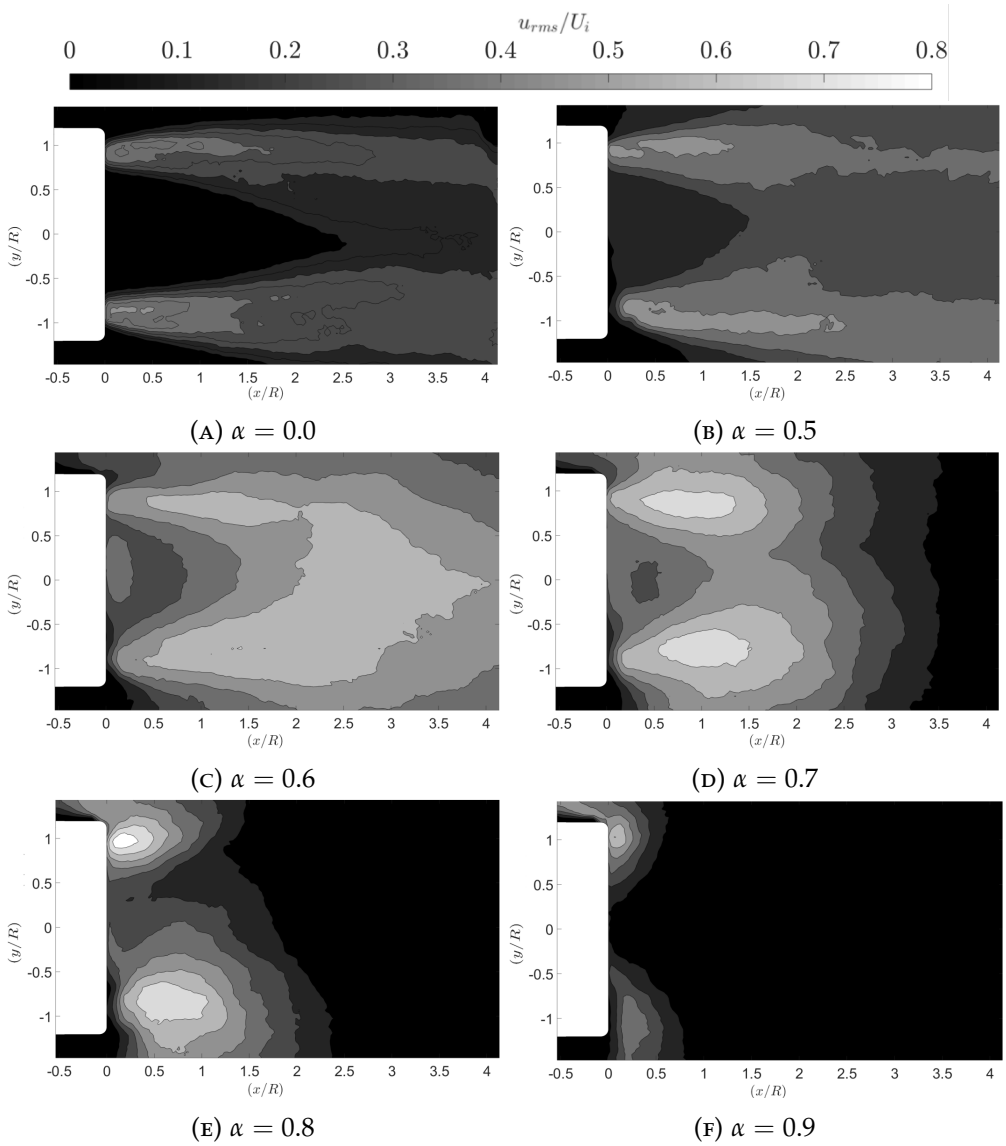

(A) $\alpha = 0.0$ (B) $\alpha = 0.5$

(C) $\alpha = 0.6$ (D) $\alpha = 0.7$

(E) $\alpha = 0.8$ (F) $\alpha = 0.9$

FIGURE 3.21: Contour plots of the RMS of the axial velocity fluctuations u_{rms} at the outlet of the ventilated OCAJ nozzle (PIV: Region 1). As the counterflow velocity $|U_o|$ increased the high RMS zones associated with the annular jet shear layer observed in figure 3.21a merged to form a large region of increased RMS on the nozzle centreline, as shown in figure 3.21c.

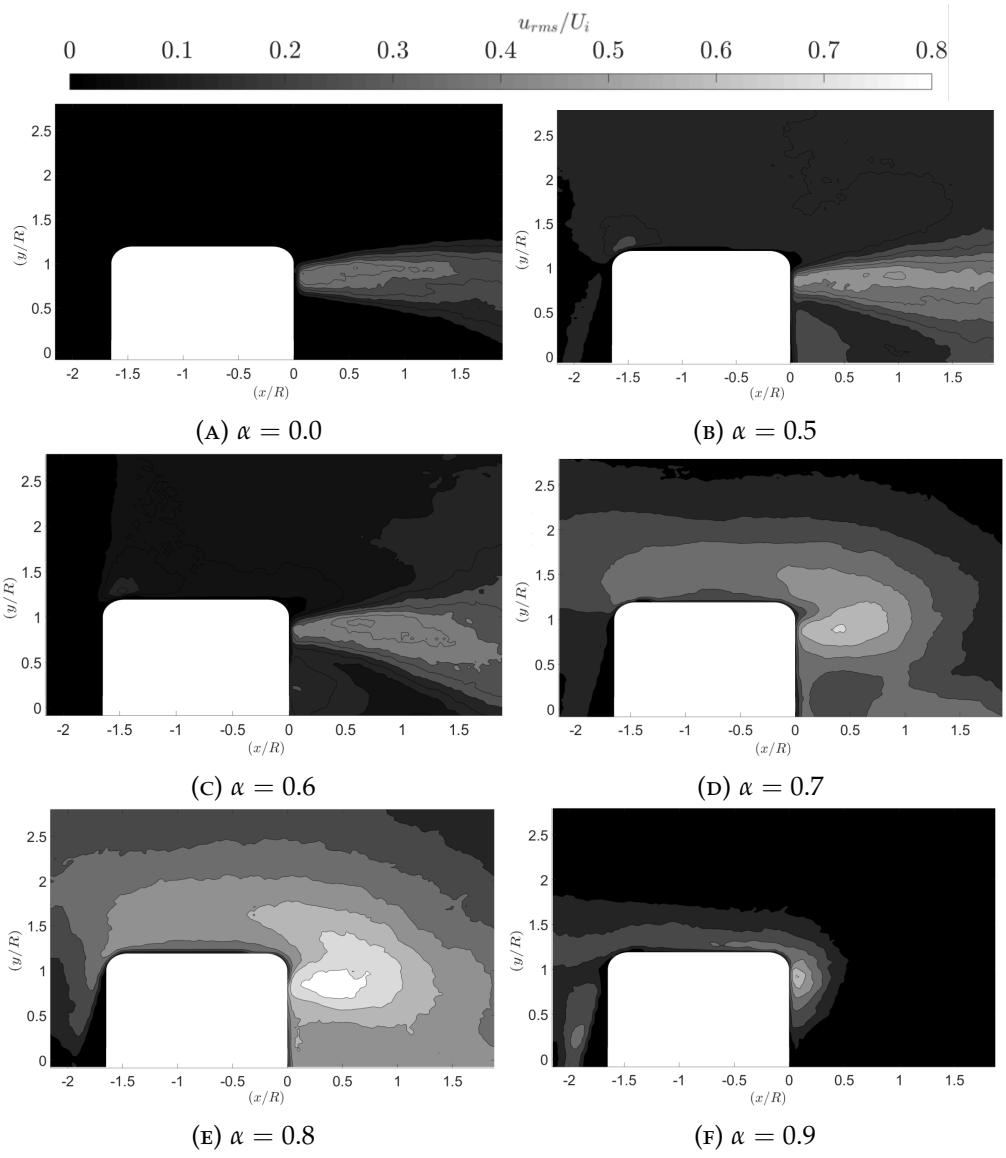

(A) $\alpha = 0.0$ (B) $\alpha = 0.5$

(C) $\alpha = 0.6$ (D) $\alpha = 0.7$

(E) $\alpha = 0.8$ (F) $\alpha = 0.9$

FIGURE 3.22: Contour plots of the RMS of the axial velocity fluctuations u_{rms} around the side of the ventilated OCAJ (PIV: Region 2).

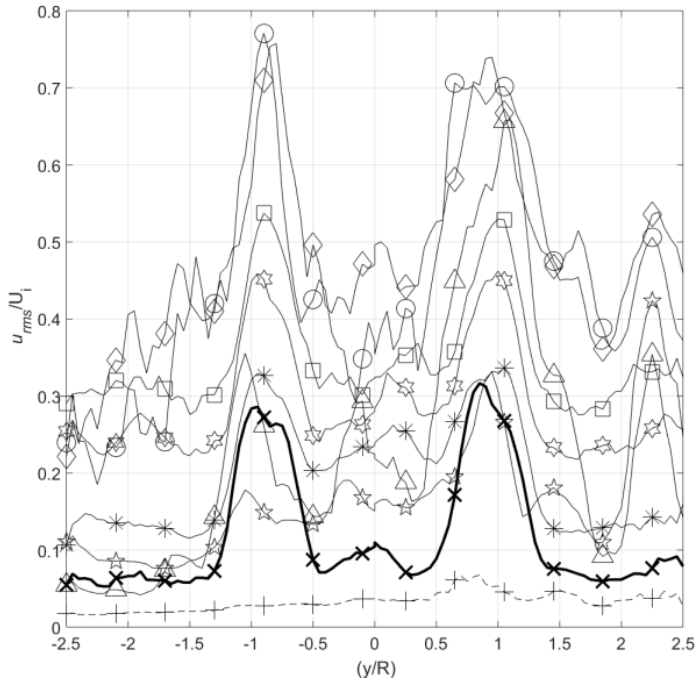

$\times\ \alpha = 0.0$ $\ast\ \alpha = 0.4$ $\star\ \alpha = 0.6$ $\square\ \alpha = 0.7$ $\diamond\ \alpha = 0.8$ $\bigcirc\ \alpha = 0.9$ $\triangle\ \alpha = 1.0$ $\star\ \alpha = 1.4$ $+\ \alpha = 2.0$

FIGURE 3.23: RMS fluctuations of the axial velocity component along the vertical axis $0.48R$ upstream from the nozzle outlet plane. All velocities presented are non-dimensionalised with respect to the notional induced velocity (U_i).

3.3.4 Effect of counter flow velocity on dynamics of the flow.

Smoke Flow Visualisation Results.

Sequential images produced from the smoke flow visualisation recordings, which show the dynamics of the flow field produced by the ventilated OCAJ operating at a velocity ratio of $\alpha = 0.7, 0.8$ and 0.9, are presented in figures 3.24, 3.25 and 3.26. Figure 3.24 shows that, at relatively low counterflow velocities $\alpha = 0.7$, where the velocity of the ventilated OCAJ is still notionally similar to that of the isolated jet, the counterflow velocity penetrates the nozzle outlet (figure 3.24). Penetration of the nozzle outlet by the counterflow results in a sudden, large scale expulsion of air from the nozzle into the counterflow, which results in the formation of a stagnation point which moves away from the nozzle outlet. The radial deflection of the free stream leads to the formation of a large vortex ring which sheds into the free stream and is deflected around the nozzle. Induced flow by the nozzle is capable of drawing these vortices back into the nozzle depending on the trajectory of the shed vortices. The persistence of the stagnation point in the flow field is variable, however the flow field shows a greater tendency to exist in this form at lower α ratios. At greater counterflow velocities, the counterflow penetrates the inlet of the nozzle, as shown in figure 3.25c, and is radially deflected around the nozzle. Despite this, the penetrated flow is drawn back into the jet flow and air is once again expelled from the nozzle leading to the formation of a large vortex ring coupled with a stagnation point, see figure 3.25f. Increasing the counterflow velocity increased the probability that the flow field would tend towards that associated with the formation of a large vortex ring, rather than that of the isolated jet until it becomes periodic at $\alpha = 0.9$. In the context of a round jet in counterflow, the flow has transitioned from an *unstable* case, through the *intermittent* case to a *stable* flow condition. A third flow condition is identifiable at higher α values, henceforth referred to as the *reversed* flow condition, which is a result of the unique properties of the ventilated open core annular jet which allows the counterflow to pass through the centre of the nozzle. In the *reversed* flow condition no jet flow passes through the nozzle outlet, instead air from the jet interacts with the counterflow inside of the nozzle and passes out through the nozzle inlet plane.

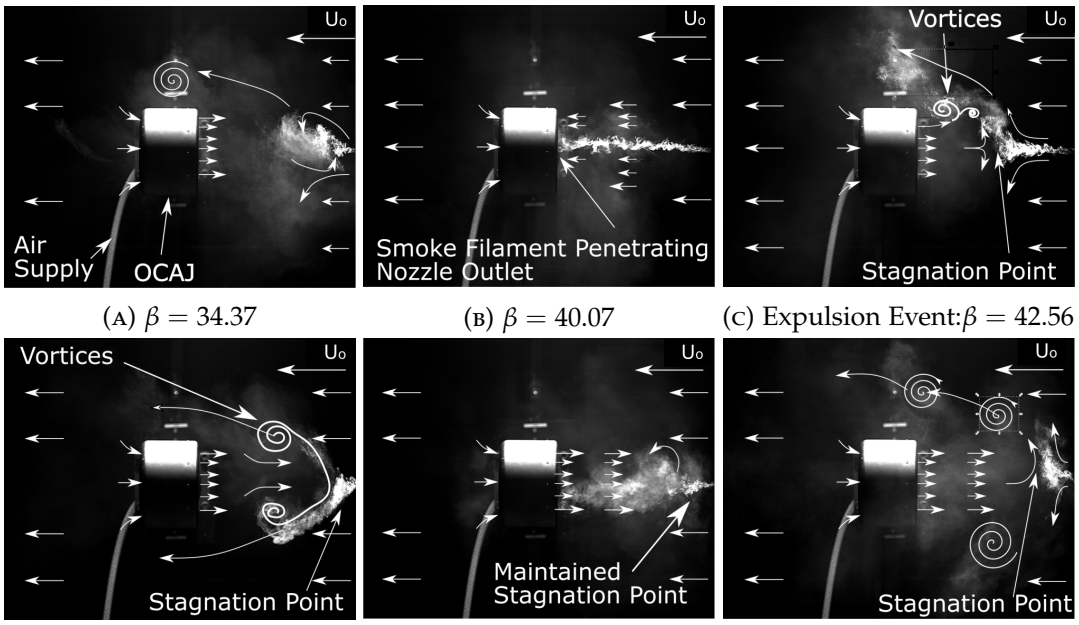

(A) $\beta = 34.37$ (B) $\beta = 40.07$ (C) Expulsion Event:$\beta = 42.56$

(D) $\beta = 45.05$ (E) $\beta = 49.34$ (F) $\beta = 62.19$

FIGURE 3.24: Sequential smoke flow visualisation images of an expulsion event observed when $\alpha = 0.7$ where $\beta = \frac{t|U_o|}{D}$. Beta is a non-dimensional parameter used to define the separation of sequential images in terms of the time it takes the free-stream flow to travel a distance equal to the jet outlet diameter (D).

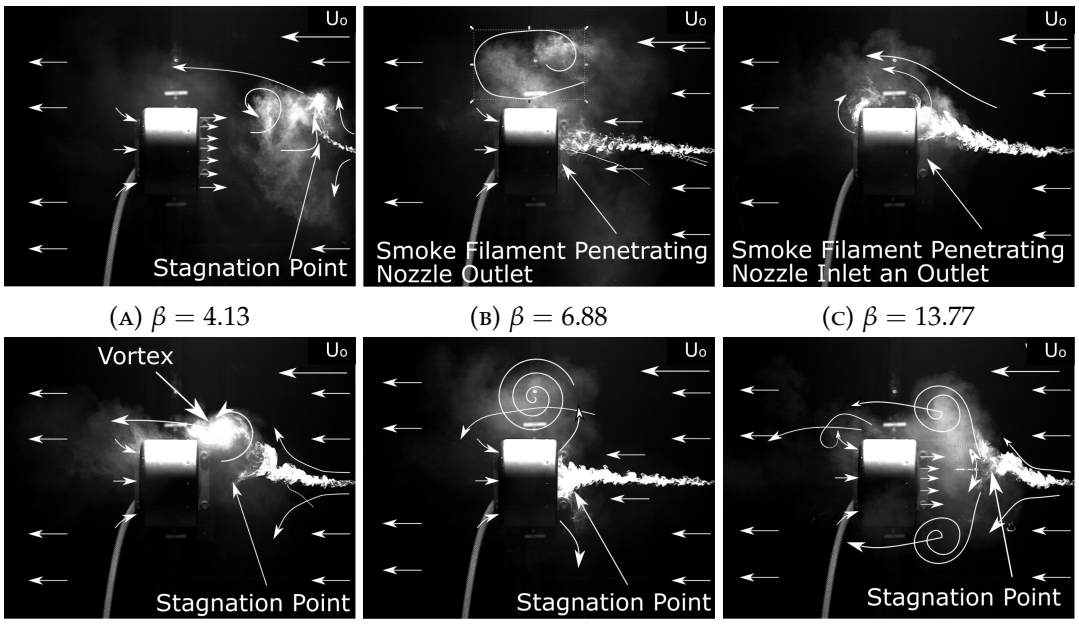

(A) $\beta = 4.13$ (B) $\beta = 6.88$ (C) $\beta = 13.77$

(D) Expulsion Event $\beta = 17.44$ (E) $\beta = 20.49$ (F) Expulsion Event $\beta = 29.52$

FIGURE 3.25: Sequential smoke flow visualisation images of an expulsion event observed when $\alpha = 0.8$ where $\beta = \frac{t|U_o|}{D}$. Beta is a non-dimensional parameter used to define the separation of sequential images in terms of the time it takes the free-stream flow to travel a distance equal to the jet outlet diameter (D).

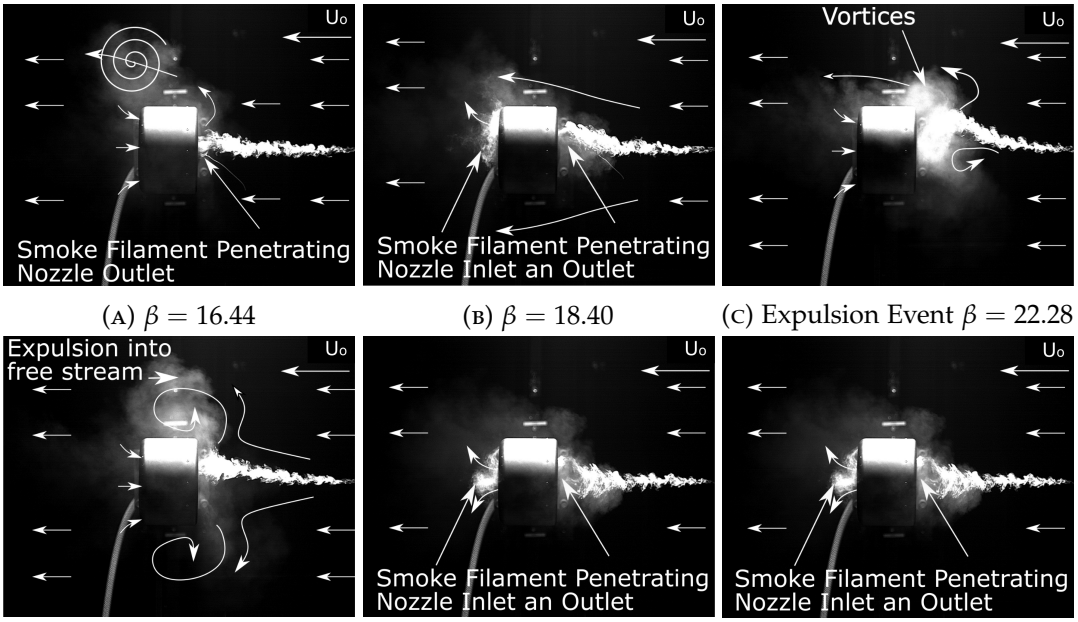

(A) $\beta = 16.44$ (B) $\beta = 18.40$ (C) Expulsion Event $\beta = 22.28$

(D) $\beta = 23.57$ (E) $\beta = 24.78$ (F) Expulsion Event $\beta = 26.79$

FIGURE 3.26: Sequential smoke flow visualisation images of an expulsion event observed when $\alpha = 0.9$ where $\beta = \frac{t|U_o|}{D}$. Beta is a non-dimensional parameter used to define the separation of sequential images in terms of the time it takes the free-stream flow to travel a distance equal to the jet outlet diameter (D).

POD RESULTS.

POD analysis of individual PIV snapshots of the flow investigated in PIV:Region 1 provides further insight into the underlying structures of the flow field observed from the smoke flow visualisation. The cumulative sum of the eigenvalues as a percentage of the total sum of the kinetic energy associated with the fluctuations for a range of α ratios is shown in figure 3.27. In the *unstable* flow condition $(\alpha \leq 0.5)$ the first ten POD modes contain approximately 8.72% of the total kinetic energy of the fluctuations, whilst the first 20 modes contain approximately 14%. Figure 3.29a shows that, in this flow regime, the first POD eigenmode is notionally similar to that of the first POD mode of the ventilated OCAJ, issuing into quiescent surrounding described earlier. Reconstructions of the flow field using the maximum (figure 3.29c), and minimum (figure 3.29e), reconstruction coefficients, show that the radial movement of air across the nozzle outlet between the jets dominant internal and external shear layers observed in the first eigenmode mode is primarily responsible for the radial flapping of the jet at a frequency of $(f \approx 0.3Hz)$. Figures 3.29d and 3.29f show that mode 2 is also responsible for the slight radial flapping of the jet, however, the contribution is far lower than that of mode 1. It should be emphasised that the magnitude of this radial flapping is small and that the unsteadiness of the flow field is still dominated by the jet shear layers. Analysis of the probability density functions (PDF) of the reconstruction coefficients for mode 1, $\Psi(1)$ and mode 2, $\Psi(2)$ plotted against the values of $\Psi(m)$ for a range of α ratios are presented in figure 3.28. When operating in the *unstable*

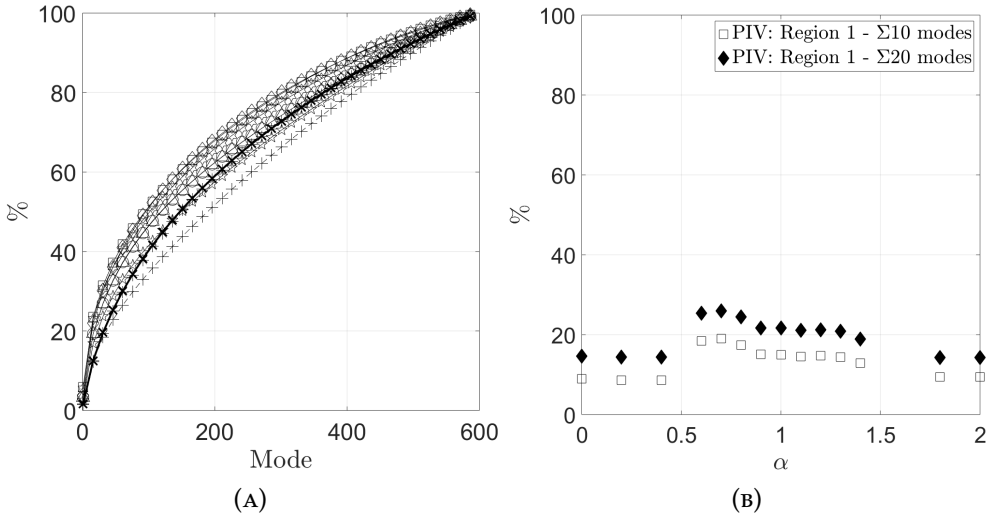

FIGURE 3.27: (a) Progressive sum of singular values as a percentage of the total sum calculated from the fluctuations of the flow field contained in (PIV: Region 1); (b) The percentage sum of the first 10 and the first 20 modes over a range of α values from 0.0 to 2.0.

flow condition, the distributions for both modes produce skewness values between $-0.12 \leq Sk \leq 0.89$ indicating that the reconstruction coefficients of the first two POD modes, responsible for the radial flapping of the jet are still symmetric about zero. All of the second POD mode's reconstruction coefficients probability density functions had small skewness values, indicating that the mode was approximately symmetric. Visualisations of the first two eigenmodes produced by the analysis of the flow field at the nozzle outlet (PIV: Region 1) operating in one of the *intermittent* flow conditions investigated ($\alpha = 0.6$) are presented in figure 3.30. Mode 1, shown in figure 3.30a, is notionally similar to that of the mean flow field produced by the jet operating in the *unstable* flow condition, whilst mode 2 can be characterised by the reversal of flow through the nozzle outlet. Reconstruction of the flow fields, presented in figure 3.30, show that both of these modes are responsible for fluctuations of the jets penetration into the counterflow. These fluctuations coincide with the location of the crescent of high RMS identified in figure 3.21c. Higher POD eigenmodes show radial flapping of the jet is still present, however its contribution to the flow field is less significant than at lower α ratios. At $\alpha = 0.7$ the PDF of the reconstruction coefficients of the first POD mode has a skewness value of $Sk = 0.37$. This indicates that the first POD mode has a greater tendency to exist in a form where the counter flow penetrates the jet. The PDF shows, that as the velocity ratio increased, the tendency of the counter flow to penetrate up to the nozzle outlet as a result of the first POD mode increased. The percentage of the total kinetic energy of the fluctuations contained in the first 10 and 20 POD modes increased as the jet transitioned from a *unstable* to a *stable* flow condition because the disordered nature of the unsteadiness decreased. Once the flow enters the *reversed* flow condition, the percentage decreased, indicating that the

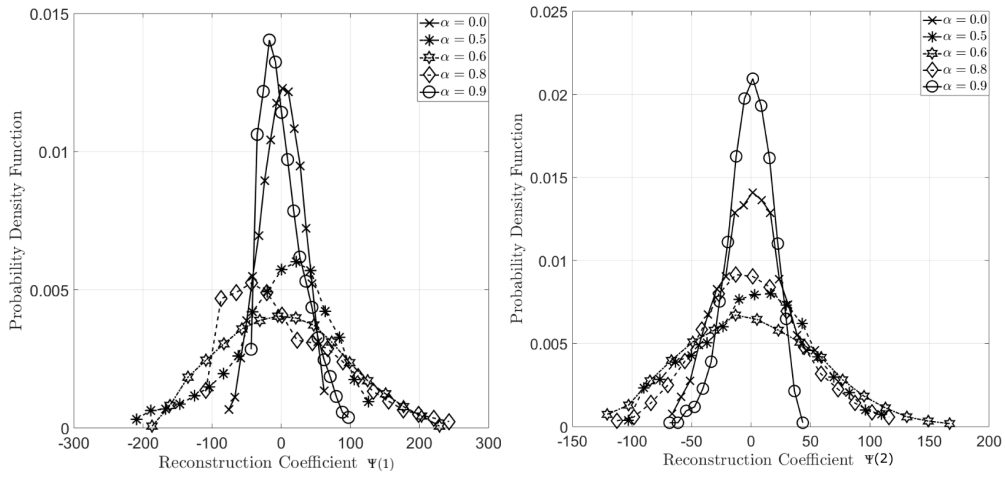

(A) (B)

Figure 3.28: Probability Density Function of the POD reconstruction coefficients $\Psi(m)$ of (PIV: Region 1) plotted against the values of $\Psi(m)$ for a range of α ratios.

number of low energy ratio POD modes increased and therefore the number of small scale structures observed in the region of interest (PIV: Region 1) increased when compared to that of the jet operating in the *intermittent* or *stable* flow conditions.

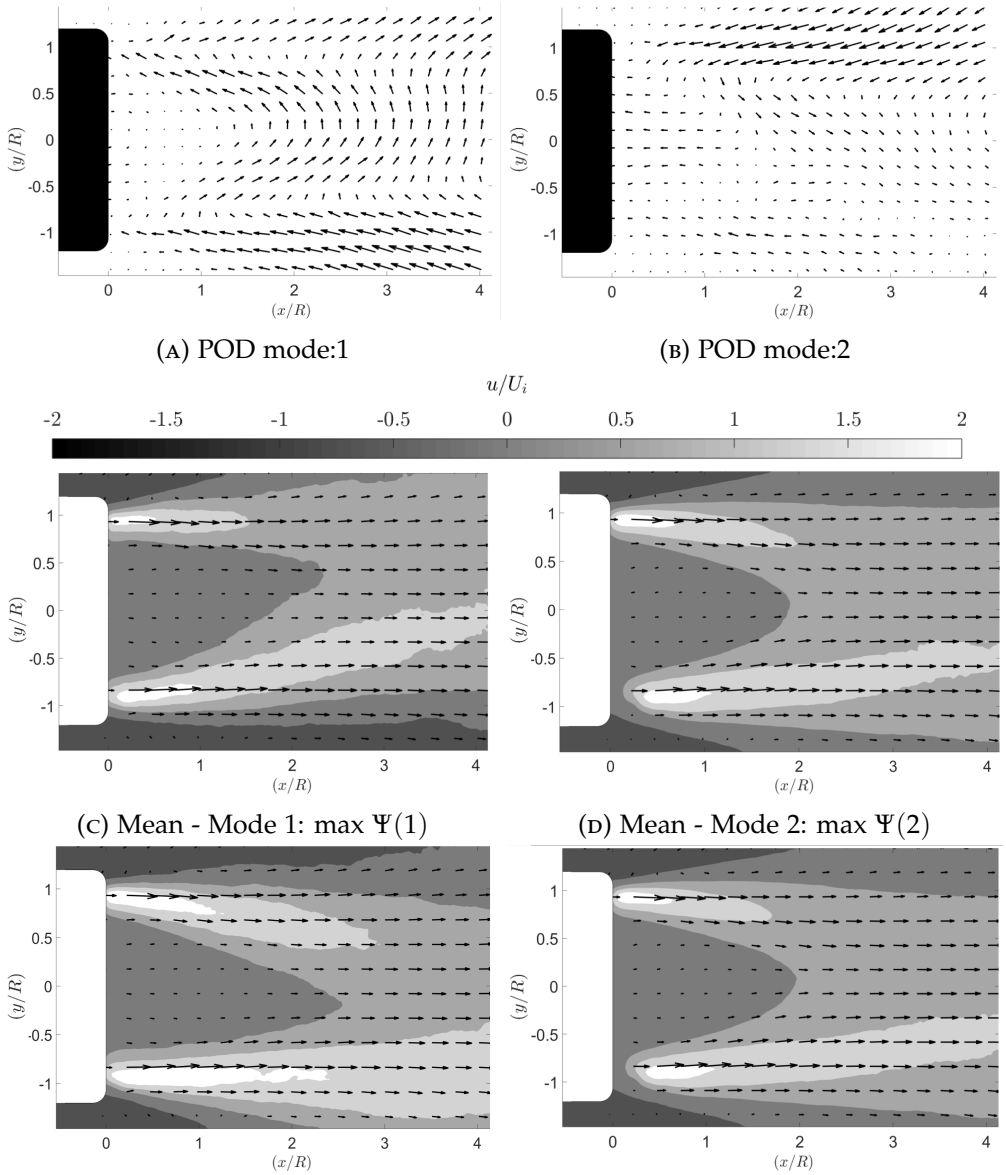

(A) POD mode:1

(B) POD mode:2

(C) Mean - Mode 1: max $\Psi(1)$

(D) Mean - Mode 2: max $\Psi(2)$

(E) Mean - Mode 1: min $\Psi(1)$

(F) Mean - Mode 2: min $\Psi(2)$

FIGURE 3.29: Visualisation of the first two POD eigenmodes of the velocity fluctuations at the nozzle outlet (PIV: Region 1) calculated from 600 instantaneous velocity fields of the jet issuing into a counterflow ($\alpha = 0.5$), (a) mode 1, (b) mode 2. The vectors lengths are scaled with respect to the maximum vector length of each individual mode. Reconstructed simulations of the velocity fields produced by the subtraction of the maximum and minimal reconstruction coefficient representations of the first two modes from the mean flow field are presented in figure (3.29c, 3.29e) and (3.29d, 3.29f), respectively. The axial velocity (u) is scaled with respect to the notional induced velocity U_i. Radial flapping of the jet flow can be observed in figure 3.29c and figure 3.29e.

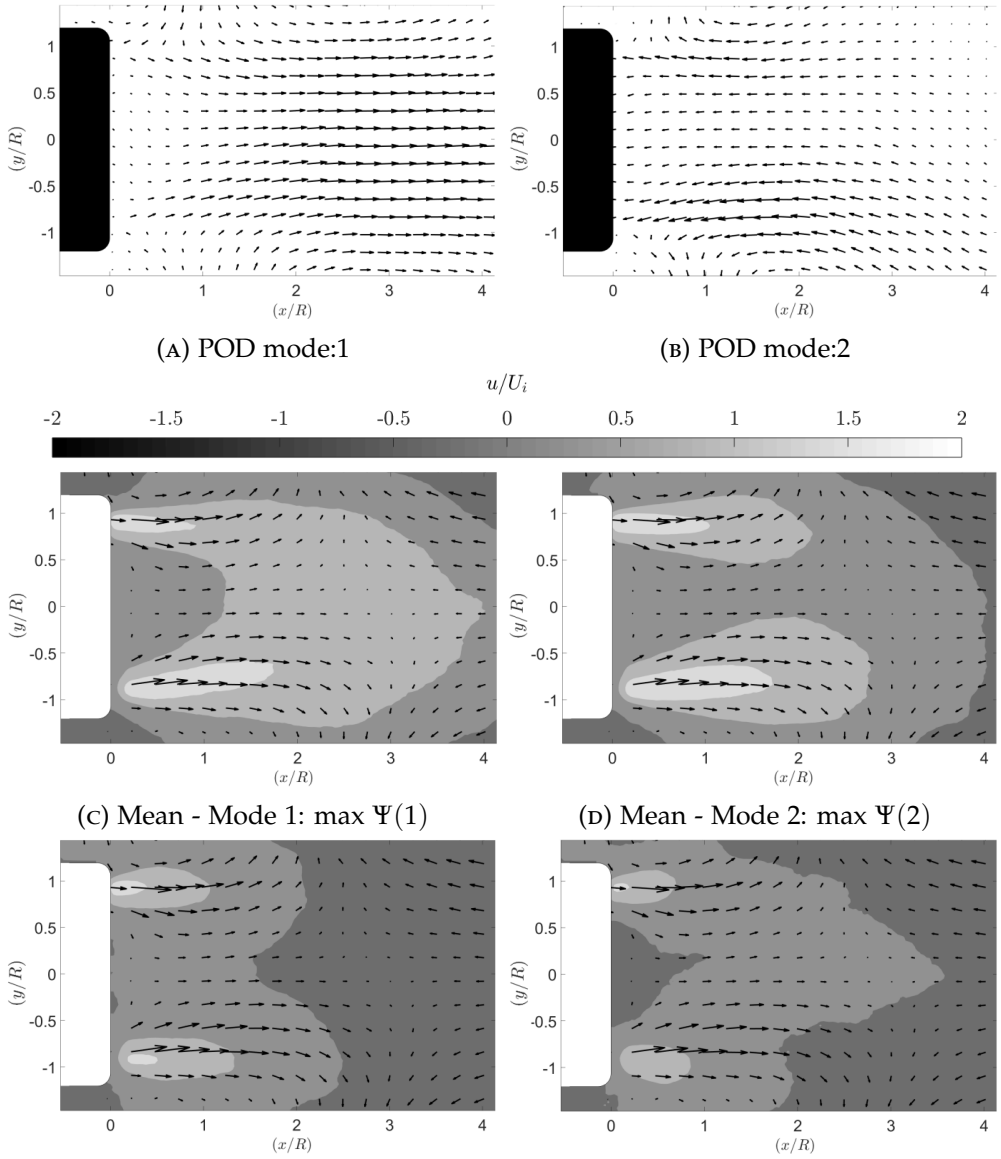

(a) POD mode:1 (b) POD mode:2

(c) Mean - Mode 1: max $\Psi(1)$ (d) Mean - Mode 2: max $\Psi(2)$

(e) Mean - Mode 1: min $\Psi(1)$ (f) Mean - Mode 2: min $\Psi(2)$

Figure 3.30: Visualisation of the first two POD eigenmodes of the velocity fluctuations at the nozzle outlet (PIV: Region 1) calculated from 600 instantaneous velocity fields of the jet issuing into a counterflow ($\alpha = 0.6$), (a) mode 1, (b) mode 2. The vectors lengths are scaled with respect to the maximum vector length of each individual modes. Reconstructed simulations of the velocity fields produced by the subtraction of the maximum and minimal reconstruction coefficient representations of the first two modes from the mean flow field are presented in figure (3.30c, 3.30e) and (3.30d, 3.30f) respectively. The axial velocity (u) is scaled with respect to the notional induced velocity U_i. Oscillation of the saddle point is observed in figure 3.30c and figure 3.30e.

3.4 CONCLUSION.

An investigation into the structure of the flow field produced by a novel ventilated OCAJ issuing into a uniform counterflow has been performed. A notional induced velocity has been shown by LDA, PIV and smoke flow visualisation to be an effective method of characterising the flow field of a ventilated OCAJ. As with a round jet, the flow field produced by a ventilated OCAJ issuing into a uniform counterflow can be characterised as transitioning from an *unstable* to a *stable* flow condition, as the jet to counterflow velocity increased. The flow field can also exist in an *intermittent* form where the *stable* and *unstable* flow conditions can coexist. The ventilated core allows a fourth flow condition to form, identified here as the *reversed* flow condition. In this condition, the jet does not pass through the nozzle outlet. Instead the counterflow passes through the nozzle forcing the jet flow to reverse direction and pass through the nozzle inlet. Whilst operating in the *unstable* flow condition, the flow field exhibits a topology typical of a ventilated OCAJ, where induced flow is drawn through the nozzle surrounded by a ring of higher velocity air associated with the jet. Increasing the counterflow velocity results in a conical region of flow penetrating towards the nozzle outlet which causes a saddle point to form on the geometric centreline of the nozzle. At counterflow velocities close to the notional induced velocity, the flow topology can exist in one of two topological forms: a region of recirculating air or that of the standard ventilated OCAJ. The diameter of this recirculation is approximately equal to the diameter of the nozzle. The formation of the recirculation is coupled with the formation of a stagnation point on the geometric centre-line of the nozzle. The saddle point can persist upstream of the nozzle outlet for prolonged periods of time at low counterflow to jet velocity ratios (α). When the nozzle enters the *intermittent* flow condition, the saddle point can penetrate through the nozzle outlet plane, where it can persist for a short period of time before being expelled upstream away from the nozzle. At higher counterflow velocity ratios the saddle point can pass through the nozzle inlet as well before it is drawn back through the nozzle and expelled upstream. The shedding of the recirculation becomes periodic when the induced to counterflow velocity ratio approached $\alpha = 0.9$. PIV results revealed that the mean centreline velocity decay profiles produced by a ventilated OCAJ issuing into a counterflow differ significantly from the hyperbolic relationships characteristic of round jets issuing into a counterflow. Initial results suggest that the mean penetration length of a ventilated OCAJ into a uniform counterflow differs from that of a round jet. However, further investigations would be required to determine the exact nature of this relationship. POD analysis showed that, in the *unstable* flow condition, the fluctuations are dominated by the first POD mode which represents the radial flapping of the jet shear layers. In the intermittent flow condition the main fluctuations of the flow field are dominated by the variation of the jets penetration into the counterflow. The results presented in this chapter show that, when introduced to a uniform counterflow, the flow field produced by the ventilated OCAJ contains many of the topological features

identified in the flow field of a shrouded rotors and an unshrouded rotor operating in the VRS, presented in chapter 2. POD analysis showed that the fluid structures responsible for the unsteadiness of the flow field produced by the shrouded rotor and the unshrouded rotor which was previously presented in chapter 2, were also observed in the flow field produced by the jet. The results presented so far in this thesis show that the mechanism by which the jet and the wake produced by both the shrouded rotor and the unshrouded rotor wake breakdown into toroidal states is similar. Indicating that the blade tip vortices, and therefore the mutual-inductance instability of helical vortices is not responsible for the development of the VRS, instead this suggests that they contribute to its development.

CHAPTER 4

THE VORTEX RING STATE OF A ROTOR WITH A LARGE ROOT CUT OUT.

4.1 INTRODUCTION.

An experimental investigation into the flow field produced by a rotor with a large root cut out, operating in axial descent, performed in the University of Glasgow De-Havilland wind tunnel, is presented. Laser Doppler Anemometry (LDA) was used to determine the velocity profile underneath the rotor, whilst Particle Image Velocimetry (PIV) and Smoke Flow Visualisation were used to investigate the dynamics of the flow field as the descent velocity was varied. The rotor had a large root cut out of 30% and was designed to produce a mean velocity profile which was notionally similar to the velocity profile produced by the ventilated OCAJ investigated in chapter 3. whilst containing blade tip vortices. In this chapter, the flow field produced by the rotor was compared to the flow field produced by a more conventional rotor with a blade root cut out of 12.5%, which had previously been investigated by Savas et al. (2009) and Stack et al. (2005).

The investigation showed that blade root cut out significantly affects the structure and the unsteady fluid dynamics of the flow field produced by a rotor when it is operating in axial descent. Measurements showed that the breakdown of the rotor wake into the toroidal recirculation characteristic of the VRS occurred over a narrower range of descent velocity ratios than seen in rotors with smaller root cut outs. The analysis of individual PIV measurement indicated that a large root cut out allowed the wind tunnel free stream to penetrate the rotor disk plane at lower descent velocities. Once the wind tunnel free stream penetrated the rotor disk plane, the flow became locked within the toroidal form until the rotor entered the wind mill brake state. The rotor did not enter the incipient flow regime.

4.1.1 AIMS AND OBJECTIVES OF THIS INVESTIGATION

The objectives and scope of this investigation are summarised below:

- Characterise the flow field produced by a rotor with a large root cut out;
- Characterise the flow field produced by a rotor with a large root cut out operating in axial decent;
- Explore the effect root cut out has on the development of the VRS.

4.2 EXPERIMENTAL METHOD

4.2.1 DESCRIPTION OF THE APPARATUS

An experimental investigation into the flow field produced by a $0.336m$ diameter (D) untwisted, untapered, fixed pitch rotor with a $0.1m$ root cutout (R_c) operating in axial descent was performed. Figure 4.1 shows a schematic diagram of the custom rotor used in this investigation, and additional rotor parameters are presented in table 4.1. The rotor had no cyclic input, and there were no lead-lag or flap degrees of freedom. Both of the carbon-fibre, uniform chord $c = 0.0315m$ blades were lightly loaded and were therefore assumed to be rigid. This rotor was chosen as it would induce a wake with a similar velocity profile to that of the OCAJ (please refer to Chapter 3). The large root cut out support had a cylindrical cross-section ensuring that this section of the rotor did not induce any flow. NACA0012 aerofoils, which are commonly used in the research of helicopters were used to induce flow outboard of the root cut out. It should be noted that the rotor used in this investigation was not designed to be representative of a typical helicopter rotor, instead the rotor was designed specifically to produce a mean velocity profile similar to that produced by the ventilated OCAJ, which induced very little flow through the centre of the nozzle compared to the higher velocity jets which surrounded the core, whilst also containing the helical vortex filaments which are characteristic of rotor wakes.

The rotor was mounted on a comprehensive ATE AeroTech Ltd model positioning system installed in the University of Glasgow DeHavilland wind tunnel. The system is capable of yaw $(210^o$ to $-150^o)$, pitch $(45^o$ to $-15^o)$ and roll $(180^o$ to $-180^o)$ angle adjustments, with an accuracy of $\pm 0.05^o$. A schematic diagram of the rotor installed on the articulated sting is shown in figure 4.2. The rotor was orientated to induce velocity (U_i) against the wind tunnel so that its speed (U_o) represents the descent velocity of the rotor. The test rig, shown in figure 4.2, had a negligible wind tunnel blockage of $\approx 3\%$. The thrust produced by the rotor was not investigated.

The rotor was powered by a $750W$ Panasonic AC servo motor model MSMA041A1C which was mounted on the end of the model positioning system as shown in figure 4.2. The rotor was operated at a rotational frequency of $66.6 \pm 1Hz$ producing a rotor tip speed of $V_{tip} = 70ms^{-1}$ and a blade tip Reynolds number of $168,500$. The rotor was connected to the motor using a $0.16m$ long $0.005m$ diameter spindle in order to reduce the effect the motor had on the aerodynamic performance of the rotor. For reference, an (x, y, z) coordinate axis system, with its origin located at the rotor hub is defined such that the y-axis is vertically upwards, and the x-axis is parallel to the wind tunnel free stream.

Once again, a commercially available Dantec Dynamics two-component Laser Doppler Anemometry (LDA) system was used to investigate the velocity profile $0.48R$

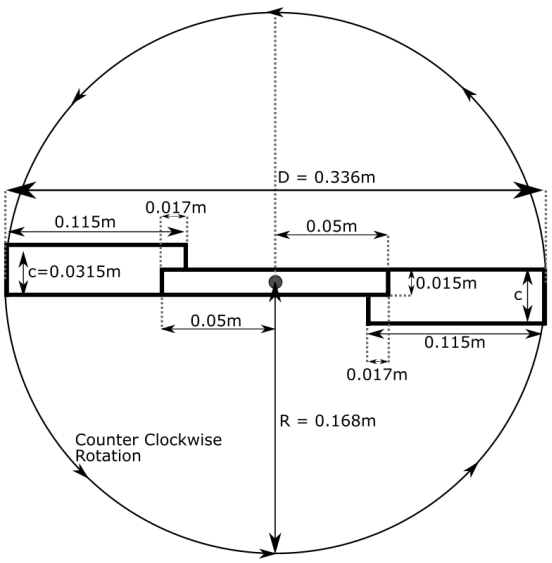

FIGURE 4.1: Schematic diagram of the rotor used in this investigation.

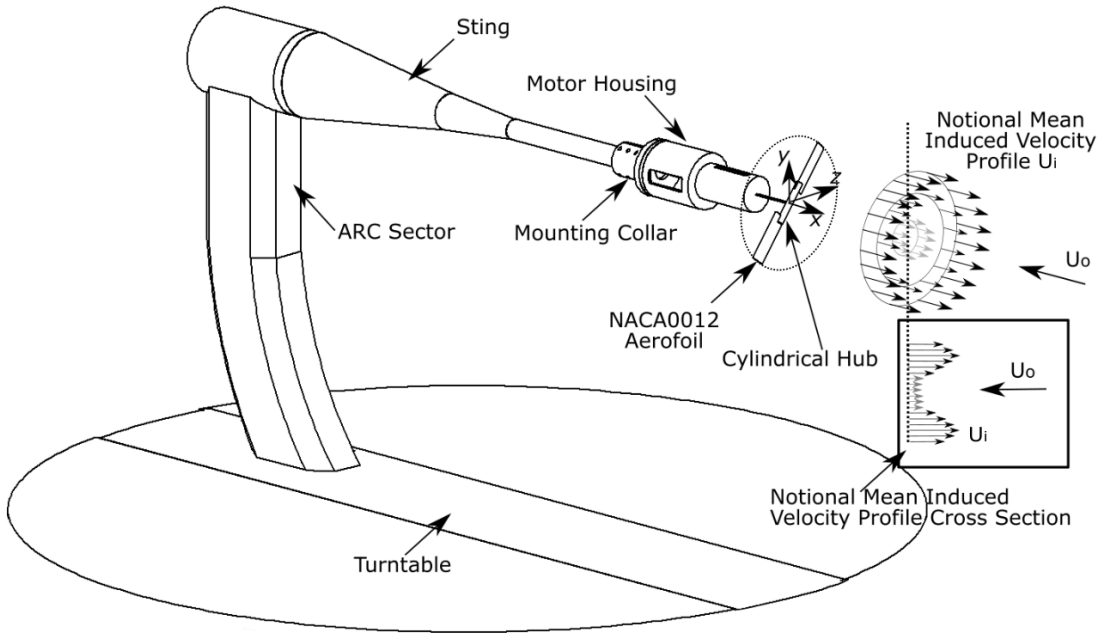

FIGURE 4.2: Schematic diagram of the rotor installed on the articulated sting installed in the DeHavilland wind tunnel.

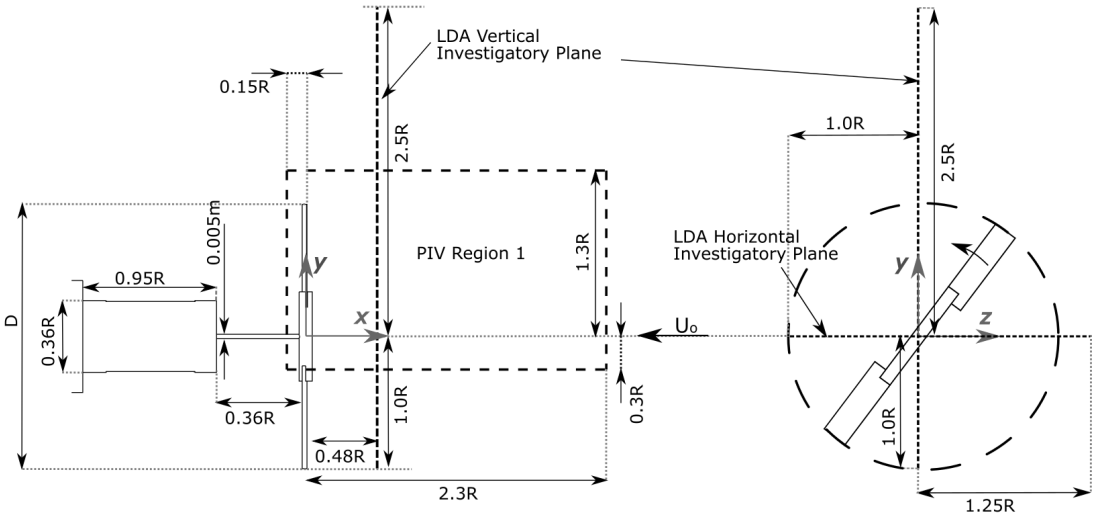

Figure 4.3: Schematic diagram of the LDA investigatory profiles of the custom rotor.

upstream of the rotor disc plane. The system consists of two diode pumped solid state $1W$ lasers at wavelengths of $488nm$ and $514nm$ mounted on a Dantec 9041T3332 3D $(1m$ x $1m$ x $1m)$ traverse system capable of scanning the measurement volume with a positional accuracy of $\pm 0.01mm$. The lasers were both orientated at an angle of 2.5^o coinciding to form a 2.62 x 0.12 x $0.12mm$ measurement volume. The system was operated in burst mode, with transit (residence) time enabled to allow the accurate calculation of the mean flow velocity for high turbulent flows as defined by Zhang (2010), George (1988) and Albrecht et al. (2013). Homogeneous seeding of the wind tunnel was achieved using a Pivtec-GmbH seeder which produced a mean olive oil particle substrate diameter of $0.9\mu m$ as stated by the manufacturer (PIVTechGmbH., 2019).

Two component PIV, in the symmetry plane along the longitudinal centre line of the rotor, was performed in order to assess the structure of the flow field. A $532nm$ wavelength Litron double cavity oscillator amplified, Nd:YAG laser with an output energy of $100mJ$ per pulse was used to deliver the light sheet. A Phantom V341 digital high speed 4 Megapixel camera with a 2560 X 1600 pixel CMOS sensor fitted with a Samyang $135mm$ focal length lens was used to acquire the raw images. A single region of interest, presented in figure 4.3 was used to investigate the flow field produced by the rotor. This was used because the flow field produced by an isolated rotor in axial descent has previously been shown to be symmetric about the centre of the rotor (Green et al., 2005). Three sets of 600 image pairs were recorded at a frequency of $200Hz$ for a range of counterflow velocities. A time delay of $\Delta t = 200\mu s$ was used for all velocity ratios investigated.

Smoke Flow Visualisation was used to investigate the structure of the flow field. Once again, a single oil based smoke filament, introduced using a Pea Soup - Wind

Tunnel Air Flow Tracer Smoke Generator model: SGS-90 heated wand, was entrained into the large recirculating vortices that formed as a result of the interaction between the rotor wake and the wind tunnel flow. Images were recorded at 300 frames per second for up to 30 seconds using an Integrated Design Tools, Inc NX3-S4, 8MP high speed camera fitted with a $f = 135\ mm\ F1.4$ Kowa lens.

4.2.2 LDA ANALYSIS METHODOLOGY AND ACCURACY.

Characterisation of the rotors outlet was performed on a grid of sample points concentrically spaced around the rotor axle, with azimuthal and radial resolutions of 15^o and $0.05R$ respectively. Each of the 433 data points was sampled over a period of 10 seconds with data burst rates maintained above 200 counts per second. The approximate accuracy of the mean flow velocity was calculated as being $0.02ms^{-1}$ which corresponds to 0.2%% of the peak rotor induced velocity. In descent 177 and 121 data points were sampled for $30s$ along the vertical and horizontal axes of symmetry of the rotor with spatial resolutions of $0.0198R$ and $0.0186R$, respectively. Optical access prevented data from being acquired at displacements of $\frac{y}{R} < -1.0$ whilst the reflection of the lasers off the sting prevented the horizontal and vertical traverses from being identical lengths. The mounts which the probe was mounted onto allowed the probe to be aligned perpendicular to the wind tunnel flow (90 ± 0.5^o), whilst the traverse was aligned parallel to the wind tunnel flow $\pm 0.5^o$.

4.2.3 PIV ANALYSIS METHODOLOGY AND ACCURACY.

Post processing of the raw PIV images was completed using the commercially available software *Davis* V8.2. The results presented in this chapter were all produced using a multi-pass cross correlation algorithm with interrogation windows of 48 x 48 pixels with a 50% overlap followed by an interrogation window of 24 x 24 pixels with a 50% overlap. The resolution of the PIV was equivalent to approximately $0.0009R$ x $0.001R/pixel$, which was sufficient to determine small features of the flow field, such as the blade tip vortices. The uncertainty of the velocity measurements was calculated to be $\varepsilon_u = \frac{0.1}{M\Delta t} = \pm 0.08ms^{-1}$ using an optical magnification factor of $M = 6.19pixel/mm$ and a maximum displacement error of $0.1pixels$ (Raffel et al., 2007) A maximum displacement error of $0.1pixels$ was used to calculate the velocity error because the software incorporates sub pixel interpolation of $0.1pixels$. The unsteadiness of the flow field was assessed by calculating the root mean square (RMS) of the fluctuations of the measured axial velocity about the mean axial velocity.

Operational Parameter	Rotor	Savas et al. (2009)
Rotor Diameter (m)	0.336	0.254
Rotor Chord (m)	0.033	0.019
Blade Geometry	untapered, untwisted	untapered, 5^o linear twist
Rotor (Hz)	66.7	4
V_{tip} (ms^{-1})	70	3.192
Chord (m)	0.034	0.019
Reynolds Number At Blade Tip	168,526	60,648
Number Of Rotor Blades	2	3
U_i (ms^{-1})	4.6	0.221
C_T	0.0086	0.01
Root Cut Out (m)	0.106 (31.5%)	0.032 (12.5%)
Solidity σ	0.0135	4
Collective Angle $(^o)$	9^o	11.6^o
Medium	Air	Water

TABLE 4.1: Table of experimental rotor parameters and operational conditions comparing the current study to the experimental investigation performed by Savas et al. (2009).

4.3 RESULTS.

4.3.1 CHARACTERISATION OF THE FLOW FIELD PRODUCED BY A HOVERING ROTOR WITH A LARGE ROOT CUT OUT.

The structure of the flow field produced by the rotor was characterised using LDA and PIV. This was deemed necessary in order to allow estimates of the averaged induced velocity across the rotor disk plane to be calculated. The averaged induced velocity (U_i) was used to scale the descent velocity of the rotor (U_o).

MEAN FLOW ANALYSIS.

LDA RESULTS.

The mean axial velocity component (u) in a cross stream plane $0.48R$ upstream *(with respect to the wind tunnel flow direction)* of the rotor disk plane is shown in figure 4.4. Based on the axial velocity profile, the notional induced velocity $(U_i = 4.6ms^{-1})$ of the rotor was calculated using equation 4.1. The notional induced velocity was used to scale the descent velocity of the rotor $(\alpha = U_o/U_i)$. LDA velocity profiles along the vertical (y) and horizontal (z) axes of symmetry of the rotor extracted from figure 4.4 are presented in figure 4.5a. The radial and tangential velocity distributions are presented in figures 4.5b and 4.5c, respectively. The results show that the mean axial induced velocity profile produced by the rotor can be characterised as a region of low velocity air surrounded by a ring of high velocity air. The extracted velocity profile presented in figure 4.5 shows that, on a plane of investigation, the axial velocity component of the rotor wake is uniform for $|r/R| \leq 0.25$. This is a result of the coalescence of the rotor wake towards the centre of the rotor, shown in figure 4.5b.

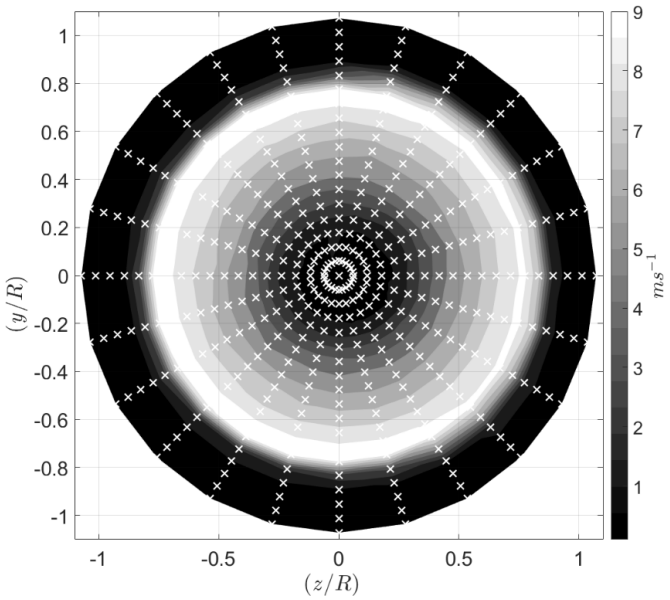

FIGURE 4.4: Averaged axial velocity component (u) produced by the rotor operating in hover. This figure was produced using LDA and each sample point location is displayed by a white cross.

Figure 4.5c shows that peaks in the tangential velocity component of $(v/U_i = \pm 0.7)$ occurred at a radial ordinate of $y/R = \pm 0.25$. Between the peaks $-0.25 \leq y/R \leq 0.25$ the tangential velocity component is linear. It should be noted that, as expected, the axial velocity component is significantly larger than the radial or tangential velocity components of the rotor wake.

The axial and radial velocity profiles presented in figure 4.5 were compared to those produced by a more conventional rotor, which was previously investigated by Savas et al. (2009). In their investigation, two component PIV measurements of the flow field produced by a three bladed, $0.254m$ diameter, untapered rotor with 5^o of linear twist operating in descent, were obtained. The rotor was operated at a low rotational frequency $(7Hz)$ in the University of California, Berkeley deep towing tank. A summary of the main features of the two separate investigations is presented in table 4.1. It should be noted that the rotor was also used by Stack et al. (2005) to visualise the development of the blade tip vortices when it was operating in the VRS. Despite the differences in rotor geometry and the operating conditions reported in table 4.1, the two rotors produced mean axial and radial velocity profiles, presented in figure 4.5, which were notionally similar. It was not possible to extract tangential velocity components from the PIV results. The negative induced velocity at the core of the more conventional rotor, observed in figure 4.5a, is believed to a be a result of the rotor mounting system which produced a blockage, located at the rotor core on the rotor inlet plane. The differences in the induced velocity profile outboard of the low velocity core, are a result of the difference in twist between the two rotors and the

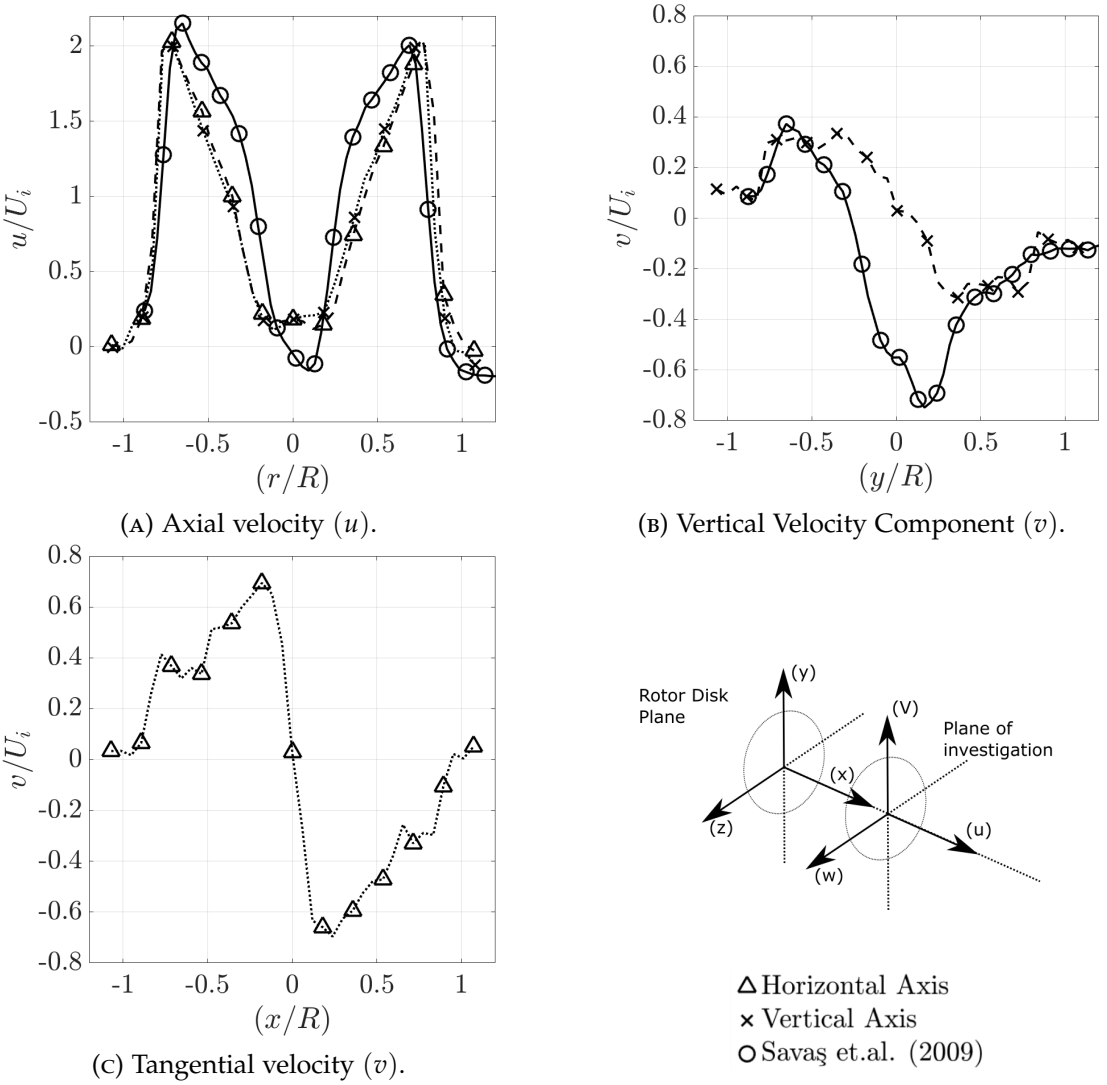

(A) Axial velocity (u).

(B) Vertical Velocity Component (v).

(C) Tangential velocity (v).

FIGURE 4.5: LDA mean velocity profiles along the horizontal and vertical axis of symmetry of the rotor when operating in hover $(\alpha = 0.0)$. The axial and radial velocity profiles presented in figure 4.5a and figure 4.5b are compared with those of a more conventional rotor investigated using PIV by Savas et al. (2009). All of the data is scaled to the hover induced velocity (U_i) of each rotor.

variation of the blade root cut out.

$$U_i = \frac{\int_0^{1.0R} 2\pi urdr}{A_i} \tag{4.1}$$

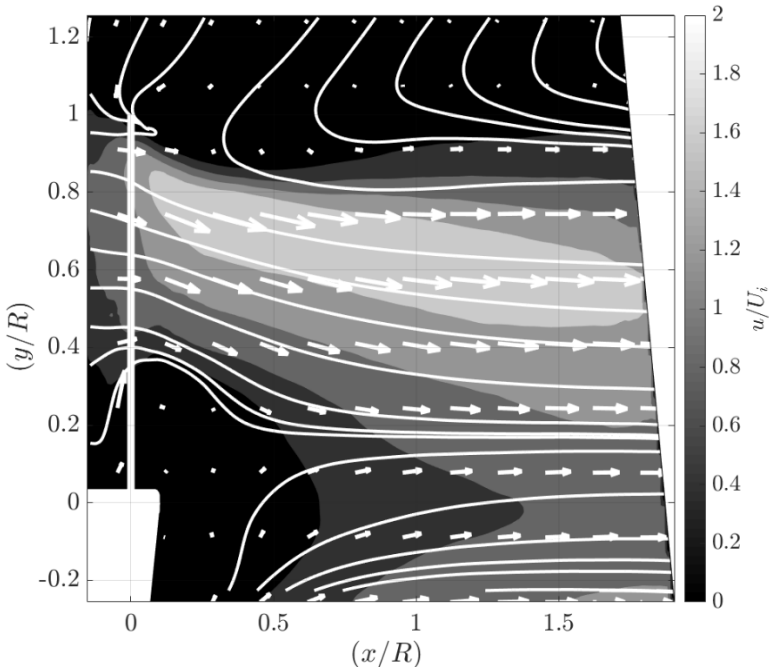

FIGURE 4.6: Mean axial velocity profile (u) produced by the rotor operating in hover. Note the velocity (u) is scaled with respect to the induced velocity U_i of the rotor.

PIV RESULTS.

The mean flow field produced by the rotor is shown in figure 4.6. Figure 4.6 shows that the mean axial velocity profile of the rotor wake can be represented as a region of low velocity flow surrounded by a ring of higher velocity air. As expected, the cylindrical rotor hub induced low velocity blade root region. The streamline patterns show that the low velocity region extends up to $0.5R$ from the rotor disk plane. At displacements greater than that $0.5R$, the streamlines show that the induced velocity of the rotor coalesces to form a stream tube which extends more than $1.8R$ from the rotor disk plane.

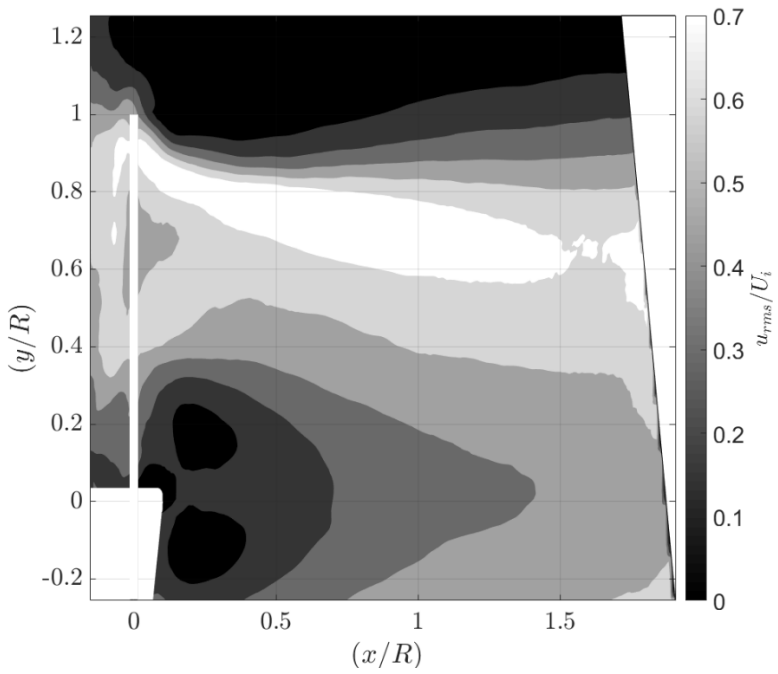

FIGURE 4.7: Root mean square of the axial velocity fluctuations (u_{rms}) produced by the custom rotor operating in hover. Note the velocity is scaled with respect to the induced velocity U_i of the rotor.

UNSTEADINESS OF THE FLOW FIELD.

The RMS of the axial velocity component (u_{rms}) of the flow field produced by the rotor is presented in figure 4.7. Figure 4.7 shows that there is a band of high velocity fluctuations inboard of the rotor blade tip, which extends away from the rotor disk plane. Analysis of individual PIV image pairs, such as the vorticity plot presented in figure 4.8, indicate that the region of high RMS is associated with the passage of the blade tip vortices along the edge of the wake stream tube. No clear blade root vortices could be observed in the flow field.

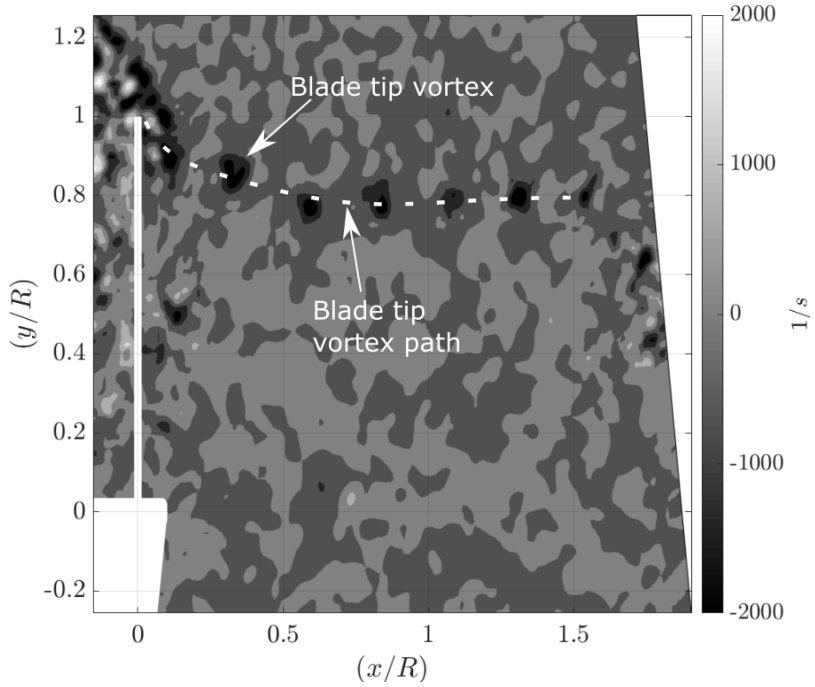

FIGURE 4.8: Instantaneous contour plots of the the third component of vorticity $[\frac{df_y}{dx} - \frac{df_x}{dy}]$ vorticity contained within the flow field produced by the rotor in hover. Note the existence of a system of blade tip vortices shed from the rotor blade tips.

4.3.2 EFFECT OF AXIAL DESCENT ON THE MEAN FLOW FIELD PRODUCED BY A ROTOR WITH A LARGE ROOT CUT OUT.

LDA RESULTS.

Figure 4.9 shows the development of the mean velocity profile produced by the rotor on a plane $0.48R$ from the rotor disk plane, as the velocity ratio was varied from $\alpha = 0.0$ to $\alpha = 2.5$. Once again, at low velocity ratios ($\alpha \leq 0.6$), the velocity components of the wake, close to the rotor, are similar to those produced by the hovering rotor. This indicates that, at low velocity ratios, the structure of the flow field produced by the rotor is unaffected by the introduction of a descent velocity. Increasing the descent velocity ratio from ($\alpha = 0.6$ to $\alpha = 0.8$) leads to the gradual reduction of the peak axial (figure 4.9a), radial (figure 4.9b) and tangential (figure 4.9c) velocity components of the rotor wake.

Increasing the descent velocity ratio to ($\alpha = 0.85$) results in the formation of a region of reverse flow in the centre of the rotor. This indicates that the wind tunnel free stream penetrates the plane of investigation in line with the centre of the rotor ($|y/R| \leq 0.3$). This is a modified manifestation of the conical region of reverse flow which penetrates up to the rotor disk plane previously identified by Brinson (1998) and Drees and Hendal (1950). In this region, the radial component of the wake reduces further. However strong radial velocity components form outboard of the region of reverse flow, as a result of the deflection of the rotor wake radially outboard. At higher velocity ratios, the percentage of the plane of investigation which experienced reverse axial flow increased until the rotor entered the windmill brake state. Smoke flow visualisation showed that this occurred at a velocity ratio of at $\alpha = 2.5$ (figure 4.10b). At this velocity ratio the entire rotor experiences reversed flow. It should be noted that, while the entire plane of investigation experience reversed flow at a velocity ratio of $\alpha = 2.0$, smoke flow visualisation of the flow field, presented in figure 4.10a revealed that the outboard sections of the rotor did not experience reversed flow until $\alpha = 2.5$. Instead, the rotor wake was deflected radially outboard in the space between the rotor disk plane and the plane of investigation. Singular smoke flow visualisation images are presented in figure 4.10 because no discernible differences in the flow field could be observed between sequential images like those presented in chapter 2 and 3.. As the descent velocity ratio increased from $\alpha = 0.85$ to $\alpha = 2.0$, the peaks in axial velocity, which surround the region of the rotor which experiences reversed flow, decreased in magnitude and broadened out as the velocity ratio increased. The radial ordinate of the peak axial velocity component also moved radially outboard.

Over a velocity range of $0.85 \leq \alpha < 2.0$, the velocity at the centre of the rotor ($y/R = 0$) remained constant at ($u/U_i = -0.6$). It is theorised that the cylindrical shape of the rotor hub is responsible for this. The deflection of the rotor wake, radially outward, results in the gradual increase in the radial velocity component outboard of the rotor ($y/R > 1.0$). Figure 4.9c shows that the tangential velocity component

of the rotor wake, reduced to zero across the rotor core ($|y/R| \geq 0.4$) at a velocity ratio of $\alpha = 0.4$. This is because at velocity ratios above $\alpha = 0.85$ this region of the plane of investigation is penetrated by the wind tunnel free stream. Further outboard ($0.4 \leq |z/R| \leq 1.0$) the swirl velocity component of the rotor wake can still be observed until $\alpha = 2.0$. This occurs because the outboard sections of the rotor blades still induce velocity even though the wind tunnel flow has penetrated the centre of the rotor. It is theorised that this is a result of the large root cut out which does not induce any significant flow in the centre of the rotor.

A comparison of the mean velocity profiles produced by the rotor and the data presented by Savas et al. (2009) on a plane $0.48R$ from the rotor disk plane is presented in figure 4.11. From figure 4.11 it is clear that, despite the differences in rotor geometry and the general topology of the flow field produced, the same trends in the mean axial velocity profiles of the two rotors can be observed. Analysis of figure 4.11 shows that, at velocity ratios below $\alpha < 0.9$ the mean axial velocity profile produced by the more conventional rotor, investigated by Savas et al. (2009) is similar to the induced velocity profile of the hovering rotor. At a velocity ratio of $\alpha = 0.9$ the mean axial velocity component of the more conventional rotor, investigated by Savas et al. (2009), is similar to the hover velocity profile of that rotor. At velocity ratios above $\alpha > 0.9$, the velocity profile of the rotor used by Savas et al. (2009) resembled that produced by the rotor used in this investigation at velocity ratios above $\alpha > 0.85$.

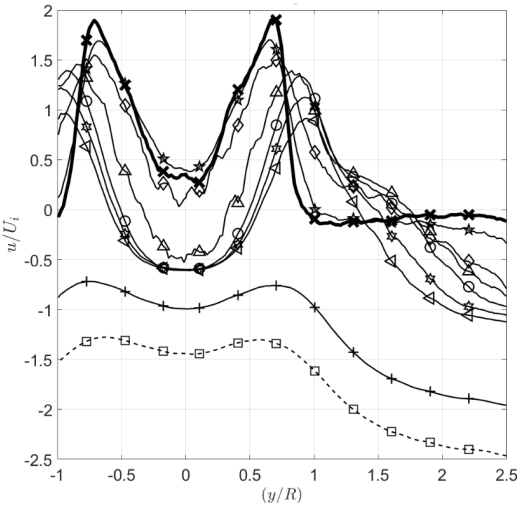

(A) Outlet axial velocity All (u).

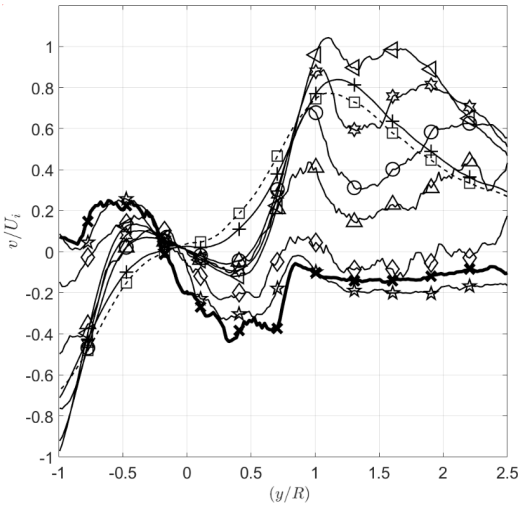

(B) Outlet Vertical velocity component (v).

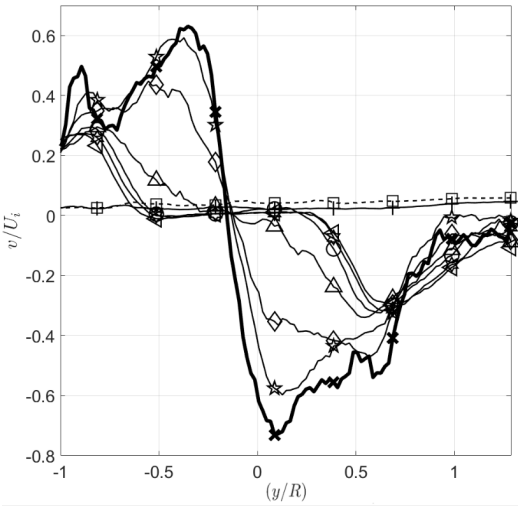

(C) Outlet Tangential velocity All (v).

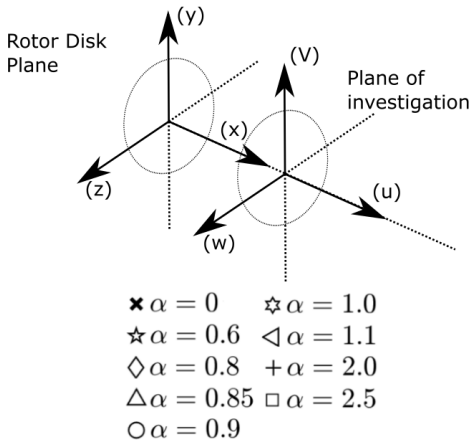

FIGURE 4.9: LDA mean velocity profiles along the vertical axis of symmetry of the rotor, $(\frac{x}{R} = 0.48)$ from the rotor disk plane. Axial (u), radial (v) and tangential velocity profiles are presented in figure 4.9a, figure 4.9b and figure 4.9c respectively. All data is scaled with respect to the notional induced velocity of the rotor (U_i).

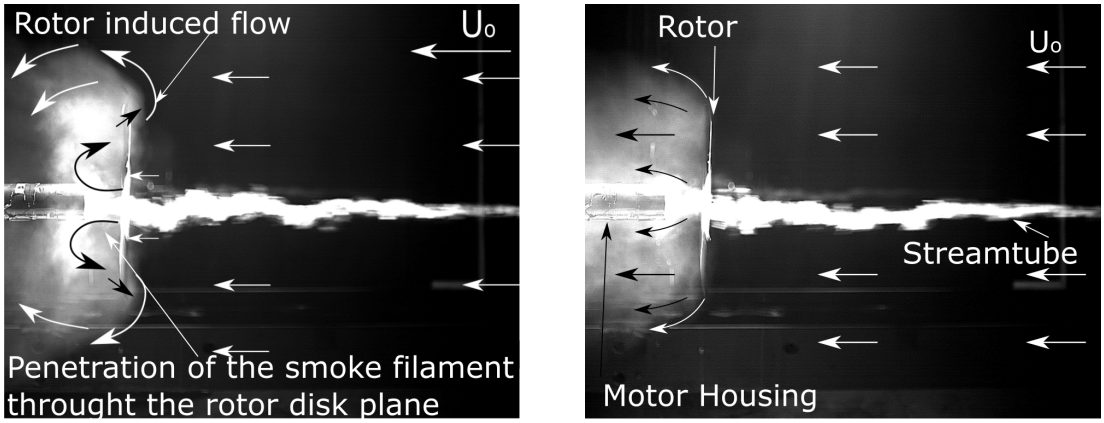

(A) $\alpha = 2.0$. (B) $\alpha = 2.5$.

FIGURE 4.10: Smoke flow visualisation image of the flow field produced by the rotor operating at a descent velocity ratio of (a) $\alpha = 2.0$, (b) $(\alpha = 2.5)$

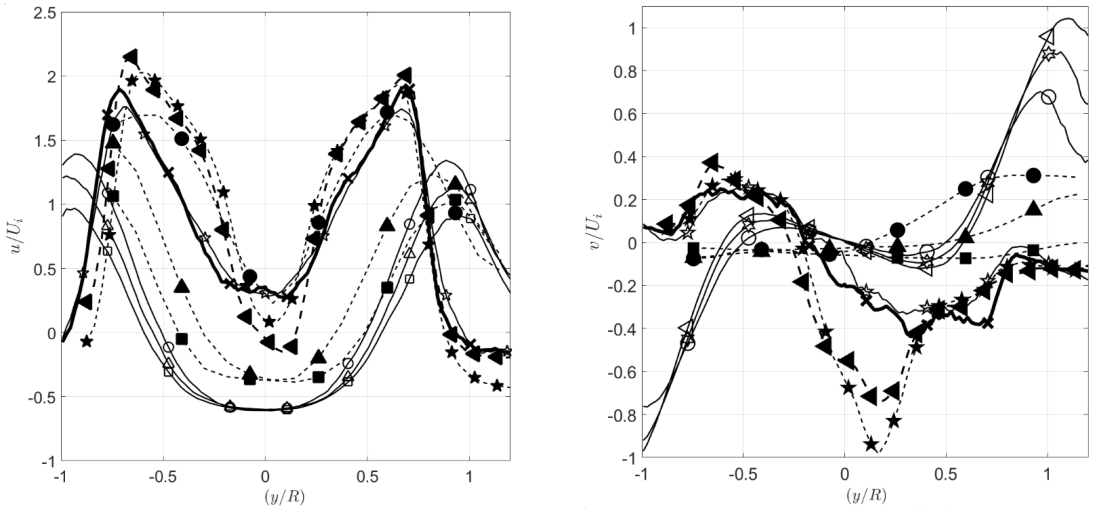

(A) Outlet axial velocity (u). (B) Outlet Vertical velocity component (v).

$\times\ \alpha = 0$ $\star\ \alpha = 0.5$ $\circ\ \alpha = 0.9$ $\triangle\ \alpha = 1.0$ $\square\ \alpha = 1.1$

Savaş et. al. $\blacktriangleleft\ \alpha = 0.0$ $\bigstar\ \alpha = 0.45$ $\bullet\ \alpha = 0.9$ $\blacktriangle\ \alpha = 1.0$ $\blacksquare\ \alpha = 1.1$

FIGURE 4.11: LDA mean velocity profiles along the vertical axis of symmetry of the rotor, $(\frac{x}{R} = 0.48)$ from the rotor disk plane. The axial (u) and radial (v) velocity profiles presented in figure 4.11a and figure 4.11b are compared with those of a more conventianal rotor investigated using PIV by Savas et al. (2009) (shown in black). All of the data is scaled to the hover induced velocity (U_i) of each individual rotor.

PIV RESULTS.

Figure 4.12 shows the development of the mean flow field produced by the rotor as the descent velocity ratio was increased from $\alpha = 0.0$ to $\alpha = 2.0$. The results show that, at low descent velocity ratios, the near field, once again, resembled the flow field produced by the rotor when it is operating in hover. The rotor wake extends more than $1.8R$ from the rotor disk plane in a coherent streamtube. Analysis of figure 4.12 shows that, at a velocity ratio of $\alpha = 0.7$, a noticeable change in flow topology occurred. The wind tunnel free stream penetrated up through the centre of the rotor disk plane whilst the rotor wake was deflected radially outboard. At higher descent velocity ratios the extent the rotor wake extended upstream, away from the rotor disk plane without being radially deflected outboard, decreased from $x/R = 1.1$ at $\alpha = 0.7$ to $x/R = 0.3$ at $\alpha = 1.6$.

More conventional rotors, which have been investigated, identified the formation of a saddle point on the geometric centreline of the rotor. The saddle point moved towards the rotor disk plane as the descent velocity ratio increased (Green et al. (2005), Savas et al. (2009)). The inability of the rotor to induce flow in the centre of the rotor, as a result of the large root cut out, is believed to be responsible for the variation of the structure of the flow field. Smoke flow visualisation showed that, at low descent velocity ratios, the interaction between the rotor wake and the wind tunnel free stream occurred outside of the region of interest (figure 4.16d). At the interaction, a saddle point forms on the geometric centre line of the rotor. At velocity ratios above $\alpha = 0.7$ the saddle point could no longer be observed in the sequential smoke flow visualisation results or the PIV results presented in figure 4.17 and figure 4.12, respectively.

Mean centreline velocity profiles produced by the rotor over a range of α values are presented in figure 4.13. In hover, the wake from the rotor accelerated as the distance from the rotor disk plane increased. This is a result of the conservation of momentum of the rotor wake and the contraction of the rotor wake. At low α values $(0.0 < \alpha \leq 0.6)$ the velocity profile of the rotor showed an increase in the acceleration of the rotor wake and in the magnitude of the axial velocity component of the rotor wake on the rotor centreline as a result of the recirculation that forms downstream of the rotor. Once the wind tunnel free stream flow penetrated up to the rotor disk plane, the mean axial velocity component became negative $(-u)$. Increasing the velocity ratio from $\alpha = 0.7$ to $\alpha = 1.0$ did not affect the velocity profile on the rotor centreline. Further increases in α increased the rate of deceleration of the wind tunnel free stream as it approached the rotor disk plane.

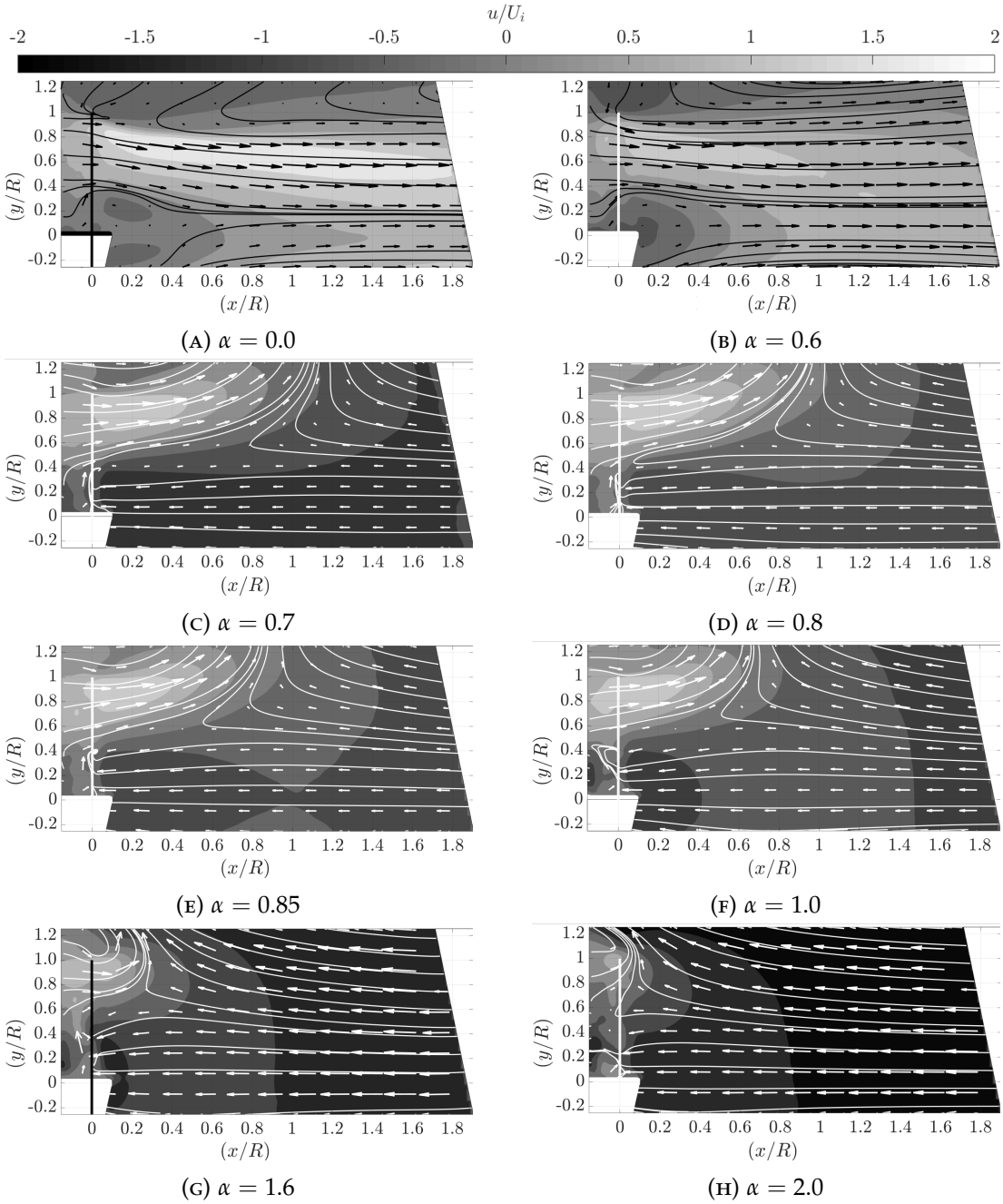

(A) $\alpha = 0.0$ (B) $\alpha = 0.6$

(C) $\alpha = 0.7$ (D) $\alpha = 0.8$

(E) $\alpha = 0.85$ (F) $\alpha = 1.0$

(G) $\alpha = 1.6$ (H) $\alpha = 2.0$

FIGURE 4.12: Averaged mean axial velocity contour plots of the rotor (PIV:Region 1) as counter flow velocity $|U_o|$ increases. Streamlines and a reduced number of velocity vectors are superimposed onto the contour plots. All of the velocity vectors are scaled with respect to the rotors induced velocity, U_i. Note no saddle point can be observed in figure 4.12.

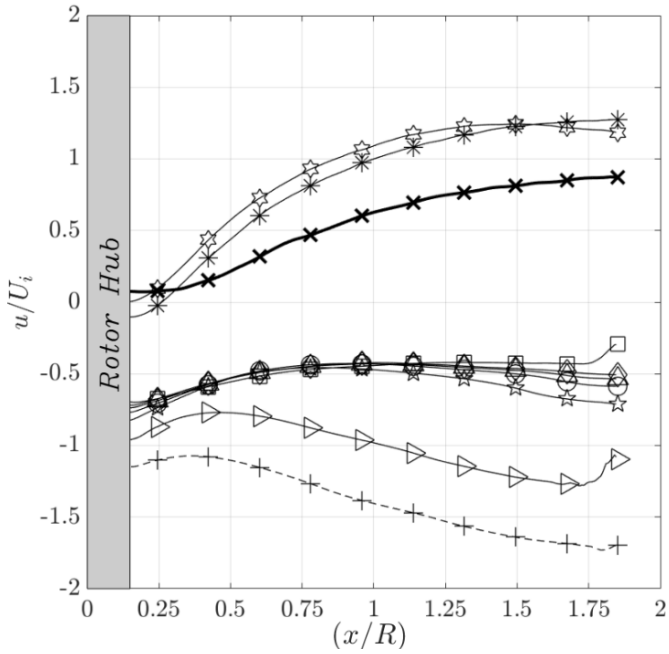

FIGURE 4.13: Mean axial velocity profile (u) produced on the centreline axis of the custom rotor operating between $\alpha = 0.0$ and $\alpha = 2.4$.

4.3.3 EFFECT OF COUNTERFLOW VELOCITY ON THE UNSTEADINESS OF THE FLOW FIELD PRODUCED BY THE ROTOR OPERATING IN AXIAL DESCENT.

PIV RESULTS.

Figure 4.15 shows contour plots of the RMS of the fluctuations of the local axial velocity about the local mean for the rotor. The RMS of the fluctuations is scaled with respect to the notional induced velocity (U_i) of the rotor. In hover, the highest RMS values are concentrated in a single track which extends from the rotor tips. The location of the highest RMS values coincide with the passage of the blade tip vortices. As the descent velocity ratio increased from $\alpha = 0.0$ to $\alpha = 0.6$ the track became broader and more diffuse. At higher velocity ratios the unsteadiness of the flow field was confined to the region of the flow field associated with the deflected rotor wake. Analysis of individual PIV image pairs, such as the vorticity plot presented in figure 4.14a, showed that the region of high RMS is associated with the passage of the blade tip vortices. The region of interest used in this investigation prevented the fate of the blade tip vortices from being determined. Analysis of individual PIV images of the flow field produced by a more conventional rotor, presented in figure 4.14b, showed that the blade tip vortices coalesce around the rotor disk (Savas et al., 2009). Further analysis of the flow field produced by the rotor, around the rotor blade tips showed that the blade tip vortices were transported around the recirculation before vortex pairing occurs.

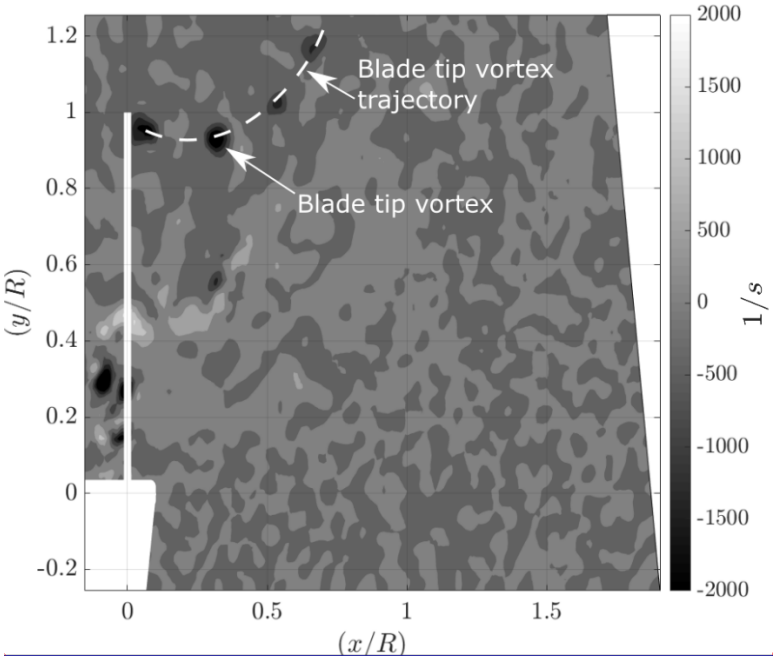

(A) $\alpha = 0.8$

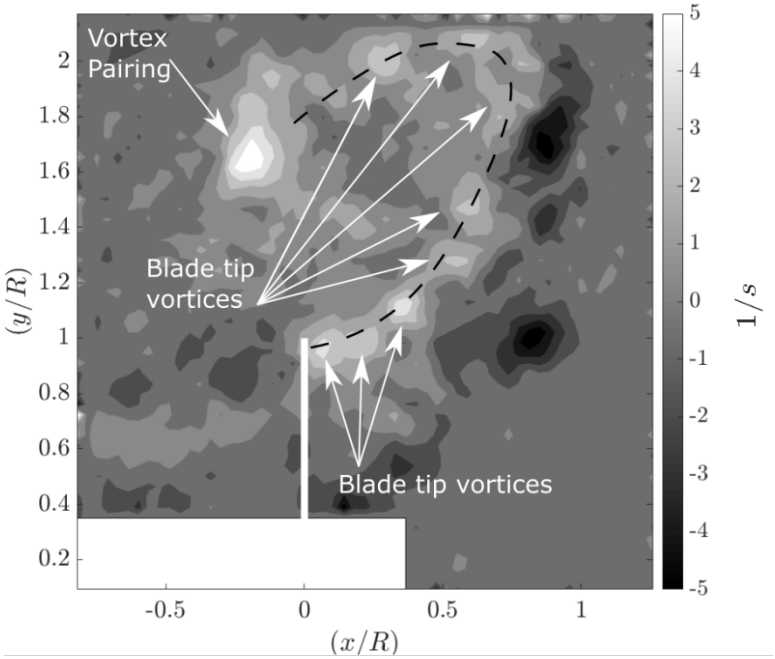

(B) Individual vorticity snapshot of the flow field produced by a rotor operating as a velocity ratio of $\alpha = 1.0$ extracted from data obtained by Savas et al. (2009).

FIGURE 4.14: Instantaneous contour plots of the the third component of vorticity $[\frac{df_y}{dx} - \frac{df_x}{dy}]$vorticity $(\frac{df_y}{dx} - \frac{df_x}{dy})$ contained within the flow field produced by the rotor operating at a descent velocity ratio of $\alpha = 0.6$, (figure 4.14a) and the flow field produced by a rotor previously investigated by Savas et al. (2009) (figure 4.14b). It should be noted that the rotors investigated were different sizes, rotating in operate directions and were operating at significantly different rotational speeds.

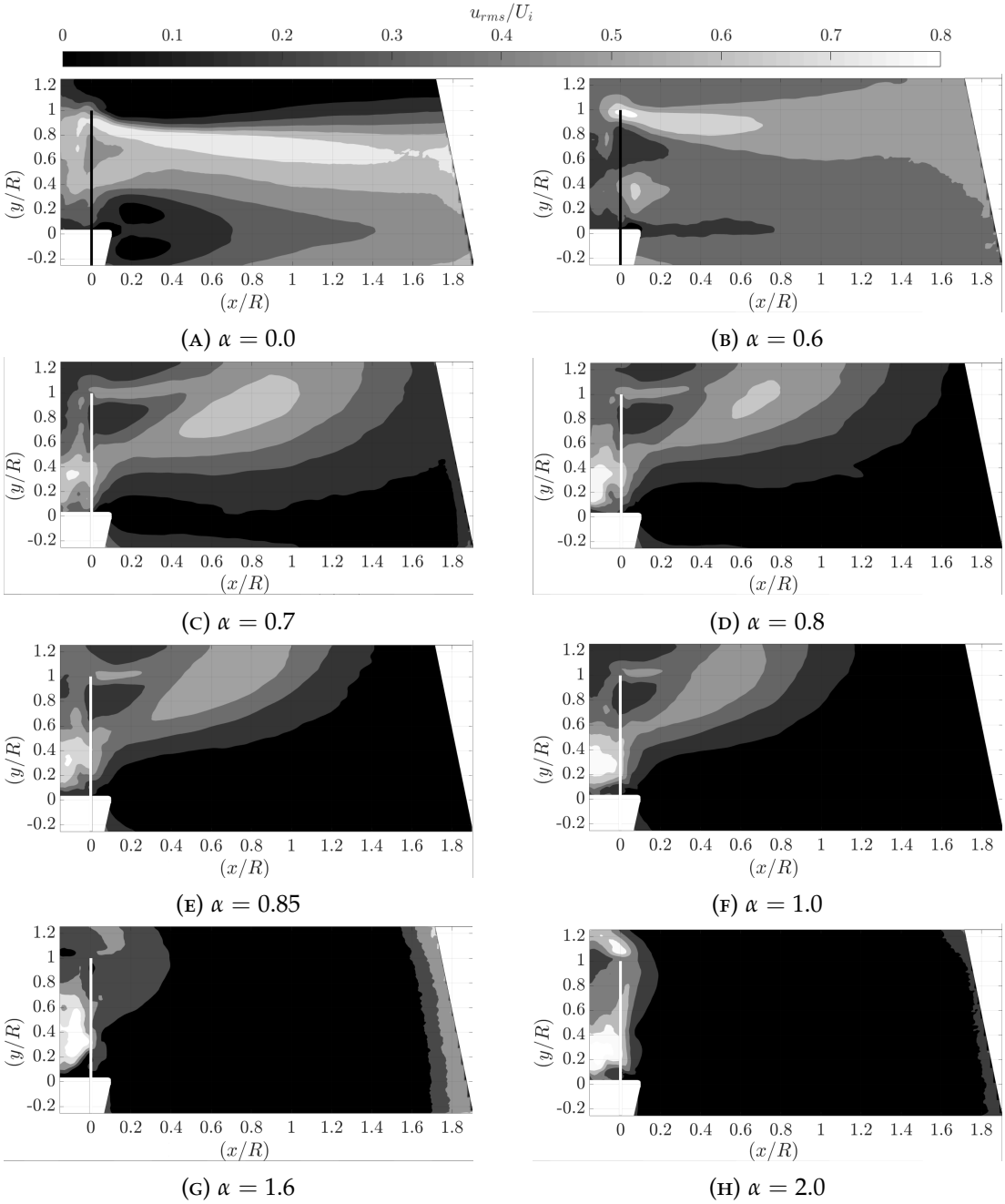

(A) $\alpha = 0.0$ (B) $\alpha = 0.6$

(C) $\alpha = 0.7$ (D) $\alpha = 0.8$

(E) $\alpha = 0.85$ (F) $\alpha = 1.0$

(G) $\alpha = 1.6$ (H) $\alpha = 2.0$

FIGURE 4.15: u_{rms} contour plots of the rotor (PIV:Region 1) as the descent velocity ratio increased from $\alpha = 0.0$ to $\alpha = 2.0$.

4.3.4 DISCUSSION.

Analysis of PIV measurements and sequential smoke flow visualisations revealed that the flow, in the region of interest, did not differ considerably from the mean flow field presented in figure 4.12. This observation contradicts the findings of Green et al. (2005) which identified a range of descent velocity ratios where the flow intermittently switched between the topology associated with a hovering rotor and the topology associated with the VRS. The analysis of smoke flow visualisation recordings and the proper orthogonal decomposition of sequential PIV images was performed in order to provide insight into this variation of the flow field.

SMOKE FLOW VISUALISATION.

Sequential images produced from the smoke flow visualisation recordings showing the dynamics of the flow field produced by the rotor operating at a velocity ratio of $\alpha = 0.7$, $\alpha = 0.9$ and 1.1 are shown in figures 4.16, 4.17 and 4.18, respectively. Figure 4.16 shows that, at a descent velocity ratio of $\alpha = 0.7$, the rotor wake extends more than $3R$ from the rotor disk plane. At the interaction between the rotor wake and the wind tunnel free stream flow, a stagnation point forms on the geometric centreline of the rotor. The entrainment of the smoke filament into the large scale recirculation that forms outboard of the rotor can be seen in figure 4.16b, 4.16c and 4.16f. The recirculation aperiodically sheds into the free stream flow.

At higher velocity ratios, the smoke filament penetrates through the rotor disk plane, as shown in figure 4.17. This is supported by the LDA and PIV data presented earlier. Upon penetrating the rotor disk plane the smoke filament is drawn back through the outboard sections of the rotor which are still inducing some flow. As expected, the deflection of the rotor wake outboard results in the formation of a large region of recirculation about the rotor blade tips. The recirculation grows until it sheds away from the rotor into the free stream flow. The growth, and subsequent shedding of the recirculation, results in the variation of the depth the rotor wake penetrates into the free stream flow. Analysis of figure 4.18 shows that as the descent velocity ratio increased the portion of the rotor which drew the penetrating smoke filament back through the rotor moved outboard.

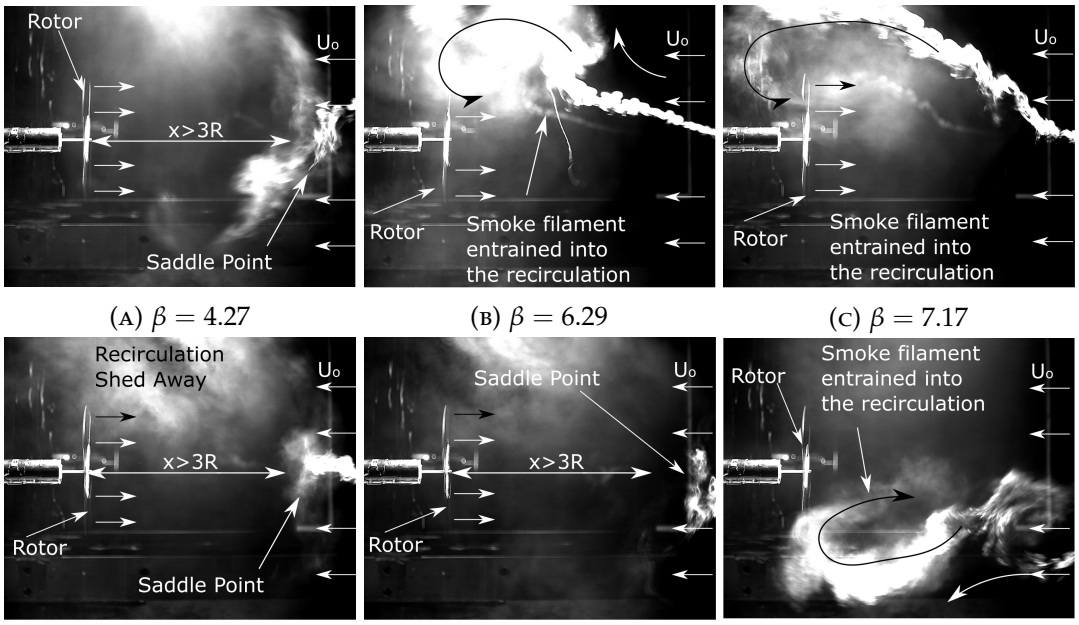

(A) $\beta = 4.27$ (B) $\beta = 6.29$ (C) $\beta = 7.17$

(D) $\beta = 8.36$ (E) $\beta = 8.74$ (F) $\beta = 10.18$

FIGURE 4.16: Sequential smoke flow visualisation images of an expulsion event observed when $\alpha = 0.7$ where $\beta = \frac{t|U_o|}{D}$. Beta is a non-dimensional parameter used to define the separation of sequential images in terms of the time it takes the free-stream flow to travel a distance equal to the rotor diameter (D).

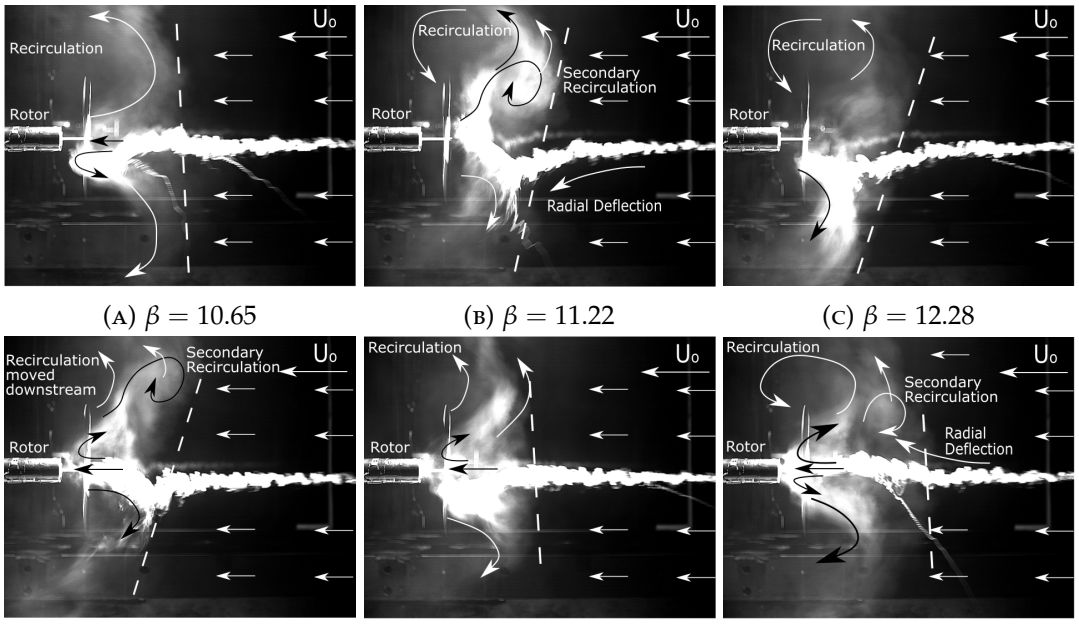

(A) $\beta = 10.65$ (B) $\beta = 11.22$ (C) $\beta = 12.28$

(D) $\beta = 13.74$ (E) $\beta = 14.15$ (F) $\beta = 14.96$

FIGURE 4.17: Sequential smoke flow visualisation images of an expulsion event observed when $\alpha = 0.9$ where $\beta = \frac{t|U_o|}{D}$. Beta is a non-dimensional parameter used to define the separation of sequential images in terms of the time it takes the free-stream flow to travel a distance equal to the rotor diameter (D).

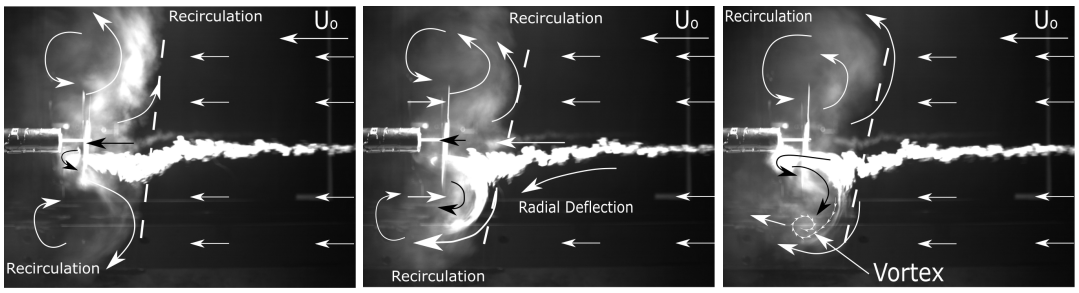

(A) $\beta = 0.89$ (B) $\beta = 1.39$ (C) $\beta = 1.69$

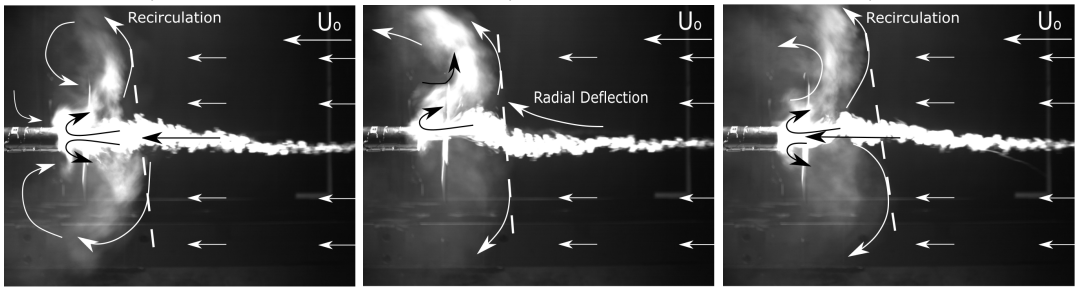

(D) $\beta = 3.48$ (E) $\beta = 4.17$ (F) $\beta = 4.97$

FIGURE 4.18: Sequential smoke flow visualisation images of an expulsion event observed when $\alpha = 1.1$ where $\beta = \frac{t|U_o|}{D}$. Beta is a non-dimensional parameter used to define the separation of sequential images in terms of the time it takes the free-stream flow to travel a distance equal to the rotor diameter (D).

POD ANALYSIS.

Visualisations of the first two eigenmodes produced by applying snapshot energy based POD to the PIV results of the hovering rotor are shown in figure 4.19. The first two POD modes, shown in figure 4.19a and figure 4.19b, indicate that the most probable and energetic representations of the flow field are dominated by the blade tip vortices. Analysis of the reconstructed flow field, shown in figure 4.19c and figure 4.19e, show that, in hover, the point of coalescence of the rotor wake varied as a result of the first POD mode.

The first two eigenmodes of the flow field produced by the rotor when it is operating at low descent velocity ratios $(0.0 < \alpha \leq 0.6)$, differ considerably from the POD modes of the hovering rotor shown in figure 4.19. The first two POD eigenmodes of the flow field produced by the rotor operating at a descent velocity ratio of $\alpha = 0.6$ are shown in figure 4.20. The first two modes, shown in figures 4.20a and 4.20b show that the first POD mode is responsible for the radial movement of air across the rotor disk plane and the passage of the blade tip vortices. Reconstructions of the flow field, presented in figure 4.20c and 4.20e, indicate that the first POD mode manifests itself as the radial flapping of the rotor wake. Spectral analysis of the reconstruction coefficients showed that this occurred at a frequency of $0.7Hz$. The second POD mode also contributes to the radial flapping of the rotor wake, however it is clear from figure 4.20 that the contribution of the second POD mode is lower than the contribution of the first POD mode. It should be noted that the influence of the blade tip vortices on

the structure of the flow field can be observed in higher POD modes.

When the descent velocity ratio was greater than $\alpha \geq 0.7$, POD analysis revealed that once the wind tunnel free stream penetrated the rotor disk plane, the unsteadiness of the flow field was confined to a region of the flow field associated with the radial deflection of the rotor wake (figure 4.21a and figure 4.21b). Analysis of the reconstructed flow fields, presented in figure 4.21c and 4.21e, showed that the first POD mode is associated with the shedding of the recirculation which forms around the rotor blade tips. This manifests itself as the variation of the penetration of the rotor wake into the wind tunnel free stream shown in figure 4.21c and figure 4.21e.

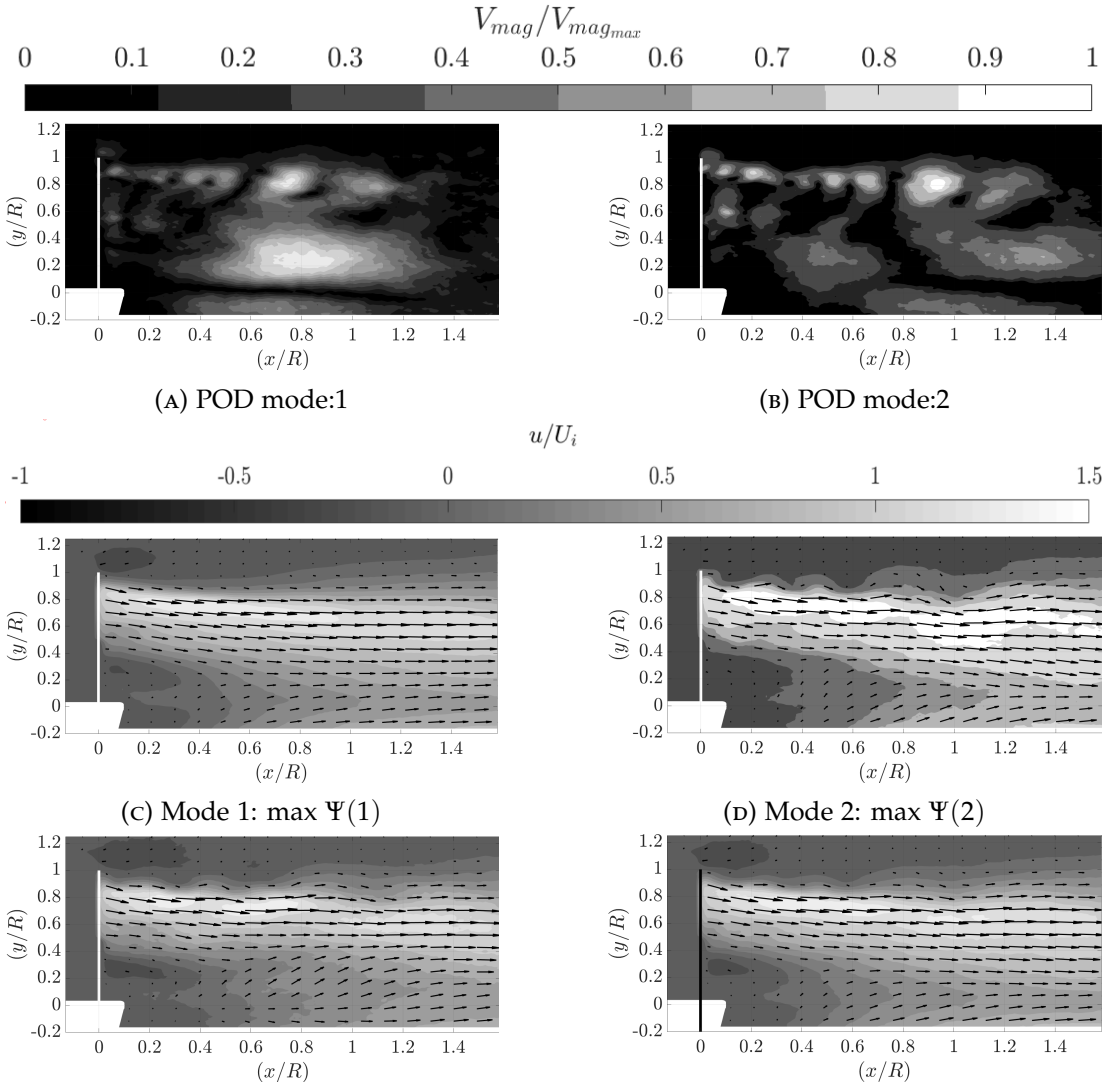

(A) POD mode:1

(B) POD mode:2

(C) Mode 1: max $\Psi(1)$

(D) Mode 2: max $\Psi(2)$

(E) Mode 1: min $\Psi(1)$

(F) Mode 2: min $\Psi(2)$

FIGURE 4.19: Visualisation of the first two POD eigenmodes of the velocity fluctuations produced by the hovering rotor $\alpha = 0.0$ are presented in figure 4.19a and figure 4.19b. The modes were calculated from a sequence of 600 instantaneous velocity fields. The vector lengths are scaled with respect to the maximum vector length of each individual mode. Reconstructed simulations of the velocity fields produced by the subtraction of the maximum (C, E) and minimal (D, F) reconstruction coefficient representations of the first two POD modes from the mean flow field are presented.

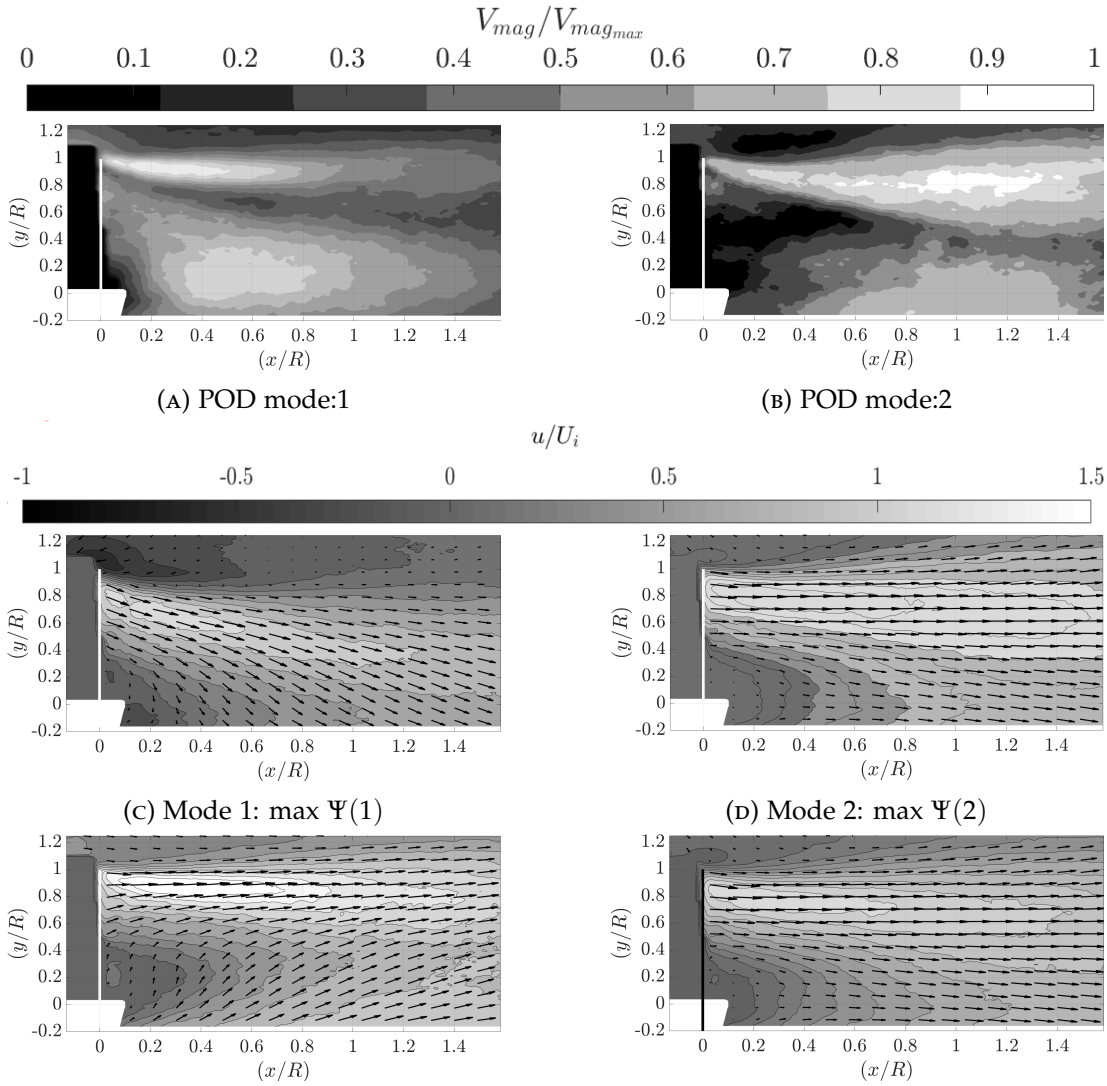

(A) POD mode:1

(B) POD mode:2

(C) Mode 1: max $\Psi(1)$

(D) Mode 2: max $\Psi(2)$

(E) Mode 1: min $\Psi(1)$

(F) Mode 2: min $\Psi(2)$

FIGURE 4.20: Visualisation of the first two POD eigenmodes of the velocity fluctuations produced by the hovering rotor $\alpha = 0.6$ are presented in figure 4.21a and figure 4.21b. The modes were calculated from a sequence of 600 instantaneous velocity fields. The vector lengths are scaled with respect to the maximum vector length of each individual mode. Reconstructed simulations of the velocity fields produced by the subtraction of the maximum (C, E) and minimal (D, F) reconstruction coefficient representations of the first two POD modes from the mean flow field are presented.

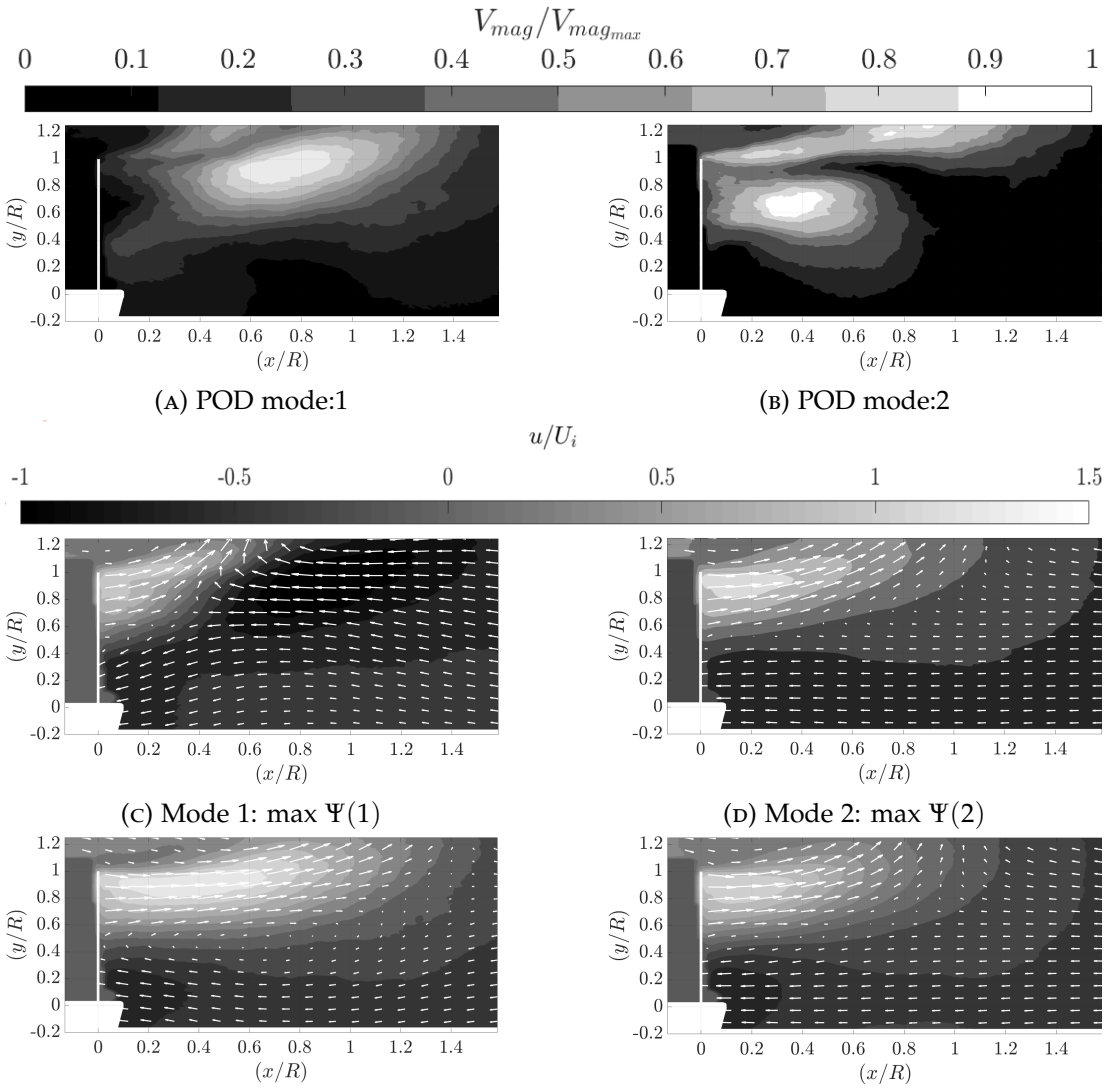

(A) POD mode:1

(B) POD mode:2

(C) Mode 1: max $\Psi(1)$

(D) Mode 2: max $\Psi(2)$

(E) Mode 1: min $\Psi(1)$

(F) Mode 2: min $\Psi(2)$

FIGURE 4.21: Visualisation of the first two POD eigenmodes of the velocity fluctuations produced by the hovering rotor $\alpha = 0.8$ are presented in figure 4.21a and figure 4.21b. The modes were calculated from a sequence of 600 instantaneous velocity fields. The vector lengths are scaled with respect to the maximum vector length of each individual mode. Reconstructed simulations of the velocity fields produced by the subtraction of the maximum (C, E) and minimal (D, F) reconstruction coefficient representations of the first two POD modes from the mean flow field are presented.

4.4 CONCLUSION

An investigation into the structure of the flow field produced by a rotor with a large root cut out (31.5%) operating in hover and axial descent has been performed using particle image velocimetry, laser doppler anemometry and smoke flow visualisation. The rotor was designed to produce a velocity profile which was notionally similar to the velocity profile produced by the ventilated open core annular jet investigated in chapter 3. The flow field produced by the rotor was compared with the flow field produced by a more conventional rotor, with a smaller blade root cut out (12.5%), previously investigated by Savas et al. (2009).

The results show that blade root cut out significantly affects the structure and the dynamics of the flow field produced by a rotor when it is operating in the vortex ring state. The breakdown of the cylindrical wake of the rotor into the toroidal recirculation associated with the vortex ring state of rotors occurs over a narrower range of descent velocity ratios. Previous investigations, using rotors with smaller root cut outs, have identified the formation of a saddle point on the geometric centre line of the rotor Green et al. (2005). The saddle point forms at the interaction between the rotor wake and the free stream. However, PIV revealed that no saddle point forms on the geometric centreline of the rotor if the rotor has a large root cut out.

The mutual inductance instability of helical vortices has previously been associated with the formation of a hairpin vortex however the results presented in this chapter indicate that the structure of the flow field may be dependent on the interaction of the low velocity flow induced by the inner portion of the rotor and the free stream flow.

CHAPTER 5

THE NATURE OF THE VORTEX RING STATE.

Having investigated the VRS of a shrouded rotor (Chapter: 2), an isolated rotor (Chapter: 2), a ventilated open core annular jet (Chapter: 3) and a rotor with a large root cut out (Chapter:4) in the previous chapters, the aim of this chapter is to elucidate what these investigations imply about development of the VRS. The results presented in each of the previous chapters are compared allowing the role of the blade tip vortices, on the development of the VRS to be explored.

5.1 DISCUSSION.

5.1.1 OPERATING AT A COUNTER FLOW/DESCENT VELOCITY RATIO OF $\alpha = 0.0$.

Figure 5.1 shows the mean flow field produced by the four experimental configurations investigated in this thesis when operating at a descent/counter flow velocity ratio of $\alpha = 0.0$. The mean flow fields produced by the isolated rotor (figure 5.1a), the shrouded rotor (figure 5.1c) and the ventilated open core annular jet (figure 5.1d) have a low velocity core surrounded by a ring of high velocity flow. Close to the rotor disk plane, the rotor with a large root cut out (figure 5.1b), induces low velocity in the core. Higher velocity flow is induced by the outer portions of the rotor blade. After the coalescence of the induced flow into a streamtube. Further downstream the flow field produced by the rotor resembles the velocity profile of the wake produced by the other three investigations, with a region of low velocity air surrounded by a ring of high velocity flow. The velocity components of the wake produced by each of the experimental configurations are compared in figure 5.2. From figure 5.2a it is clear that, at a velocity ratio of $\alpha = 0.0$, the mean axial velocity profile produced by all four experimental configurations are notionally similar. The rotors all produce wakes with significant swirl, as shown by the tangential velocity profiles presented in figure 5.2c.

In contrast, the wake from the ventilated OCAJ contains negligible amount of swirl. Analysis of figure 5.2b shows that the wake produced by the rotor with a large root cut out is the only one that contains a significant radial velocity component. Chapter 4 showed that this occurred as a result of the large root cut out which prevented flow from being induced in the centre of the rotor.

Whilst the average flow fields are comparable, instantaneous vorticity plots of the flow fields produced, presented in figure 5.3, indicate that the structure of the flow fields produced in the experiments differ considerably. The wake produced by the unshrouded rotor (Chapter: 2) and the rotor with the large root cut out (Chapter: 4) both consist of a system of helical vortices trailed from the rotor blades, whilst the wake from the ventilated OCAJ consists of a jet shear layer and flow which is entrained through the nozzle by the pressure difference that forms between the nozzle inlet and outlet planes. As described in chapter 2, the wake from the shrouded rotor did not contain any clearly defined vortical structures. It is proposed that a helical vortex structure may be present inside the shroud, which may have broken down by the time the wake passes through the shroud outlet plane, however further experiments would be required to determine if this hypothesis is correct. Despite this variation the unsteadiness of the flow field produced by all four experimental configurations is confined to the edge of the streamtube which extend away from the rotor disk plane, the nozzle outlet plane and the shroud outlet plane. Analysis of figure 5.4 shows that the magnitude of the unsteadiness is similar for all experimental configurations investigated.

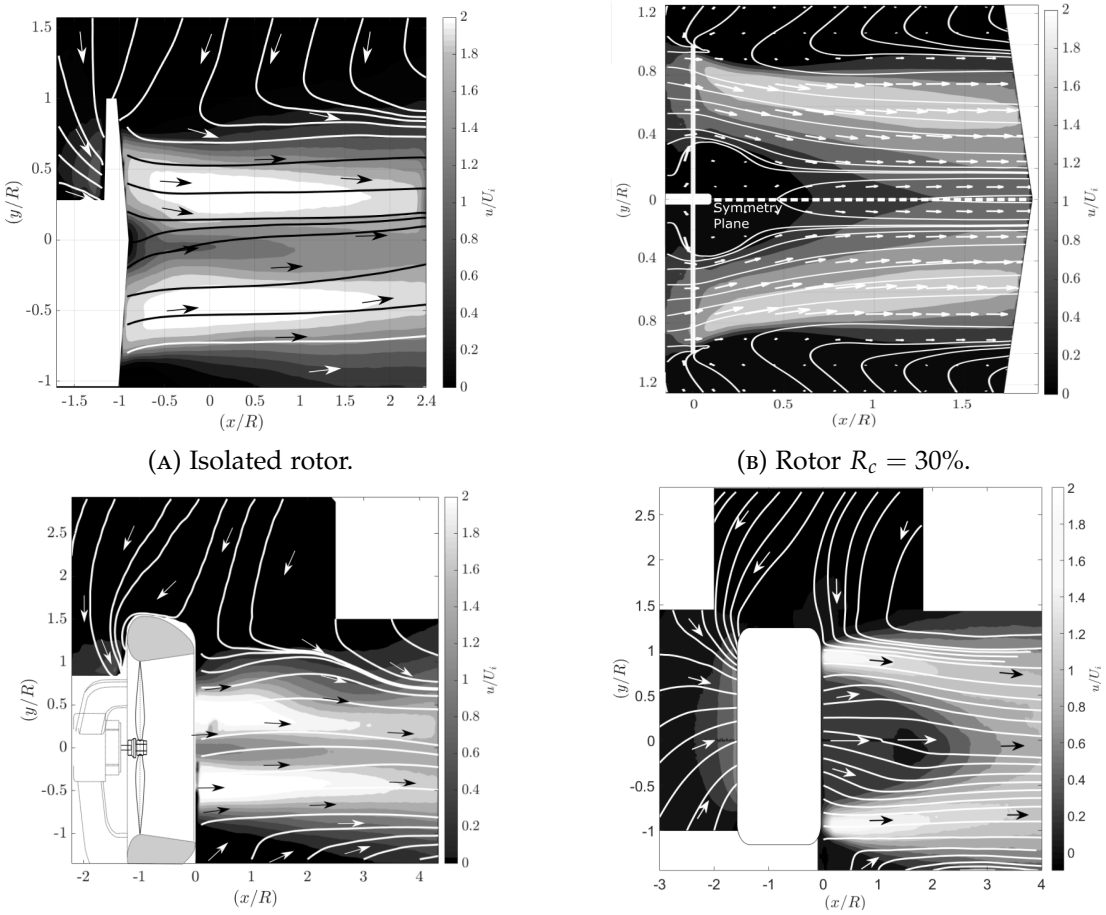

(A) Isolated rotor.

(B) Rotor $R_c = 30\%$.

(C) Shrouded rotor.

(D) Ventilated OCAJ.

FIGURE 5.1: Mean axial velocity profile (u) produced by the isolated rotor (5.1a), the rotor with a large root cut out (5.1b), the shrouded rotor (5.1c) and the ventilated open core annular jet (5.1d) when they are operating at descent velocity ratios $\alpha = 0.0$. The velocity profile of each experimental configuration has been non-dimensionalised using the notional induced velocity (U_i) of each configuration. A symmetry plane has been applied to the results presented in figure 5.1b to illustrate the structure of the flow field produced by the rotor presented in figure 5.1b. The variable R represents the radius of the rotor, the shroud outlet or the nozzle outlet of the respective experiments.

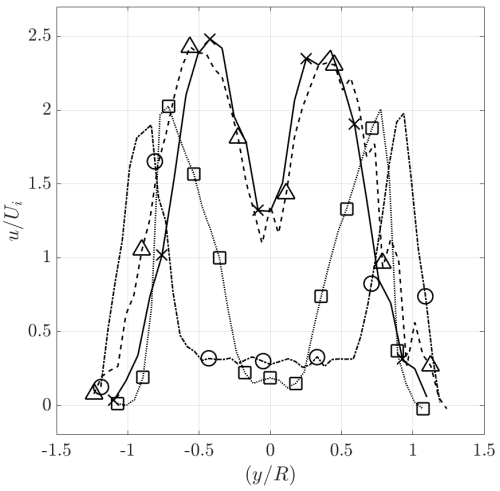

(A) Axial velocity.

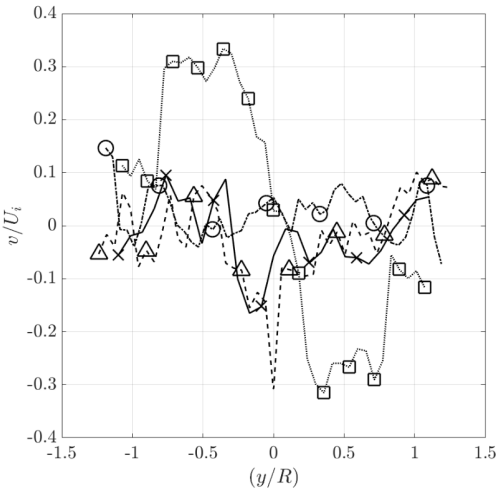

(B) Vertical velocity component (v).

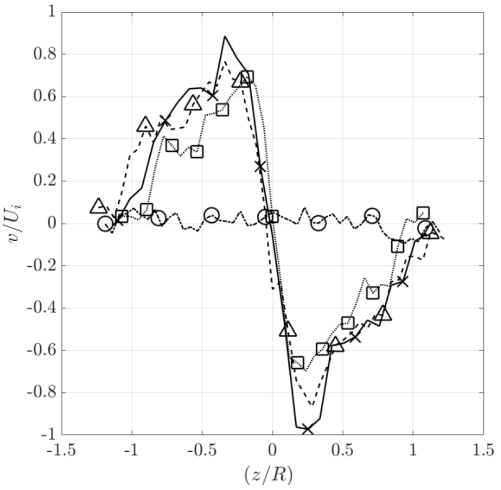

(C) Tangential velocity.

× Unshrouded Rotor
△ Shrouded Rotor
□ Rotor R_c = 30%
○ OCAJ

FIGURE 5.2: A comparison of the mean velocity profiles of the wake produced by the isolated rotor, the shrouded rotor, the ventilated OCAJ and the rotor with a large root cut out on a plane $0.48R$ from the rotor disk planes, the shroud outlet plane and the nozzle outlet plane respectively. The variable R represents the radius of the rotor, the shroud outlet or the nozzle outlet depending on which experiment was being investigated.

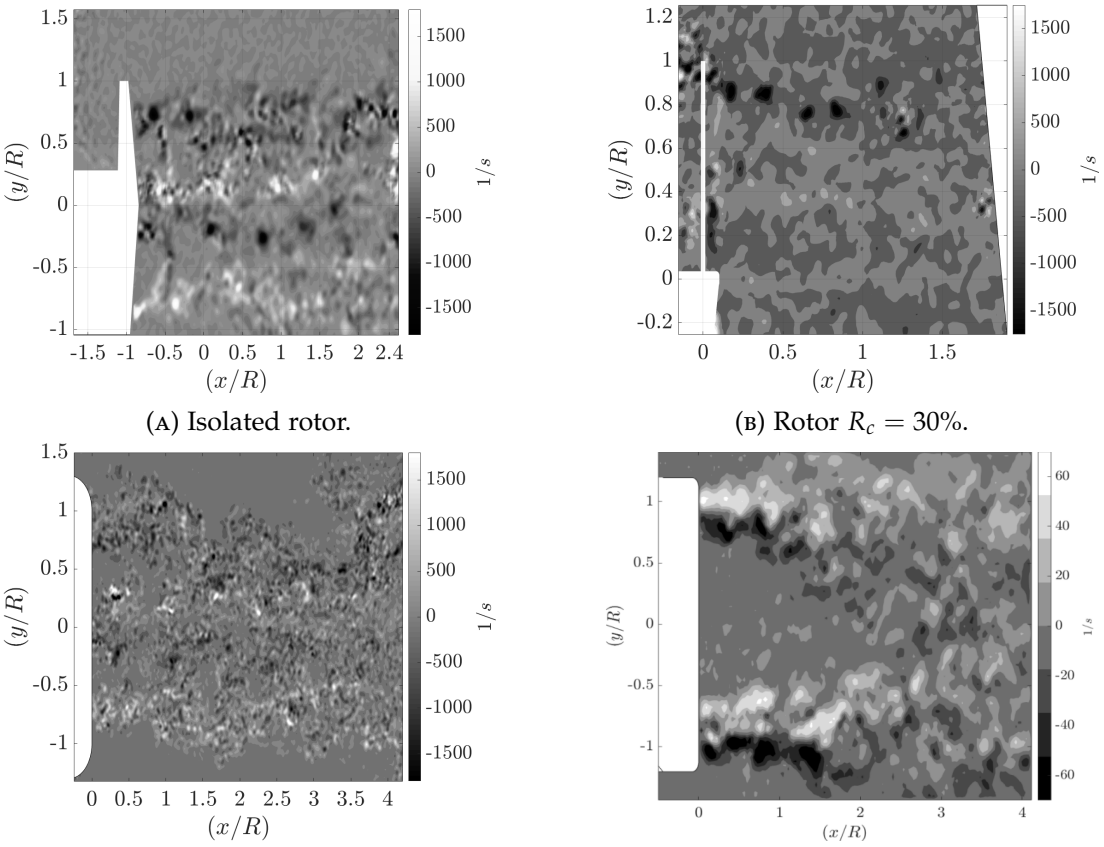

(A) Isolated rotor.

(B) Rotor $R_c = 30\%$.

(C) Shrouded rotor.

(D) Ventilated OCAJ.

FIGURE 5.3: Instantaneous contour plots of the third component of vorticity $[\frac{df_y}{dx} - \frac{df_x}{dy}]$ vorticity contained within the flow field produced by the isolated rotor (figure 5.3a), the rotor with a large root cut out (figure 5.3b), the shrouded rotor (figure 5.3c) and the ventilated OCAJ (figure 5.3d) when they are each operating at a velocity ratio of $\alpha = 0.0$. The variable R represents the radius of the rotor, the shroud outlet or the nozzle outlet of the respective experiment.

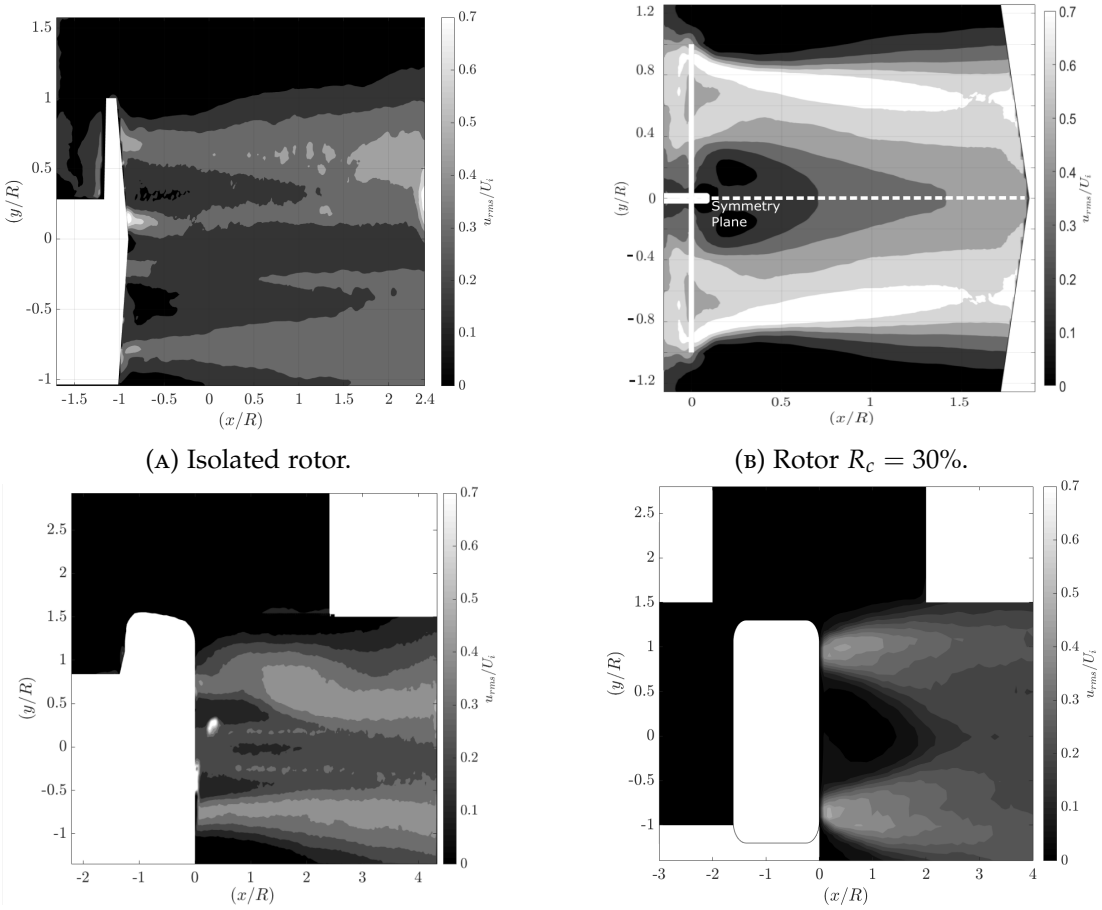

(A) Isolated rotor.

(B) Rotor $R_c = 30\%$.

(C) Shrouded rotor.

(D) Ventilated OCAJ.

FIGURE 5.4: Contour plots of the RMS of the fluctuations about the mean axial velocity profile (U_{rms}) produced by the unshrouded rotor (figure 5.4a), the rotor with the large root cut out (figure 5.4b), the shrouded rotor (figure 5.4c) and the ventilated open core annular jet (figure 5.4d) operating at a velocity ratio of $\alpha = 0.0$. Note the RMS of the fluctuations is scaled with respect to the induced velocity U_i and the variable R represents the radius of the rotor, the shroud outlet or the nozzle outlet of each individual experiment.

5.1.2 OPERATING AT A COUNTER FLOW/DESCENT VELOCITY RATIO OF $\alpha > 0.0$

At low descent velocity ratios the flow field produced by the isolated rotor (Chapter:2), the shrouded rotor (Chapter:2), the ventilated open core annular jet (Chapter:3) and the rotor with the large root cut out (Chapter:4) were all unaffected by the introduction of a counter flow. Smoke flow visualisation showed that the interaction between the wake and the counter flow occurred outside the PIV's regions of interest. At the interaction a saddle point formed on the geometric centre line of the rotor or nozzle. PIV also showed that as the counter flow velocity ratio increased the saddle point approached the rotor disk plane, the shroud outlet plane or the nozzle outlet plane. The mean flow fields produced by the isolated rotor, the shrouded rotor and the ventilated open core annular jet, presented in figure 5.5 showed that the saddle point penetrated through the rotor disk plane, the shroud outlet plane or the nozzle outlet plane as the velocity ratio increased. The fate of the saddle point once it penetrated through the rotor disk plane, the shroud outlet plane or the nozzle outlet plane was not investigated in this thesis. The formation of a saddle point on the geometric centreline of a rotor operating in axial descent was previously shown by Green et al. (2005) to be a prominent feature of the flow field produced by a rotor descending into the VRS. A round jet issuing into a uniform counter flow was shown by Bernero and Fiedler (2000) to also form a saddle point at the interaction between the jet flow and the counterflow. Once the saddle point penetrated the rotor disk plane, the shroud outlet plane or the nozzle outlet plane the flow field formed the conical region of reversed flow previously identified by Brinson (1998).

PIV showed that the saddle point that formed in the flow field of the rotor with a large root cut out did not penetrate up to the rotor disk plane. Instead the counter flow penetrated up through the rotor disk plane at a lower velocity ratio ($\alpha = 0.7$) and the rotor wake was deflected radially outboard. The inability of the cylindrical rotor hub to induce flow in the center of the rotor is believed to be responsible for this variation of the flow field. Figure 5.6 shows the mean location of the saddle points extracted from the centreline axial velocity profiles of both the shrouded and unshrouded rotor and the ventilated OCAJ. It is clear from figure 5.6 that the wake produced by both the shrouded rotor and the unshrouded rotor penetrates a similar distance from the shroud outlet plane or the rotor disk plane. The ventilated OCAJ penetrates a shorter distance into the counter flow than the shrouded or the unshrouded rotor wakes.

In each of the experimental configurations the formation of a saddle point on the geometric centre line of the rotor, the shroud or the nozzle leads to the formation of large regions of recirculating flow outboard of the rotor blade tips, the shroud outlet or the nozzle outlet. At low velocity ratios the recirculation forms upstream of the rotor disk plane, the shroud outlet plane or the nozzle outlet plane as the velocity ratio increased and the saddle point approached the shroud outlet plane or the nozzle

outlet plane. For the shrouded rotor and the ventilated OCAJ the recirculation moved towards the lip of the shroud and the nozzle of the ventilated OCAJ. Further increases in the counter flow lead the recirculation to form around the side of the shroud and the nozzle, as shown in figure 5.7. The recirculation continues to form around the side of the shroud and the nozzle as the velocity ratio increased until the velocity ratio became sufficient to ensure that the shrouded rotor wake and the ventilated OCAJ does not pass through the shroud outlet plane or the nozzle outlet plane. Instead the counter flow passes through the shroud outlet plane and the nozzle outlet plane whilst also passing smoothly around the side of the shroud or the nozzle as shown in figure 5.8. At a velocity ratio of $\alpha = 2.0$ the shrouded rotor (figure 5.8a) and the ventilated OCAJ (figure 5.8b) are both operating in a state analogous to the windmill brake state of an isolated rotor.

The development of the flow field produced by the shrouded rotor and the ventilated OCAJ resembles the development of the flow field produced by the unshrouded rotor. As expected the centre of recirculation formed by the unshrouded rotor moved from upstream of the rotor to above the rotor disk plane as the descent velocity ratio increased, as shown in figure 5.5. The recirculation continues to form above the rotor disk plane until the rotor enters the windmill brake state. The shrouded rotor and the ventilated OCAJ entered the windmill brake state at velocity ratios of $\alpha = 2.0$ and $\alpha = 0.9$ respectively.

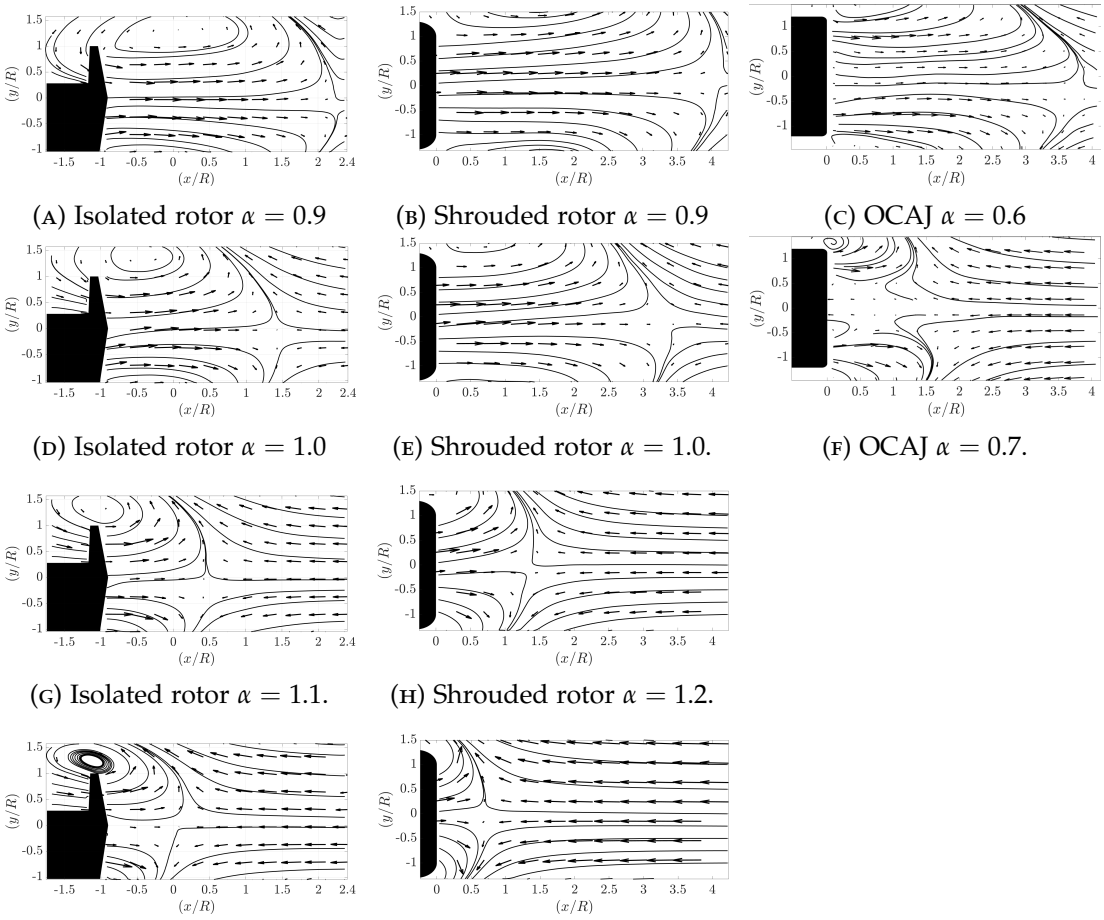

(A) Isolated rotor $\alpha = 0.9$ (B) Shrouded rotor $\alpha = 0.9$ (C) OCAJ $\alpha = 0.6$

(D) Isolated rotor $\alpha = 1.0$ (E) Shrouded rotor $\alpha = 1.0$. (F) OCAJ $\alpha = 0.7$.

(G) Isolated rotor $\alpha = 1.1$. (H) Shrouded rotor $\alpha = 1.2$.

(I) Isolated rotor $\alpha = 1.3$. (J) Shrouded rotor $\alpha = 1.3$.

FIGURE 5.5: Mean flow fields produced by the isolated rotor, the shrouded rotor and the ventilated open core annular jet.

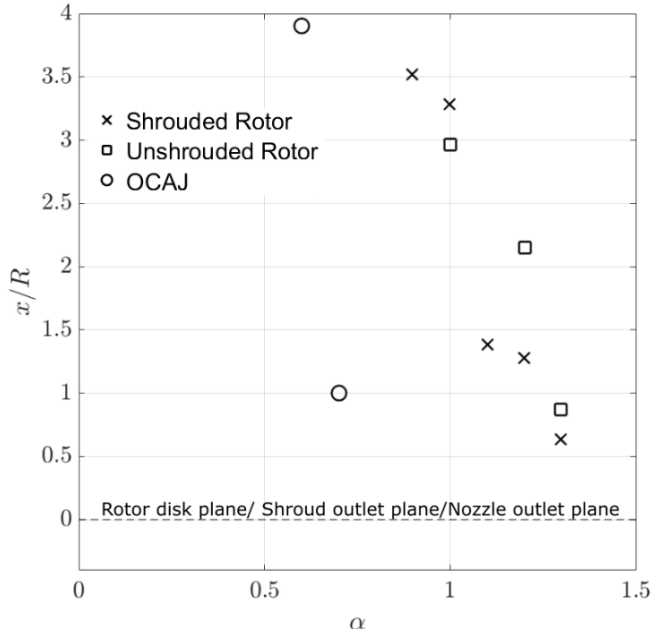

FIGURE 5.6: Mean location of the saddle point obtained from PIV measurements of the flow field produced by a isolated rotor, an unshrouded rotor and a ventilated OCAJ.

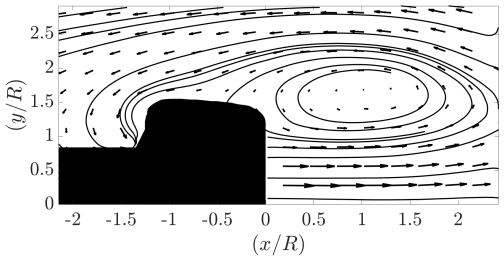

(A) Shrouded rotor $\alpha = 1.0$

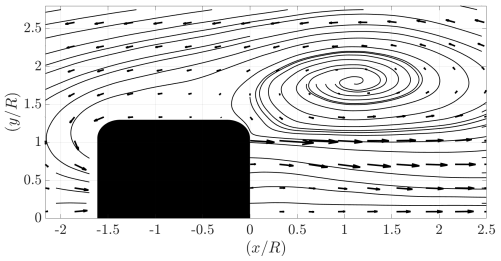

(B) OCAJ $\alpha = 0.7$

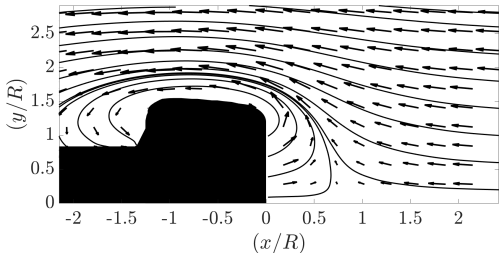

(C) Shrouded rotor $\alpha = 1.3$

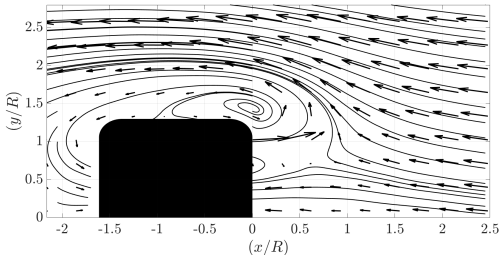

(D) OCAJ $\alpha = 0.8$

FIGURE 5.7: Mean flow field produced by the isolated rotor, the shrouded rotor and the ventilated open core annular jet.

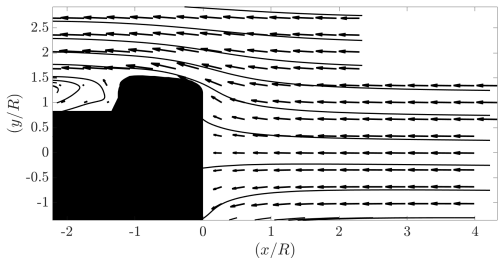

(A) Shrouded rotor $\alpha = 2.0$

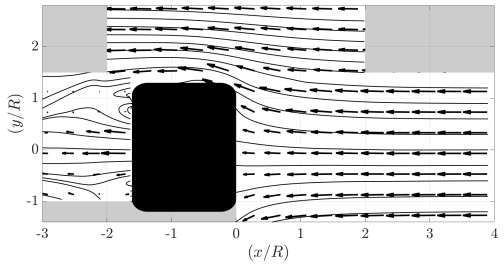

(B) Ventilated OCAJ $\alpha = 0.9$

FIGURE 5.8: Mean flow field produced by the shrouded rotor and the ventilated OCAJ when they are operating at velocity ratios of $\alpha = 2.0$ and $\alpha = 0.9$ respectively. At this velocity ratio both the shrouded rotor and the ventilated OCAJ are operating in a state analogous to the windmill brake state.

5.1.3 UNSTEADINESS OF THE FLOW FIELD

Whilst it has been shown that the mean flow fields produced by a ventilated OCAJ operating in a uniform counter flow, a shrouded rotor and an unshrouded rotor operating in axial descent are similar, the flow fields produced are highly unsteady, therefore the fluid dynamics of each experimental configuration was analysed. The comparison of the fluid dynamics of the various experimental configurations was performed to ensure that the development of the flow field was the same.

Despite the differences in the structure of the flow fields the unsteadiness of the flow field produced by the shrouded rotor, the ventilated OCAJ and the unshrouded rotor are notionally similar. At low velocity ratios the unsteadiness is confined to two regions, associated with the passage of the blade tip vortices or the jet shear layers, which extend away from the rotor disk plane, the shroud outlet plane and the nozzle outlet plane (figure 5.4). At velocity ratios where a saddle point forms on the geometric centre line of the rotor or the nozzle, a region of highly unsteady flow forms on the geometric centre line of the rotor and the nozzle outlet plane. The saddle point is contained within the region of high RMS values. The RMS of the fluctuations is similar in magnitude to the notional induced velocity (U_i) of each individual experiment, as shown in figure 5.9. Without the saddle point the unsteadiness of the flow field produced by the rotor with a large root cut out, shown in figure 5.9d, is confined to the region of the flow associated with the passage of the blade tip vortices as they are deflected radially outboard by the counterflow.

Streamline plots of the reconstructed simulations of the velocity fields produced by subtracting the maximum and minimal reconstruction coefficient forms of the first POD mode of each experiment from their respective mean flows are presented in figure 5.10. From figure 5.10 it is clear that at some velocity ratios, the flow fields produced by the shrouded rotor, the ventilated OCAJ and the isolated rotor all switch between two flow topologies. As with an isolated rotor operating in the VRS (Green et al., 2005), the flow intermittently switches between the flow topology associated with the operation of the experimental configurations at low velocity ratios and a topology associated with the fully developed VRS. The velocity ratios at which this occurs varies between each experimental investigation. Analysis of the probability density functions of the reconstruction coefficients showed that the frequency of excursion of the various flow fields into the VRS topology increased as the velocity ratio increased. It is interesting to note that the OCAJ produced a toroidal vortex which periodically sheds from the nozzle outlet at a frequency of $3.1Hz$ whilst operating at a velocity ratio of $\alpha = 0.9$. All other experimental configurations showed that the recirculation shed aperiodically from the rotor blade tips or the outlet of the shroud.

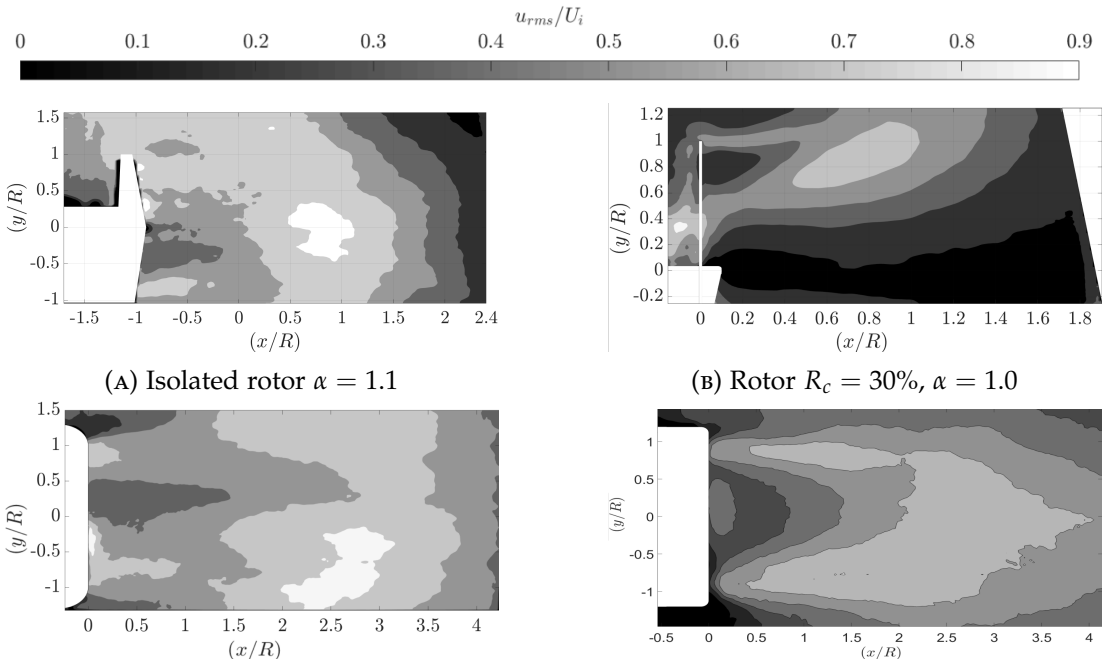

(A) Isolated rotor $\alpha = 1.1$

(B) Rotor $R_c = 30\%$, $\alpha = 1.0$

(C) Shrouded rotor $\alpha = 0.9$

(D) OCAJ $\alpha = 0.6$

FIGURE 5.9: RMS of the axial velocity component of the flow field produced by the isolated rotor, the shrouded rotor and the ventilated open core annular jet.

5.2 THE NATURE OF THE VRS

Linear stability analysis of helical vortex filaments, performed by Gupta and Loewy (1974) and Widnall (1972) identified the existence of small geometric perturbations to the helix that manifest themselves with wavelengths equal to a few core diameters or several helix diameters. Analysis of the interaction between adjacent vortex filaments, performed by Widnall (1972) identified the mutual-inductance instability of helical vortices. In hover the growth of these instabilities lead to the breakdown of the helical structure some distance from the rotor disk plane. In descending flight, the breakdown of the wake occurs in the vicinity of the rotor resulting in the formation of the VRS (Newman et al. (2003), Ahlin and Brown (2007), Ahlin and Brown (2009) and Brown et al. (2004)). Free-wake simulations of a helicopter rotor in axial descent performed by Bhagwat and Leishman. (2000),Leishman et al. (2004) and Ananthan and Leishman (2006) associated the mutual-inductance instability of helical vortices with the leapfrogging of blade tip vortices identified by (Stack et al. (2005)). High resolution CFD of a rotor entering the VRS, using the vorticity transport model developed by Brown (2000), and performed by Ahlin and Brown (2009) showed that the blade tip vortices reorientated themselves as a result of the 'mutual-inductance' instability of helical vortices and the growth on non-linear short wave disturbances identified by Widnall (1972), Leishman et al. (2004), Bhagwat and Leishman. (2000) and Ananthan and Leishman (2006). The breakdown of the blade root vortex system is believed to be responsible for the formation of the saddle point and the conical region of reverse flow which penetrates towards the rotor disk plane identified by Green et al. (2005)

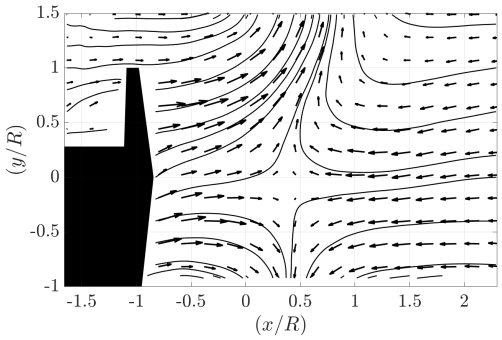

(A) Isolated rotor $\alpha = 1.1$ Min $\Psi(1)$

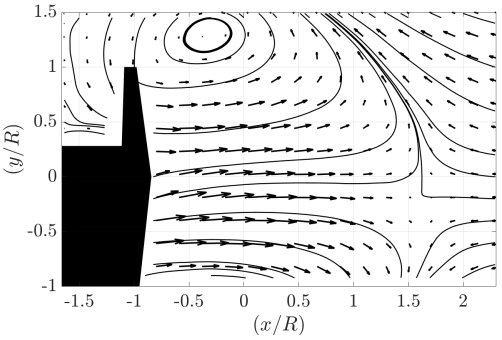

(B) Isolated rotor $\alpha = 1.1$ Max $\Psi(1)$

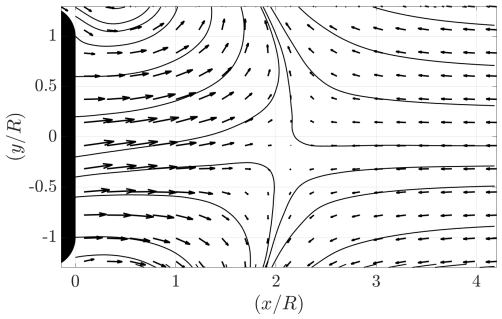

(C) Shrouded rotor $\alpha = 1.1$ Min $\Psi(1)$

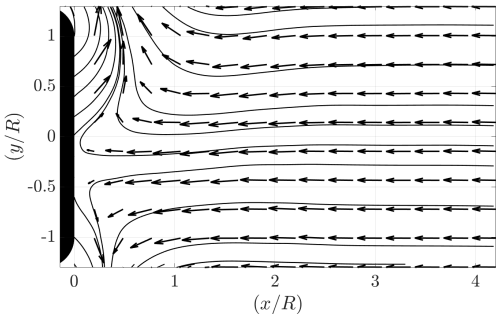

(D) Shrouded rotor $\alpha = 1.1$ Max $\Psi(1)$

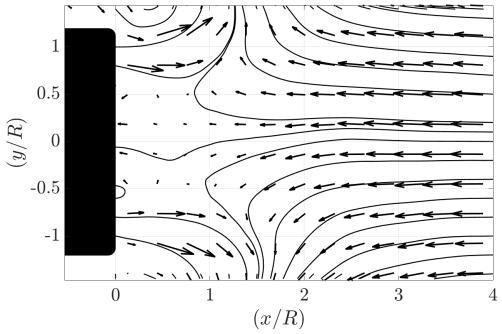

(E) OCAJ $\alpha = 0.6$ Min $\Psi(1)$

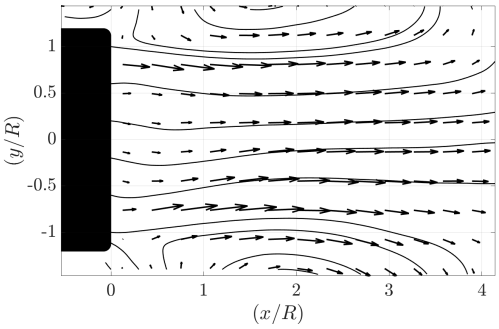

(F) OCAJ $\alpha = 0.6$ Max $\Psi(1)$

FIGURE 5.10: Streamline plots of the reconstructed velocity field produced by the subtraction of the maximum and minimal reconstruction coefficient forms of the first POD modes of the flow field produced by the unshrouded rotor, the shrouded rotor and the ventilated OCAJ when they are operating at a velocity ratio where the first POD mode is associated with the variation of the penetration of the saddle point from the rotor disk plane, the shroud outlet plane or the nozzle outlet plane.

and Brinson (1998). The breakdown of the blade root vortices leads to the disruption of the rotor wake for several rotor revolutions before they reform. This mechanism is used to explain the incipient flow regime identified by Green et al. (2005). Outboard of the rotor, leapfrogging of the blade tip vortices leads to the build up of vorticity around the rotor blades tips Savas et al. (2009). The build up and the subsequent shedding of the recirculation is responsible for the large thrust fluctuations associated with rotors operating in the VRS. A schematic diagram depicting the structures of the flow field produced by a rotor when it enters the VRS is shown in figure 5.11.

However, it is clear from the results presented in this thesis that the same flow topological features (the saddle point and the recirculation) and the same wake kinematics (the incipient flow regime) are present in the flow fields produced by a shrouded rotor, when it is operating in axial descent, and a ventilated OCAJ, when it is operating in a uniform counterflow. This is despite the fact no helical trailed vortex systems could be observed in the wake produced by the shrouded rotor or the ventilated OCAJ. In fact, due to the differences in the way the ventilated OCAJ and the rotors generate the notionally similar mean velocity profiles presented in figure 5.1 the role of the trailed helical vortex system and therefore the role of the mutual inductance instability of helical vortices has on the development of the VRS may be limited.

The results presented in this thesis suggest that the VRS may be a manifestation of an axially induced flow interacting with a uniform counterflow. The induced flow field consist of a region of low velocity flow surrounded by a ring of high velocity flow. At low velocity ratios the interaction between the low velocity core and the counter flow leads to the formation of a saddle point in line with the centre of the low velocity core. As a result of the saddle point the high velocity flow surrounding the low velocity core and the counterflow are deflected radially outboard forming a large torus of recirculating air. The recirculation continues to grow in size until it sheds downstream. Consequently the wake collapses allowing the counter flow to penetrate some distance towards the source of the induced flow. Once the recirculation has shed away from the source, the induced flow penetrates back into the counterflow, forcing the saddle point away from the source of the induced flow. At greater velocity ratios the distance the induced flow penetrates into the counter flow decreases and, at some velocity ratios, the counterflow can penetrate intermittently through the centre of the source of the induced flow. Further increases in velocity ratio lead the counter flow to penetrate the source of the induced flow permanently. The movement of the saddle point, towards the source of the induced flow, indicates the recirculation moves towards the source of the induced flow. For an isolated rotor the centre of the recirculation moves from below the rotor to above the rotor disk plane as the velocity ratio increases as shown in figure 5.12b (Green et al., 2005). For a shrouded rotor and a ventilated OCAJ the centre of the recirculation moves from below the shroud outlet plane and the nozzle outlet plane to around the lip of the shroud outlet and the nozzle outlet, as shown in figure 5.12. Further increases in the velocity ratio lead

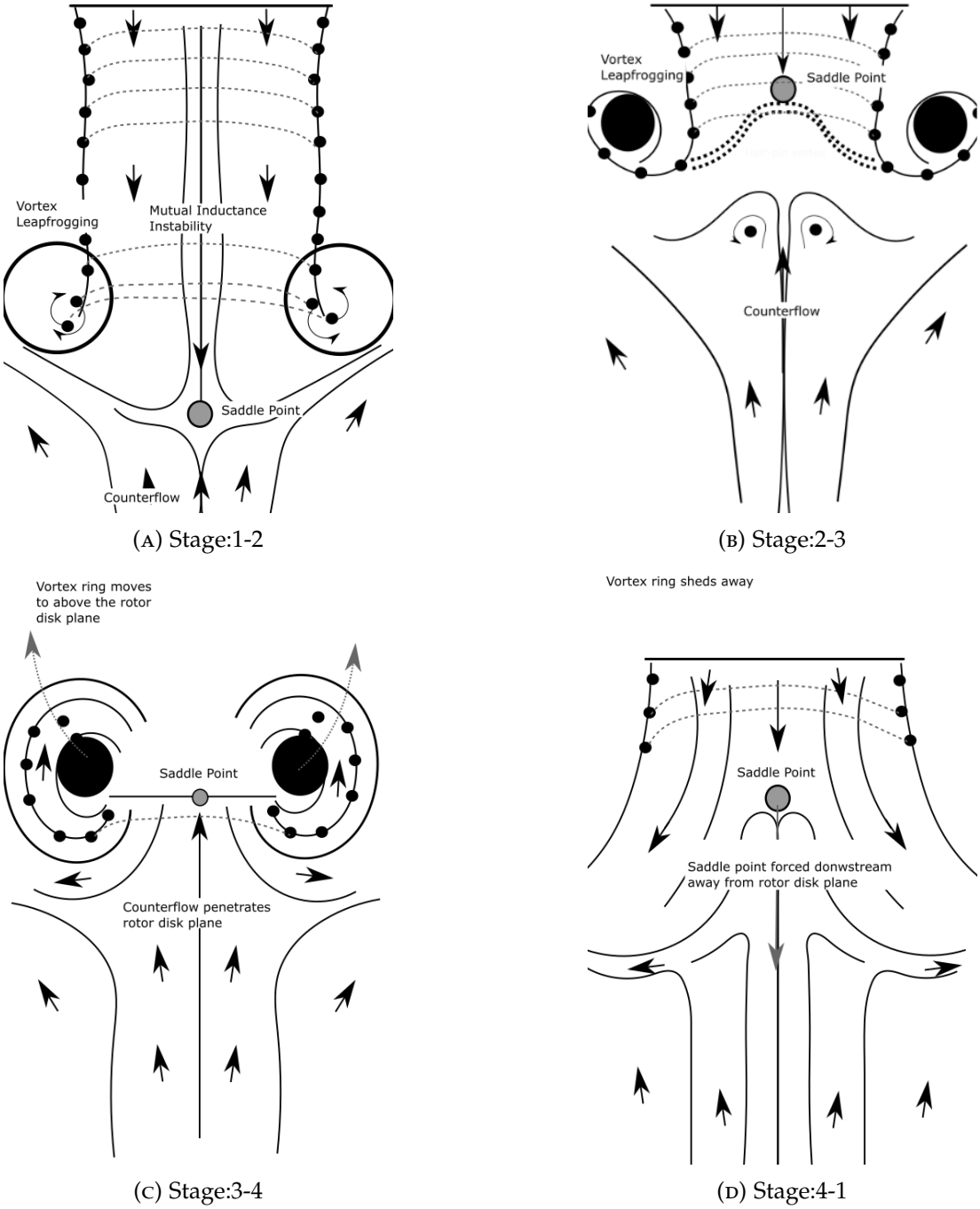

(A) Stage:1-2

(B) Stage:2-3

(C) Stage:3-4

(D) Stage:4-1

Figure 5.11: Schematic diagram depicting the mechanism responsible for the development of the VRS for an isolated rotor according to the mutual inductance instability theory of helical vortex filaments developed by Leishman et al. (2004).

the recirculation to form around the side of the shroud and the nozzle. The ability of a rotor wake to recirculate directly around the rotor disk plane, is responsible for the different manifestation of the VRS observed in figure 5.12 and figure 5.11c. The percentage of the rotor which the counter flow penetrates increases as the counter flow velocity ratio increased, until the rotor entered the windmill brake state.

Once the counter flow permanently penetrates through the rotor disk plane of an unshrouded rotor, the flow becomes locked within the toroidal form. The analysis of the rotor with a large root cut out showed that the root cut out significantly affects the velocity ratio at which the counter flow penetrates through the rotor disk plane. The results indicate that the blade root cut out significantly affects the unsteadiness of the flow field produced by a rotor as it operates in the VRS. It is proposed that the mutual-inductance instability of helical vortices and the leapfrogging of blade tip vortices contribute to the development and growth of the recirculation. However, they may not drive the kinematics of the wake as has been suggested in the past (Stack et al. (2005), Leishman et al. (2004), and Ahlin and Brown (2007)). Instead the results indicate that the VRS is a manifestation of an axially induced flow interacting with a uniform counterflow. The low velocity core of a rotor's induced velocity profile contributes to the development of the saddle point and the subsequent formation of the VRS. The shrouded rotor and the ventilated OCAJ both entered the notional VRS at lower velocity ratios than the unshrouded rotor. It is postulated that whilst individual rotors of multi-rotor unmanned aerial vehicles may enter the VRS, the entire UAV may enter a global VRS. Further research would be required in order to investigate this.

Actuator disk theory is a low order model which applies momentum theory to a streamtube that passes through the rotor disk plane. The flow through the rotor is assumed to be one-dimensional, quasi-steady, incompressible and inviscid. The rotor wake contains no discrete vortex filaments and does not incorporate any of the complex flow features associated with rotor wakes. In actuator disk theory the rotor is represented as a discontinuity over which a pressure jump occurs. Despite the numerous simplifications to the structure of the flow field actuator disk theory makes, it has been a useful tool for predicting the onset of the VRS. Spalart (2003) used the failure of the stream tube model to predict the onset of the VRS. The conclusion that the development of the VRS is driven by the interaction of axial flow with a uniform counterflow goes some way to explaining the efficacy with which a low order model, such as actuator disk theory is able to predict the mean induced velocity of a rotor when it is operating in axial descent and determine the velocity ratio at which the VRS will occur.

Unfortunately steady state wind tunnel tests, such as the ones presented in this thesis, do not simulate the transition of the rotor through the VRS because the descent velocity ratio is not coupled with the thrust of the rotor. Steady conditions exist prior to, and after the transition Brand et al. (2011). In steady wind speed tunnel tests the

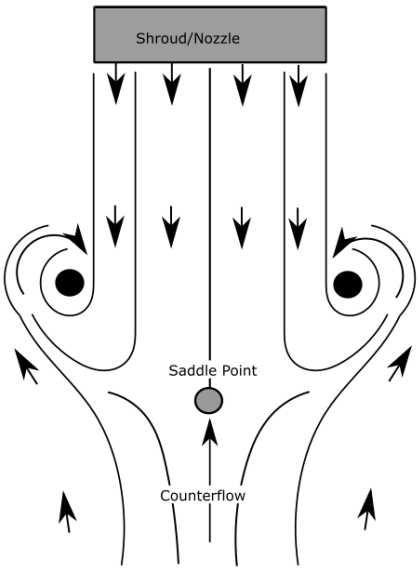

(A) Stage: 1-2

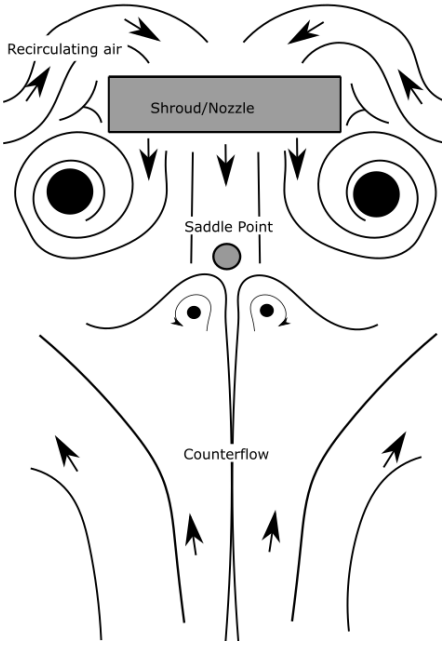

(B) Stage: 2-3

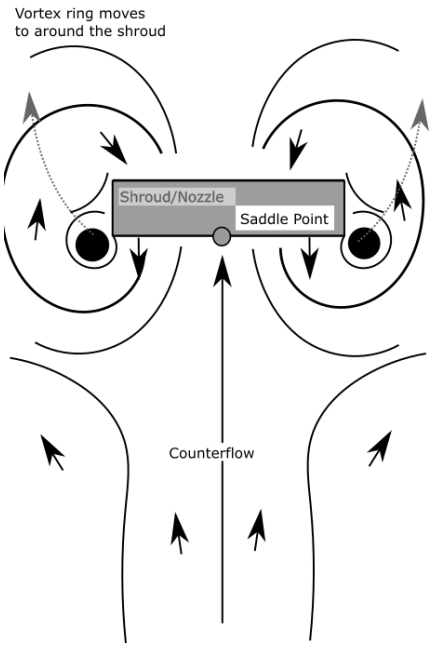

(C) Stage: 3-4

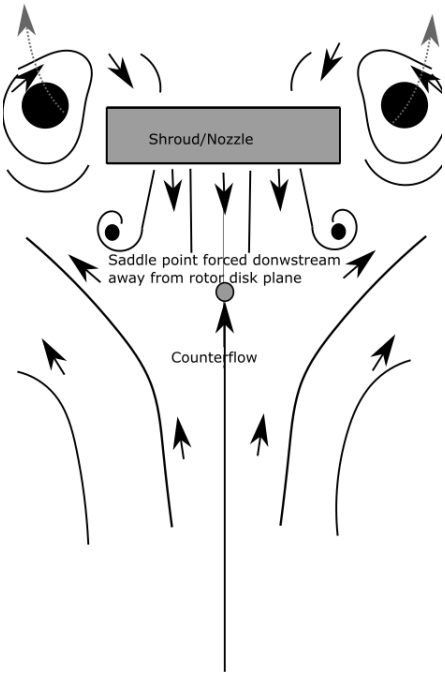

(D) Stage: 4-1

FIGURE 5.12: Sketches of the sequence of development of the flow field produced by the saddle point of the Unshrouded rotor, the shrouded rotor and the OCAJ.

vortex ring undergoes repeated relative motions through the rotor disk plane.

CHAPTER 6

SUMMARY AND CONCLUSIONS

The main findings of this investigation can be summarised into four categories: (i) the wind tunnel testing of a shrouded rotor; (ii) the wind tunnel testing of a ventilated OCAJ; (iii) the wind tunnel testing of a rotor with a large root cut out; (iv) the comments on the nature of the VRS. The findings of the aforementioned categories are summarised below.

6.1 CONCLUSIONS

6.1.1 ANALYSIS OF THE FLOW FIELD PRODUCED BY A SHROUDED ROTOR OPERATING IN AXIAL DESCENT.

An investigation into the structure of the flow field produced by a shrouded rotor and an unshrouded rotor operating in axial descent was performed. Laser Doppler Anemometry (LDA) measurements in the region below the shroud outlet plane and the unshrouded rotor were used to calculate the notional induced velocity of the shrouded rotor and the isolated rotor. POD analysis showed that, whilst the unsteadiness of the flow field produced by an unshrouded rotor is dominated by the passage of the blade root and tip vortices, the wake from a shrouded rotor is dominated by the radial flapping of the wake, which occurs because the wake from the shrouded rotor did not contain any clear helical vortex system. Particle Image Velocimetry (PIV) measurements of the flow field below the shroud identified the formation of a saddle point at the interaction between the shrouded rotor wake and the counterflow on the geometric centreline of the rotor. The saddle point approached the shroud outlet plane as the descent velocity ratio increased. When operating in axial descent, the shrouded rotor entered a state analogous to the VRS. The shrouded rotor entered the VRS at a lower descent velocity than the unshrouded rotor. The shrouded rotor entered the VRS when the descent velocity ratio was approximately equal to the mean induced velocity at the shroud outlet plane. At descent velocity rates just below the notional

induced velocity of the shrouded rotor, the flow enters an incipient regime similar to that produced by a unshrouded rotor. In this range, POD analysis showed that the the flow near the shroud intermittently switches between the topology associated with the shrouded rotor when it is operating in hover and the toroidal form associated with the VRS. At higher velocity ratios the shrouded rotor entered a state analogous to the windmill brake state of an unshrouded rotor. In the windmill brake state the counterflow penetrates through the centre of the shroud whilst also passing around the outside of the shroud.

The results presented in chapter 2 indicated that the mechanism by which the wake produced by the shrouded rotor broke down into the toroidal form associated with the VRS was similar to that produced by the unshrouded rotor. However, the wake from the shrouded rotor did not contain any clear helical vortex system. This is significant because the 'mutual-inductance' instability of helical vortex filaments Leishman et al. (2004) and the leapfrogging of the blade tip vortices Stack et al. (2005) was believed to be responsible for the development of the VRS. However, the results presented in chapter 2 suggest that the breakdown of the rotor wake into the toroidal form of the VRS is a result of the interaction between an axially induced flow, which consists of a low velocity core surrounded by a ring of higher velocity air, and a uniform counterflow.

6.1.2 ANALYSIS OF THE FLOW FIELD PRODUCED BY A VENTILATED OCAJ OPERATING IN A UNIFORM COUNTERFLOW.

An investigation into the structure of the flow field produced by a ventilated OCAJ operating in a uniform counterflow was performed. As with a round jet, the flow field produced by a ventilated OCAJ issuing into a uniform counterflow can be characterised as transitioning from a *unstable* to an *stable* flow condition as the jet to counterflow velocity ratio increased. In the *unstable* flow condition, at low velocity ratios, the interaction between the jet and the counter flow occurs in the far field, whilst the near field resembles the jet issuing into quiescent surroundings. PIV analysis showed that, at the interaction between the jet flow and the counterflow, a saddle point forms on the geometric centreline of the nozzle. As the counterflow velocity ratio increased, the distance the jet penetrates into the counterflow reduced, therefore the saddle point approached the outlet of the nozzle.

At counterflow velocities close to the notional induced velocity profile, the flow topology enters an incipient flow regime where a vortex ring aperiodically forms, and is shed from the lip of the nozzle outlet. Further increases in the counterflow velocity ratio lead the ventilated OCAJ to enter the *stable* flow condition, where the vortex ring sheds periodically from the nozzle outlet. At higher velocity ratios the ventilated OCAJ entered a state analogous to the windmill brake state of a shrouded rotor. In the windmill brake state, the counterflow penetrates through the centre of the shroud

whilst also passing around the outside of the shroud. In this state, the jet flow exits the nozzle through the inlet of the nozzle rather than the outlet.

The results presented in chapter 3 show that the structure and unsteadiness of the flow field produced by a jet issuing into a counterflow was similar to that produced by the shrouded rotor and an unshrouded rotor operating in axial descent discussed in chapter 2. Further analysis of the unsteadiness of the flow field performed using POD showed that the fluid structures responsible for the unsteadiness of the flow field produced by the shrouded rotor and the unshrouded rotor discussed in chapter 2 were also observed in the flow field produced by the jet. Indicating that mechanism responsible for the formation of the axially induced flow does not significantly affect the mechanism with which the flow field enters the notional VRS. This implies that the blade tip vortices produced by rotors are not responsible for the breakdown of the rotor wake into the toroidal form of the VRS. They may however still contribute to the development and the unsteadiness of the flow field.

6.1.3 ANALYSIS OF THE FLOW FIELD PRODUCED BY A ROTOR WITH A LARGE ROOT CUT OUT OPERATING IN AXIAL DESCENT.

An investigation into the structure of the flow field produced by a rotor with a large root cut out operating in axial descent was performed. The rotor produced a flow field which was similar to the one produced by the ventilated OCAJ. The results showed that the root cut out significantly affects the structure and the dynamics of the VRS. The large root cut out allowed the counterflow to penetrate through the rotor disk plane at lower velocity ratios and the rotor did not enter an incipient flow regime. Instead the rotor wake broke down into the toroidal form, associated with the VRS, over a narrow range of descent velocity ratios. Once the counterflow penetrated through the rotor disk plane the flow became locked within the toroidal form associated with the VRS. The structure of the flow field is dependent upon the build up and subsequent shedding of vorticity from around the rotor blade tips.

6.1.4 ANALYSIS OF THE FLUID DYNAMICS OF THE VORTEX RING STATE.

Despite the differences in the structure of the flow field produced by each of the experimental configurations investigated, when introduced to a counterflow all four experimental configurations developed into the VRS. The results presented in this thesis show that the VRS may be a manifestation of an axially induced flow interacting with a uniform counterflow. The role of the blade tip vortices on the development of the flow field has been drawn into question, by the different manifestations of the VRS produced by the shrouded rotor and the ventilated OCAJ.

6.2 FUTURE WORK AND RECOMMENDATIONS

6.2.1 THE VRS OF A SHROUDED ROTOR

- Modify the test rig to allow the mean penetration length x_p to be investigated at displacements greater than $4R$ from the rotor disk plane. This would enable the relationship between x_p and the descent velocity ratio to be determined.
- Investigate the structure of the flow field inside the shroud using LDA or PIV. This would require the modification of the test rig to allow optical access inside the shroud.
- Modify the test rig to allow the forces and moments produced by the rotor and the shroud. This would require the redesign of the test rig to incorporate two loadcells.
- Modify the test rig to allow the pressure on the surface of the shroud to be measured. This would enable quantitative surface pressure data and lift distribution data to be obtained.
- Redesign the test rig mount to allow the variation of the descent velocity angle γ. This would allow the flight envelope of the shrouded rotor to be investigated.
- High fidelity CFD simulations of the flow field produced by the shrouded rotor used in this investigation can provide insight into the structure of the flow field inside of the shroud. The experimental data provided in this chapter would be used to validate these simulations.
- Modify the rotor to investigate the effect blade tip clearance δ_{tip} has on the structure of the flow field produced by a shrouded rotor operating in axial descent.
- Modify the test rig to incorporate a counter rotating propeller. This would enable the investigation of how different shrouded rotor configurations affect the formation of the VRS.
- Modify the test rig to allow the flow field produced by a more conventional shrouded rotor with a shroud centre body to be investigated.

6.2.2 THE VRS OF A VENTILATED OPEN CORE ANNULAR JET

- Investigate the effect of jet confinement. This would require the development of a purpose built test rig allowing the cross sectional area of the counter flow velocity to be varied.
- Modify the test rig to allow the mean penetration length x_p to be investigated at displacements from the nozzle outlet greater than $(i.e(\frac{x}{R}) < 4)$. This would enable the relationship between x_p and the counter flow velocity ratio for an

open core annular jet to be determined and compared to the linear relationship of a round jet issuing into counterflow.

- Investigate the fluid mixing properties of a OCAJ issuing into counterflow. This would require the development of a custom test rig allowing the fluid used in the OCAJ to differ from that of the counter flow velocity. Through additional development this could be extended to investigate fuel mixing properties of an OCAJ issuing into a uniform counterflow.
- Investigate the jets growth rate.

6.2.3 THE VRS OF A ROTOR WITH A LARGE ROOT CUT OUT

- Modify the test rig to allow the forces and moments produced by the rotor to be investigated.
- Modify the test rig to investigate the effect rotor root cut out has on the structure of the flow field produced by a rotor operating in axial descent. This would require the manufacture of several different rotors with different root cut outs.
- Investigate the effect descent angle and yaw angle have on the development of the flow field produced by a rotor operating in descent.
- Modify the test rig to allow the effect helicopter fuselages have on the structure of the flow field produced by a rotor operating in descent.

6.2.4 THE NATURE OF THE VRS

- Further investigations into the role blade tip vortices have on the development of the VRS could be performed. Modifying the blade loading, the rotor geometry (twist/taper) or the geometry of the blade tips would allow the effect of the blade tip vortices to be investigated.
- Stability analysis of the flow field produced by each of the experimental test campaigns.
- Investigate the development of the VRS using variable speed wind tunnel testing. This would require the development of a test rig which allowed the wind tunnel speed to vary in response to the thrust of the rotor.

BIBLIOGRAPHY

A. Abrego, M. D. Betzina, and K. R. Long. A small-scale tiltrotor model operating in descending flight. *In 28th European Rotorcraft Forum, Bristol, England.*, 2002.

A. G. Ahlin and R. E. Brown. Predicting the onset of the vortex ring state under accelerated flight conditions. *American Helicopter Society, 61st Annual Forum, Grapevine, Texas*, 2005.

A. G. Ahlin and R. E. Brown. The vortex dynamics of the rotor vortex ring phenomenon. *American Helicopter Society, 63rd Annual Forum, Virginia Beach, Virginia*, 2007.

A. G. Ahlin and R. E. Brown. Wake structure kinematics in the vortex ring state. *J. American Helicopter Society.*, 54(3):32003, 1–18, 2009.

G. A. Ahlin. *The fluid dynamics of the helicopter vortex ring phenomenon.* PhD thesis. University of London, 2007.

J. Ahn. Parametric design of a ducted fan system in forward flight and static conditions. *American Helicopter Society International Specialists Meeting on Unmanned Rotorcraft: Design, Control and Testing, Chandler*, 2005.

A. Akturk and C. Camci. Double ducted fan (ddf) as a novel ducted fan inlet lip separation control device. *The International Powered Lift Conference.*, pages 148–170, 2010.

A. Akturk, A. Shavalikul, and C. Camci. Piv measurements and computational study of a 5-inch ducted fan for v/stol uav applications. *47th AIAA Aerospace ciences Meeting and Exhibit, Orlando, Florida.*, 2009.

H. E. Albrecht, M. Borys, N. Damaschke, and C. Tropea. Laser doppler and phase doppler measurement techniques. *Springer Science and Business Media*, 2013.

S. Ananthan and J. G. Leishman. Rotor wake aerodynamics in large amplitude maneuvering flight. *J. American Helicopter Society.*, 51(3):225–243, 2006.

J. Arendt, H. A. Badcock, and J. Schuster. Penetration of a jet into a counterflow. *ASCE J. Hydr. Division*, 82:1038–8–11, 1956.

A. Azuma and A. Obata. Induced flow variation of the helicopter rotor operating in the vortex ring state. *J. Aircraft.*, 5(4):381–386, 1968.

J. B. Barlow, Jr W. H. Rae, and A. Pope. *Low-Speed Wind Tunnel Testing.* Wiley-Interscience, John Wiley & Sons, 1999.

P. M. Basset and M. Brocard. A fenestron model for improving the helicopter yaw dynamics flight simulation. *30th European Rotorcraft Forum, Marseilles, France*, 2004.

S. Beltaos and N. Rajaratnam. Circular turbulent jets in an opposing infinite stream. In R.Kellerhals, editor, *Proceedings of the first canadian hydraulics conference held at the university of Alberta.*, volume 4 of *1*, pages 220–237, University of Alberta, Water Resources Centre USA, 1973. University of Alberta.

S. Bernero. *A turbulent jet in counterflow.* PhD thesis. Berlin: Technical University Of Berlin, 2000.

S. Bernero and H. E. Fiedler. Application of particle image velocimetry and proper orthogonal decomposition to the study of a jet in a counterflow. *Experiments In Fluids*, 29(1):S274–281, 2000.

M. D. Betzina. Tiltrotor descent aerodynamics: A small-scale experimental investigation of vortex ring state. *American Helicopter Society, 57th Annual Forum, Washington DC.*, 2001.

J. M. Bhagwat and G. J. Leishman. Stability analysis of helicopter rotor wakes in axial flight. *J. American Helicopter Society*, 45(3):165–178, 2000.

D. Black and C. Rohrbach. Shrouded propellers - a comprehensive study. *AIAA 5th Annual Meeting and Technical Display.*, page 994, 1968.

D. M. Black, H. S. Wainauski, and C. Rohrbach. Shrouded propellers - a comprehensive performance study. *AIAA 5th Annual Meeting and Technology Display, Philadelphia.*, 1968.

R. Bontempo and M. Manna. Effects of the duct thrust on the performance of ducted wind turbines. *J. Energy.*, 99(1):274–287, 2016.

G. De. Bothezat. The general theory of blade screws. *NACA report no.29*, 1919.

A. Brand, R. Kisor, R. Blyth, D. Mason, and C. Host. V-22 high rate of descent (hrod) test procedures and long record analysis. *American Helicopter Society, 60th Annual Forum, Maryland*, 2004.

A. Brand, M. Dreier, R. Kisor, and T. Wood. The nature of vortex ring state. *J. American Helicopter Society.*, 56(2):22001, 2011.

P. Brinson. Experimental investigation of the vortex ring condition. *In 24th European Rotorcraft Forum, Marseille*, 1998.

P. Brotherhood. Flow through a helicopter rotor in vertical descent. *Aeronautical Research Committee, R&M No.2735*, 1949.

R. E. Brown. Rotor wake modelling for flight dynamic simulation of helicopters. *AIAA Journal.*, 38(1):57–63, 2000.

R. E. Brown, J. G. Leishman, S. J. Newman, and F. J. Perry. Blade twist effects on rotor behaviour in the vortex ring state. *In 28th European Rotorcraft Forum, Bristol, England*, 2002.

R. E. Brown, A. J. Line, and G. A. Ahlin. Fuselage and tail-rotor interference effects on helicopter wake development in descending flight. *American Helicopter Society, 60th Annual Forum, Maryland*, 2004.

W. Castle and R. B. Gray. Empirical relationship between induced velocity, thrust, and rate of descent of a helicopter rotor as determined by wind tunnel tests on four model rotors. *NACA TN No. 2472*, 1951.

W. Castles. Flow induced by a rotor in power-on vertical descent. *NACA TN 4330*, 1958.

C.H.C. Chan and K.M. Lam. Centreline velocity decay of a circular jet in a counter-flowing stream. *Physics Of Fluids*, 10(3):637–644, 1998.

D. R. Clark. Aerodynamic design rationale for the fan-in-fin on the s-67 helicopter. *American Helicopter Society 31st Annual National Forum, Washington DC. Preprint No. 904*, 1975.

M. G. Clemmons. Antitorque safety and the rah-66 fantail. *American Helicopter Society 48th Annual Forum Proceedings, Washington DC*, pages 169–175, 1992.

H. Coandă. Lifting device coanda effect. *US Patent*, (n. 3,261,162), 1936.

Y. Colin, B. Bertrand, T. Patron, and V. Phoi. Quadcopter. *US Patent No. US D747,775 S*, 2016.

Piasecki Aircraft Corporation. 16h-1 pathfinder, 1962. https://piasecki.com/wp-content/uploads/2018/12/16H-1-Pathfinder.pdf.

Piasecki Aircraft Corporation. 16h-1a pathfinder ii, 1965. https://piasecki.com/wp-content/uploads/2018/12/16H-1A-Pathfinder-II.pdf.

J. P. Cycon, K. M. Rosen, and A. C. Whyte. Unmanned flight vehicle including counter rotating rotors positioned within a toroidal shroud and operable to provide all required vehicle flight controls. *US Patent No. 5,152,478*, 1992.

J. R. Dailey, N. R. Augustine, J. B. Davis, and E. E. Covert. Report of the panel to review the v-22 program. *Technical report, Memorandum for the secretary of defence*, page 14, 2001.

DantecDynamics. Measurement principles of lda, 2020. https://www.dantecdynamics.com/, Last accessed on 01/010/2020.

J. M. Drees and W. P. Hendal. The field of flow through a helicopter rotor obtained from wind tunnel smoke tests. *J. Aircraft Engineering.*, 23(266), 1950.

J. M. Drees and W. P. Hendal. Airflow patterns in the neighbourhood of helicopter rotors. *J. Aircraft Engineering.*, 23(266):107–111, 1951a.

J. M. Drees and W. P. Hendal. Airflow patterns in the neighbourhood of helicopter rotors: A description of some smoke tests carried out in a windâĂŘtunnel at amsterdam. *J. Aircraft Engineering and Aerospace Technology.*, 23(266):107–111, 1951b.

B. Durand. Airspeed measurement arrangement in a helicopter. *British patent 1,515,387*, 1978.

FAA. *Helicopter Flying Handbook: FAA-H-8083-21B*. United States Department of Transportation, Federal Aviation Administration, Airman Testing Branch, 2019.

J. E. Fairchild, N. N. Batra, and R. L. Stewart. Influence of design parameters on fan-in-fin static performance. *American Helicopter Society29th Annual National Forum*, 1973.

A. Faulkner and F. Buchner. Flight investigation of a helicopter low airspeed estimation system based on measurements of control parameters. *In 6th European Rotorcraft Forum, Bristol, England*, 1980.

F. F. Felker and R. M. McKillip. Comparison of predicted and measured rotor performance in vertical climb and descent. *American Helicopter Society, 57th Annual Forum, Washington D.C.*, 1994.

K. R. Ferrell and J. J. Shapley. Special study of autorotational procedures. *Technical report AD676820, U.S. Army Aviation Test Activity.*, 1968.

J. Fleming, T. Jones, P. Gelhausen, and D. Ennus. Improving control system effectiveness for ducted fan vtol uavs operating in crosswinds. *2nd AIAA Unmanned Unlimited Ststems, Technologies and Operations - Aerospace, San Diego.*, 2003.

H. S. Fletcher. Experimental investigation of lift, drag, and pitching moment of five annular airfoils. *NACA-TN-4117.*, 1957.

R. W. Fox, A. T. McDonald, and P. J. Pritchard. *Intoduction to Fluid Mechanics*. Wiley, John & Sons, Incorporated, 2008.

P. D. Gammack, F. Nicolas, and K. J. Simmonds. Bladeless fan. *US Patent Office*, (US 8, 308,445 B2), 2009.

V. M. Ganzer and W. H. Rae. An experimental investigation of the effect of wind tunnel walls on the aerodynamic performance of a helicopter rotor. *NASA TN D-415.*, 1960.

Z. Gao. New achievements in helicopter aerodynamics. *Aviation Industry Publications (Translated from chinese to english by W. Chan, 2003).*, 1999.

W. K. George. Quantitative measurement with the burst-mode laser doppler anemometer. *J. Experimental Thermal and Fluid Science*, 1(1):29–40, 1988.

A. Gessow. Flight investigation of effects of rotor blade twist on helicopter performance in the high-speed and vertical-autorotation-descent conditions. *NACA TN No. 1666*, 1948.

H. Glauert. The analysis of experimental resutls in the windmill brake and vortex ring states of an airscrew. *Aeronautical Research Council, R&M No. 1026*, 1926.

K. W. Goodson and K. J. Grunwald. Aerodynamic characteristics of a powered semispan tilting shrouded-propeller vtol model in hovering and transition flight. *NASA TN D-981.*, 1962.

W. Graf, J. Fleming, and W. Ng. Improving ducted fan uav aerodynamics in forward flight. *46th AIAA Aerospace Sciences Meeting and Exhibit.*, page 430, 2008.

R. B. Green, C. J. Doolan, and R. M.Cannon. Measurements of the orthogonal blade-vortex interactions using a particle image velocimetry technique. *J. Experiments in Fluids*, 29(4):369–379, 2000.

R. B. Green, E. A. Gillies, and R. E. Brown. The flow field around a rotor in axial descent. *J. Fluid Mechanics.*, 534:237–261, 2005.

L. Gui and S. T. Wereley. A correlation-based continuous window-shift technique to reduce the peak-locking effect in digital piv image evaluation. *Experiments In Fluids*, 32(4):506–517, 2002.

K. J. Gunwald and K. W. Goodson. Aerodynamic loads on an isolated shrouded-propeller configuration for angles of attack from -10 degrees to 110 degrees. *Tech Report, National Aeronautics and Space Administration, Washington DC.*, 1962.

B. P. Gupta and R. G. Loewy. Theoretical analysis of the aerodynamic stability of multiple, interdigitated helical vortices. *AIAA Journal.*, 12(10):1381–1387, 1974.

N. Gupta and J. Plump. Design of a vtol micro air vehicle that incorporates counter-rotating reversible thrust propellers. *AUVSI Unmanned Systems Conference, Baltimore, MD*, 2001.

F. B. Gustafson. Flight tests of the sikorsky hns-1 (army yr-4b) helicopter i- experimental data on level-flight performance with original blades. *NACA L5C10*, 1945.

F. B. Gustafson and A. Gessow. Flight tests of the sikorsky hns-1 (army yr-4b) helicopter ii- hovering and vertical-flight performance with the original and an alternate set of main-rotor blades, including a comparison with hovering performance theory. *NACA L5D09a*, 1945.

N. D. Ham and H. H. Moser. Preliminary investigation of a ducted fan in lifting flight. *J. American Helicopter Society.*, 3(3):17–29, 1958.

G. Hamel. Aeroplane. *US Patent No. 1,463,694*, 1923.

H. K. Harr, P. J. Hollifield, and R. P. Smith. Flight investigation of bell model 206 ring fin. *American Helicopter Society 41st Annual Forum Proceedings, Fort Worth, TX*, pages 327–337, 1985.

D. F. Hopkins and J. M. Robertson. Two-dimensional incompressible fluid jet penetration. *J. Fluid Mechanics*, 29(2):273–287, 1967.

W. R. M. Van Hoydonck, H. Haverdings, and M. D. Pavel. A review of rotorcrft wake modelling methods for flight dynamics applications. *In 35th European Rotorcraft Forum, Hamburg*, 2009.

H. H. Hubbard. Sound measurements of five shrouded propellers at static conditions. *NACA-TN-2024.*, 1950.

M. Jafari, H. Afshin, B. Farhanieh, and H. Bozorgasareh. Numerical aerodynamic evaluation and noise investigation of a bladeless fan. *J. Applied Fluid Mechanics*, 8(1): 133–142, 2015.

M. Jafari, H. Afshin, B. Farhanieh, and H. Bozorgasareh. Experimental and numerical investigation of a 60cm diameter bladeless fan. *J. Applied Fluid Mechanics*, 9(2): 935–944, 2016a.

M. Jafari, H. Afshin, B. Farhanieh, and A. Sojoudi. Numerical investigation of geometric parameter effects on the aerodynamic performance of a bladeless fan. *Alexandria Engineering Journal*, 55(1):223–233, 2016b.

M. Jafari, A. Sojoudi, and P. Hafezisefat. Numerical study of aeroacoustic sound on performance of bladeless fan. *Chinese Journal of Mechanical Engineering*, 30(2):483–494, 2017.

W. Johnson. Model for vortex ring state influence on rotorcraft flight dynamics. *NASA/TP-213477.*, 2005.

T. Jukes, J. Lirvat, F. Nicolas, S. Padhani, and G. R. Hunt. Flow control using annular jets. *European Drag Reduction and Flow Control, Cambridge*, 2015.

R. Keane and R. Adrianl. Optomization of particle image velocimetry. part i: double pulsed systems. *Measurement Science and Technology*, 1:1202–1215, 1990.

R. Kisor, R. Blyth, A. Brand, and T. MacDonald. V-22 low speed/high rate of descent (hrod) test results. *American Helicopter Society, 60th Annual Forum, Maryland*, 2004.

N. W. M. Ko. Annular jets of large inner diameter. *J. Sound and Vibration*, 69(4):616–621, 1980a.

N. W. M. Ko. Annular jets of small inner diameter. *J. Sound and Vibration*, 68(3):468–472, 1980b.

O. König and H. E. Fiedler. The structure of round turbulent jets in counterflow: A flow visualization study. *In Advances in Turbulence III, (eds. A .V. Johansson and P. H. Alfredsson)*, pages 61–66, 1991.

W. Krüger. On wind tunnel tests and computations concerning the problem of shrouded propellers. *Tech Report, National Advisory Committee for Aeronautics.*, 1949.

R. Kyle, Y. C. Lee, and W. Früh. Propeller and vortex ring state for floating offshore wind turbines during surge. *J. Renewable Energy.*, 155(2):645–657, 2020.

K.M. Lam. and H.C. Chan. Round jet in ambient counterflowing stream. *J. Hydraulic Engineering*, 123(10):895–903, 1997.

M. Lazareff. The aerodynamics of v/stol aircraft. *AGARD-VKI Lecture Series, ASGAR-Dograph 126.*, pages 237–289, 1968.

V. Leble and G. Barakos. Forced pitch motion of wind turbines. *Journal of Physics: Conference Series.*, 753(2):022042, 2016.

A. F. Lehman and J. A. Besold. Test section size influence on model helicopter rotor performance. *USAAVLABS TR 71-6.*, 1971.

G. J. Leishman. *Principles of Helicopter Aerodynamics with CD Extra.* Cambridge University Press, 2006.

G. J. Leishman, M. J. Bhagwat, and S. Ananthan. The vortex ring state as a spatially and temporally developing wake instability. *J. American Helicopter Society.*, 49(2): 160–175, 2004.

H. E. Lemont. Ringfin augmentation effects. *American Helicopter Society 38th Annual Forum Proceedings, Anaheim, CA*, pages 451–460, 1982.

H. Li, H-S. Deng, and Y-B. Lai. Numerical and experimental research on the outlet flow field for the air multiplier. *J. Applied Thermal Engineering*, 93(1):652–659, 2016.

L. Lipera, J. D. Colbourne, M. B. Tischler, M. H. Mansur, M. C. Rotkowitz, and P. Patangui. The micro craft istar micro air vehicle: Control system design and testing. *American Helicopter Society 57th Annual Forum Proceedings, Washington, D.C.*, 2001.

C. N. Lock, H. Bateman, and H. C. H. Townsend. An extension of the vortex theory of airscrews with applications to airscrews of small pitch, including experimental results. *Aeronautical Research Council, R&M No. 1014*, 1925.

R. L. Maki and D. J. Giulianetti. Aerodynamic stability and control of ducted-propeller aircraft. *Conference of V/STOL and STOL Aircraft, Ames Research Center, Moffett Field no.9. NASA-SP-116*, pages 115–128, 1966.

M. Marino, A. Fisher, R. Clothier, S. Watkins, S. Prudden, and C. S. Leung. Rotor wake interactions with an obstacle on the ground. *International Journal of Micro Air Vehicles.*, 7(3):285–299, 2015.

P. Martin and C. Tung. Performance and flowfield measurements of a 10-inch ducted rotor vtol uav. *American Helicopter Society 60th Annual Forum Proceedings, Baltimore*, 2004.

R. Mason, F. Nocolas, and R. Pitt. Bladeless is more. *ANSYS Advantage*, 4(2):5–7, 2010.

W. D. Morgan, B. J. Brinkworth, and G. V. Evans. Upstream penetration of an enclosed counterflowing jet. *Industrial & Engineering Chemistry Fundamentals*, 15(2):125–127, 1976.

K. W. Mort. Performance characterisation of a 4-foot-diameter ducted fan at zero angle of attack for several fan blade angles. *NASA D-3122, Ames Research Centre, Moffett Field.*, 1965.

H. H. Moser. Some effects of the shroud on the forward flight performance of the lifting fan. *J. American Helicopter Society.*, 4(2):39–44, 1959.

R. Mouille. The feneston shrouded tail rotor of the sa.341 gazelle. *J. American Helicopter Society.*, 15(4):31–37, 1970.

R. Mouille and F. d'Ambra. The fenestron a shrouded tail rotor concept for helicopters. *American Helicopter Society 42nd Annual Forum Proceedings, Washington DC.*, pages 597–606, 1986.

D. W. Murphy and J. P. Bott. On the lookout: The air mobile groudn security and surveillance system (amgsss) has arrived. *Unmanned Systems.*, 13(4), 1995.

I. V. Naumov, R. F. Mikkelson, V. L. Okulov, and J. N. Sørensen. Piv and lda measurements of the wake behind a wind turbine model. *J. of Physics:Conference Series. The Science of Making Rorque from wind.*, 524, 2014.

N. E. Nelson. The ducted fan in vtol aircraft design. *J. American Helicopter Society.*, 4 (1):53–56, 1959.

S. Newman. *The Foundations Of Helicopter Flight.* Butterworth Heinemann, 1994.

S. Newman, R. Brown, J. Perry, S. Lewis, M. Orchard, and A. Modha. Comparative numerical and experimental investigations of the vortex ring phenomenon in rotorcraft. *American Helicopter Society, 57th Annual Forum, Washington D.C*, 2001.

S. Newman, R. E. Brown, J. Perry, S. Lewis, M. Orchard, and A. Modha. Predicting the onset of wake breakdown for rotors in descending flight. *J. American Helicopter Society.*, 48(1):28–38, 2003.

S. Newman, R. Brown, F. Perry, G. Ahlin, I. Simmons, A. Modha, and M. Khelifa. Revisiting the effects of blade geometry on rotor behaviour in descending flight. *In 30th European Rotorcraft Forum, Marseilles, France.*, 2004.

W. A. Newson. Aerodynamic characteristics of four-duct tandem vtol-aircraft configurations. *NASA TND-1481*, 1963.

J Nogueira, A Lecuona, and P A Rodríguez. Data validation, false vectors correction and derived magnitudes calculation on PIV data. *Measurement Science and Technology*, 8(12):1493–1501, 1997.

G. F. Oweis, D. Fry, C. J. Chesnaskas, S. D. Jessup, and S. L. Ceccio. Development of a tip-leakage flow - part 1: the flow over a range of reynolds numbers. *J. Fluids Eng.*, 128(4):751–764, 2006a.

G. F. Oweis, D. Fry, C. J. Chesnaskas, S. D. Jessup, and S. L. Ceccio. Development of a tip-leakage flow - part 2:comparison between the ducted and unducted rotor. *J. Fluids Eng.*, 128(4):765–773, 2006b.

G. D. Padfield. *Helicopter flight dynamics.* Blackwell Science, Oxford, 1996.

S. A. Padhani, G .R. Hunt, and T. N. Jukes. The turbulent jet from a slender annular slot ventilated by a self induced flow through the open core. *J. Phys Rev. Fluids.*, 3 (1):014602–0146034, 2018.

L. P. Parlett. Aerodynamic characteristics of a small-scale shrouded propeller at angles of attack from 0^o to 90^o. *NACA-TN-3547.*, 1955.

B. Patter-Rouland, G. Lalizel, J. Moreau, and E. Rouland. Flow analysis of an annular jet by particle image velocimetry and proper orthogonal decomposition. *Measurement Science and Technology*, 12:1404–1412, 2001.

J. L. Pereira. Hover and wind-tunnel testing of shrouded rotors for improved micro air vehicle design. *PhD. Thesis.*, 2008.

F. J. Perry, W. Y. F. Chan, I. A. Simons, R. E. Brown, and G. A. Ahlin. Modelling the mean flow through a rotor in axial flight including vortex ring conditions. *J. American Helicopter Society.*, 52(3):224–238, 2007.

D. A. Peters. Hingeless rotor frequency response with unstead inflow. *Proceedings AHS NASA - Ames Specialists Meeting On Rotorcraft Dynamics, NASA SP - 352, Moffett Field, Calif.*, 1974.

D. A. Peters and S. Chen. Momentum theory, dynamic inflow and the vortex ring-state. *J. American Helicopter Society.*, 27(3):18–24, 1982.

F. N. Piasecki. Compound helicopter with shrouded tail propeller. *US Patent No. 3,241,791*, 1966.

D. J. Pickles, R. B. Green, and M. Giuni. Rotor wake interactions with an obstacle on the ground. *The Aeronautical Journal.*, 122(1251):57–63, 2018.

PIVTechGmbH. Pivpart160 product information, 2019. https://www.pivtec.com/, Last accessed on 14/04/2019.

R.J. Platt. Static tests of a shrouded and a unshrouded propeller. *Tech Report, National Advisory Committee for Aeronautics.*, 1948.

A. K. Prasad. Stereoscopic particle image velocimetry. *Experiments In Fluids*, 29(2): 103–116, 2000.

W. H. Rae and S. Shindo. Comments on v/stol wind tunnel data at low forward speeds. *In 3rd CAL/AVLABS SYmposium, Aerodynamics of Rotary Wing and V/STOL Aircraft, Vol II, Cornel Aerodynamics Laboratory, Buffalo, NY*, 1969.

M. Raffel, C. Willert, S. Wereley, and J. Kompenhans. *Particle Image Velocimetry, A Practical Guide. Second Edition*. Springer, 2007.

J. P. Reeder and F. B. Gustafson. On the flying qualities of helicopters. *NACA-TN-D-1799.*, 1949.

D. Reimer. *Fundamentals of flight: FM 3-04.203*. U.S. Army Field Manual, 2007.

W. Rhee, L. Myers, and D. McLaughlin. Aeroacoustics of vertical lift ducted rotors. *15th AIAA/CEAS Aeracoustics Conference (30th AIAA Aeroacoustics Conference).*, page 3333, 2013.

W. B. Rhodes. Initial military flight tests of the x-22a vstol research aircraft. *J. Aircraft.*, 7(2):169–174, 1970.

E. Ribeiro, T. Polachini, G. Carvalho, J. Romero, and R. Cabral. Theromphysical properties of different olive oils: evaluating density and rheology through a fluid dynamic approach. *European Journal Of Lipid Science And Technology*, 119:1–10, 2017.

M. Ryu, L. Cho, and J. Cho. Aerodynamic analysis of the ducted fan for a vtol uav in crosswinds. *Transactions of the Japan Society for Aeronautical and Space Sciences.*, 59(2): 47–55, 2016.

M. Ryu, L. Cho, and J. Cho. The effect of tip clearance on performance of a counter-rotating ducted fan in a vtol uav. *Japan Society.*, 60(1):1–9, 2017.

M. Samimy and S. Lele. Motion of particles with inertia in a compressible free shear layer. *Physics of Fluids A: Fluid Dynamics*, 3(8):1915–1923, 1991.

O. Savas, R. B. Green, and F. X. Caradonna. Coupled thrust and vorticity dynamics during vortex ring state. *J. American Helicopter Society.*, 54(2):22001, 2009.

J. Scheiman. A tabulation of helicopter rotor-blade differential pressures, stresses, and motions as measured in flight. *NASA TM-X 952*, 1964.

W. C. Schultz and C. Vistai. Thrust enhancing propeller duct assembly for water craft . *US Patent No. 4,637,801*, 1984.

A. N. Sekundov. The propogation of a turbulent jet in an opposing stream. *In turbulent jets of air, plasma and real gas, (ed. G.N. Abramovish), Moscow Aviation Inst.*, pages pp.99–1097, 1969.

C. Sheng, Q. Zhao, and N. P. Bi. Numerical investigations of ducted fan hover performance for fiw applications. *53rd AIAA Aerospace Sciences Meeting.*, page 1935, 2015.

M. Sivapragasam, M.D. Deshpande, S. Ramamurthy, and P. White. Turbulent jet in confined counterflow. *Sadhana*, 39(3):713–729, 2014.

S. Skinner. *Study of a C-wing configuration for passive drag and load alleviation.* PhD thesis. Aerospace Sciences Research Division. Univeristy of Glasgow, 2018.

SKYbrary. As3b vicinity sumburgh airport shetland islands uk 2013. URL `https://www.skybrary.aero/index.php/Main_Page#operational-issues`.

P.R. Spalart. On the simplae actuator disk. *J. Fluid Mechanics.*, 494:399–405, 2003.

J. Stack, F. X. Caradonna, and O. Savas. Flow visualizations and extended thrust time histories of rotor vortex wakes in descent. *J. American Helicopter Society.*, 50(3): 279–288, 2005.

W. Stewart. Helicopter behaviour in the vortex-ring conditions. *Aeronautical Research Council, R&M No. 3117*, 1951.

L. Stipa. Experiments with intubed propellers. *NACA Technical Memorandum 655, Washington DC.*, 1932.

K. N. Sui and Y. V. Ivanov. The investigation of the development of a circular jet in the inital region of an opposing jet of large dimension. *Izv. Akad. Nuak Est. SSR, Ser. Tekhn. i Fiz. Nauk*, 8(2):78–83, 1959.

S. Taamallah. A qualitative introduction to the vortex-ring-state, autorotation and optimal autorotation. *In 36th European Rotorcraft Forum, Paris, France*, 2010.

A. Taghizad, L. Binet, J. Jimenez, and D. Heuze. Experimental and theoretical investigations to develop a model of rotor aerodynamics adapted to steep descents. *American Helicopter Society, 58th Annual Forum,Montreal*, 2002.

K. Taira, S. L. Brunton, S. T. M. Dawson, C. W. Rowley, T. Colonius, B. J. Mckeon, O.T. Schmidt, S. Gordeyev, V. Theofilis, and L. S. Ukeiley. Modal analysis of fluid flows: An overview. *AIAA Journal*, 55(12):4013–4041, 2017.

R .T. Taylor. Experimental investigation of the effect of some shroud design variables on the static thrust characteristics of a small-scale shrouded propeller submerged in a wing. *NACA-TN-4126.*, 1958.

J. F. Thompson and S. C. Roberts. Shrouded propeller research at mississippi state university leading to application of the united states army xv-11a. *Proceedings of the CAL/USAAVLABS Symposium on Aerodynamic Problems Associated with V/STOL Aircraft, Vol II: Propulsion and Interference Aerodynamics, Buffalo*, 1966.

A. Vuillet. Operational advantages and power efficiency of the fenestrons as compared to a conventional tail rotor. *Vertiflite.*, 35(5):24–29, 1989.

A. Vuillet and F. Morelli. New aerodynamic design of the fenestron for imporved performance. *12th European Rotorcraft Forum, GarmischPartenkirchen, Federal Republic of Germany, Paper No. 8.*, 1986.

S. Wang. Analytical approach to the induced flow of a helicopter rotor in vertical descent. *J. American Helicopter Society.*, 35(1):92–98, 1990.

H. A. Warda, S. Z. Kassab, K.A. Elshorbagy, and E.A.Elsaadawy. An experimental investigation of the near-field region of free turbulent round central and annular jets. *J. Flow Measurement and Instrumentation*, 10(1):1–14, 1999.

K. Washizu, A. Azuma, J. Koo, and T. Oka. Experiments on a model helicopter rotor operating in the vortex ring state. *J. Aircraft.*, 3(3):225–230, 1966a.

K. Washizu, A. Azuma, J. Koo, and T. Oka. Experimental study on the unsteady aerodynamics of a tandem rotor operating in the vortex ring state. *American Helicopter Society, 22nd Annual Forum, Maryland*, 1966b.

J. F. Wei. Flap-lag stability of helicopter and windmill rotor blades in powered flight and autorotation by a perturbation method. *Master of Science Thesis, Washington University*, 1978.

R. J. Weir. Aerodynamic design considerations for a free-flying ducted propeller. *AIAA Atmospheric Flight Mechanics Conference, Minneapolis*, pages 420–431, 1988.

S. E. Widnall. The stability of a helical vortex filament. *J. Fluid Mechanics.*, 54(4): 641–663, 1972.

S. B. Wilson and S. Schnepf. Ground loiter for oavs and mavs. *American Helicopter Society 58th Annual Forum Proceedings, Montreal, Canada*, 2002.

J. Wolkovitch. Analytical prediction of vortex-ring boundaries for helicopters in steep descent. *J. American Helicopter Society.*, 17(3):13–19, 1972.

G. P. Wright, J. T. Driscoll, and J. D. Nickerson Jr. Handling qualities of the h-76 fantail tm demonstrator. *American Helicopter Society 47th Annual Forum Proceedings, Phoenix, AZ*, pages 123–135, 1991.

H. Xin and Z. Gao. A prediction of the vortex-ring state boundary based on mdel tests. *Transactions of Nanjing University Of Aeronautics and Astonautics.*, 11(2), 1994.

P. F. Yaggy and K. W. Mort. A wind-tunnel investigation of a tilting ducted fan configuration. *NASA TN D-785, Ames Research Centre, Moffett Field, CA and Langley Research Centre, Langley.*, 1961.

P. F. Yaggy and K. W. Mort. Wind-tunnel tests of two vtol propellers in descent. *NASA TN D-1766.*, 1962.

J. E. Yeates. Flight measurements of the vibration experienced by a tandem helicopter in transition, vortex-ring state, landing approach and yawed flight. *NACA TN No. 4409*, 1958.

M. Yoda and H. E. Fiedler. The round jet in a uniform counterflow: flow visualization and mean concentration measurements. *J. Experiments In Fluids*, 21(6):427–436, 1996.

L. Young, E. Aiken, J. Johnson, and J. R. D. Andrews .... New concets and perspectives on mocro-rotorcraft and small autonomous rotary wing vehicles. *AIAA Applied Aerodynamics Conference, St. Louis .*, 2002.

Z. Zhang. *LDA Application Methods: Laser Doppler Anemometry for Fluid Dynamics*. Springer, 2010.

APPENDIX A

APPENDIX A: EXPERIMENTAL METHODOLOGY SUPPLEMENT

A.1 DE-HAVILLAND WIND TUNNEL

A.1.1 WIND TUNNEL BENCHMARKING

VELOCITY PROFILING

Calibration of the wind tunnel velocity was performed by measuring the velocity at 12 positions within the wind tunnel test section as the wind tunnel fan was varied from 7 to 120 rpm. Each of the data points, presented in figure A.1a was sampled for a period of 60s and the average of all of the data points are presented in figure A.1b. The relationship between the wind tunnel speed and the fan rpm was found to be linear.

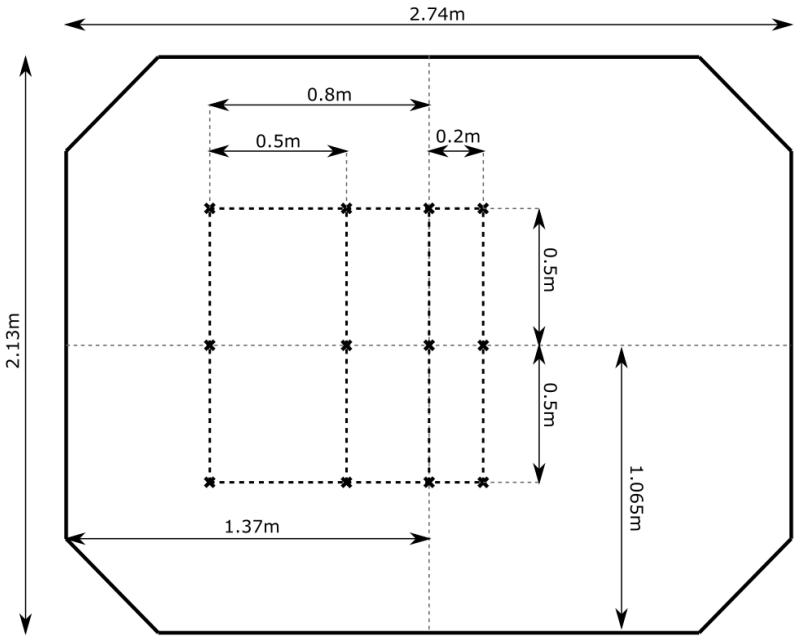

(A) Schematic diagram of the DeHavilland wind tunnel LDA benchmark locations.

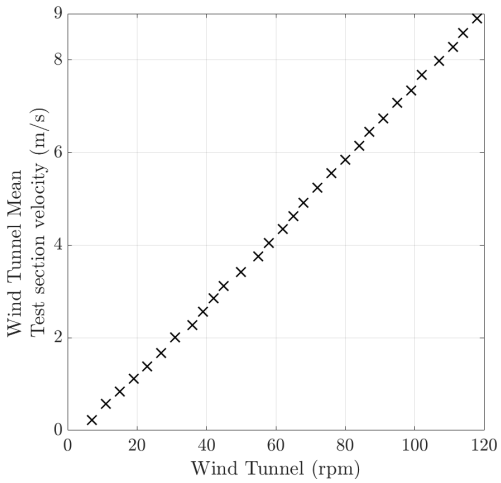

(B) Mean velocity profile.

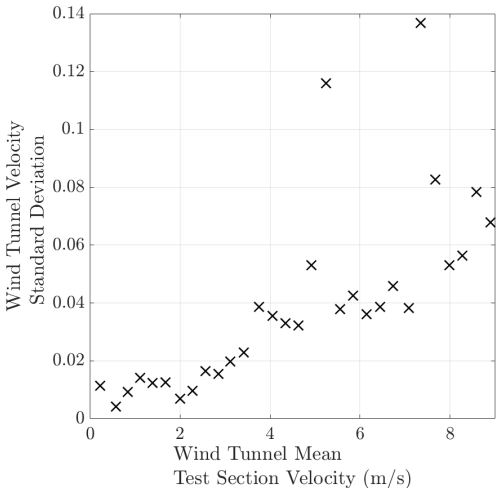

(C) Standard Deviation of the flow field inside of the test section.

FIGURE A.1: Benchmark data for the wind tunnel

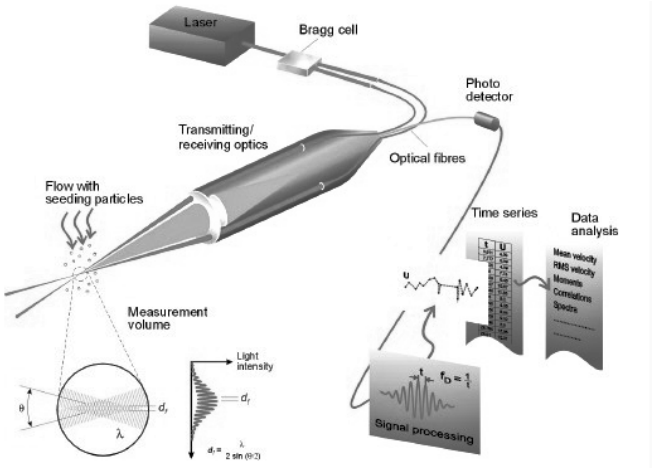

FIGURE A.2: Schematic diagram of a typical experimental arrangement for performing laser doppler anemometry within a wind tunnel. Image taken from DantecDynamics. (2020).

A.2 LDA WORKING PRINCIPLES

Laser Doppler Anemometry is non-intrusive, point measurements system that is commonly used to investigate the velocity of fluid flows, reversing flows, rotating machinery and in chemically reacting or high temperature environments. LDA typically provides high spatial and temporally resolved data. Two component and three component LDA was utilised in this thesis, however a brief description of the principles of single component LDA are provided for simplicity. For more information see Zhang (2010).

A continuous wavelength laser, is split into two lasers using a Bragg cell. The Bragg cell produces two beams of equal intensity with frequencies of f_o and f_{shift} which are focused along fibre optic cables into a probe head. The optical probe focuses the beams and aligns them to intersect at the point of interest. Constructive and destructive interference between the laser beams, at the point of intersection, modulate the light intensity signal of the light beams. This produces parallel planes of high intensity light called fringes. The fringe distance d_f is defined using the equation A.1.

$$d_f = \frac{\lambda}{2\sin(\theta/2)} \tag{A.1}$$

Seeding particles scatter the light as they pass through the measurement volume. The scattered light then monitored using a receiver lens and a photo detector. The scattered light is Doppler shifted. Doppler bursts, which are sinusoidal with a Gaussian envelope can then generated by the photo-detector, which converts the fluctuating light intensity to an electrical signal. At this point it is necessary to state that a filter installed before the photo-detector filters out any background wavelengths to ensure that the signal is clean. It should be noted that the Doppler shift and the

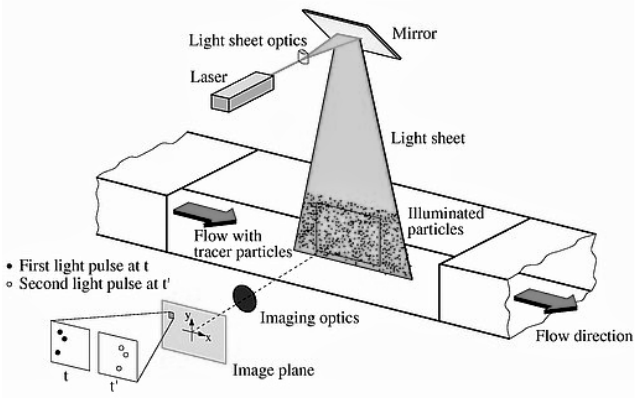

FIGURE A.3: Schematic diagram of a typical experimental arrangement for performing Particle Image Velocimetry within a wind tunnel. Image taken from Raffel et al. (2007).

Doppler frequency f_D are proportional to the velocity component perpendicular to the bisector of the two laser beams. Fast-Fourier Transform of the Doppler bursts allow the Doppler frequency of each particle to be calculated. Therefore the velocity of the particles can be calculated using equation A.2.

$$V = d_f f_D \tag{A.2}$$

A.3 PIV WORKING PRINCIPLES

Particle Image Velocimetry(PIV) is a laser optical measurements technique which yields non-intrusive, indirect velocity measurements of a flow field. It is regularly used in the research of fluid flow, turbulence, spray atomization and combustions processes. Stereoscopic and tomographic PIV allows for all three velocity components of the flow field to be investigated, however only planar (2 component) was used in this thesis. A very brief description of two component PIV and some of the parameters that must be considered when processing and acquiring PIV is presented in this appendix. For more information see Raffel et al. (2007).

In PIV tracer particles contained within the flow field are illuminated using a light sheet. The light sheet is usually generated using a laser however LED light sheets can be used. A camera then captures each light pulse in a separate image frame. Once a sequence of two light pulses has been recorded, a vector map of the instantaneous flow field can be produced. Figure A.3 shows a schematic diagram of a typical experimental arrangement when performing PIV within a wind tunnel.

When evaluating the flow field the region of interest is divided into interrogation areas. Cross correlation [1] is then used to determine the displacement vector of each

[1]Cross-correlation is statistical analysis tool that allows for the objective comparison of two different

interrogation area. It is assumed that all of the particles contained with an interrogation area move homogeneously between the two illuminations. The displacement vector Δx is then used to calculate the velocity of the of the particles contained within the interrogation area using equation A.3 where Δt is the time interval separating two observed states of the tracer.

$$u(x,t) = \frac{\Delta x(x,t)}{\Delta t} \tag{A.3}$$

TRACER PARTICLES

In PIV the velocity of the flow field is measured indirectly, by measuring the displacement of seeding tracer particle in the flow. Therefore, the dynamics of the seeding particles must be considered. It is assumed that the seeding particles follow the flow exactly, the particles do not alter the flow and the particles do not interact with each other (Raffel et al., 2007). The validity of these assumptions was assessed using the particle relaxation time τ_p, the flow time scale of the fluids motion τ_{flow} and the Stokes number S_t. In this thesis the flow was seeded using a olive oil based, Pivtec-GmbH Aerosol Generator PivPart160 series device installed downstream of the test section. The aerosol generator generated mean olive oil particle diameter d_p of $1\mu m$ PIVTechGmbH. (2019). The flow tracing capabilities of a particle of diameter d_p and particle density ρ ($\rho_{oliveoil} \approx 912 kgm^{-3}$ between $6 - 35^oC$ (Ribeiro et al., 2017) is characterised using the particle relaxation time τ_p.)

$$\tau_p = \frac{d_p^2 \rho_p}{18\mu_f} \tag{A.4}$$

The particle relaxation time is a measure the tendency of the particles to attain a velocity equal to the surrounding flow. The flow time scale of the fluids motion τ_{flow} is defined using the equation below (Samimy and Lele, 1991), where δ is a characteristic dimension of the flow (The boundary layer thickness in the centre of the empty wind tunnel, was used as the characteristic dimension for this investigation $\delta = 0.0503m$ Skinner. (2018) and ΔU is the flow slip velocity (Raffel et al., 2007).

$$\tau_{flow} = 10\frac{\delta}{\Delta U} \tag{A.5}$$

The effect of particle dynamic effects when suspended in a specific flow field is quantified by the modified Stokes drag law for small spherical particles (Raffel et al., 2007). The Stokes number is defined as the ratio of particle aerodynamic response

matrices. In this case the matrices relate to the same interrogation area in both image frames **?**

$\delta[m]$	τ_p $[\mu m]$	τ_{flow} $[\mu m]$	S_t
0.05	2.8	50300	5.5x10^{-5}

TABLE A.1: Capability of seeding particles for flow tracing.

time to the flow time scale. Stokes numbers less than $S_t << 1$ indicate that the tracer particles follow the fluid motion accurately. A summary of the associated time scales is shown in table A.1.

$$S_t = \frac{\tau_p}{\tau_{flow}} \tag{A.6}$$

Raffel et al. (2007) showed that the root mean square of the tracing error is less than $< 1\%$ if the Stokes number of the particles is ≤ 0.06. From table A.1 it is clear that the seeding particles used in this investigation can be assumed to follow the flow exactly, are non-intrusive and do not interact with each other within the flow.

Another parameter that affects PIV is the seeding particle image density Keane and Adrianl (1990). Keane and Adrianl (1990) showed that to achieve a valid detection probability of 90% each of the interrogation windows must contain at least fifteen seeding particles. If the seeding particle density per interrogation window, exceeds the contrast of the camera system the image can becomes overexposed. This can impair the detection of individual particles and peak locking can occur as individual particles loose definition.

CALIBRATION

Calibration of the PIV system was performed using the LaVision FlowMaster software which uses automated mark detection, of a LaVision 3085 calibration plate. The calibration generates a transfer function that allow the known geometric properties of the calibration plate, which is mounted in line with the laser light sheet, to be mapped onto the camera chip coordinate system. The average deviation of the de-warped marker position to the ideal regular grid was ≤ 0.2 pixels for each calibration. The camera distance and the perspective angle of the camera to the laser light sheet was calculated during the calibration process. The angle of the camera to the laser light sheet was never greater than 0.001^o for all experimental data sets.

APPENDIX B

APPENDIX B: SHROUDED ROTOR EXPERIMENTAL DATA SUPPLEMENT

B.1 PIV

B.1.1 MEAN FLOW CONVERGENCE

The mean flow field produced by the isolated rotor, the shrouded rotor (Region 1) and the shrouded rotor (Region 2) when the number of image pairs investigated was varied from $N = 100$ to $N = 600$ are shown in figure B.1, B.3 and B.5 respectively. Figure B.2, B.4 and B.6 shows the statistical convergence of the axial and radial velocity components of the flow field produced by the unshrouded rotor, the shrouded rotor (PIV: Region 1) and the shrouded rotor (PIV: Region 2). Using equation B.1 it is clear that the axial and radial velocity components of the flow field converged to within 5% of the average flow field after approximately 540 image pairs were processed.

$$\frac{|\sum_1^N [U]/N - \sum_1^{600} [U]/600|}{[\sum_1^{600} [U]/600]_{max}}.100 \tag{B.1}$$

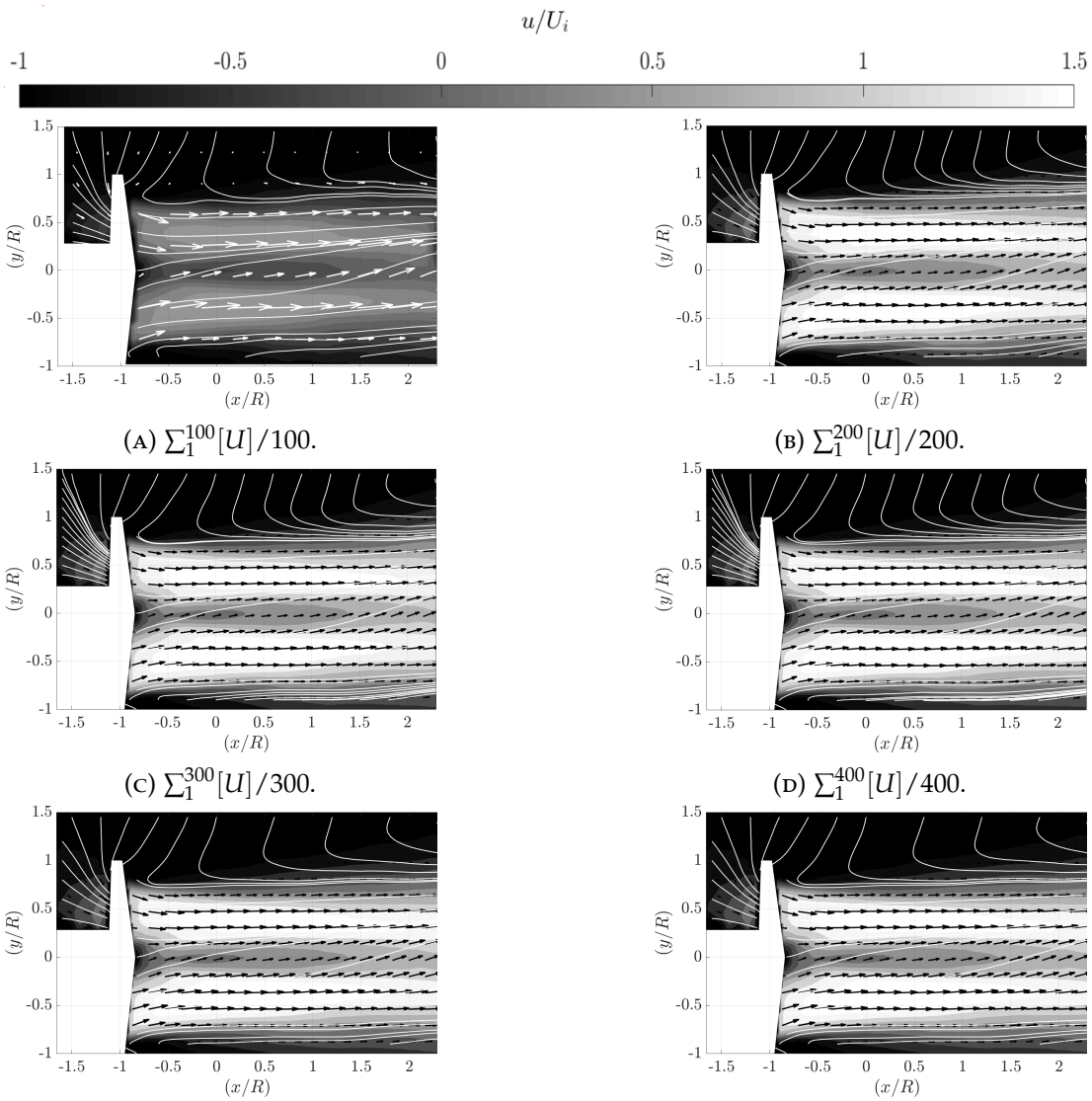

(A) $\sum_1^{100}[U]/100$.

(B) $\sum_1^{200}[U]/200$.

(C) $\sum_1^{300}[U]/300$.

(D) $\sum_1^{400}[U]/400$.

(E) $\sum_1^{500}[U]/500$.

(F) $\sum_1^{600}[U]/600$.

FIGURE B.1: Appendix Convergence of the velocity profile

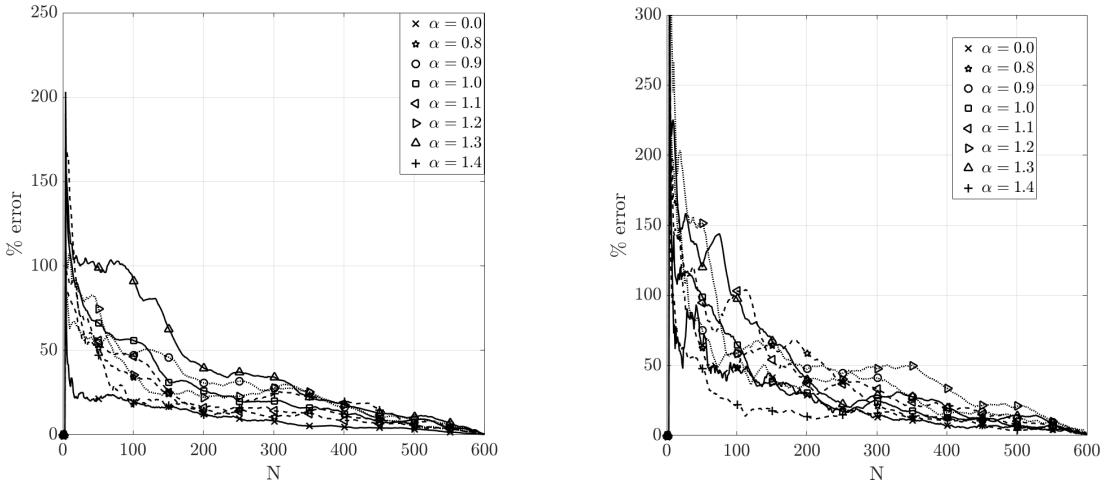

(A) Axial velocity

(B) Radial Velocity

FIGURE B.2: Convergence of the radial and axial velocity components of the Unshrouded rotor at a velocity ratio of $\alpha = 0.0$.

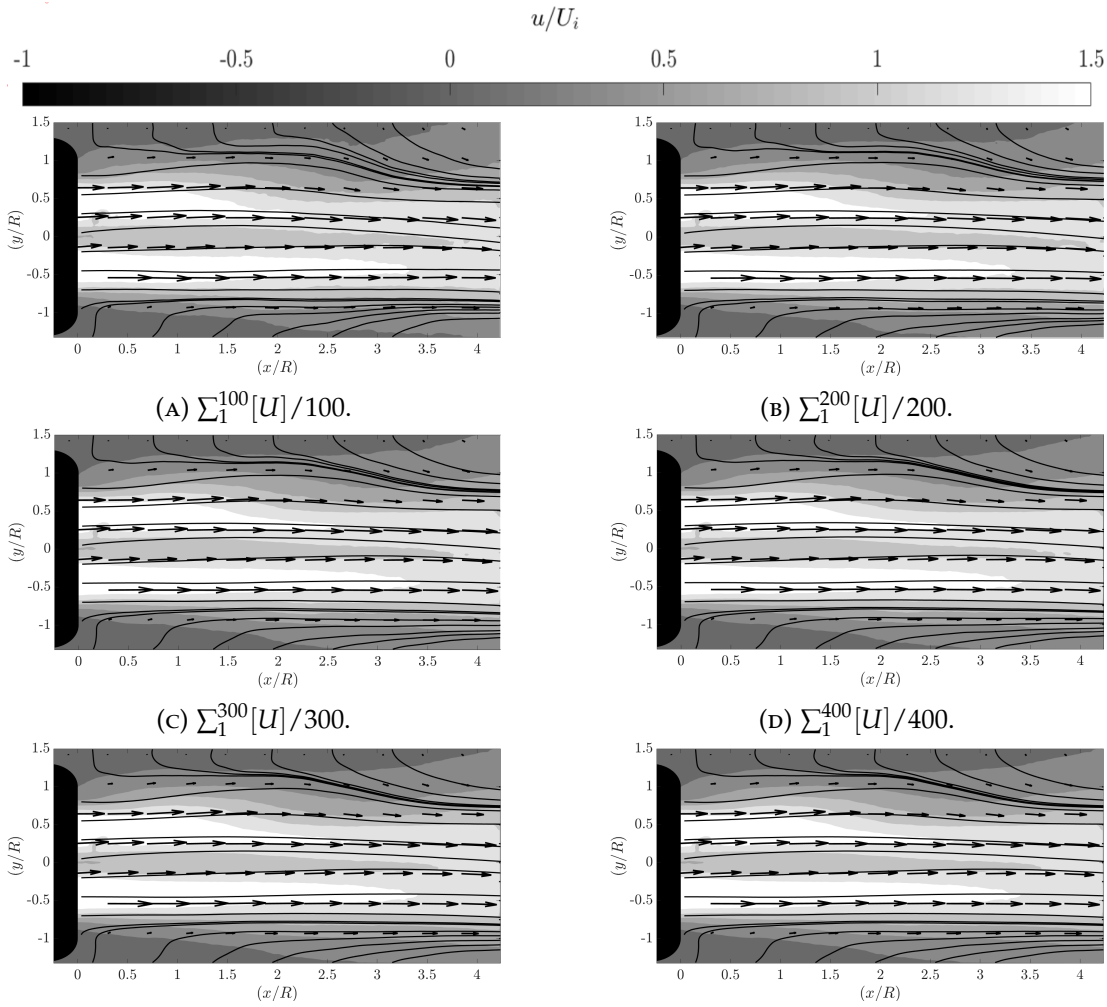

(A) $\sum_1^{100}[U]/100$.

(B) $\sum_1^{200}[U]/200$.

(C) $\sum_1^{300}[U]/300$.

(D) $\sum_1^{400}[U]/400$.

(E) $\sum_1^{500}[U]/500$.

(F) $\sum_1^{600}[U]/600$.

FIGURE B.3: Appendix Convergence of the velocity profile of the shrouded rotor at a velocity ratio of $\alpha = 0.0$

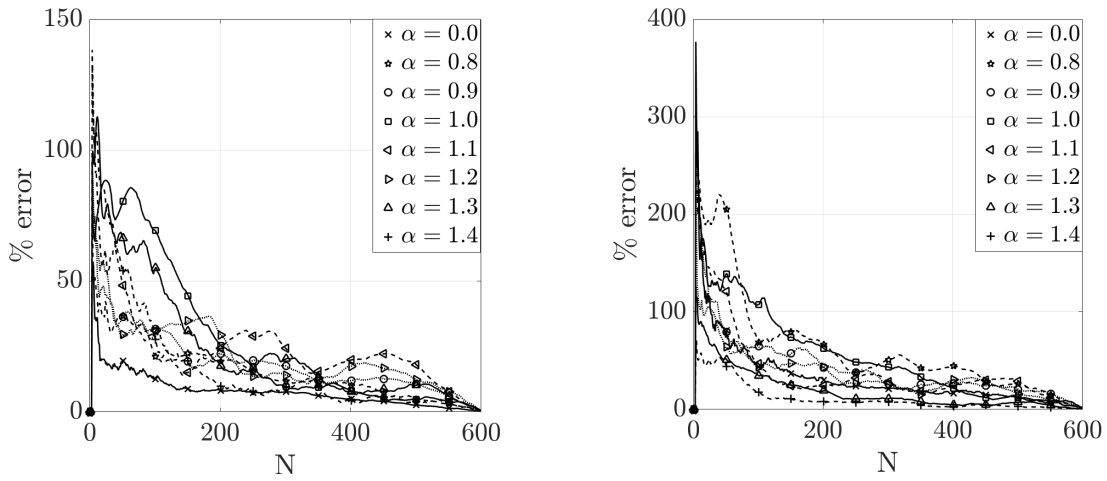

(A) Axial velocity

(B) Radial Velocity

FIGURE B.4: Convergence of the radial and axial velocity components of the Shrouded rotor

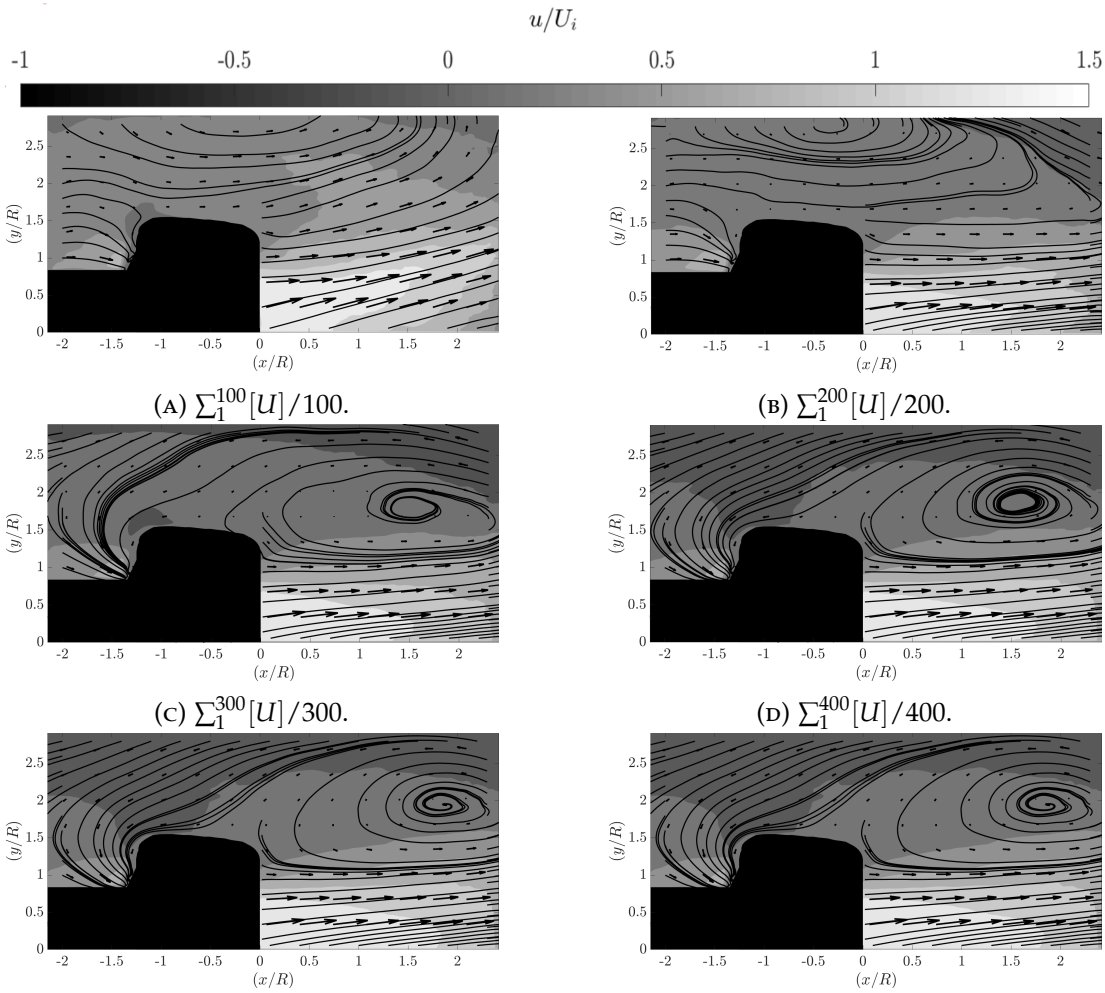

(A) $\sum_1^{100}[U]/100$.

(B) $\sum_1^{200}[U]/200$.

(C) $\sum_1^{300}[U]/300$.

(D) $\sum_1^{400}[U]/400$.

(E) $\sum_1^{500}[U]/500$.

(F) $\sum_1^{600}[U]/600$.

FIGURE B.5: Appendix Convergence of the velocity profile of the shrouded rotor at a velocity ratio of $\alpha = 0.0$ Region 2

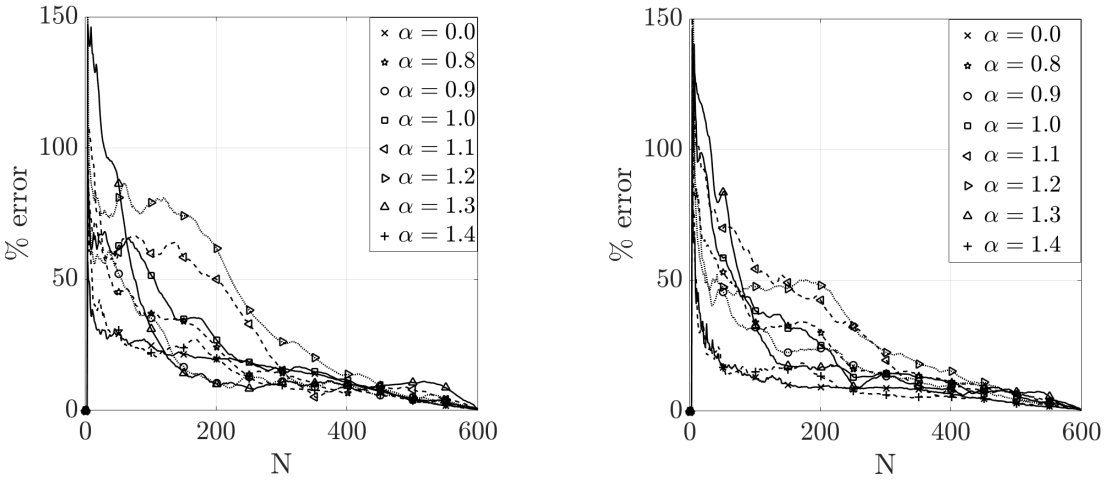

(A) Axial velocity

(B) Radial Velocity

FIGURE B.6: Convergence of the radial and axial velocity components of the Shrouded rotor Region 2

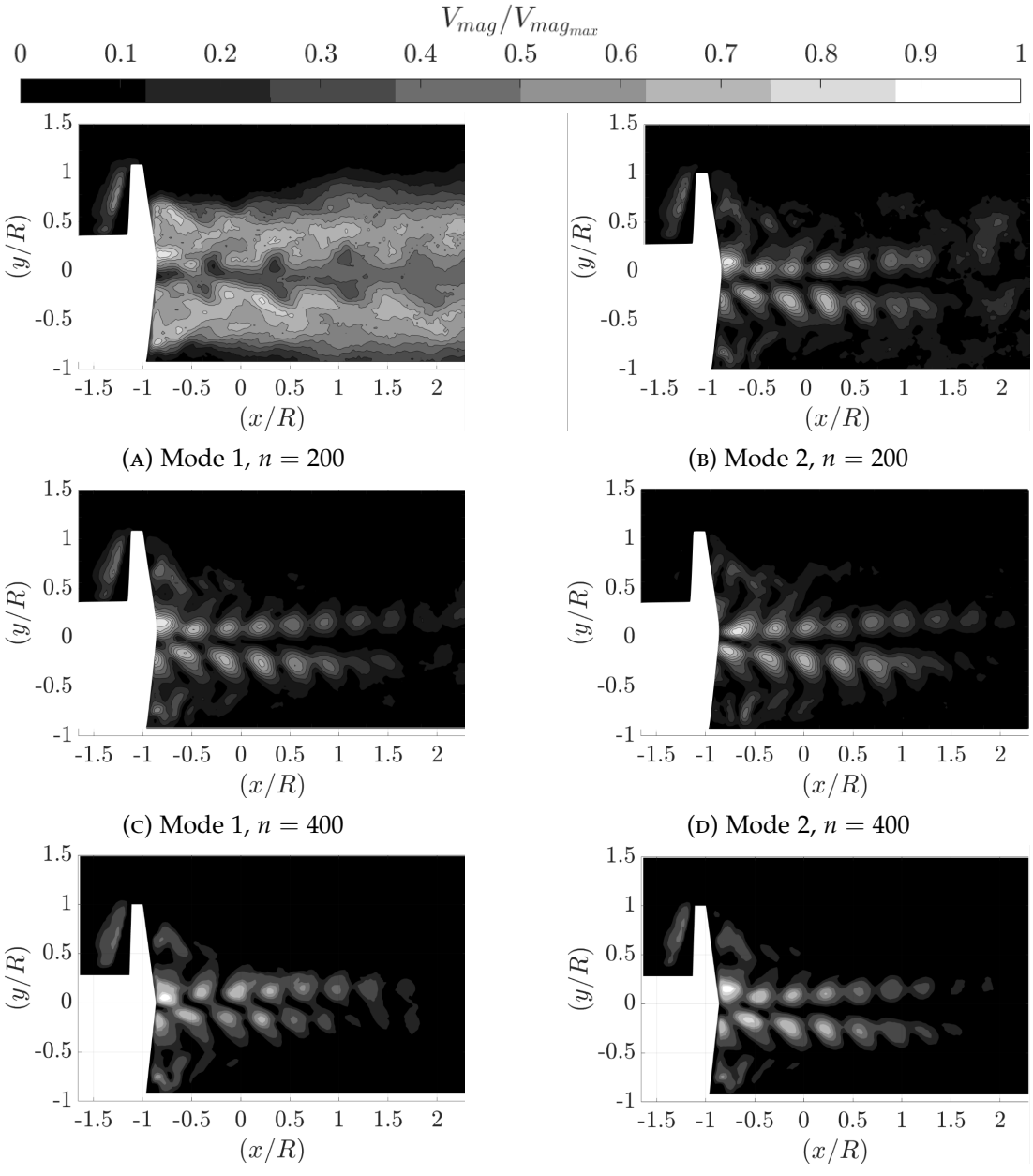

(A) Mode 1, $n = 200$

(B) Mode 2, $n = 200$

(C) Mode 1, $n = 400$

(D) Mode 2, $n = 400$

(E) Mode 1, $n = 600$

(F) Mode 2, $n = 600$

Figure B.7: Convergence analysis demonstrating the structure of the first 2 POD modes produced by the isolated rotor operating at a velocity ratio of $\alpha = 0.0$ as the number of vector maps processed was varied from 200 to 600.

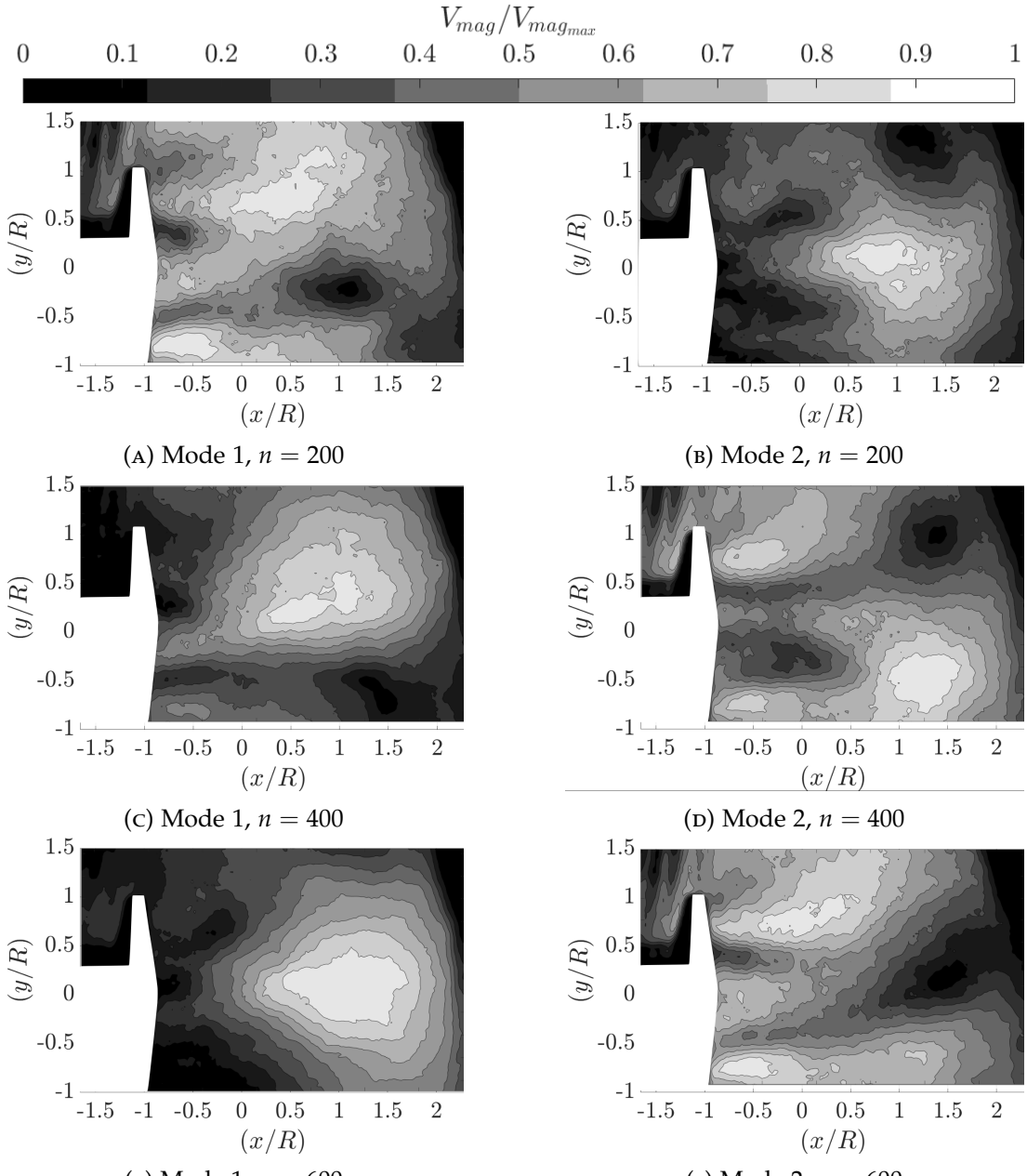

(A) Mode 1, $n = 200$

(B) Mode 2, $n = 200$

(C) Mode 1, $n = 400$

(D) Mode 2, $n = 400$

(E) Mode 1, $n = 600$

(F) Mode 2, $n = 600$

FIGURE B.8: Convergence analysis demonstrating the structure of the first 2 POD modes produced by the isolated rotor operating at a velocity ratio of $\alpha = 1.0$ as the number of vector maps processed was varied from 200 to 600.

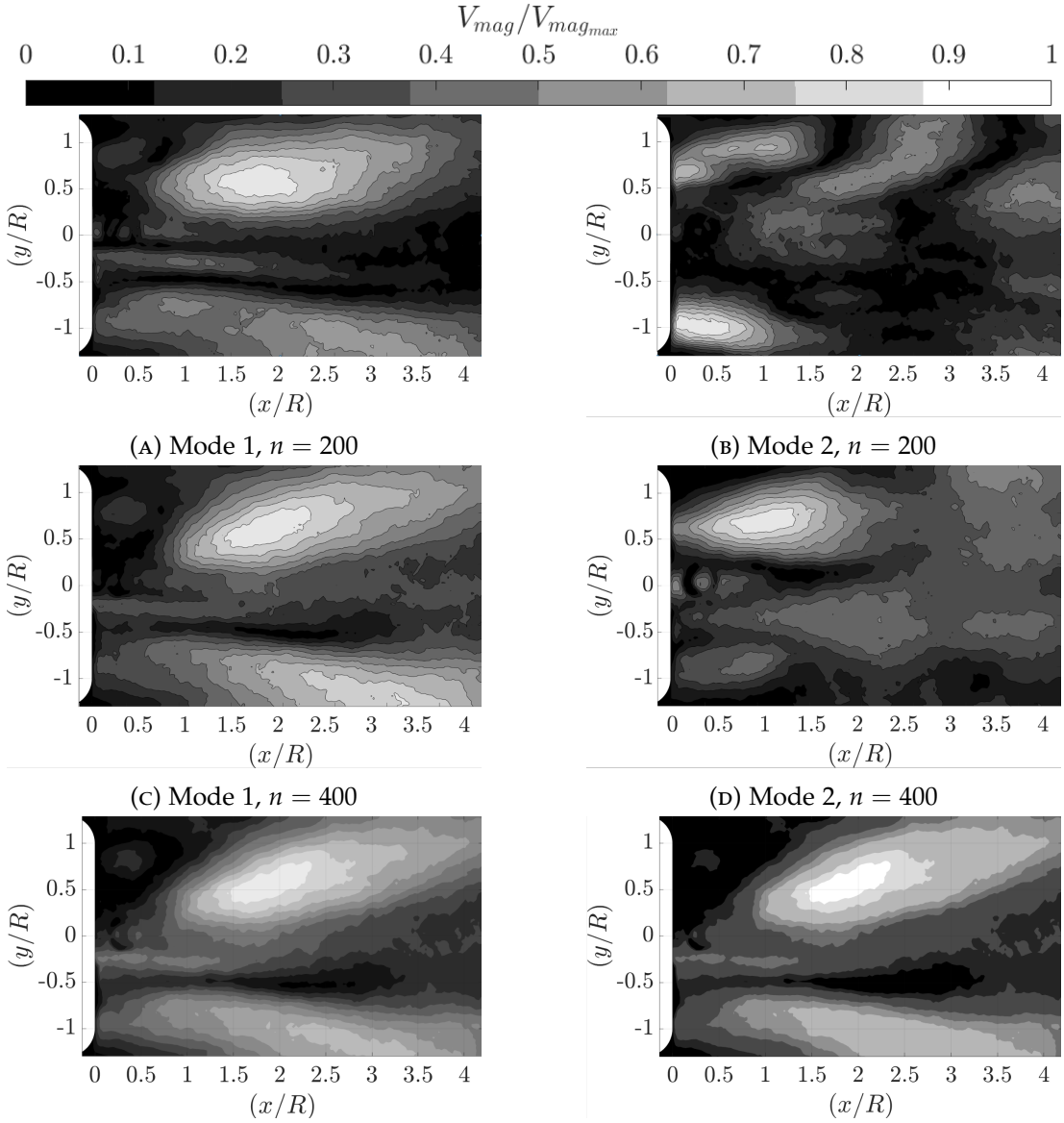

(A) Mode 1, $n = 200$

(B) Mode 2, $n = 200$

(C) Mode 1, $n = 400$

(D) Mode 2, $n = 400$

(E) Mode 1, $n = 600$

(F) Mode 2, $n = 600$

Figure B.9: Convergence analysis demonstrating the structure of the first 2 POD modes produced by the shrouded rotor (PIV Region: 1) operating at a velocity ratio of $\alpha = 0.0$ as the number of vector maps processed was varied from 200 to 600.

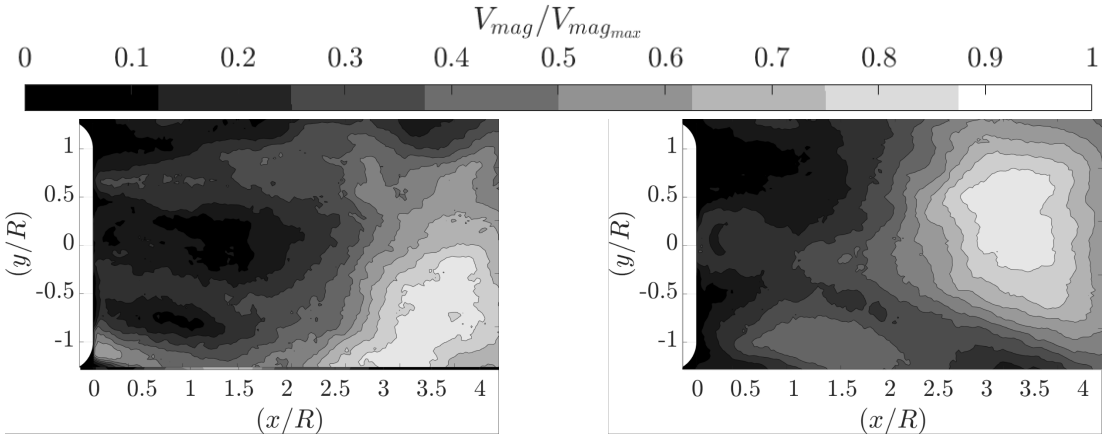

(A) Mode 1, $n = 200$

(B) Mode 2, $n = 200$

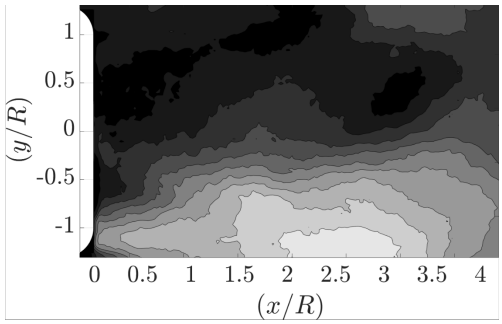

(C) Mode 1, $n = 400$

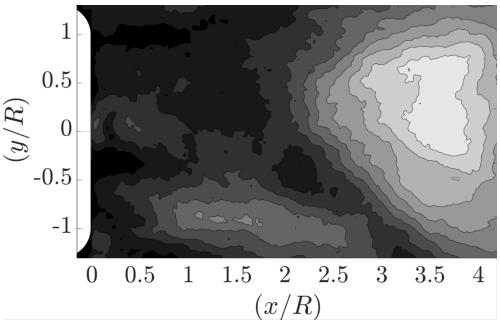

(D) Mode 2, $n = 400$

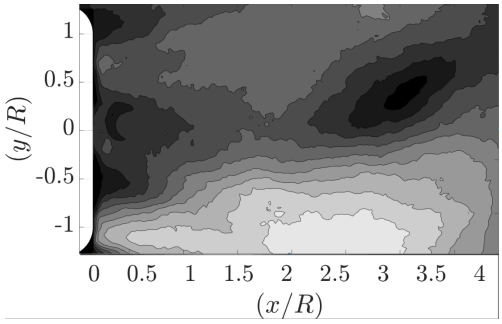

(E) Mode 1, $n = 600$

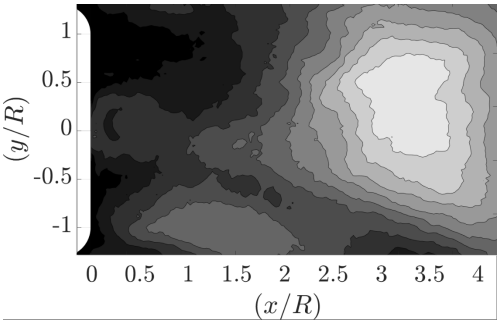

(F) Mode 2, $n = 600$

FIGURE B.10: Convergence analysis demonstrating the structure of the first 2 POD modes produced by the shrouded rotor (PIV Region: 1) operating at a velocity ratio of $\alpha = 0.9$ as the number of vector maps processed was varied from 200 to 600.

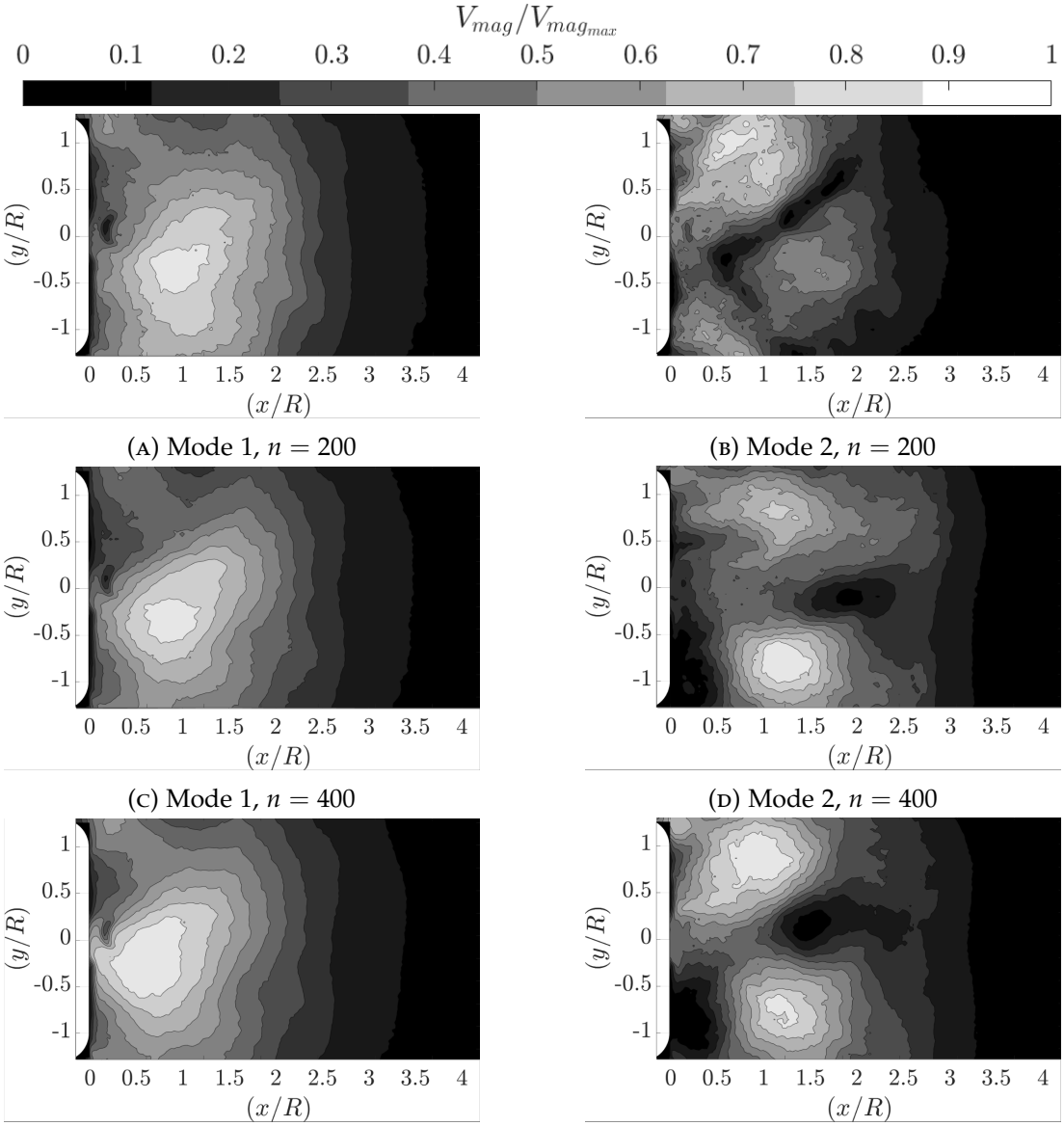

(A) Mode 1, $n = 200$

(B) Mode 2, $n = 200$

(C) Mode 1, $n = 400$

(D) Mode 2, $n = 400$

(E) Mode 1, $n = 600$

(F) Mode 2, $n = 600$

Figure B.11: Convergence analysis demonstrating the structure of the first 2 POD modes produced by the shrouded rotor (PIV Region: 1) operating at a velocity ratio of $\alpha = 1.1$ as the number of vector maps processed was varied from 200 to 600.

APPENDIX C

OPEN CORE ANNULAR JET EXPERIMENTAL DATA SUPPLEMENT

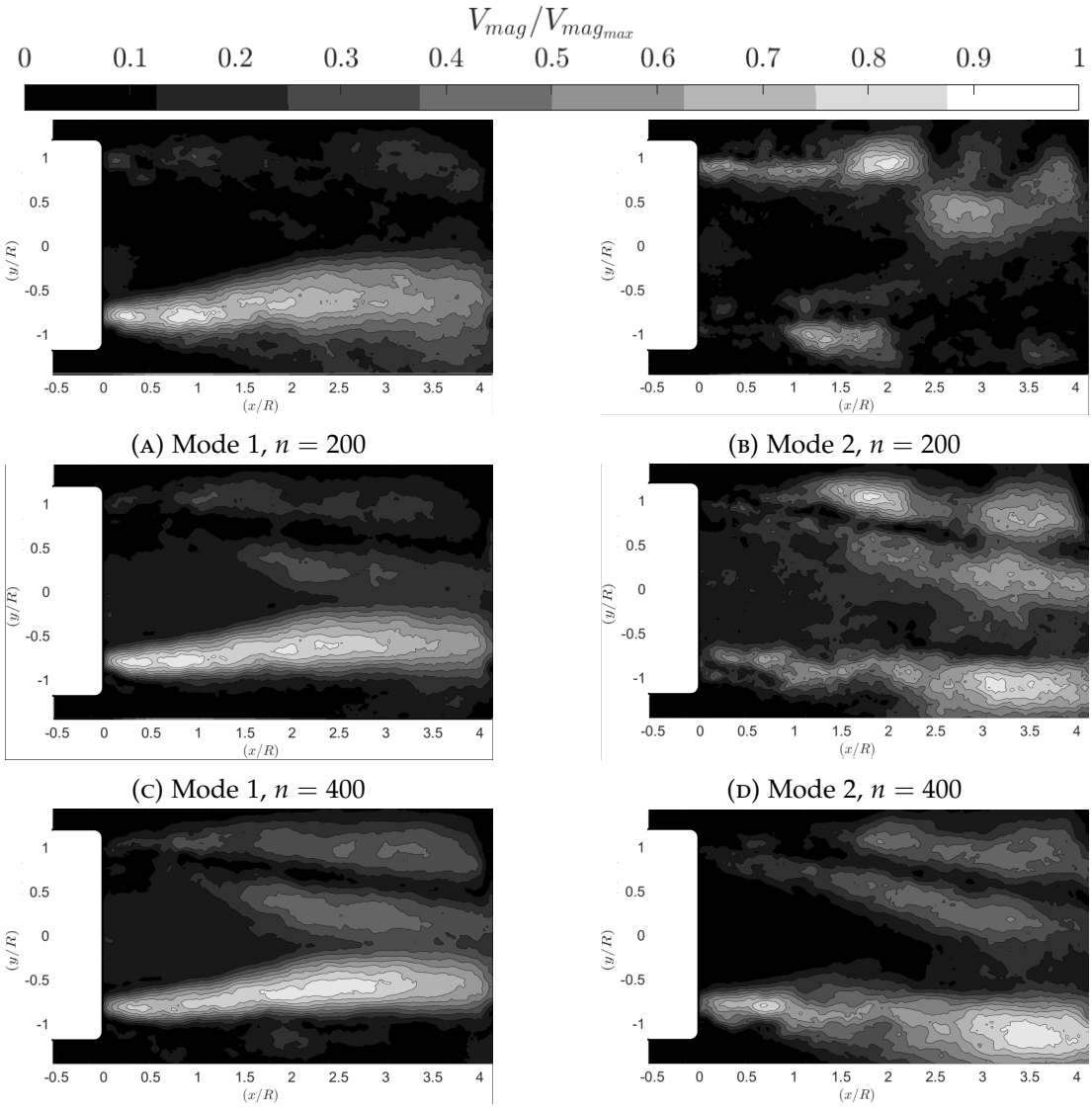

(A) Mode 1, $n = 200$

(B) Mode 2, $n = 200$

(C) Mode 1, $n = 400$

(D) Mode 2, $n = 400$

(E) Mode 1, $n = 600$

(F) Mode 2, $n = 600$

FIGURE C.1: Convergence analysis demonstrating the structure of the first 2 POD modes produced by the ventilated OCAJ (PIV Region: 1) operating at a velocity ratio of $\alpha = 0.0$ as the number of vector maps processed was varied from 200 to 600.

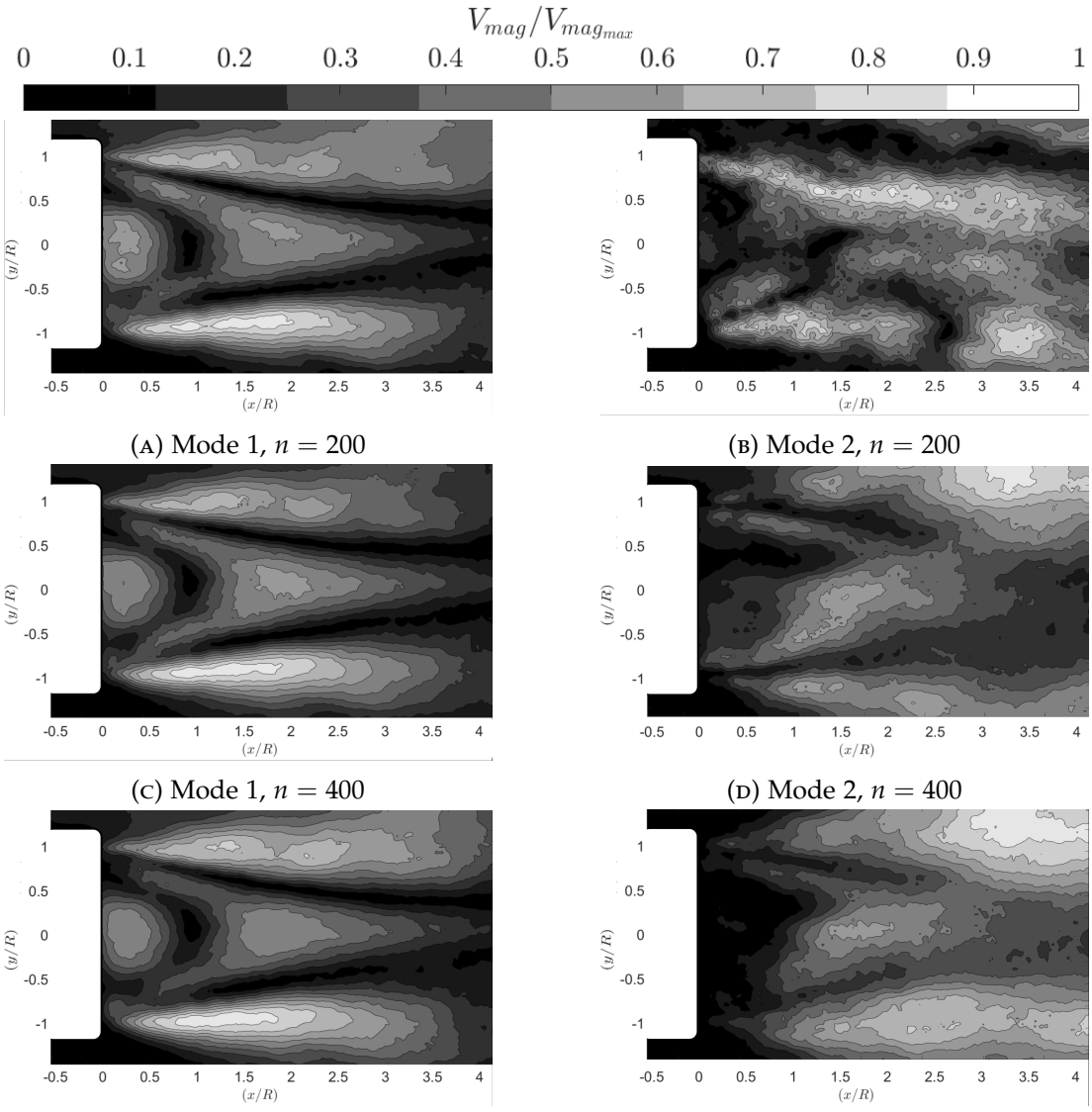

(A) Mode 1, $n = 200$

(B) Mode 2, $n = 200$

(C) Mode 1, $n = 400$

(D) Mode 2, $n = 400$

(E) Mode 1, $n = 600$

(F) Mode 2, $n = 600$

FIGURE C.2: Convergence analysis demonstrating the structure of the first 2 POD modes produced by the ventilated OCAJ (PIV Region: 1) operating at a velocity ratio of $\alpha = 0.5$ as the number of vector maps processed was varied from 200 to 600.

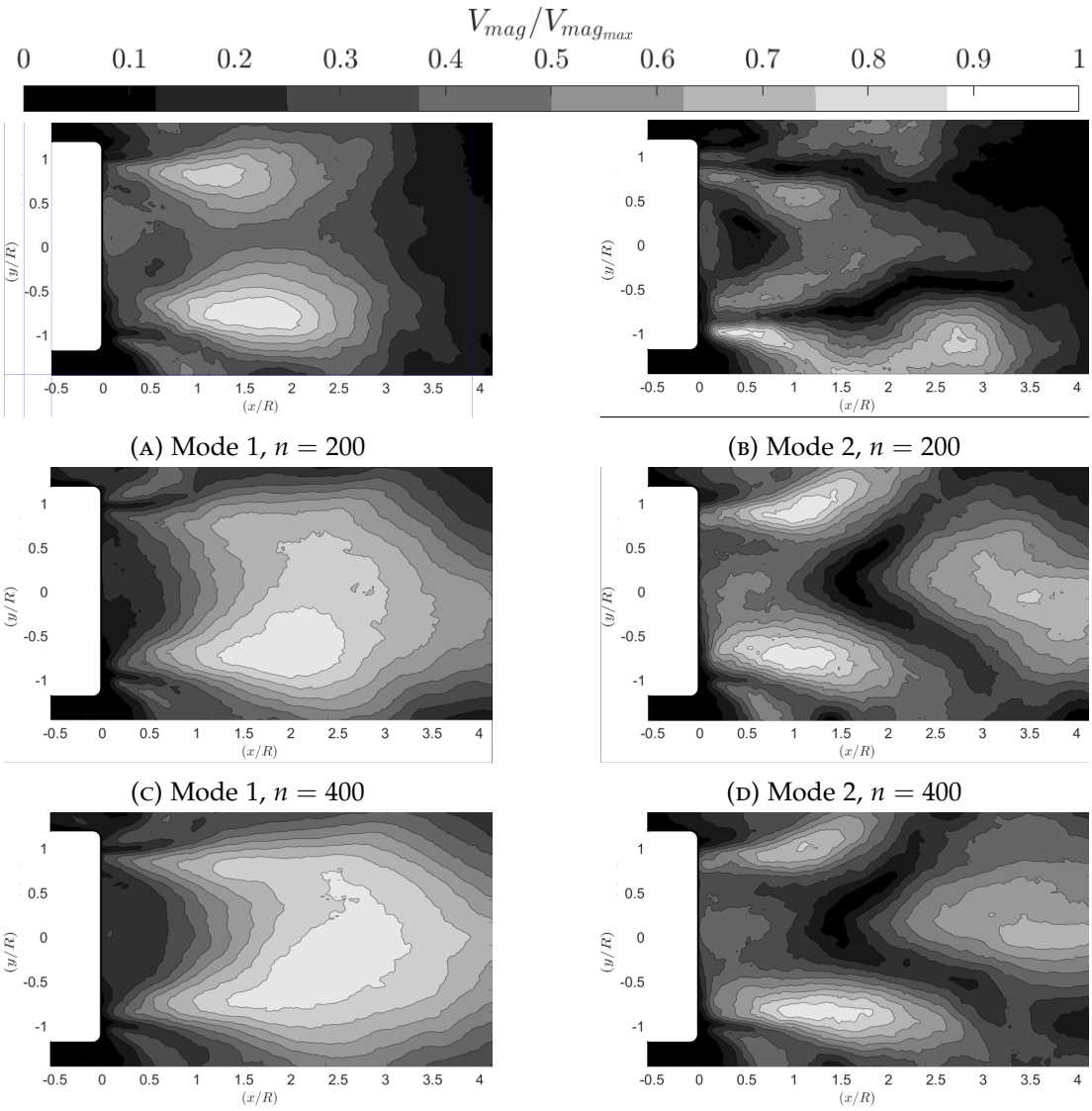

(A) Mode 1, $n = 200$

(B) Mode 2, $n = 200$

(C) Mode 1, $n = 400$

(D) Mode 2, $n = 400$

(E) Mode 1, $n = 600$

(F) Mode 2, $n = 600$

FIGURE C.3: Convergence analysis demonstrating the structure of the first 2 POD modes produced by the ventilated OCAJ (PIV Region: 1) operating at a velocity ratio of $\alpha = 0.6$ as the number of vector maps processed was varied from 200 to 600.

APPENDIX D

APPENDIX C: ROTOR IN AXIAL DESCENT EXPERIMENTAL DATA SUPPLEMENT

D.1 PIV

D.1.1 MEAN FLOW CONVERGENCE

The convergence of the axial and radial velocity components of the PIV results of the flow field produced by the rotor with a large root cut out over a range of descent velocity ratios are presented in figure D.2. The convergence of the flow field was calculated using equation D.1 where $[U]$ is the matrix of velocity vectors contained within the flow field and N is the number of image pairs. The maximum variation of the rolling average from the mean was then divided by the maximum velocity component contained within the average of the entire sequence in order to measure the convergence of the flow field. From figure D.2 it is clear that, over the entire velocity range, the axial and radial velocity components of the flow field converged to within 5% of the average flow field after approximately 500 image pairs were processed.

$$\frac{|\sum_1^N [U]/N - \sum_1^{600} [U]/600|_{max}}{[\sum_1^{600} [U]/600]_{max}}.100 \tag{D.1}$$

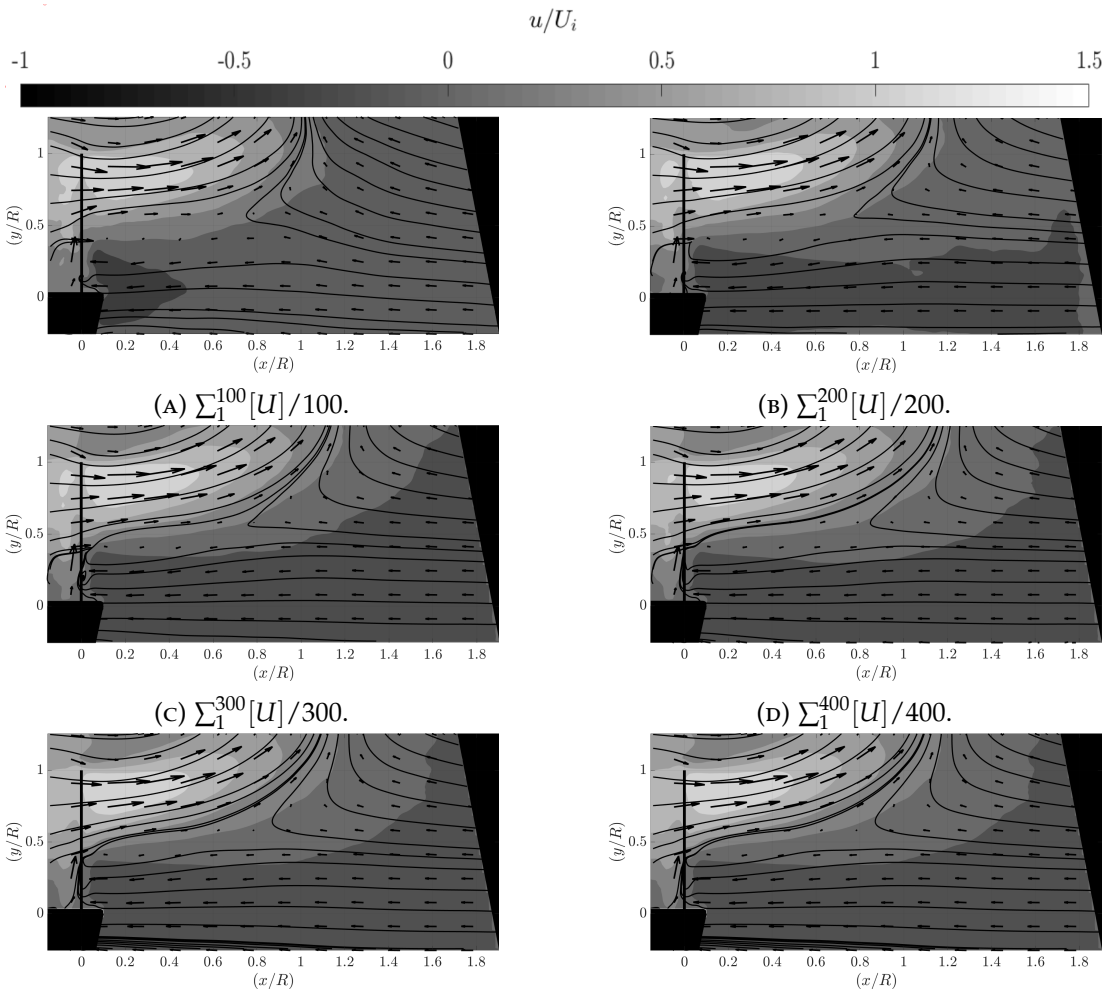

(A) $\sum_1^{100}[U]/100$.

(B) $\sum_1^{200}[U]/200$.

(C) $\sum_1^{300}[U]/300$.

(D) $\sum_1^{400}[U]/400$.

(E) $\sum_1^{500}[U]/500$.

(F) $\sum_1^{600}[U]/600$.

FIGURE D.1: Appendix Convergence of the velocity profile of the shrouded rotor at a velocity ratio of $\alpha = 0.7$.

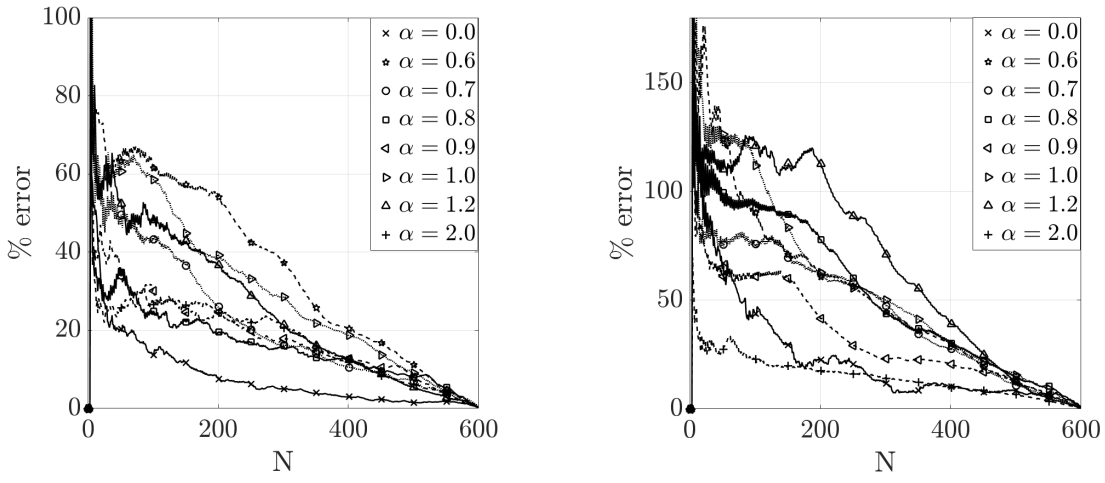

(A) Axial velocity

(B) Radial Velocity

FIGURE D.2: Convergence of the radial and axial velocity components of the Custom rotor Region 2

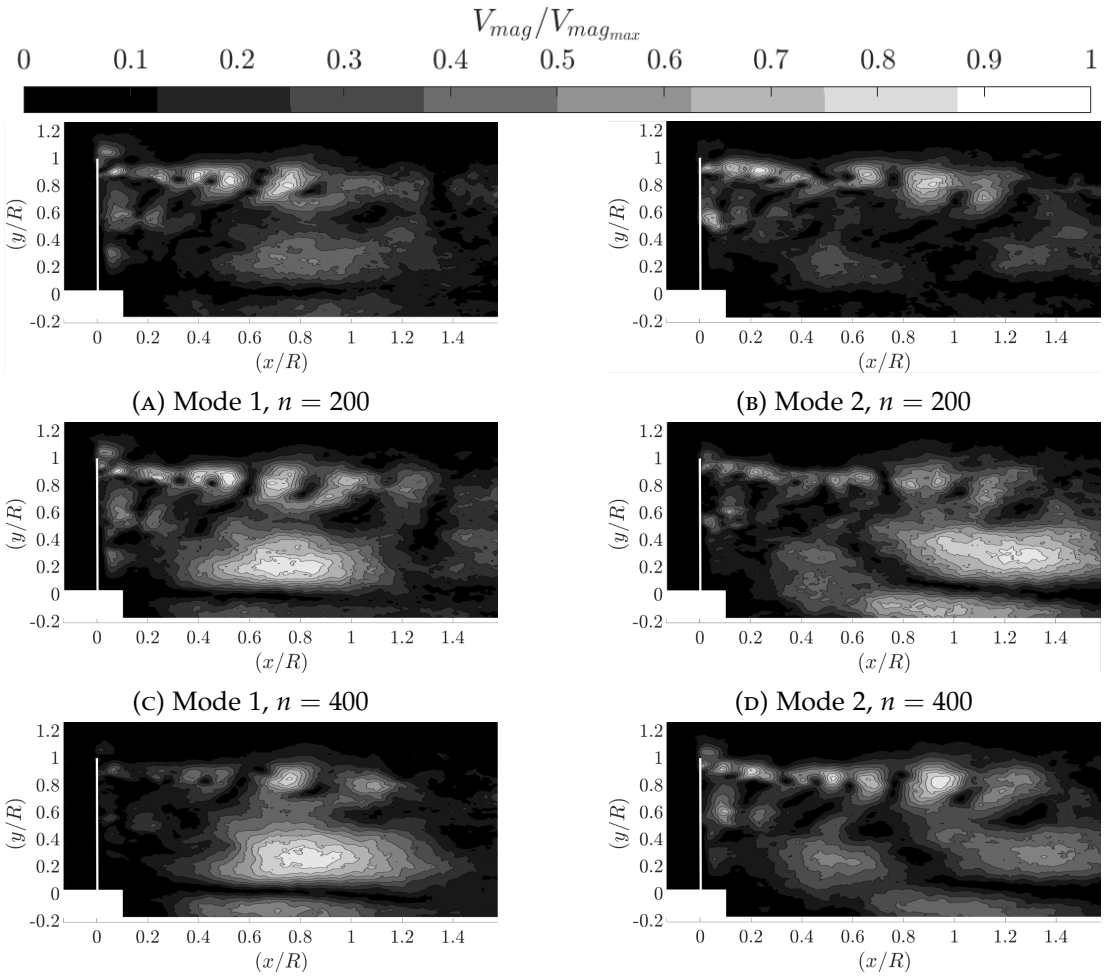

(A) Mode 1, $n = 200$

(B) Mode 2, $n = 200$

(C) Mode 1, $n = 400$

(D) Mode 2, $n = 400$

(E) Mode 1, $n = 600$

(F) Mode 2, $n = 600$

Figure D.3: Convergence analysis demonstrating the structure of the first 2 POD modes produced by the Rotor with a large root cut out $R_c = 30\%$ operating at a velocity ratio of $\alpha = 0.0$ as the number of vector maps processed was varied from 200 to 600.

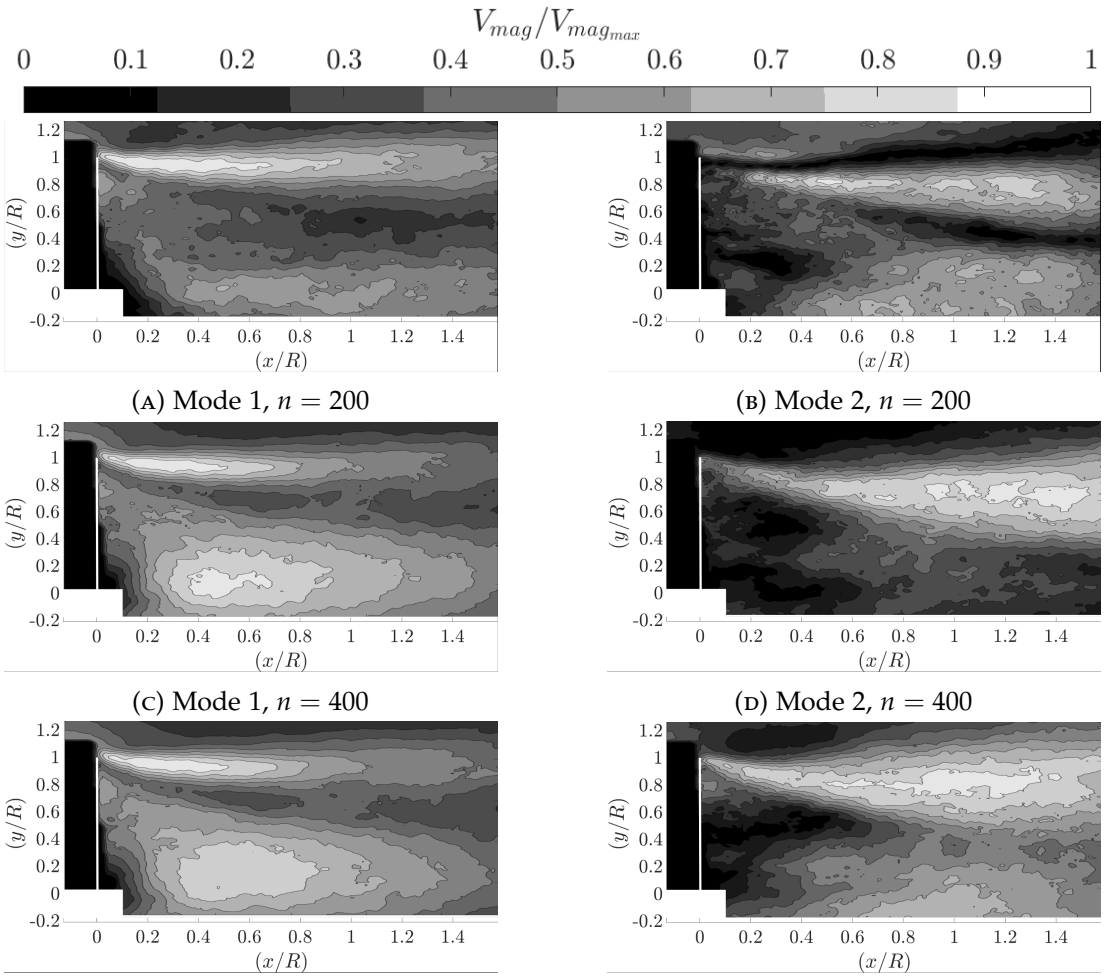

(A) Mode 1, $n = 200$

(B) Mode 2, $n = 200$

(C) Mode 1, $n = 400$

(D) Mode 2, $n = 400$

(E) Mode 1, $n = 600$

(F) Mode 2, $n = 600$

FIGURE D.4: Convergence analysis demonstrating the structure of the first 2 POD modes produced by the Rotor with a large root cut out $R_c = 30\%$ operating at a velocity ratio of $\alpha = 0.6$ as the number of vector maps processed was varied from 200 to 600.

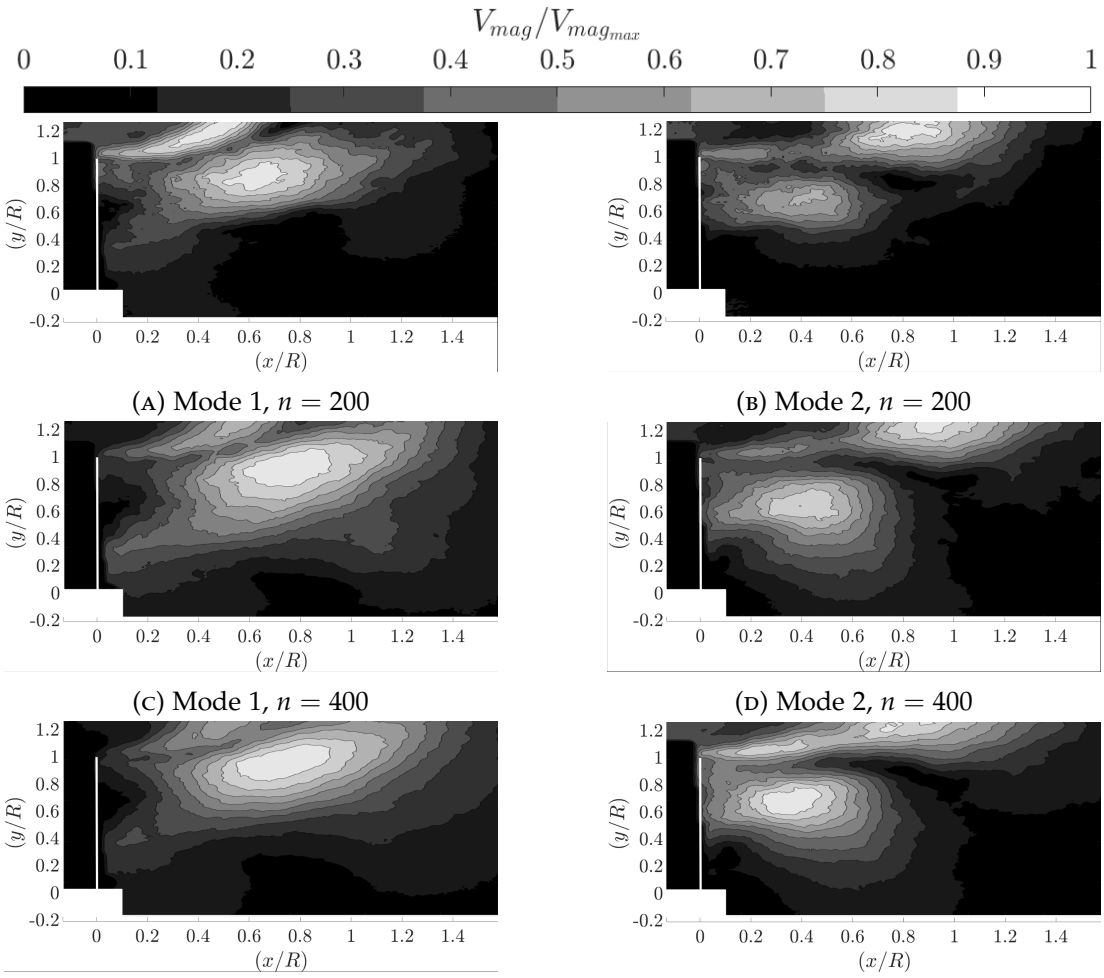

(A) Mode 1, $n = 200$

(B) Mode 2, $n = 200$

(C) Mode 1, $n = 400$

(D) Mode 2, $n = 400$

(E) Mode 1, $n = 600$

(F) Mode 2, $n = 600$

FIGURE D.5: Convergence analysis demonstrating the structure of the first 2 POD modes produced by the Rotor with a large root cut out $R_c = 30\%$ operating at a velocity ratio of $\alpha = 0.8$ as the number of vector maps processed was varied from 200 to 600.

APPENDIX E

APPENDIX D: MOMENTUM THEORY

E.1 MOMENTUM THEORY OF A ROTOR IN AXIAL DESCENT.

(Newman, 1994)

E.1.1 NOMENCLATURE

- Disk Area = A
- wake area = A_2
- atmospheric static pressure = p
- atmospheric density = ρ
- atmospheric pressure above the rotor disc plane = P_u
- atmospheric pressure below the rotor disc plane = P_l
- velocity induced by the rotor = V_i
- velocity in the wake far downstream = V_2

E.1.2 ASSUMPTIONS FOR THIS MODEL:

1. The rotor has an infinite number of blades.
2. The rotor is modelled as a constant pressure difference across the rotor disk area.
3. Constant induced velocity across the entire rotor disk area.
4. Vertical velocity is continuous across and through the entire rotor disk plane.
5. Rotor induced pure axial velocity flow. (i.e. no swirl or radial velocity component to the rotor wake).

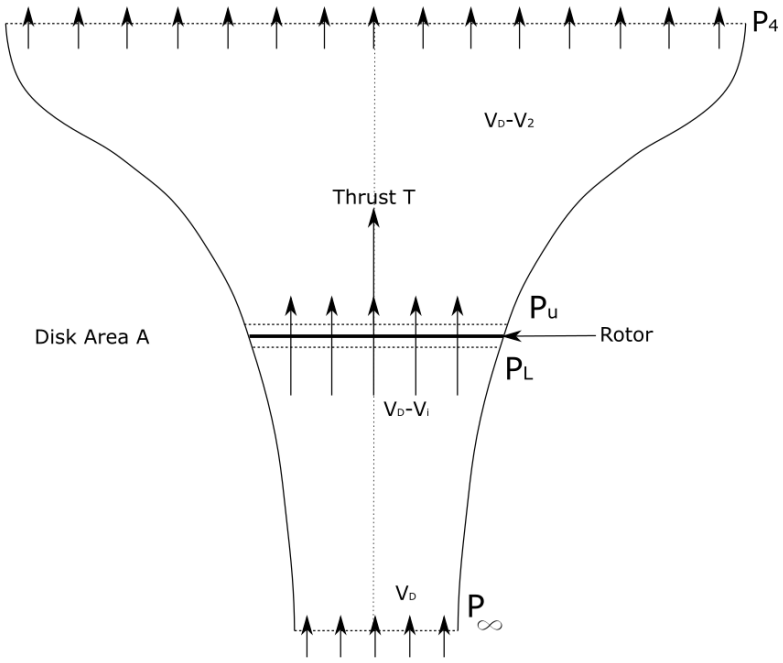

FIGURE E.1: Assumed flow field produced by an actuator disc in descent.

6. The rotors inflow and wake are contained within a continuous stream tube which contains the rotor disc. Flow outside of the stream tube has no effect on the rotor performance.

E.1.3 CALCULATION

Bernoulli equation below the rotor:

$$P_\infty + \frac{1}{2}\rho V_D^2 = P_l + \frac{1}{2}\rho(V_D - V_i)^2 \tag{E.1}$$

Bernoulli equation above the rotor:

$$P_u + \frac{1}{2}\rho(V_D - V_i)^2 = P_\infty + \frac{1}{2}\rho(V_D - V_2)^2 \tag{E.2}$$

Subtracting $P_l - P_u$:

$$P_l - P_u = \rho(\frac{1}{2}V_2^2 + V_2 V_D) \tag{E.3}$$

Rotor Thrust can be expressed as:

$$T = A(P_l - P_u) \tag{E.4}$$

Applying momentum theory:

$$T = \rho A(V_D - V_i)V_2 \tag{E.5}$$

By applying: $M_{flow} = \rho A V_i$ we get

$$T = \rho A V_i V_2 \tag{E.6}$$

Substituting in we get:

$$V_i = \frac{1}{2} V_2 \tag{E.7}$$

and

$$V_i^2 - V_D V_i + V_o^2 = 0 \tag{E.8}$$

By applying $V_D = -V_C$ we get two equations for the variation of the induced velocity of the rotor with axial velocity.

$$V_i^2 + V_C V_i + V_o^2 = 0 \tag{E.9}$$

Applying a non-dimensional form by dividing through by V_o^2 we get

In climb: for $\tilde{V_C} \geq 0$

$$\tilde{V_i}^2 + \tilde{V_C} \tilde{V_i} - 1 = 0 \tag{E.10}$$

In descent: $\tilde{V_C} \leq 0$

$$\tilde{V_i}^2 + \tilde{V_C} \tilde{V_i} + 1 = 0 \tag{E.11}$$

where: $\tilde{V_i} = \frac{V_i}{V_o}$, and $\tilde{V_C} = \frac{V_C}{V_o}$